ELLIPSOMETRY OF THE ELECTRIFIED INTERFACE

A Thesis submitted for the Degree of
Doctor of Philosophy
at the University of Southampton
by

Peter John Pearson

March 1983

Department of Chemistry

To Carol
To Jonathan
To my Parents

UNIVERSITY OF SOUTHAMPTON

ABSTRACT

FACULTY OF SCIENCE

CHEMISTRY

Doctor of Philosophy

ELLIPSOMETRY OF THE ELECTRIFIED INTERFACE

by Peter John Pearson

Use has been made of an automatic nulling ellipsometer, capable of monitoring changes in the polarisation state of reflected light with high sensitivity and speed, to study several aspects of ionic and organic adsorption at the mercury and platinum-aqueous electrolyte interfaces.

The ellipsometer was used to monitor, continuously, the changes of the optical parameters, Δ and Ψ, as a function of electrode potential in studies of ionic adsorption and the adsorption of organic materials onto mercury. The method of computerised data acquisition employed enabled the optical studies of adsorption to be extended by using a wide range of wavelengths in the visible to near ultra-violet spectral region. This additional wavelength information has clearly shown the inadequacy of macroscopic models used to describe ionic adsorption.

For dilute solutions of isoquinoline, the potential dependent changes in Ψ were complicated by effects other than simple changes in inner layer refractive index. For more concentrated solutions the changes in both Δ and Ψ were satisfactorily accounted for by an adsorbed layer exhibiting uniaxial anisotropy. Analysis of the data collected for different wavelengths gave similar results, after allowing for normal dispersion of the inner layer refractive index, which are in agreement with the recently proposed model for this system.

The optical properties of rhodamine B adsorbed on mercury have been determined by *in situ* spectroscopic ellipsometry. After correcting the experimental Δ, Ψ dispersion curves for the effects of an absorbing medium the optical constants of the adsorbed layer were found for all wavelengths in the range 300 nm to 650 nm. The extinction coefficient of the adsorbed dye showed a red shift of about 60 nm together with a weakening of the extinction compared to that of the bulk solid dye.

Analysis of the data obtained for the adsorption of rhodamine B onto platinum failed to yield reasonable film optical properties. The strong similarity between the Δ dispersion curves for the two substrates suggests that the properties of the adsorbed layer on platinum are similarly shifted.

Acknowledgements.

I wish to express my gratitude to Professor Graham Hills for his encouragement, advice and help not only in matters related to this work, and also for giving me the opportunity of working in his group.

I also wish to thank Dr. Gammini Gunawardena for his guidance in the early stages, and for continued friendship and interest throughout all stages of this work.

I would like to express my sincere gratitude to Dr. Robert Greef whose role as mentor and friend has made my stay at Southampton both rewarding and enjoyable.

I would also like to extend my gratitude to my colleagues of the electrochemistry groups at Southampton and Cleveland for their help and frienship. The help of the technical staff, especially that of Mr Roy Horley and Mr Clive Godden, is gratefully acknowledged. I also thank Miss Pat Thomas for help with the typing and to Professor Boris Cahan of Case Western Reserve University for fruitful discussions and for the use of computing facilities in his laboratory.

I am grateful to the S.R.C for financial support and to I.B.M., Manufacturing Technology Centre, Southampton for making available the ellipsometer used in this investigation.

Finally, my sincere thanks to my wife and son for their endless support, encouragement and patience and to my parents for guidance and support.

INDEX

Page

CHAPTER 1: INTRODUCTION

1.1. General and historical introduction

1.2. Ionic adsorption studies

1.3. Organic adsorption studies

1.4. Specroscopic ellipsometry

1.1 General and historical introduction

Ellipsometry, in its broadest sense, is concerned with the analysis of polarised light, the most general state of which is termed elliptical, with no restrictions placed on the cause of the polarisation state. Any polarisation state can be produced by the superposition of two monochromatic electromagnetic waves whose electric vectors are orthogonal. The resultant vectorial sum may be completely characterised by two quantities describing the phase difference, $\delta_x - \delta_y$, and the relative electric field amplitudes, $|E_x|/|E_y|$ of the orthogonal components. The term ellipsometry is now generally reserved to describe the measurement of changes in polarisation state produced when a beam of light of well defined and known polarisation state is specularly reflected from a plane surface. Since changes in ratio of vector amplitudes and phase differences are measured rather than absolute values, the technique is capable of high resolution and is insensitive to fluctuations of the light source intensity. Another reason for the high sensitivity of the method is that the measured quantities are usually azimuth angles and changes of 0.001° can be resolved on modern research instruments.

The development of modern ellipsometry can be traced back to the discovery, by Malus (1775-1812), that light could be polarised by reflection. The effect was quantified sometime later by Fresnel (1788-1827) who presented formulae relating reflection coefficients to angles of incidence and refraction and to refractive index, on the basis of experimental results obtained from transparent media. However, Jamin found that for incident angles near the Brewster angle the reflection of light from many solids and liquids deviated from Fresnel's law, in that appreciable ellipticity in the reflected beam was observed. The failure of these laws was explained by Rayleigh (1842-1919) who, after studying the reflection of light from water and water covered by a 'greasy' contaminant, concluded that surface films were responsible for ellipticity in the reflected beam. The production of elliptically polarised light by a filmed surface was quantified by Drude who, by applying appropriate boundary conditions to Maxwell's equations, obtained a general expression valid for films of any thickness on any substrate. The so called Drude equation forms the basic equation of ellipsometry and relates the two parameters, $\tan\psi = r_p/r_s$ and $\Delta = \delta_p - \delta_s$ to the optical constants of substrate, film and medium. Historical reviews of ellipsometry have been given by Rothen[1] and Hall[2].

One of the main advantages of the ellipsometric and related reflectance techniques in studies of the electrode-electrolyte interface is that it provides a method for the in situ investigation of superficial processes and often yields information specific to surface phenomena not directly accessible by any other technique. Other methods which give information about surface properties (electron spectroscopy and diffraction for example) require the removal of the electrode from the controlled environment of an electrochemical cell and exposure to conditions (vacuum and electron impact) which undoubtedly change the surface region of the sample. The ellipsometric technique has been applied to studies of adsorption, anodic film formation, corrosion and electrodeposition. A number of reviews on applications of ellipsometry[3,4] and the proceedings of four international conferences[5-8] are available.

Recent advances in instrumentation and the availability of dedicated micro-computers have led to a new generation of automatic ellipsometers which have considerably shortened the time required to collect data. Modern ellipsometers can be divided into two instrumental categories: self-compensating and non-compensating. Self-compensating ellipsometers, for the most part, simulate manual operation at greater speed either by mechanical or electronic means. The characterisation of elliptically polarised light by compensating or null ellipsometers, as they are often called, is based on the restoration of linear polarisation by introducing a phase difference between the two orthogonal components of the elliptic state. The phase difference is produced by a compensator (a wave retardation device) and the restored linear polarisation is recognised by the extinction of light when viewed through a linear analyser whose transmission axis is normal to the electric vector of the restored state. The automation of the nulling technique by mechanical means has been described by Ord[9] and electronic automation employing magneto-optical devices (Faraday cell) by Layer[10]. The automatic ellipsometer used in this investigation employs a combination of both mechanical and electronic methods to achieve the null condition and responds to changes in null angles typically within 0.1 s.

Non-compensating ellipsometers in which the elliptic state is determined from the intensity of light reflected from a surface as a function of analyser azimuth have been reported[11,12]. The availability of intensity data from such instruments has been used to advantage by Cahan and Chen[13] to extract a third parameter, the relative reflectivity, which enabled them to determine the optical properties (n and k) and film thickness of the passive film on iron without auxiliary information normally required in normal (two parameter) ellipsometry.

In addition to the speed of operation of modern ellipsometers, considerable improvements in sensitivity have been achieved by more critical design and fabrication of mechanical components and more sensitive electronic methods of angular encoding. With decreased data acquisition times and increased sensitivity, in situ spectroscopic ellipsometry and reflectance techniques offer a potential source of more detailed information on a molecular level. For example, Bewick and Kunimatsu[14] have obtained absorption spectra of water adsorbed on platinum and gold electrodes in the wavelength range corresponding to O-H vibrational energies and have tentatively suggested that changes in the structure of water at the interface are observed.

To gain information on the optical properties of adsorbed species or surface layers one has to assume a suitable model for the interphasal region. In many cases a three layer model is assumed in which the film, of unknown optical constants and thickness, is bounded by the substrate and by electrolyte of known optical properties. The three layer model can only be considered an approximation of the true structure of an electrode-electrolyte interface because it is well established that the strong electric field across the interface perturbs not only the electrolyte adjacent to a superficial film (the diffuse layer) but also the optical properties of a surface layer of the electrode. Under certain circumstances however, the three layer model provides a reasonable basis for the analysis of ellipsometric data and has been succesfully employed, for example, in following the growth of anodic films[15] or in studies of organic adsorption[16], where the changes in Δ and Ψ are generally much larger than diffuse layer and electroreflectance contributions.

In studies of anion adsorption however, the changes in ellipsometric parameters are small and the contribution to the overall optical effect from the diffuse layer and changes in the surface properties of the electrode cannot be ignored. Although several theoretical treatments of the electroreflectance effect have been presented and applied to experimental results, there does not exist a generally accepted nor universally applicable model for the effect. Indeed, recent theoretical treatments have re-examined the hypothetical vacuum-perfect-metal (often called jellium) interface from a microscopic point of view, and concluded that the surface region of a metal cannot be characterised by its bulk optical properties nor can the surface be accurately described in terms of anisotropic or inhomogeneous properties. Nevertheless, ellipsometry has been used as a powerful tool in observing interfacial phenomena and has provided confirmation of, or helped in the formulation of alternatives to, models developed from the more conventional electrochemical approaches.

1.2 Ionic adsorption studies

Many ellipsometric studies of the electrode-elecrolyte interface have been performed using light of one wavelength, usually 546.1 nm (the mercury green line). To some extent this has been due to the time consuming manual adjustment of prism azimuths required to achieve the null condition in earlier ellipsometers. The measurement of ellipsometric parameters for a large number of wavelengths would be exceedingly time consuming and would pose serious problems in the analysis of data collected over extended time scales because of the accumulation of adventitious impurities, invariably present in electrolytes to some degree, at the interface. In addition to temporal considerations, many manual ellipsometers did not have sufficient angular resolution to observe, with any accuracy, the small deviations in the parameter Ψ (typically an order of magnitude smaller than the corresponding changes in Δ). In previous ellipsometric studies of anion adsorption at metal electrodes[17,18] only changes in Δ, at one wavelength, were reported and the analyses presented were necessarily restricted to changes in surface excesses of materials with assumed bulk optical properties and of assumed film thickness.

Although "off null" techniques were developed to monitor changes in the optical properties of the interface continuously, the principle advantage of the null technique was lost since changes in the intensity of light incident on the interface became important. The "off null" techniques were restricted to following effects such as phase formation, where large changes in Δ and Ψ were to be expected. The much smaller changes observed in ionic adsorption studies were measured for a series of discrete electrode potentials, taking a skilled operator several minutes to determine the nulling angles at each electrode potential employed. Apart from the more recent studies of double layer phenomena by modulated reflectance spectroscopic techniques, the electroreflectance effect has been ignored or assumed negligibly small. In analysing reflectance data (Hg[19], Pb[20], and Au[21] in fluoride electrolytes) it was assumed that the linear variation in relative reflectivity with charge on the electrode, over a large range of charges and for a particular wavelength and angle of incidence, was due to the electroreflectance effect. It was further assumed that the small deviations from linearity, observed at extreme cathodic and anodic charges, were due to an increase in the amount of water in the inner layer.

The automatic nulling ellipsometer used in the present study enabled the ellipsometric parameters to be monitored continuously as the electrode potential was swept continuously. The significant reduction in the time required to collect data enabled the changes in Δ and Ψ to be monitored for a wide range of wavelengths of incident light, in a time scale comparable to that required by the earlier manual ellipsometers to record the changes in Δ and Ψ at one wavelength and at a few discrete electrode potentials. Ellipsometric data were recorded for fluoride and sulphate electrolytes (reported in sections 5.1 and 5.1.2 respectively) in the hope that, in addition to improved sensitivity available on the instrument used here, the wavelength dependence would lead to a better understanding of the electroreflectance effect at the mercury-aqueous electrolyte interface.

The studies of chloride adsorption (see section 5.1.1) represent an extension of the previously reported ellipsometric investigations of specific adsorption, in that the effect of wavelength on the potential dependence of Δ and Ψ was studied. This investigation was undertaken to test the validity of the recently proposed models.

1.3 Organic adsorption studies

The changes in Δ and Ψ observed when an organic molecule is adsorbed on a metal substrate are expected to be much larger than the changes observed for ionic adsorption in view of the higher refractive index of most organic compounds compared to the ionic refractivities of simple ions. Even though the adsorption of organic molecules should be easier to observe by ellipsometric techniques, very little has been published on the subject. Again, the previous studies of organic adsorption from electrolyte solutions were normally restricted to a single wavelength of incident light and the ellipsometric parameters extracted by a manual nulling technique for a few discrete electrode potentials. The optical properties of several adsorbed aromatic compounds were found to be uniaxially anisotropic[16,22]. If the properties of adsorbed organic molecules do not differ significantly from the free species in solution then, in principle, the optical constants determined from ellipsometric data at one wavelength should be related to the optical constants at other wavelengths by a dispersion relationship similar to that of the bulk material. One of the aims of this investigation was to extend the work of previous ellipsometric investigations of isoquinoline adsorption onto mercury by a study of the effect of wavelength on the potential dependence of Δ and Ψ to test the suggestions made in the previous work.

1.4 Spectroscopic ellipsometry

In situ spectroscopic methods have been used to obtain information related to the electronic spectra of molecules, exhibiting strongly allowed electronic transitions in the visible spectral region, adsorbed on metal surfaces[23,24]. The problems associated with large and anomolous refractive index changes of the incident medium around the wavelength of maximum absorbance (which causes changes in the measured values of Δ and Ψ in addition to changes due to the properties of an adsorbed layer on the electrode surface) was overcome in Ref. 24 by removing the electrode from the cell in which the adsorbed layer was formed and placing it into a cell containing only base electrolyte.

In a study of the properties of rhodamine B adsorbed on platinum and silver electrodes by modulated reflectance spectroscopy, Plieth[23] has obtained results indicating that the absorbance maximum of the adsorbed dye was significantly shifted. The refractive index of the dye containing electrolyte was taken into account, by Plieth, by empirically shifting the spectrum ($\Delta R/R$ vs. λ) vertically until the regions of the spectrum, remote from the absorbance maximum, coincided with the spectrum recorded under similar conditions but without the dye present in solution. To obtain optical constants of a material from reflectance measurements, which determines the modulus of the complex reflectivity, a knowledge of the phase changes due to reflection is required. The phase information can be calculated from the reflectivity data, if measured over a sufficiently wide range of frequencies, by using the Kramers-Kronig dispersion relations. Experimental measurements of reflectivity, particularly for electrochemical systems, can only be made over a limited frequency range so some method of extrapolating the measured reflectivities to spectral regions either side of the range of interest has to be employed. To assess the feasibility if in situ spectroscopic methods for studying the properties of adsorbed dye molecules, while in contact with an absorbing medium, ellipsometric studies of the adsorption of rhodamine B onto mercury and platinum electrodes were undertaken and are presented in sections 5.3 and 5.3.1

CHAPTER 2: THEORETICAL ASPECTS

2.1 Polarised Light

Monochromatic light may be completely described in terms of its frequency, phase, progagation direction, amplitude and direction of the electric and magnetic vectors. The simplest electromagnetic field is that of a plane wave where the direction of the electric vector is constant and is said to be plane or linearly polarised. The electric vector of a wave of this type varies with position $\mathbf{r}$ and time t according to

$$E(\mathbf{r},t) = [|E| \cos(\omega t - \mathbf{k}.\mathbf{r})]\mathbf{U}_0 \qquad (2.1)$$

where $\mathbf{U}_0$ represents a unit vector in the direction of the linear polarisation, perpendicular to the direction of propagation which is given by the wave vector $\mathbf{k}$ (see Fig. 2.1). Equation (2.1) represents a uniform transverse electric travelling plane wave for which the locus of points in space where the electric field oscillates in phase is a plane. The field at all points over the plane (wave front) are identical in phase, amplitude and polarisation. The distance that separates two such constant phase planes of phase difference 2π defines the wavelength, λ, which is related to $\mathbf{k}$ by

$$|\mathbf{k}| = 2\pi/\lambda \qquad (2.2)$$

The phase velocity of the wave is defined as the speed by which a plane advances in the direction of propagation, so that the magnitude of the field in the plane remains constant. The phase velocity is given by

$$\nu = \omega\lambda/2\pi \qquad (2.3)$$

and hence

$$\mathbf{k} = \omega/\nu \qquad (2.4)$$

The superposition of two such plane waves of the same frequency but different phase and amplitude will in general result in elliptically polarised light. The tip of the electric vector describes a helix in space, or at a given plane in space traces an ellipse as a function of time (see Fig. 2.2). To describe the polarisation state of light, it is generally sufficient to resolve the electric vector into two orthogonal linear components perpendicular to the propagation direction. In the analysis of light reflected or refracted at a plane boundary between two media it is convenient to describe these orthogonal components with respect to the plane containing the incident, reflected and refracted rays. The two vectors are taken to be parallel (p) and perpendicular (s) to the plane of

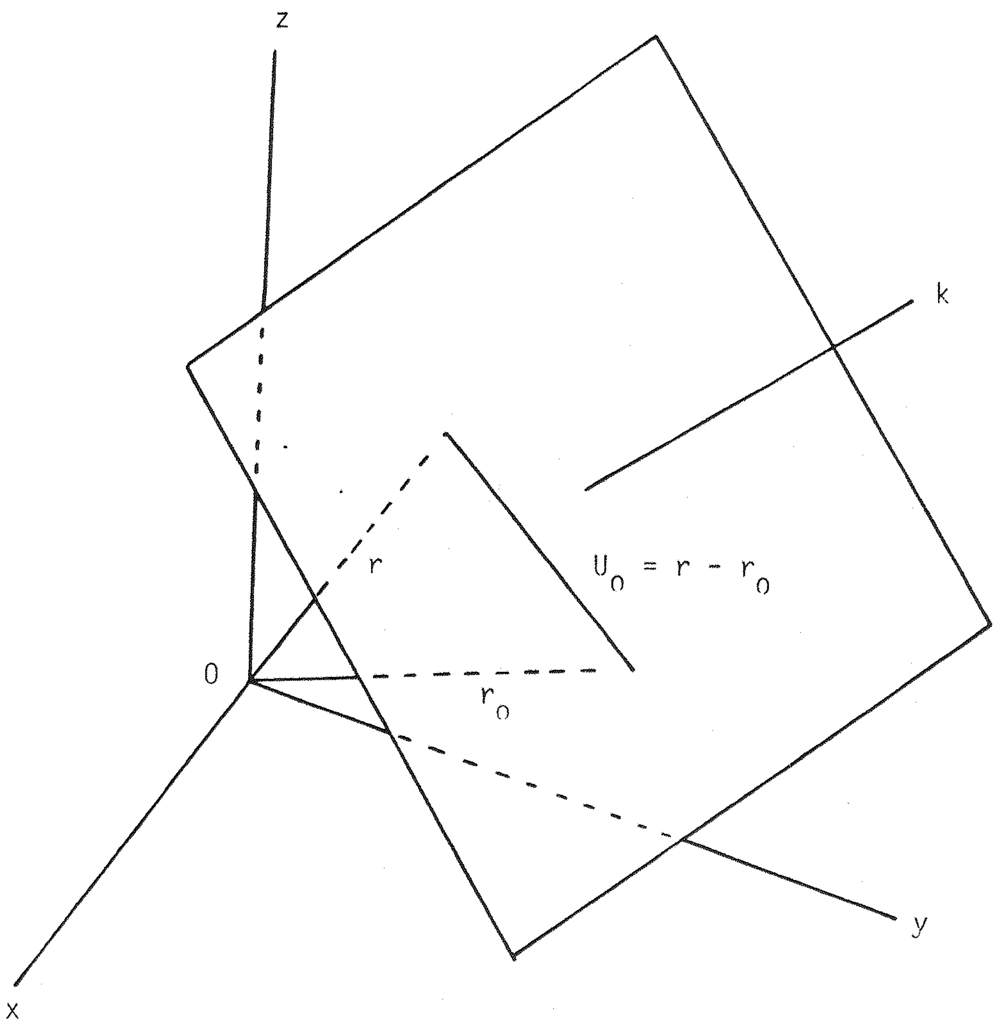

Figure 2.1. A plane wave moving in the k direction.

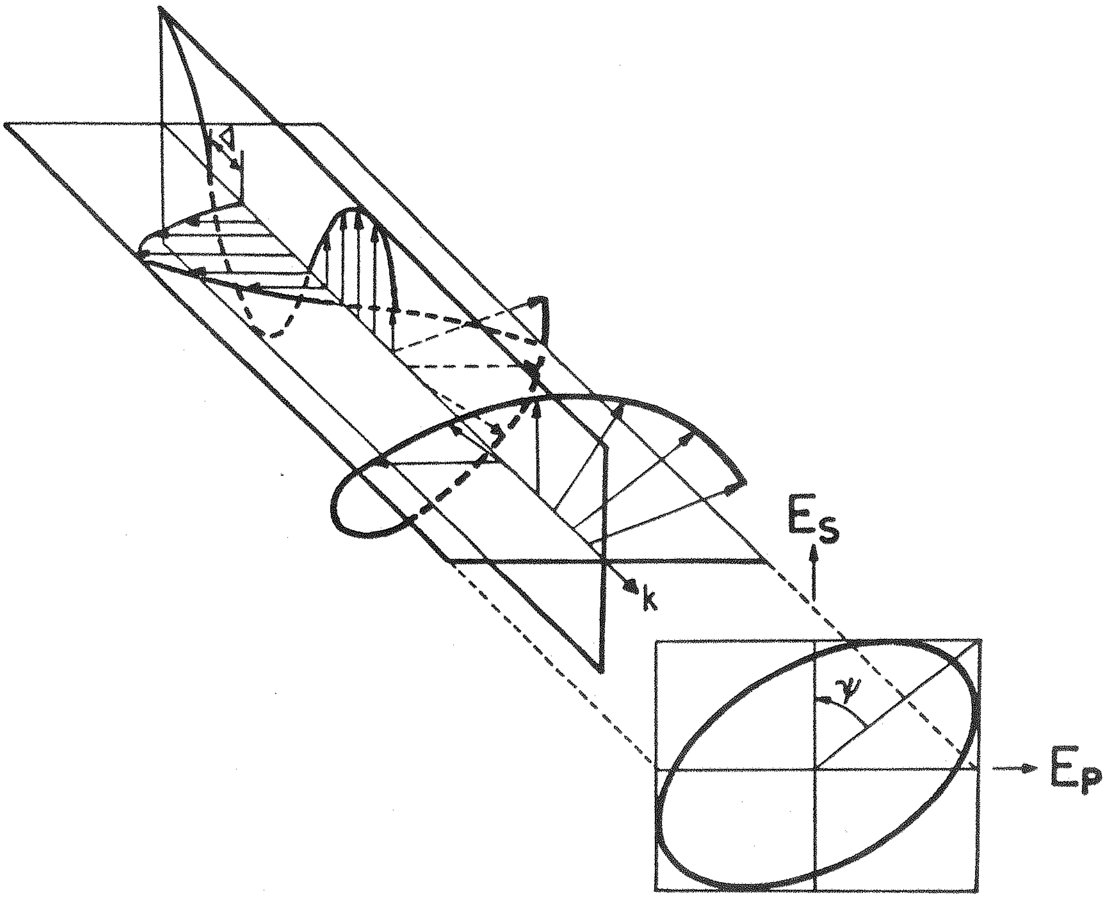

Figure 2.2. Elliptical polarisation resulting from the superposition of two orthogonal linear polarised states.

incidence (Fig. 2.3). The electric vectors for the two orthogonal components may be described mathematically as

$$E_p = |E_p|\cos(\omega t + \delta_p) \tag{2.5}$$

$$E_s = |E_s|\cos(\omega t + \delta_s) \tag{2.6}$$

where δ represents the phase of the wave. The physical parameters describing the ellipse are the ratio of the electric field amplitudes $|E|$ of p and s components, and the difference, Δ, of the time-independent phase of the two components

$$|E_p|/|E_s| = \tan \Psi \tag{2.7}$$

$$\delta_p - \delta_s = \Delta \tag{2.8}$$

The electric and magnetic vectors of all electromagnetic oscillations are known to vary sinusoidally with time. The amplitude and phase of the oscillation of each component is the only information that is required to describe monochromatic light since the time dependence is understood and invariant. The amplitude and phase information about a sinusoidally varying quantity can be combined to form a complex number which is referred to as the phasor representation of that quantity. By using the phasor representation, the addition of two oscillations of different phase may be simply performed as an addition of the two vectors in the complex plane without reference to lengthy trigonometric quantities. The vector describing the x component of the electric field oscillation varies with time as $|E_x|\cos(\omega t + \delta_x)$, which can be expressed in phasor form as

$$E_{xc} = |E_x| \exp(i\delta_x) \tag{2.9}$$

where the subscript c is used to denote that the phasor representation of the quantity is used. To restore the time dependence, the following operation is performed

$$E_x = \mathrm{Re}[E_{xc} \exp(i\omega t)] \tag{2.10}$$

where Re signifies that the real part of the complex quantity is taken. Expanding Eq. (2.10) gives

$$E_x = \mathrm{Re}\{|E_x| \exp[i(\omega t + \delta_x)]\} \tag{2.11}$$

which is equivalent to the starting vector equation since the Gauss equation gives

$$\exp[i(\omega t + \delta)] = \cos(\omega t + \delta) + i\sin(\omega t + \delta) \tag{2.12}$$

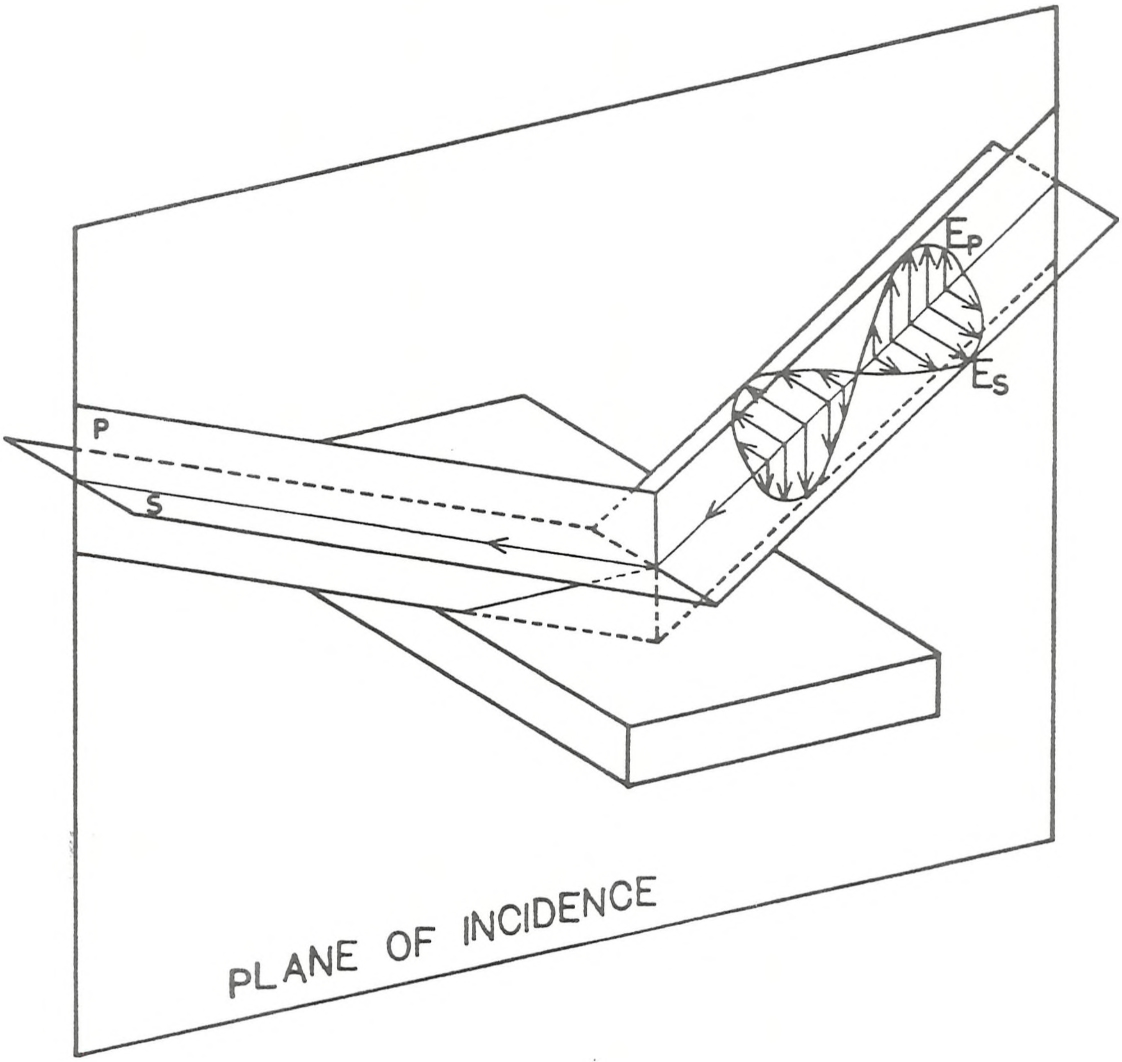

Figure 2.3. Reflection of polarised light. The s and p components have electric vectors normal and parallel to the plane of incidence respectively.

The time dependent term has been chosen as exp(iωt), the alternative being exp(-iωt). This is the convention adopted by the participants of the 1968 International Conference on Ellipsometry25. The conventions agreed upon at that meeting will be used here.

2.2. Reflection from a dielectric surface

The reflection of light from a plane boundary between two isotropic dielectric materials can be quantitatively described by the Fresnel amplitude reflection coefficients (r). These coefficients give the ratio of reflected to the incident electric field amplitudes. The reflection coefficients for p and s components are

$$r_{p1,2} = E_p'/E_p \tag{2.13}$$

$$r_{s1,2} = E_s'/E_s \tag{2.14}$$

and were related to the angles of incidence and refraction and the refractive indices by Fresnel in 1823 on the basis of his elastic theory of light (see Fig. 2.4)

$$r_{p1,2} = \frac{n_1\cos\phi_2 - n_2\cos\phi_1}{n_1\cos\phi_2 + n_2\cos\phi_1} = \frac{\tan(\phi_1 - \phi_2)}{\tan(\phi_1 + \phi_2)} \tag{2.15}$$

$$r_{s1,2} = \frac{n_1\cos\phi_1 - n_2\cos\phi_2}{n_1\cos\phi_1 + n_2\cos\phi_2} = - \frac{\sin(\phi_1 - \phi_2)}{\sin(\phi_1 + \phi_2)} \tag{2.16}$$

Although his theory is no longer accepted, the equations were verified experimentally and the same equations may be deduced from the electromagnetic theory of light. The angles of refraction may be calculated using Snell's law.

$$n_1\sin\phi_1 = n_2\sin\phi_2 \tag{2.17}$$

When $n_2 > n_1$ it follows from Snell's law that $\phi_1 > \phi_2$ so that from Eq. (2.16) r_s is negative for all values of ϕ_1 while r_p is positive at $\phi_1 = 0°$ and decreases until it is zero when $\phi_1 + \phi_2 = 90°$ since $\tan\pi/2$ is infinite. The angle of incidence at which this occurs is called the polarising or Brewster angle (ϕ_p). As ϕ_1 increases beyond ϕ_p, r_p becomes more negative. The negative sign associated with the reflection coefficients are indicative of a phase shift of π radians. Thus, r_s is always out of phase by π radians, whereas, r_p is only out of phase with respect to the incident beam if $\phi_1 > \phi_p$.

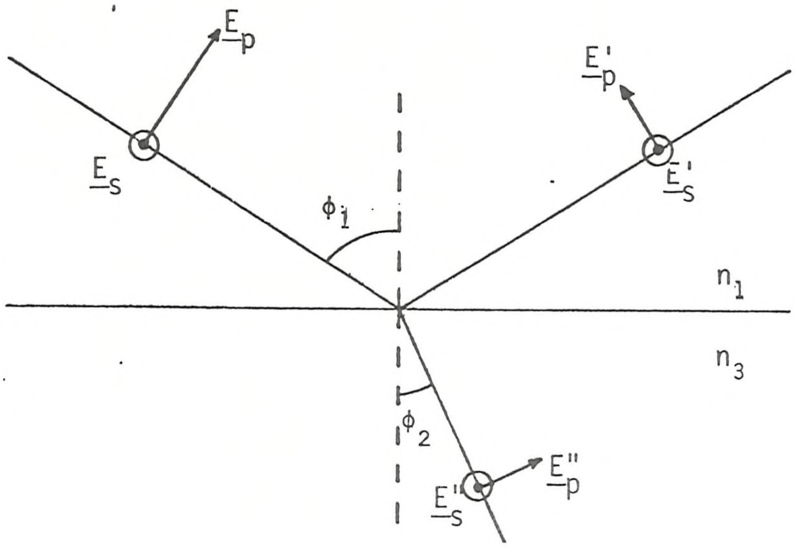

Figure 2.4. Reflection and refraction at a dielectric surface. The vectors $\underline{E}_s$ are normal to the plane of incidence and are denoted by the symbol ⊙; ϕ_1, angle of incidence; ϕ_2, angle of refraction; n_1, refractive index of incident medium; n_2, refractive index of substrate.

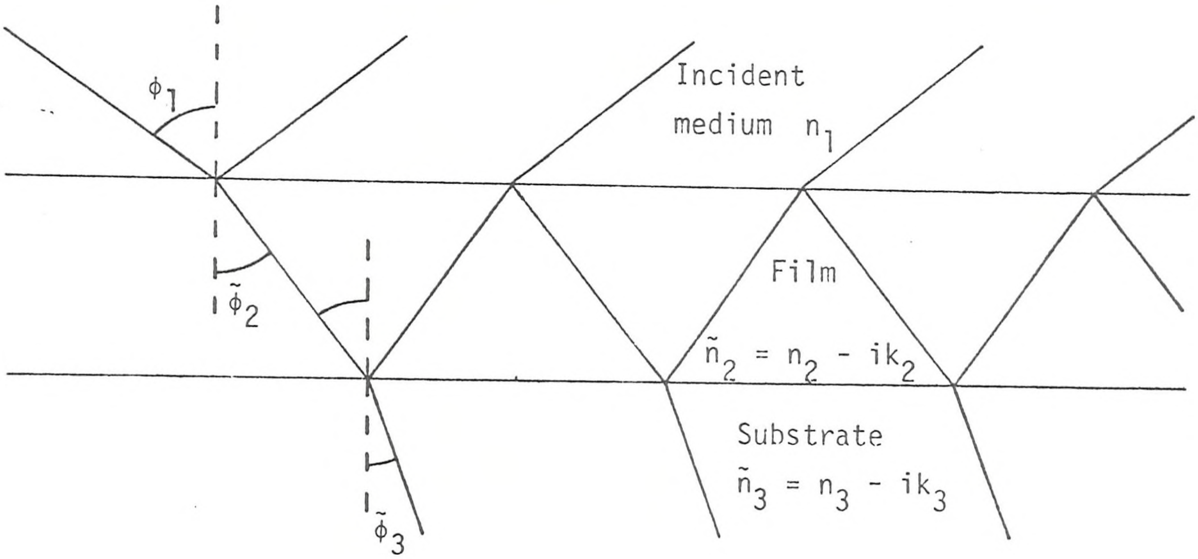

Figure 2.5. Reflection from an idealised film covered surface.

2.2.1. Reflection from a metal surface

Metals are characterised by the presence of free electons which are free in the sense that they are not localised and are able to move under the influence of an applied electric field. An electromagnetic wave incident on the metal surface can send the free electrons into oscillations which are damped by collisions with the thermally agitated lattice or by lattice imperfections. The reflected electric vector will therefore be attenuated and phase shifts in both p and s components introduced. The Fresnel equations can be adapted to describe reflection from a metal surface by introducing a complex refractive index

$$\hat{n} = n - ik \qquad (2.18)$$

where n is the real part of the refractive index and has its usual meaning, $i = -1$ and k the extinction coefficient is related to the absorption coefficient, α, in the Lambert law. The complex refractive index and wave propagation through such a medium will be discussed more fully in section 2.6.2. Application of Snell's law (Eq. 2.17) to complex refractive indices results in complex angles of refraction which are related to the fact that for obliquely incident polarised light the planes of equal amplitude and planes of equal phase are not coincident for light propagating through an absorbing medium[26]. The Fresnel coefficients are also complex and may be written in exponential form

$$\hat{r}_p = \frac{|E_p'|}{|E_p|}\exp[i(\delta_p' - \delta_p)] \qquad (2.19)$$

$$\hat{r}_s = \frac{|E_s'|}{|E_s|}\exp[i(\delta_s' - \delta_s)] \qquad (2.20)$$

where δ is the phase of the oscillation related to a reference. If $|r|$ represents the modulus of the amplitude attenuation and Δ the change in phase due to reflection, the Fresnel equations become

$$\hat{r}_p = |r_p| \exp i\Delta_p \qquad (2.21)$$

$$\hat{r}_s = |r_s| \exp i\Delta_s \qquad (2.22)$$

An ellipsometer is used to determine the ratio, ρ, of the complex reflection for p and s components

$$\rho = \hat{r}_p/\hat{r}_s \qquad (2.23)$$

The complex reflection coefficients can be related to angles and refractive indices, as before, by using Eqs. (2.15) and (2.16) but remembering that n_2 and $\emptyset_2$ for metals will be complex.

2.2.2. Reflections from a film covered surface

The quantitative treatment of light reflected from a film covered surface was formulated by Drude in 1889. The Drude equation, relating the complex amplitude of the reflected and transmitted waves to the amplitude of plane polarised light incident on the interphase, was derived by summing the Fresnel reflection and transmission coefficients associated with multiple reflection (see Fig. 2.5). If the film is assumed to be parallel sided, isotropic and semi-infinite in extent with thickness d and refractive index n_2 on an isotropic substrate of index n_3, then the multiply reflected and transmitted waves can be summed to infinity, leading to the expression

$$\hat{R} = \frac{\hat{r}_{12} + \hat{r}_{12}\exp(-2i\beta)}{1 + \hat{r}_{12}\hat{r}_{23}\exp(-2i\beta)} \qquad (2.24)$$

where $\hat{R}$ is the overall complex refelction coefficient, $\hat{r}_{12}$ is the reflection coefficient at the ambient-film interface, $\hat{r}_{23}$ for the film-substrate interface and $\beta = 2\pi d\cos\emptyset_2/\lambda$ is the phase change produced by a single traversal of the wave in the film. Two such equations exist for the p and s components of the wave. The complex Fresnel reflection coefficients can be related to angles of incidence and refraction and the optical constants describing each of the phases by

$$\hat{r}_{pj,m} = \frac{n_m\cos\emptyset_j - n_j\cos\emptyset_m}{n_m\cos\emptyset_j + n_j\cos\emptyset_m} \qquad (2.25)$$

$$\hat{r}_{sj,m} = \frac{n_j\cos\emptyset_j - n_m\cos\emptyset_m}{n_j\cos\emptyset_j + n_m\cos\emptyset_m} \qquad (2.26)$$

for $j = 1,2$ and $m = j + 1$. The three angles are interrelated by Snell's law (Eq. 2.17)

$$n_1\sin\emptyset_1 = n_2\sin\emptyset_2 = n_3\sin\emptyset_3 \qquad (2.27)$$

From measurements of incident and reflected polarisation states, the ratio

$$\rho = \hat{R}_p/\hat{R}_s \qquad (2.28)$$

of the overall complex amplitude reflection coefficients for the p and s components is determined. Substitution of Eq. (2.19) and Eq. (2.20) into Eq. (2.28) and rearranging gives

$$\rho = \frac{|E_p'|/|E_s'|}{|E_p|/|E_s|} \exp i[(\delta_p' - \delta_s') - (\delta_p - \delta_s)] \qquad (2.29)$$

which by comparison with Eqs. (2.7) and (2.8) gives

$$\rho = \frac{\tan\Psi_r}{\tan\Psi_i}\exp[i(\Delta_r - \Delta_i)] \qquad (2.30)$$

where the subscripts r and i refer to reflected and incident waves respectively. Equation (2.30) is often given in a simplified form

$$\rho = \tan\Psi \exp(i\Delta) \qquad (2.31)$$

Substituting for $\hat{R}_p$ and $\hat{R}_s$ from Eqs. (2.24) to (2.26) into Eq. (2.28) gives the Drude equation

$$\rho = \frac{[\hat{r}_{p1,2} + \hat{r}_{p2,3}\exp(-2i\beta)][1 + \hat{r}_{s,12}\hat{r}_{s2,3}\exp(-2i\beta)]}{[\hat{r}_{s1,2} + \hat{r}_{s2,3}\exp(-2i\beta)][1 + \hat{r}_{p,12}\hat{r}_{p2,3}\exp(-2i\beta)]} \qquad (2.32)$$

Equation (2.32) relates the ellipsometrically determined angles Δ and to the optical properties of a three-phase system.

2.3 Calculation of Δ and Ψ from ellipsometer readings

The angles Δ and Ψ, determined ellipsometrically, are related to the experimentally observable azimuths of the optical components comprising the ellipsometer. The exact form of the expression relating Δ and Ψ to the measured azimuths will depend on the order in which the optical components are placed in the light path. The essential components of a nulling ellipsometer have been described previously and the mathematical treatment which follows applies to the sequence: polariser (P), linear retarder (Q), sample, analyser (A). The null condition may be attained by adjusting the azimuths of any two of the polarising or retarding prisms. The azimuth settings of P, A and Q producing the null condition can then be used to evaluate Δ and Ψ. Equations relating P, A and Q to Δ and Ψ can be derived by predicting the general state of polarisation as light passes through each of the components or is reflected from the sample surface. This type of analysis is considerably simplified by treating the polarisation state of light as a single vector quantity and each of the optical devices as a matrix.

2.3.1 Mathematical treatment of polarised light

Jones vectors and matrices

A concise representation of polarised light is that of a two element column vector introduced by Clark-Jones[27] in 1941. The vector cannot, however, describe partially polarised waveforms or polychromatic light.

The electric vector of a single monochromatic wave of arbitrary polarisation propagating in the z direction of a Cartesian co-ordinate system may be expressed, in phasor form, as

$$\mathbf{E}(z) = |E_x| \exp(i\delta_x) + |E_y|\exp(i\delta_y) \tag{2.33}$$

This expression for the complex amplitude may be represented as a 2 element column vector known as the Jones vector.

$$\mathbf{E}(z) = \begin{bmatrix} |E_x| \exp(i\delta_x) \\ |E_y| \exp(i\delta_y) \end{bmatrix} \tag{2.34}$$

The Jones vector is a complex vector and as such is not a vector in real space but in mathematical space and serves only as a representation of the wave. Any completely polarised wave may be represented by a Jones vector, and any change of polarisation would be represented by a change in the Jones vector. Such a change can be accomplished mathematically by a 2 x 2 matrix which acts as an operator changing one 2 x 1 column vector into another linearly related column vector. Any optical device which changes the polarisation state of a light beam passing through it may, therefore, be represented as a 2 x 2 matrix.

The polarisation state of light emerging from an optical device is simply obtained by multiplying the 2 x 2 matrix describing the element by the Jones vector describing the incident wave.

$$\mathbf{E}' = \begin{bmatrix} E_x' \\ E_y' \end{bmatrix} = \begin{bmatrix} a & b \\ c & d \end{bmatrix} \begin{bmatrix} E_x \\ E_y \end{bmatrix} = \begin{bmatrix} aE_x + bE_y \\ cE_x + dE_y \end{bmatrix} \tag{2.35}$$

The Jones vectors have been simplified for convenience by using the identity

$$E = |E|\exp(i\delta)$$

The matrix for a linear polariser with transmission axis parallel to the x axis can be found by separating Eq. (2.35) into two terms

$$aE_x + bE_y = E'_x$$

$$cE_x + dE_y = E'_y = 0$$

E'_y is zero because the emerging beam contains only oscillations in the x direction and b must also be zero since none of the y component is transmitted, hence

$$a = E'_x/E_x$$

This ratio represents the transmission of the polariser which will be unity for an ideal device. The Jones matrix describing this device is

$$\begin{bmatrix} 1 & 0 \\ 0 & 0 \end{bmatrix}$$

Using conventional matrix algebra, the matrix $[P_\alpha]$ of a polariser at some non-principal azimuth is obtained from the matrix $[P_0]$ of a polariser at its principal azimuth. The procedure involves the rotator and counter-rotator matrices denoted by $[S(\alpha)]$ and $[S(-\alpha)]$ respectively. $[P_\alpha]$ is then given by

$$[P_\alpha] = [S(-\alpha)][P_0][S(\alpha)]$$

$$[P\alpha] = \begin{bmatrix} \cos\alpha & -\sin\alpha \\ \sin\alpha & \cos\alpha \end{bmatrix} \begin{bmatrix} 1 & 0 \\ 0 & 0 \end{bmatrix} \begin{bmatrix} \cos\alpha & \sin\alpha \\ -\sin\alpha & \cos\alpha \end{bmatrix}$$

Multiplying this expression using the standard rules of matrix algebra, i.e., working from right to left, gives the Jones matrix for a homogeneous linear polariser at some general azimuth α to the x axis.

$$[P_\alpha] = \begin{bmatrix} \cos^2\alpha & \cos\alpha\sin\alpha \\ -\sin\alpha\cos\alpha & \sin^2\alpha \end{bmatrix}$$

Procedures similar to those outlined can be followed to obtain the Jones matrix for other optical devices. For a linear retarder the full Jones vectors (Eq. 2.34) describing the incident and transmitted light must be used because phase information is required. Considering orthogonal components of polarised light in the fast (f) slow (s) plane of the retarder

$$\begin{bmatrix} |E'_f|\exp(i\delta'_f) \\ |E'_s|\exp(i\delta'_s) \end{bmatrix} = \begin{bmatrix} a & b \\ c & d \end{bmatrix} \times \begin{bmatrix} |E_f|\exp(i\delta_f) \\ |E_s|\exp(i\delta_s) \end{bmatrix}$$

light emerging from the retarder — matrix of the retarder — light of arbitary polarisation state incident on the retarder

Expansion of the above expression gives

$$|E'_f|\exp(i\delta'_f) = a|E_f|\exp(i\delta_f) + b|E_s|\exp(i\delta_s)$$

$$|E'_s|\exp(i\delta'_s) = c|E_f|\exp(i\delta_f) + d|E_s|\exp(i\delta_s)$$

By inspection b = c = 0 and

$$a = |E'_f|\exp(i\delta'_f)/|E_f|\exp(i\delta_f) \qquad (2.36)$$

$$d = |E'_s|\exp(i\delta'_s)/|E_s|\exp(i\delta_s) \qquad (2.37)$$

A retarder is characterised by the transmittance, T, along the fast and slow axes and by the phase retardation, Δ, along each axis.

$$\begin{aligned} T_f &= |E'_f|/|E_f|, \quad \Delta_f = \delta_f - \delta'_f \\ T_s &= |E'_s|/|E_s|, \quad \Delta_s = \delta_s - \delta'_s \end{aligned} \qquad (2.38)$$

The ratio T_s/T_f represents the relative amplitude attenuation of light passing through the retarder and may be expressed as the tangent of an angle Ψ_c. The retarder may then be characterised by a single complex transmission ratio, ρ_c

$$\rho_c = (T_s/T_f)\exp(-i\Delta_s + i\Delta_f) = \tan\Psi_c\exp(-i\Delta_c) \qquad (2.39)$$

Substituting Eq. (2.38) into Eq. (2.36) and Eq. (2.37) enables the Jones matrix to be constructed

$$[J_{ret}] = \begin{bmatrix} T_f\exp(-i\Delta_f) & 0 \\ 0 & T_s\exp(-i\Delta_s) \end{bmatrix}$$

and by using Eq. (2.39), the matrix for a linear retarder may be written

$$T_f\exp(-i\Delta_f)\begin{bmatrix} 1 & 0 \\ 0 & \rho_c \end{bmatrix} \qquad (2.40)$$

The premultiplier may be dropped if transmission and retardation relative to the fast axis are considered. An ideal retarder would have equal transmittance along both axes.

The surface is characterised by the ratio of the complex reflection coefficients of p and s components. Using the defining equation

$$\rho = \frac{|\hat{r}_p|}{|\hat{r}_s|}\exp[i(\Delta_p - \Delta_s)]$$

the Jones matrix for the surface can be formulated

$$[J_{surf}] = \begin{bmatrix} |\hat{r}_p|\exp(i\Delta_p) & 0 \\ 0 & |\hat{r}_s|\exp(i\Delta_s) \end{bmatrix}$$

or

$$[J_{surf}] = \hat{r}_s\exp(i\Delta_s)\begin{bmatrix} \rho & 0 \\ 0 & 1 \end{bmatrix} \qquad (2.41)$$

The changes in the polarisation state of light travelling through the optical components of an ellipsometer can now be described. The sequence of operators $[J_{surf}][J_{ret}]$ acting on the Jones vector for linearly polarised light emerging from the polariser, $[V_p]$, will give the vector describing the light reflected from the surface and incident on the analyser $[V_A]$. The Jones vector $[V_P]$ of light from the polariser, normalised (unit intensity) and expressed in a coordinate system with x and y axes coinciding with the p-s coordinate system is

$$[V_P] = \begin{bmatrix} \cos P \\ \sin P \end{bmatrix} \qquad (2.42)$$

where P is the azimuth of the polariser measured counterclockwise from the plane of incidence. The matrix describing the retarder (Eq. 2.40), is defined in the fast-slow plane of the device and before using it to operate it on $[V_P]$ a coordinate transformation must be applied

$$[J_{ret}] = \begin{bmatrix} \cos Q & -\sin Q \\ \sin Q & \cos Q \end{bmatrix}\begin{bmatrix} 1 & 0 \\ 0 & \rho_c \end{bmatrix}\begin{bmatrix} \cos Q & \sin Q \\ -\sin Q & \cos Q \end{bmatrix}$$

which, on expansion, gives

$$[J_{ret}] = \begin{bmatrix} \cos^2 Q+\rho_c\sin^2 Q & \cos Q\sin Q-\rho_c\sin Q\cos Q \\ \sin Q\cos Q-\rho_c\sin Q\cos Q & \sin^2 Q+\rho_c\cos^2 Q \end{bmatrix}$$

where Q is the azimuth of the fast axis measured from the plane of incidence. The light from the retarder and incident on the sample may now be described

$$\begin{aligned}[V_I] &= [J_{ret}][V_P] \\ &= \begin{bmatrix} \cos Q\cos(P+Q)-\rho_c\sin Q\sin(P-Q) \\ \sin Q\cos(P-Q)+\rho_c\cos Q\sin(P-Q) \end{bmatrix}\end{aligned}$$

and light reflected from the surface

$$[V_A] = [J_{surf}][V_I]$$

$$[V_A] = \begin{bmatrix} \rho[\cos Q\cos(P-Q)-\rho_c\sin Q\sin(P-Q)] \\ \sin Q\cos(P-Q)+\rho_c\cos Q\sin(P-Q) \end{bmatrix} \qquad (2.43)$$

For this light to be extinguished by the analyser it must be linearly polarised and is therefore capable of being described by a Jones vector of the form

$$\begin{bmatrix} \cos(e) \\ \sin(e) \end{bmatrix}$$

Equating this vector with $[V_A]$ gives

$$\tan(e) = \frac{\sin Q\cos(P-Q) + \rho_c\cos Q\sin(P-Q)}{\rho[\cos Q\cos(P-Q) - \rho_c\sin Q\sin(P-Q)]} \qquad (2.44)$$

The analyser must be set to 90° from e to give the null condition so

$$\tan A = - 1/\tan(e)$$

therefore, inverting, negating and dividing Eq. (2.44) by $\cos Q\cos(P-Q)$

$$\tan A = \frac{\rho[\rho_c\tan Q\tan(P-Q)-1]}{\tan Q + \rho_c\tan(P-Q)}$$

or

$$\rho = \frac{\tan A[\tan Q + \rho_c\tan(P-Q)]}{\rho_c\tan Q\tan(P-Q) - 1} \qquad (2.45)$$

2.4 Four zones

The null condition for given values of Δ and Ψ resulting from reflection can be achieved by four different, distinct, combinations of polariser, analyser and retarder azimuth settings. This can be demonstrated by using Eq. (2.45) assuming that the retarder acts as an ideal quarter-wave retarder with fast axis azimuth set at $\pm\pi/4$. In nulling ellipsometry, it is conventional to take measurements with the retarder at a fixed azimuth and adjust the polariser and analyser azimuths to achieve the null condition. The choice of $\pm\pi/4$ for the retarder fast axis azimuth has been arrived at by considering the effect of azimuth setting on errors introduced by polariser, analyser and retarder imperfections[28,29]. The effect of imperfections and azimuth errors of the polariser and analyser are minimised, while the analyser imperfections and azimuth errors (which are not as important as those of the polariser or retarder) are not minimised.

For an ideal quarter-wave retarder, $\Delta_c = -\pi/2$ and $T_c = 1$, Eq. (2.39) becomes

$$\rho_c = T_c\exp(-i\Delta_c) = -i \qquad (2.46)$$

where $T_c = T_s/T_f$.

By using Eq. (2.46) and $Q = \pi/4$, where Q is the retarder fast axis azimuth, and using the identity

$$(1 - i\tan\theta)/(1 + i\tan\theta) = \exp(-i2\theta)$$

Eq. (2.45) becomes

$$\rho = -\tan A\exp[-i2(P-\pi/4)] \qquad (2.47)$$

If the angles P and A represent one set of nulling angles, an associated pair P' and A' of distinct nulling angles can be related to the original pair by

$$P' = P + \pi/2 \quad \text{and} \quad A' = \pi - A \qquad (2.48)$$

which can be verified by substitution of these values into Eq. (2.47)

$$-\tan A'\exp[-i2(P'-\pi/4] = -\tan(\pi-A)\exp[-i2(P+\pi/2-\pi/4)]$$
$$= -\tan A\exp[-i2(P-\pi/4)]$$

If the azimuth of the retarder is now set at $-\pi/4$ Eq. (2.47) becomes

$$\rho = \tan A\exp[i2(P+\pi/4)] \qquad (2.49)$$

Again, if P and A represent one set of nulling angles another distinct pair P' and A' can be found which are related to P and A by Eq. (2.48).

These sets of values which produce the null condition fall into four groups or zones which are identified with the quadrants on the equator of the Poincare sphere*. A definition of the zone numbering is given in Table 2.1[30].

When the nulling angles have been determined, rotation by π of any of the azimuths will not affect the result so there are 32 possible

---

*The Poincare sphere gives a pictorial representation of polarised light where each point on the sphere represents a different polarisation form[31].

sets of readings on the ellipsometer. This multiplicity of nulls is avoided if all angles are reduced to lie between 0° and 180°.

Table 2.1

Definition of Zone Numbering

Zone	Azimuth of Polariser Transmission Axis	Azimuth of Retarder Fast Axis
1	0° - 45°	135°
2	45° - 90°	45°
3	90° - 135°	135°
4	135° - 180°	45°

2.5 Component Imperfections

For a perfectly aligned ellipsometer with ideal optical components, the values of Δ and ψ for a given surface, measured in each of the four zones would be identical. In practice, however, the results are different because of component imperfections, azimuth angle errors, beam deviation, surface irregularities and finite band width of the beam. By averaging the values of Δ and ψ obtained in four zones the effects due to many of the component imperfections cancel out. By a detailed analysis on the effect of component imperfections on the measured values of Δ and ψ it has been shown that the remaining error in Δ is due to cell window birefringence and in ψ is due to depolarisation of the polariser light output[32]. It is possible however, to obtain a corrected value of Δ and ψ from ellipsometric measurements in one zone if imperfection parameters describing the devices are known or measured.

2.5.1 Effects due to an imperfect retarder

An error in the measured values of Δ and ψ is likely to be introduced by the retarder. It is common practice in nulling ellipsometry to use a quarter wave retarder whose ideal characteristics would be equal transmittance along the fast and slow axes and relative phase retardation of exactly $\pi/2$. While mica wave plates are available which give very close to ideal characteristics at one particular wavelength, achromatic devices such as the 3-reflection prism retarder employed in this investigation will have a complex transmittance ratio, ρ_c, which will vary with wavelength.

It is possible to determine the value of ρ_c at a particular wavelength by measuring Δ and ψ in two zones. If the retarder fast axis is set at Q° and P_1, A_1 and P_2, A_2 are the nulling angles in two zones, then by Eq. (2.45)

$$\rho = \frac{\tan A_1[\tan Q + \rho c\tan(P_1-Q)]}{\rho_c\tan Q\tan(P_1-Q) - 1} \qquad (2.50)$$

and

$$\rho = \frac{\tan A_2[\tan Q + \rho c\tan(P_2-Q)]}{\rho_c\tan Q\tan(P_2-Q) - 1} \qquad (2.51)$$

Subtracting Eq. (2.51) from Eq. (2.50) and rearranging gives

$$\rho_c^2[\tan(P_1-Q)\tan(P_2-Q)] + \rho_c\left[\frac{\tan A_1(\tan Q\tan(P_2-Q) - \tan(P_1-Q)/\tan Q)}{\tan A_1 - \tan A_2}\right.$$
$$\left.- \frac{\tan A_2(\tan Q\tan(P_1-Q) - \tan(P_2-Q)/\tan Q)}{\tan A_1 + \tan A_2}\right] = 0 \qquad (2.52)$$

Solving for ρ_c gives

$$\rho_c = \frac{B \pm i[-B^2 - \tan(P_1-Q)\tan(P_2-Q)]^{1/2}}{-\tan(P_1-Q)\tan(P_2-Q)} \qquad (2.53)$$

where

$$B = \tan A_1[\tan(P_2-Q)\tan Q - \tan(P_1-Q)/\tan Q]/2(\tan A_1-\tan A_2)$$
$$-\tan A_2[\tan(P_1-Q)\tan Q - \tan(P_2-Q)/\tan Q]/2(\tan A_1-\tan A_2) \qquad (2.54)$$

Equation (2.39) can be expressed as

$$\rho_c = T_c\cos\Delta_c - iT_c\sin\Delta_c \qquad (2.55)$$

where $T_c = T_s/T_f$. Comparing Eqs. (2.55) and (2.53) enables T_c and Δ_c to be found

$$T_c = 1/[-\tan(P_1-Q)\tan(P_2-Q)]^{1/2} \qquad (2.56)$$

Since T_c is real and positive, $\tan(P_1-Q)\tan(P_2-Q)$ must be negative, the positive square root of Eq. (2.56) is used and

$$\tan\Delta_c = \pm[-B^2 - \tan(P_1-Q)\tan(P_2-Q)]^{1/2}/B \qquad (2.57)$$

Δ_c is defined by the phase difference $\Delta_f - \Delta_s$ (Eq. 2.38) so that

$0° < \Delta_c < 180°$ and, therefore, $\sin\Delta_c$ is positive. Then, by Eq. (2.55), the imaginary part of ρ_c is negative and since the denominator of Eq. (2.53) has been shown to be positive, the positive root of Eq. (2.57) is taken. Once the values of T_c and Δ_c have been determined experimentally for data obtained in two zones at a particular wavelength, they can be used in Eq. (2.45) to obtain the values of Δ and Ψ without need for 2 or 4 zone averaging, provided that corrections have been made for any other component imperfections.

2.5.2 The Stokes vector and Mueller calculus

The use of Jones vectors and matrices used in the type of analysis previously discussed sometimes leads to long algebraic expressions, or cannot be used at all (e.g., in the treatment of depolarisation). A sometimes more convenient and more generally applicable description is the Stokes vector, first formulated in 1852. Unlike the Jones vector, it is capable of describing any polarisation state including unpolarised light and beams of finite band width. The Stokes vector consists of a set of 4 quantities, called Stokes parameters, each having the dimensions of intensity corresponding to a time averaged quantity. The parameters are defined by

$$S_0 = \langle E_x^2 \rangle + \langle E_y^2 \rangle \tag{2.58}$$

$$S_1 = \langle E_x^2 \rangle - \langle E_y^2 \rangle \tag{2.59}$$

$$S_2 = \langle 2E_xE_y\cos\delta \rangle \tag{2.60}$$

$$S_3 = \langle 2E_xE_y\sin\delta \rangle \tag{2.61}$$

where δ represents the phase angle between two orthogonal components comprising the beam and the <> brackets denote time-averaged quantities. The first term, S_0, represents the intensity of the light while S_1, S_2 and S_3 specify the state of polarisation. If the beam is unpolarised, the electric vector is changing rapidly with time in both amplitude and phase. In this case, S_0 still represents the intensity but the other parameters average to zero. For completely polarised light

$$S_0^2 = S_1^2 + S_2^2 + S_3^2 \tag{2.62}$$

so, the intensity, I, is given by

$$I = S_0 = (S_1^2 + S_2^2 + S_3^2)^{1/2} \tag{2.63}$$

and if V is the degree of polarisation

$$V = (S_1^2 + S_2^2 + S_3^2)^{1/2}/I \tag{2.64}$$

The Stokes parameters can be regarded as the components of a column matrix or 4-vector[33] and, as with the Jones vector, a square matrix can be constructed which may represent an optical device, and can be used as an operator changing one state of polarisation into another related state. The 4 x 4 matrix operator is called the Mueller matrix and when used in conjunction with Stokes vectors enables the effect of component imperfections on the measured values of Δ and ψ to be analysed without placing any restriction on the nature of the imperfection. Effects such as depolarisation introduced by optical components have been discussed and imperfection matrices derived for all of the optical components encountered in conventional ellipsometric arrangements[34].

Mueller matrices describing optical devices were originally formulated by guessing what the elements of the 4 x 4 matrix might be and then testing whether the matrix led to results that are known to be correct for light of different polarisation states. A transformation matrix has been derived which gives a Mueller matrix in terms of the elements of a Jones matrix describing completely polarised light[34].

2.5.3 Cell Window Imperfections

Ellipsometric studies on surfaces often require that the sample be enclosed in a controlled environment e.g., in high vacuum or in an electrolyte solution. In such cases, polarised light passes through cell windows placed before and after the sample surface. Strain is often introduced into the cell windows when they are sealed into the cell or by the action of the external pressure when a vacuum cell is evacuated. The main error caused by introducing cell windows into an ellipsometric arrangement is, therefore, expected to arise from strain birefringence; the cell window then behaves as a retarder of unknown complex transmittance and fast axis azimuth.

As an example of the use of Mueller matrices and Stokes vectors, the effect of cell windows on the ellipsometric parameters will be analysed.

In the following treatment, it is assumed that a cell window may be characterised by a fast axis azimuth, θ, and relative retardation, δ_r. The general Mueller matrix for a linear retarder at any azimuth and with any value δ_r is given by[31]

$$[M_{ret}] = \begin{bmatrix} 1 & 0 & 0 & 0 \\ 0 & D^2-E^2+G^2 & 2DE & -2EG \\ 0 & 2DE & -D^2+E^2+G^2 & 2DG \\ 0 & 2EG & -2DG & 2G^2-1 \end{bmatrix} \qquad (2.65)$$

where

$D = S_1 \sin\delta_r/2$

$E = S_2 \sin\delta_r/2$

$G = \cos\delta_r/2$

and S_1 and S_2 are the second and third Stokes parameters of the normalised fast eigenvector of the retarder. Polarised light of any ellipticity incident on the cell window may be expressed by the Stokes vector

$$(1, \cos2\theta, \sin2\theta\cos\delta, \cos2\theta\sin\delta) \qquad (2.66)$$

the vector often being written horizontally to conserve space. Combining Eqs. (2.66) and (2.67) leads to the Mueller matrix for a cell window with imperfections due to strain birefringence assuming that the retardance is small (i.e. $\delta \approx \sin\delta$) is

$$[M_w] = \begin{bmatrix} 1 & 0 & 0 & 0 \\ 0 & 1 & 0 & -\alpha_i \\ 0 & 0 & 1 & \beta_i \\ 0 & -\alpha_i & -\beta_i & 1 \end{bmatrix} \qquad (2.67)$$

where $\alpha_i = \delta_i \sin2\theta$, $\beta_i = \delta_i \cos2\theta$ and $i = 1$ or 2, identifying the windows before and after the cell and only first order terms in δ_i have been retained. The matrix for the linear quarter wave retarder with fast axis azimuth at 45° can be found by using Eq. (2.65), or by using its Jones matrix (Eq. 2.40) and the transformation matrix. The matrix for such a retarder is

$$[M_{ret}] = \begin{bmatrix} 1 & 0 & 0 & 0 \\ 0 & 0 & 0 & -1 \\ 0 & 0 & 1 & 0 \\ 0 & 1 & 0 & 0 \end{bmatrix} \qquad (2.68)$$

The matrix for the sample surface can be found by multiplying the Mueller matrix of a linear retarder of retardance Δ and that of a linear partial polariser of relative amplitude attenuation $(T_{min}/T_{max})^{1/2} = \tan\Psi$

$$[M_{surf}] = \begin{bmatrix} 1 & -\cos2\Psi & 0 & 0 \\ -\cos2\Psi & 1 & 0 & 0 \\ 0 & 0 & \sin2\Psi\cos\Delta & \sin2\Psi\sin\Delta \\ 0 & 0 & -\sin2\Psi\sin\Delta & \sin2\Psi\cos\Delta \end{bmatrix} \quad (2.69)$$

The Stokes vector describing the light leaving the polariser can be expressed as

$$[\ V_P\ ] = (1,\ \cos2P,\ \sin2P,\ 0) \quad (2.70)$$

Multiplying this vector by the matrices describing the ellipsometer in the sequence

$$[\ V_A\ ] = [\ M_{W2}\ ][\ M_{surf}\ ][\ M_{W1}\ ][\ M_{ret}\ ][\ V_P\ ] \quad (2.71)$$

where $[V_A]$ is the Stokes vector representing the polarisation state of light entering the analyser, gives

$$[\ V_A\ ] = \begin{bmatrix} 1 + \alpha_1\cos2\Psi\cos2P \\ -\cos2\Psi - \alpha_1\cos2P - \alpha_2\sin2\Psi\cos(\Delta+2P) \\ \sin2\Psi[\sin(\Delta+2P) + (\beta_1+\beta_2)\cos(\Delta+2P)) \\ -\alpha_2\cos2\Psi + \sin2\Psi[\cos(\Delta+2P) - (\beta_1+\beta_2)\sin(\Delta+2P)] \end{bmatrix} \quad (2.72)$$

At the null condition, light reflected from the surface will be linearly polarised and therefore, may be described by the Stokes vector

$$(I,\ \cos2\theta\ ,\ \sin2\theta\ ,\ 0) \quad (2.73)$$

Comparing this with Eq. (2.72) gives

$$\alpha_2\cos2\Psi + \sin2\Psi[\cos(\Delta+2P) - (\beta_1+\beta_2)\sin(\Delta+2P)] = 0 \quad (2.74)$$

If the light entering the analyser is polarised at θ°, then for null the analyser azimuth, A, must be set to θ ± 90°. Then

$$\tan2A = \tan(2\theta + 180°) = \tan2\theta \quad (2.75)$$

equating the ratio of the second and third Stokes parameters of Eqs. (2.72) and (2.73) gives

$$\tan 2A = \frac{\sin 2\Psi[\sin(\Delta+2P) + (\beta_1+\beta_2)\cos(\Delta+2P)]}{-\cos 2\Psi - \alpha_1\cos 2P - \alpha_2\sin 2\Psi\cos(\Delta+2P)} \quad (2.76)$$

If P_o and A_o are solutions for Eqs. (2.74) and (2.76) for the ellipsometer without windows (α_i and $\beta_i = 0$), Eq. (2.74) becomes

$$\sin 2\Psi\cos(\Delta+2P_o) = 0 \quad (2.77)$$

and Eq. 2.76 gives

$$\tan 2A_o = \tan 2\Psi\sin(\Delta+2P_o) \quad (2.78)$$

From Eq. (2.77), $\cos(\Delta+2P_o) = 0$ since Ψ and hence, $\sin 2\Psi$ would only be zero for reflection from a film free transparent substrate at the Brewster angle. Therefore

$$\Delta + 2P_o = \pm 90°, \pm 270° \quad (2.79)$$

Two sets of solutions are obtained:

If $\Delta + 2P_o = 90°$, then the solution lies in zone 2 (see section 2.4, table 2.1) and Eq. (2.78) becomes

$$\tan(2A_o) = \tan 2\Psi \quad (2.80)$$

or $$A = \Psi \quad (2.81)$$

and $$2P_o = -\Delta + 90° \quad (2.82)$$

If $\Delta + 2P_o = -90°$ then the solution lies in zone 4

$$\tan 2A_o = -\tan 2\Psi \quad (2.83)$$

$$A_o = -\Psi \quad (2.84)$$

$$2P_o = -\Delta - 90° \quad (2.85)$$

Small differences in these values will result from a re-determination of the ellipsometric parameters when the cell windows are in place. For zone 2

$$2P_o = -\Delta + 90° + \delta \quad (2.86)$$

where δ is a small error introduced by birefringence of the windows. Substituting this into Eq. (2.74) and neglecting second and higher powers of δ and terms such as $\beta_1\delta$ and $\beta_2\delta$ gives

$$\delta = \alpha_2/\tan 2\Psi - \beta_1 - \beta_2 \quad (2.87)$$

and Eq. (2.86) becomes

$$2P = -\Delta + 90° + \alpha_2/\tan 2\Psi - \beta_1 - \beta_2 \qquad (2.88)$$

If the error in the analyser azimuth angle is ε then

$$A_0 = A + \varepsilon = \Psi + \varepsilon \qquad (2.89)$$

Substituting both Eqs. (2.86) and (2.89) into Eq. (2.76) and neglecting the higher powers of ε and terms containing $\alpha\varepsilon$, $\alpha\delta$, <u>etc</u>. gives

$$A = \psi - \alpha_1 \cos 2P \sin 2\Psi/2 \qquad (2.90)$$

The cos2P term may be expressed in terms of Δ by substitution from Eq. (2.88) if the error products α_1, α_2 and β_1, β_2 can be ignored.

$$A = \Psi + \alpha_1 \sin\Delta \sin 2\Psi \qquad (2.91)$$

Solutions for zone 4 can be found by repeating the above procedure starting with Eqs. (2.84) and (2.85). The solutions for zones 1 and 3 are obtained by replacing the matrix given in Eq. (2.69) with the matrix of a quarter wave retarder with fast axis azimuth at -45°. The four sets of solutions are summarised in Table 2.2.

<u>Table 2.2</u>

<u>First order corrections to ellipsometer readings</u>

<u>for cell window birefringence</u>

	Q	P	A
zone 1	135°	$(+\Delta-90°-\alpha_2/\tan 2\Psi+\beta_1+\beta_2)/2$	$\Psi - \alpha_1 \sin\Delta \sin 2\Psi/2$
zone 2	45°	$(-\Delta+90°+\alpha_2/\tan 2\Psi-\beta_1-\beta_2)/2$	$\Psi + \alpha_1 \sin\Delta \sin 2\Psi/2$
zone 3	135°	$(+\Delta+90°-\alpha_2/\tan 2\Psi+\beta_1+\beta_2)/2$	$-\Psi + \alpha_1 \sin\Delta \sin 2\Psi/2$
zone 4	45°	$(-\Delta-90°+\alpha_2/\tan 2\Psi+\beta_1+\beta_2)/2$	$-\Psi - \alpha_1 \sin\Delta \sin 2\Psi/2$

The values of α_2, β_1 and β_2 can be found by first determining the azimuth angles P_0 and A_0 and hence, Δ and ψ for a surface with the cell windows removed (α_1 is calculated from Eq. (2.91)). Ellipsometric readings for P and A for the same surface with the cell windows in place are then recorded in 3 zones. The values of Δ and Ψ must be the same as the values determined previously (Δ and ψ are defined by the surface only) but the 3 sets of azimuth angles will be given by the equations in the above table. The correction terms for the cell can then be calculated enabling the values of Δ and Ψ to be calculated from the ellipsometer reading for any surface in the cell. The above treatment for first order corrections for imperfect cell windows assumes a perfect quarter wave retarder in the ellipsometer. However, if the imperfection parameters for the retarder are known they can be applied to the correct values of Δ and Ψ calculated from P_0 and A_0.

2.6 The interaction of light with matter

The propagation of an electromagnetic field in free space is characterised by the vectors **E**, the electric field strength, and **B**, the magnetic flux density. Maxwell's equations governing the behavior of electric and magnetic fields in free space are[35]

$$\nabla \cdot E = \rho/\varepsilon_0 \tag{2.92}$$

$$\nabla \cdot B = 0 \tag{2.93}$$

$$\nabla \times E = -\partial \mathbf{B}/\partial t \tag{2.94}$$

$$\nabla \times \mathbf{B} = \mu_0 \mathbf{J} + \mu_0 \varepsilon_0 \partial E/\partial t \tag{2.95}$$

where **J** is the displacement current density, μ_0 is the permeability of free space, ε_0 is the permittivity of free space and ρ is the electric charge density.

2.6.1 Wave propagation in non-conducting media

To describe the propagation of an electromagnetic wave through a medium, the values of ε_0 and μ_0 are substituted for the permitivity of the medium, ε, and its magnetic permeability, μ. A polarisation vector, **P**, must also be included to take into account the induced dipole moments arising from the external field acting upon the internal charge distribution of the medium. For most materials, **P** and **E** are proportional and can be related by

$$\mathbf{P} = \mathbf{E}(\varepsilon - \varepsilon_0) \tag{2.96}$$

The field within a medium is altered by the external field and the new field may be described by

$$\mathbf{D} = \varepsilon_0 E + \mathbf{P} \tag{2.97}$$

where **D** is called the displacement vector. Combining Eqs. (2.96) and (2.97) gives one of the so-called constitutive (or material) equations

$$\mathbf{D} = \varepsilon E \tag{2.98}$$

To account for magnetic polarisation effects in the medium it is necessary to introduce an auxiliary vector **H**, the magnetic field strength. The magnetic analogue of Eq. (2.98) is given by

$$\mathbf{B} = \mu \mathbf{H} \tag{2.99}$$

The third of the constitutive equations is given by Ohm's law and relates the current density **J** to the electric field component

$$\mathbf{J} = \sigma E \tag{2.100}$$

where σ is the conductivity of the medium. Maxwell's equations, together with the constitutive equations can be used to predict how an electromagnetic field will interact with a medium. Taking the curl of Eq. (2.94) gives

$$\nabla \times (\nabla \times E) = \frac{-\partial}{\partial t} (\nabla \times \mathbf{B}) \tag{2.101}$$

substituting for $\nabla \times \mathbf{B}$ from Eq. (2.95) and using the identity $\nabla \times (\nabla \times \_) = \nabla(\nabla \cdot \_) - \nabla^2\_$ leads to

$$\nabla^2 E - \mu\varepsilon \frac{\partial^2 E}{\partial t^2} - \mu \frac{\partial E}{\partial t} = \nabla(\rho/\varepsilon) \tag{2.102}$$

since $\nabla(\nabla^2 E) = \nabla(\rho/\varepsilon)$ from Eq. (2.92). For an uncharged non-conducting medium, $\rho = \sigma = 0$ and Eq. (2.102) then becomes

$$\nabla^2 E - \mu\varepsilon \frac{\partial^2 E}{\partial t^2} = 0 \tag{2.103}$$

Equation (2.103) is of the same form as standard equations of wave motion provided that the velocity of the wave is

$$\nu = 1/\sqrt{(\varepsilon\mu)} \tag{2.104}$$

The velocity of light in free space will be given by

$$c = 1/\sqrt{(\varepsilon_o\mu_o)} \tag{2.105}$$

and the ratio of the velocity of an electromagnetic wave in vacuum to that in a medium gives the absolute refractive index, n, of that medium and is, therefore, given by

$$n = \frac{c}{\nu} = \sqrt{\frac{\varepsilon\mu}{\varepsilon_o\mu_o}} \tag{2.106}$$

The relative permeability, μ/μ_0, is generally close to unity, Eq. (2.106) then yields the well known Maxwell's relation*

$$n = \sqrt{\frac{\varepsilon}{\varepsilon_0}} \tag{2.107}$$

Maxwell's relation, with $\varepsilon/\varepsilon_0$ assigned as the static dielectric constant, gives excellent agreement for many simple gases which do not disperse light. Equation (2.107) gives a good approximation for liquid hydrocarbons but breaks down for many other liquids and solids. If the relation is to be retained, then it must be assumed that the dielectric constant, K, is a function of the frequency of the electromagnetic field. The dependence of K on frequency (dispersion) can be formulated by taking into account the atomic structure of matter.

2.6.2 Wave propagation in conducting media

A characteristic feature of conducting media is the ability of charges (electrons) to circulate within the medium, thus constituting a current. For an uncharged conductor ($\rho = 0$) Eq. (2.102) becomes

$$\nabla^2 E - \mu\varepsilon\frac{\partial^2 E}{\partial t^2} - \mu\sigma\frac{\partial E}{\partial t} = 0 \tag{2.108}$$

The term $\partial E/\partial t$ represents the presence of damping of the electric field within the medium. The internal field is set up by the external electric field driving the conduction electrons into oscillation and the damping or progressive attenuation of the field as it propagates through the medium can be identified with the excited electrons colliding with the thermally agitated lattice or with imperfections. For a monochromatic wave of angular frequency the electric field may be represented in phasor form by $\mathbf{E} = |E|\exp(i\omega t)$ and hence, $\partial/\partial t = i\omega$, Eq. (2.108) can therefore be rewritten

$$\nabla^2 E + \mu\varepsilon\omega^2 E - \mu\sigma i\omega E = 0 \tag{2.109}$$

---

*The relative permittivity, $\varepsilon/\varepsilon_0$, defines the dielectric constant and is sometimes given the symbol K. In the SI system of units, used here and throughout this thesis the permittivity has units of FM^{-1} and the permittivity of free space $\varepsilon_0 = 8.854\times10^{-12}$ FM^{-1}. In the cgs system of units ε and ε_0 are the dielectric constants of the medium and free space respectively and both are dimensionless.

or

$$\nabla^2 E + \hat{k}^2 E = 0 \qquad (2.110)$$

where $\hat{k}^2 = \omega^2 \mu(\varepsilon - i\sigma/\omega)$.

Equation (2.110) is formally identical with the corresponding equation for non-conducting media, Eq. (2.103), if the real dielectric permittivity, , in Eq. (2.110) is replaced by

$$\hat{\varepsilon} = \varepsilon - i\sigma/\omega$$

where $\hat{\varepsilon}$ is the complex dielectric permittivity and is more usually expressed in terms of the complex dielectric constant

$$K = \hat{\varepsilon}/\varepsilon_0 = K' - iK'' \qquad (2.111)$$

Along with a complex dielectric constant a complex phase velocity, $\hat{v}$, and a complex refractive index, $\hat{n}$, can be introduced by analogy with Eqs. (2.104) and (2.106)

$$\hat{v} = 1/\sqrt{(\mu\hat{\varepsilon})}, \quad \hat{n} = c/\hat{v} = \sqrt{(\hat{\varepsilon}/\varepsilon_0)} \qquad (2.112)$$

The quantity K is frequently referred to as the dielectric function to distinguish this frequency dependent variable from the static dielectric constant. The complex index of refraction is defined as

$$\hat{n} = n - ik \qquad (2.113)$$

where a real part of the refractive index has its usual meaning <u>i.e.</u>, $n = c/\hat{v}$ and k is the extinction coefficient. The quantities n and k may be expressed in terms of the material constants K and σ by the following:

Squaring Eq. (2.113) gives

$$\hat{n}^2 = n^2 - k^2 - i2nk \qquad (2.114)$$

and from Eqs. (2.111) and (2.112)

$$\hat{n}^2 = \hat{\varepsilon}/\varepsilon_0 = \hat{K} = \varepsilon - i\sigma/\omega = K' - iK'' \qquad (2.115)$$

Equating the real and imaginary parts of Eqs. (2.114) and (2.115) gives

$$K' = n^2 - k^2 \qquad (2.116)$$

and

$$\sigma/\omega = K'' = 2nk \qquad (2.117)$$

Equation (2.110) is formally identical with the wave equation for a non-conducting medium if the wave vector is complex. The simplest solution of a time harmonic wave is that of a plane wave. Such a wave propagating in the y direction can then be written (c.f. Eq. (2.1))

$$E = |E|\cos(\omega t - |\hat{\mathbf{k}}|y) \qquad (2.118)$$

The above equation can be written as a function of n since by analogy with Eq. (2.4) $|\hat{k}| = \omega/\hat{v} = \omega\hat{n}/c$

$$E = |E|\cos(\omega t - \omega\hat{n}y/c) \qquad (2.119)$$

Subtituting for $\hat{n}$ from Eq. (2.113) and casting the result in exponential form yields

$$E = |E|\exp[-i\omega ky/c]\exp[i\omega(t - ny/c)] \qquad (2.120)$$

The real part of this expression, which represents the electric vector is

$$E = |E|\exp(-i\omega ky/c)\cos(\omega t - \omega ny/c) \qquad (2.121)$$

and is a plane wave advancing in the y direction with a speed c/n whose amplitude is exponentially attenuated. Since the irradiance, I, or energy density of the wave is proportional to the time average of E^2, it follows that I decreases in accordance with the relation

$$I(y) = I_0\exp(-\alpha y) \qquad (2.122)$$

where I_0 is the irradiance at $y = 0$ (the interface) and $\alpha = 2\omega k/c$ is called the absorption or attenuation coefficient. The energy density will fall by a factor of 1/e after the wave has propagated a distance $1/\alpha$, known as the penetration depth. Since $\nu = \lambda/2\pi$, it can easily be shown that

$$1/\alpha = \lambda/4\pi k \qquad (2.123)$$

and for mercury the penetration depth of light of in the spectral range from the near infra-red to the near ultra-violet is almost constant at about 1 nm.

2.7 Dispersion theory

Application of the Maxwell material equations (see Eqs. (2.98) to (2.100)) to the propagation of light through a medium characterised by the dielectric constant, magnetic permeability and electric conductivity leads to the Maxwell relation (Eq. (2.107)). The refractive index should equal the square root of the dielectric constant which was assumed to be a characteristic constant of the material. The relationship gives a good approximation for some simple gases and liquids but there is a strong deviation for most solids and liquids other than simple hydrocarbons, for example. The relationship may be retained however, if K is considered to be dependent on the frequency of the field, in which case K is termed the dielectric function to distinguish it from the static dielectric constant. The frequency dependence of the dielectric function can only be treated by taking into account the atomic structure of matter. The classical theories of dispersion are due mainly to Lorentz for insulating materials and to Drude for metals

2.7.1 Dispersion in dielectric media - The Lorentz oscillator model

Lorentz attempted to explain some of the properties of insulating materials on the assumption that electrons are bound to the nucleus by elastic forces. Under the influence of an applied electromagnetic field, the atoms or molecules will become polarised which, in turn, contribute to the total field within the medium. The local field acting on a particular molecule may be estimated by considering it to be surrounded by a sphere which is sufficiently large that beyond it the medium can be treated as a continuum. The resultant field at the centre of the sphere, produced by the dipoles within, can be shown to be zero for a site with a cubic or completely random environment if the molecules are considered as point dipoles aligned parallel to the applied field. The field produced by the polarisation charge on the surface of the sphere is calculated by assuming that all dipoles within the medium are again aligned parallel to the field. Since the polarisation is the dipole moment per unit volume and is equal to the surface density of the induced charge, the field can be calculated using Coulomb's law. The local field acting on the reference molecule is then[36,37]

$$E' = E + \frac{P}{3\varepsilon_0} \qquad (2.125)$$

where E is the macroscopic field within the insulator and is less than the applied field, $\mathbf{E}^{ext}$ because the free ends of the dipoles at the surface of the material constitute a surface charge which reduces the effect of $\mathbf{E}^{ext}$. The reduced field is given by $\mathbf{E} = \mathbf{E}^{ext}/K$ where K is the dielectric constant of the incident medium.

The dipole moment, $\mathbf{p}$, resulting from an external field is proportion to the local field $\mathbf{E}'$

$$\mathbf{p} = \alpha E' \qquad (2.126)$$

where α is the mean polarisability. The total electric moment per unit volume is given by $\mathbf{P} = N\mathbf{p} = N\alpha E'$ and by substituting for $\mathbf{E}'$ from

Eq. (2.125) leads to

$$P = N\alpha E + \frac{N\alpha P}{3\varepsilon_0} \tag{2.127}$$

The polarisability can be related to the dielectric constant by substitution from Eq. (2.96) into Eq. (2.127) and leads to the following expressions

$$\begin{aligned} \varepsilon/\varepsilon_0 &= K = \frac{1 + 2N\alpha/3\varepsilon_0}{1 - N\alpha/3\varepsilon_0} \\ \alpha &= \frac{K - 1}{K + 2}\,\frac{3\varepsilon_0}{N} = \frac{n^2 - 1}{n^2 + 2}\,\frac{3\varepsilon_0}{N} \end{aligned} \tag{2.128}$$

which are forms of the Lorenz-Lorentz equation.

For a particular frequency (and hence constant n), and since the density of a substance is proportional to N then

$$\frac{n^2 - 1}{(n^2 + 2)\rho} = \text{constant} \tag{2.129}$$

This expression has been verified experimentally for a wide range of substances and density changes such as those occuring in the transition from liquid to vapour. The quantity $(n^2 - 1)/(n^2 + 2)\rho$ is termed the specific refractivity and the equation

$$A = \frac{M}{\rho}\,\frac{n^2 - 1}{n^2 + 2} \tag{2.130}$$

defines the molar refractivity. The molar refractivity of a mixture of substances which do not interact with each other has been shown to equal the sum of the contributions due to each substance.

If a non-polar molecule is subject to an incident electromagnetic wave, the electrons and nuclei will be displaced and a time varying dipole moment generated. The vectorial sum of all such induced dipole moments per unit volume is essentially the polarisation vector, or density of dipoles, introduced in Eq. (2.127). In order to express the dependence of polarisation and refractive index on the frequency of the field it is necessary to find the displacement **r** of each charged particle from its equilibrium position. The force exerted by the field (electric and magnetic components) on an electron of charge e moving with a velocity of ν is given by the Lorentz law

$$\mathbf{F} = e(E' + \nu/c \times \mathbf{B}') \tag{2.131}$$

If it is assumed that the velocity of the electron is small compared with c, then the contribution from the magentic field may be neglected. A rigorous determination of the displacement of nuclei and electrons under the action of an electromagnetic field requires a quantum mechanical treatment. Nevertheless, the classical approach leads to a very similar result and provides a useful conceptual model.

Electrons in insulators behave to a good approximation, as if they were bound to equilibrium position by a quasi-elastic restoring force, $F_e = -\kappa\underline{r}$. The molecule then resembles a classical harmonic oscillator being driven by the external field. The equation of motion of an electron in a field, E', under these conditions is

$$m\partial^2\mathbf{r}/\partial t^2 + \kappa\mathbf{r} = eE' \qquad (2.132)$$

where m is the mass of the electron. In the absence of an external field (E' = 0), the equation of motion can be solved easily giving

$$\mathbf{r} = A\cos[\ (\kappa/m)t - \emptyset)] \qquad (2.133)$$

where A and $\emptyset$ are constants. By making the substitution $\omega_0 = \sqrt{\kappa/m}$, Eq. (2.133) can be identified with a simple harmonic motion of frequency ω_0 which, for this case, represents the natural frequency of the unperturbed electron (also called the resonance frequency). The equation $\mathbf{r} = \mathbf{r}_0\exp(-i\omega t)$ is a more general solution to Eq. (2.132) and is equivalent to the solution given in Eq. (2.133) for a suitably chosen constant $\mathbf{r}_0$. Using this as the solution to the electron's motion in the perturbed case leads to

$$\mathbf{r} = \frac{eE\exp(-i\omega t)}{m(\omega_0^2 - \omega^2)} \qquad (2.134)$$

The electronic contribution to the dipole moment of an atom or molecule is $\mathbf{p} = e\mathbf{r}$; the overall dipole moment should contain a term resulting from the displacement of the nucleus, but since the nuclear masses are much heavier than the electron mass, their contribution, to a first approximation, may be neglected. Assuming that each molecule has only one electron with resonance frequency ω_0 and that there are N molecules per unit volume, the total polarisation, **P**, is given by

$$\mathbf{P} = N\mathbf{p} = Ne\mathbf{r} = \frac{Ne^2E'}{m(\omega_0^2 - \omega^2)} \qquad (2.135)$$

substituting for **p** from eq. (2.126)

$$\alpha = \frac{e^2}{m(\omega_o^2 - \omega^2)} \qquad (2.136)$$

and substituting for α from Eq. (2.128) leads to

$$\frac{K - 1}{K + 2} = \frac{n^2 - 1}{n^2 - 1} = \frac{Ne^2}{3\varepsilon_o m(\omega_o^2 - \omega^2)}$$

For a gas, n (and K) is close to unity so that $n^2 + 1 \simeq 3$ and hence the above equation ecomes

$$K = n^2 = 1 + \frac{Ne^2}{\varepsilon_o m(\omega_o^2 - \omega^2)} \qquad (2.137)$$

For $\omega < \omega_o$ the dielectric function and hence n are greater than unity and monotonically increase with increasing ω (decreasing λ) and the dispersion is said to be normal. At the resonance frequency ($\omega = \omega_o$) Eq. (2.137) suggests that K and n are infinite. The singularity arises only formally however, since damping of the electron motion due to scattering mechanisms, such as collisions between atoms and to radiation damping*, has been omitted. A resisting force, $\gamma\partial\mathbf{r}/\partial t$, is therefore introduced into Eq. (2.132) to account for energy less mechanisms:

$$m\frac{\partial^2\mathbf{r}}{\partial t^2} + \gamma\frac{\partial\mathbf{r}}{\partial t} + \kappa\mathbf{r} = eE' \qquad (2.138)$$

The solution to this equation is complex and given by

$$\hat{r} = \frac{eE}{m(\omega_o^2 - \omega^2) + i\Gamma\omega}$$

where $\Gamma = \gamma/m$ and Eq. (2.136) becomes

$$\hat{\alpha} = e^2/[m(\omega_o^2 - \omega^2) + i\Gamma\omega]$$

The polarisability is now complex and as a result, it differs in phase from that of the local field. This leads to a formal introduction of the complex dielectric function and refractive index

$$\hat{K} = \hat{n}^2 = 1 + \frac{Ne}{\varepsilon_o m(\omega_o^2 - \omega^2 + i\Gamma\omega)} \qquad (2.139)$$

---

*Re-radiation of electromagnetic energy due to accelerating electrons.

For a medium containing molecules with more than one resonance frequency, Eq. (2.139) can be extended by summing the effect of all oscillators

$$\hat{K} = \hat{n}^2 = 1 + \frac{Ne^2}{\varepsilon_o m} \sum_j \frac{f_j}{\omega_j^2 - \omega^2 + i\Gamma\omega} \qquad (2.140)$$

where f_j is the number of electrons corresponding to the resonance frequency ω_j. In this classical model, the terms f_j are expected to be integers, however, in order to agree with experimental results, they are found frequently to be less than unity and often by a significant factor.

The fundamental dispersion (Eq. 2.140) derived from classical arguments is formally identical to the corresponding quantum mechanical formulation36, however, the meanings of the terms f_j and ω_j are quite different. ω_j now represents the transition frequency of an electron between two energy levels separated by an energy $\hbar\omega_j$ and the parameter f_j is called the oscillator strength and is a measure of the probability of a quantum mechanical transition.

For regions of the spectrum which contain no resonance frequencies, $\omega_j^2 - \omega^2$ is large compared to $\Gamma\omega$, the dispersion formula (Eq. 2.139), may be written

$$K = n^2 = 1 + \sum_j \frac{A_j \lambda^2 \lambda_j^2}{\lambda^2 - \lambda_j^2} \qquad (2.141)$$

where $A = \dfrac{Ne^2 f_j}{\varepsilon_o 4\pi^2 c^2 m}$ and $\lambda_j = \dfrac{2\pi c}{\omega_j}$

Equation (2.141) is known as Sellmeir's dispersion formula. If there is only one resonance frequency, then for wavelength considerably longer than that associated with the resonance, λ^2 is much larger than λ_j^2 and Eq. (2.141) reduces to

$$n^2 = 1 + A\;1 - \frac{\lambda_j^2}{\lambda^2}^{\,-1} = 1 + A + \frac{B}{\lambda^2} + \frac{C}{\lambda^4} + \cdots \qquad (2.142)$$

where $B = A\lambda_j^2$ and $C = A\lambda_j^4$. Equation (2.142) is of the same form as Cauchy's dispersion formula;

$$n = A + B/\lambda^2 + c/\lambda^4 \qquad (2.143)$$

in which the constants were determined empirically by Cauchy by measuring n at three wavelengths. The formula gives good agreement with experimental values of n for gases, transparent glasses and dilute aqueous electrolytes in the visible region of the spectrum. For many purposes, it is sufficiently accurate to retain only the first two terms in the expression.

Returning to Eq. (2.140) and using suitable values for Γ, ω_j and f_j, the frequency dependence of $\hat{K}$ and $\hat{n}$ for a classical Lorentzian oscillator in the region of a resonance frequency may be calculated. Fig. 2.6 shows the complex dielectric function as a function of photon energy for a material containing a single absorber with a single transition frequency. The figure shows the result for the case in which $\hbar\omega_0 = 2\text{eV}$ and $\hbar\Gamma = 0.2$ eV. The maximum in K'' occurs at the transition energy $\hbar\omega_0$ and the region of anomalous dispersion is given by the maximum and minimum in K' which are displaced from the $h\omega_0$ by $\pm\,\hbar\Gamma/2$. The half width of the K'' peak is given by Γ and the height of the maximum in K'' can be expressed as

$$K''(\text{max}) = Nfe^2/(\varepsilon_0 m\Gamma\omega_0) \tag{2.144}$$

2.7.2 Dispersion in metals - The Drude free electron model

The classical theory of the optical properties of metals is based on a free electron model proposed by Drude. The model assumes that there are no interactions between the conduction electrons and ion cores so that the conduction electrons are free to move everywhere within the medium. The equation of motion of a conduction electron in an electromagnetic field is obtained simply by setting the restoring force in Eq. (2.139) to zero. The solution, from Eq. (2.141) setting $\omega_0 = 0$, is given by

$$\hat{K} = 1 - \frac{Ne^2}{\varepsilon_0 m(\omega^2 + i\Gamma\omega)} \tag{2.145}$$

again $\Gamma = \gamma/m$ where γ now represents a damping term due to the scattering of electrons associated with electrical resistivity. It can be shown that $\Gamma = 1/\tau$ 38, where τ is the mean free time between collisions.

For a perfect metal, $\tau \rightarrow \infty$ so that Eq. (2.145) approximates to

$$\hat{n}^2 = \hat{K} = 1 - \frac{Ne^2}{\varepsilon_0 m\omega^2}$$

and the properties of a perfect metal will depend on the magnitude of $Ne^2/\varepsilon_0 m\omega^2$. If the factor is less than unity the refractive index will be real and therefore the metal will be transparent. The refractive index becomes complex however, when $Ne^2/\varepsilon_0 m\omega^2$ is greater than unity and

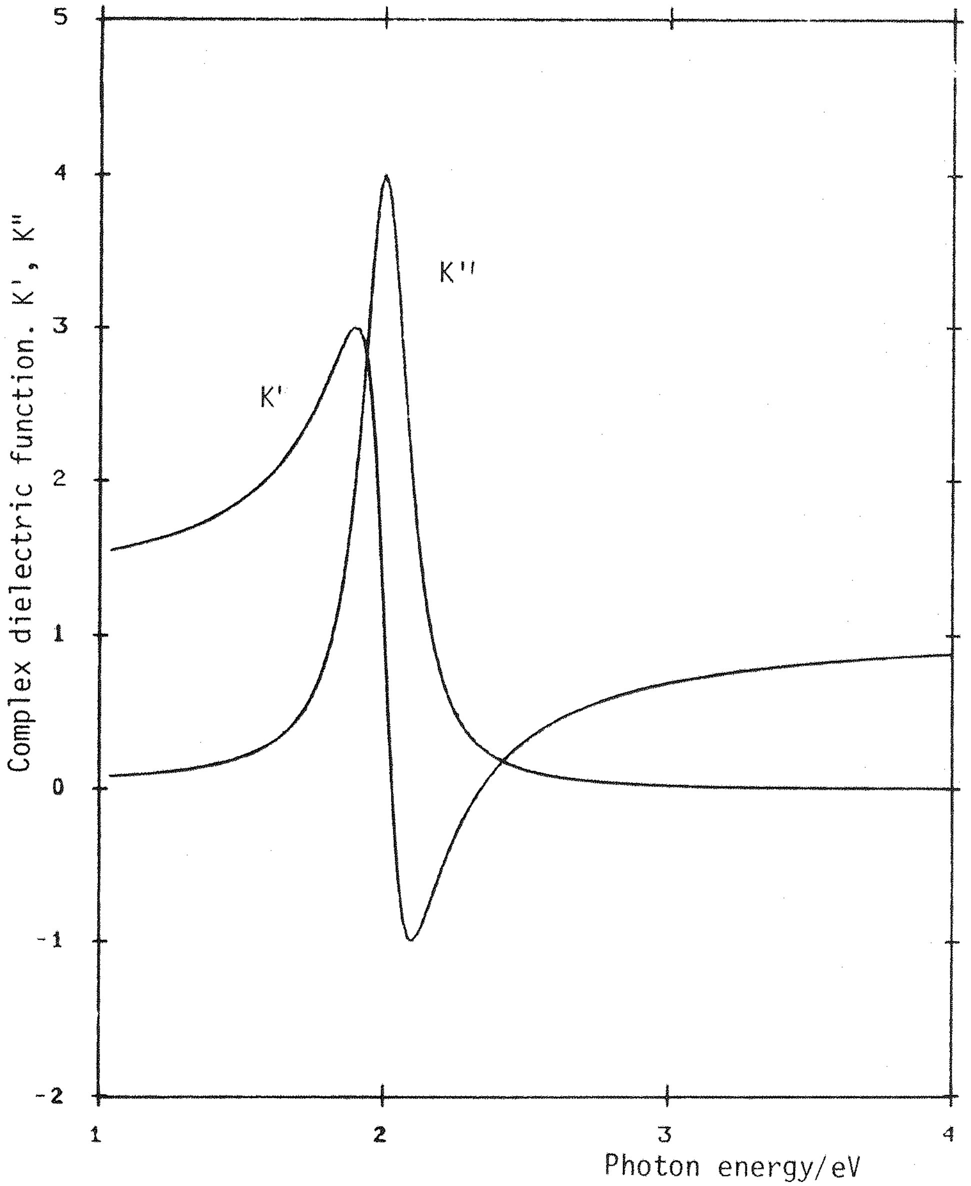

Figure 2.6. Complex dielectric function spectrum. Curves calculated from the Lorentzian oscillator model for a single oscillator.

the metal becomes reflecting. When $Ne^2/\varepsilon_0 m\omega^2 = 1$ the metal will be just transparent, which corresponds to a frequency given by

$$\omega_p = \sqrt{\frac{Ne^2}{\varepsilon_0 m}} \tag{2.146}$$

called the plasma or cut-off frequency since it is the frequency above which light will not propagate into the metal. At the plasma frequency, $n \approx 0$, which implies an infinite phase velocity ($\hat{\nu} = c/\hat{n}$) and hence, infinite wavelength. All electrons are therefore oscillating in phase at the plasma frequency. A plasma oscillation is a collective oscillation of the electrons which means that many electrons are moving in phase over an extended region. The condition for plasma oscillation is $K = K' - iK'' = 0$ and occurs therefore at frequencies where $K' = 0$ and $K_2 << 1$.

To illustrate these points and the validity of the Drude model, a plot of the dielectric function, calculated from Eq. (2.145) and experimental values[51] for mercury are shown in Fig. 2.7

The reflectivity, calculated from the Drude model, is predicted to fall rapidly to values approaching zero at frequencies higher than the plasma frequency. For $\omega < \omega_p$ the reflectivity if predicted to be close to 100% and no structure in the spectral dependence of the reflectivity is predicted on either side of the plasma frequency. However, for solid metals, some structure is always observed. In aluminium[39], for example, a small dip in the reflectivity is observed at 1.4eV some 14eV before the plasma resonance. Silver shows a large reflectivity at frequencies higher than the plasma frequencies[40]; and copper does not exhibit a plasma resonance but the reflectance spectrum does show several absorption bands.[41] The above observation, not predicted by the Drude model, can only be accounted for by consideration of the band structure of solids.

2.7.3 Optical properties of liquid metals

With few exceptions, the optical properties of liquid metals agree well with the Drude free electron theory

$$\hat{K} = 1 - \frac{N^* e^2}{\varepsilon_0 m(\omega^2 + i\omega/\tau)} \tag{2.147}$$

after some slight adjustment of N^*, the density of conduction electrons and τ, the relaxation time. It has been shown experimentally for a wide range of liquid metals that τ is close to the value predicted from measured d.c. conductivities, σ, where σ is given by

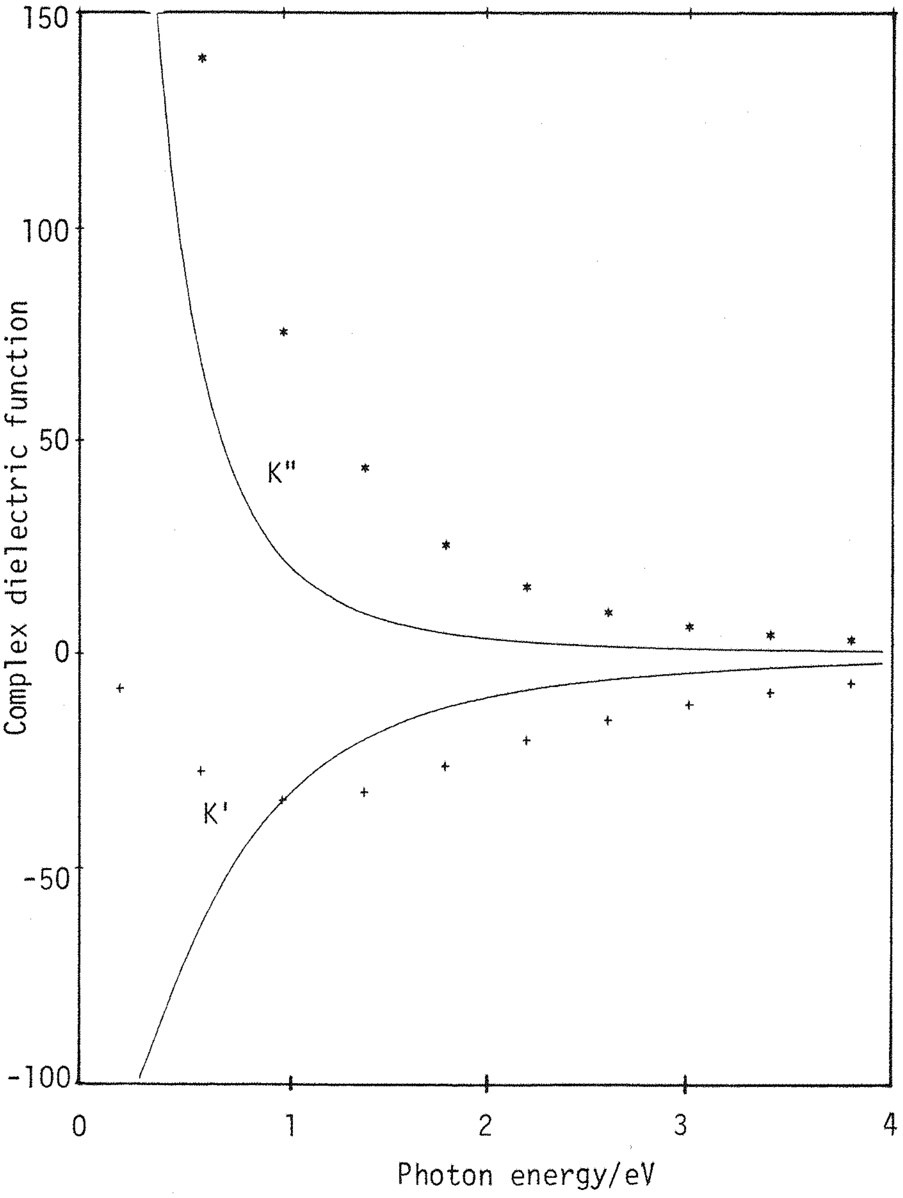

Figure 2.7. Complex dielectric function spectrum of mercury. ——— , predicted from Drude free electron model; +,*, data taken from Ref. 51.

$$\sigma = \frac{Ne^2\tau}{m} \tag{2.148}$$

and N^*/N, where N^* is the effective density of electrons, is often close to unity.

The optical properties of many solid metals for wavelengths in the near infra-red can be explained reasonably well by the free electron model. However, in the visible to near ultra-violet range, the reflectivity drops off rapidly and the optical constants show structure not consistant with the simple model. In copper, for example, a reflectance of nearly 100% is observed at wavelengths greater than 600nm but falls off rapidly at shorter wavelengths[41]. The drop in reflectivity near 600nm is caused by the onset of an interband transition. In copper, the d bands lie 2eV below the Fermi energy and the strong absorption observed at 600nm (≃2eV) is due to the excitation of electrons lying in the d band up to the Fermi level. The optical properties of liquid copper[42] however, shows no evidence of interband transitions over a wide range of wavelengths (200 to 800nm). Similar observations have been made for a number of liquid metals although in some cases the ellipsometrically determined dielectric function does not agree too well with the Drude predictions[43]. Nevertheless, the structure observed in the reflectivity and dielectric function of solid metals associated with interband transitions, is not apparent in the liquid state of the metal, except in the far ultra-violet where excitation of core electrons becomes possible. Notable exceptions are mercury and the alkali metals.

2.7.4 The optical properties of mercury

There has been considerable controversy concerning the optical properties of liquid mercury with respect to the applicability of the Drude free electron model. The optical constants have been determined by a number of researchers[44-46] from reflectivity measurements at normal incidence over a wide range of wavelengths and according to these authors, the properties agree well with the Drude formulae. The optical properties determined ellipsometrically[46-48] at larger angles of incidence, however, differ considerably from the Drude result for wavelength greater than 300nm.

Several attempts have been made to reconcile the apparent discrepancy between the observations cited above. Smith[49] proposed a semi-empirical model in which the scattering of an electron following a collision becomes so strong in the presence of an electromagnetic field that the direction of the electron tends to reverse itself. Bloch and Rice[50] have proposed a model in which the surface of the mercury comprises a diffuse transition zone over which the properties of the system change continuously from those of the bulk metal to those of the contact medium. In this transition zone, where the density of mercury decreases from its bulk value to zero, they assume that a density exists where the electron states become localised. The properties of the localised states may then be characterised by the Lorentzian oscillator model. Using this model, Bloch and Rice[50] were able to account for the differences between the normal incidence reflectivity and ellipsometric data. Crozier and Murphy[48], again using an inhomogeneous surface transition layer model in which the dielectric function was assumed to change continuously in a direction normal to the surface, were able to arrive at essentially the same result by replacing the transition zone with a multilayer model.

Arakawa[51], on the other hand, has carefully analysed much of the experimental data published and concluded that if reasonable errors are included into the data then there is essentially no difference between the normal incidence reflectivity and ellipsometric data.

The reflectivity data by Crozier and Murphy[48] for both p and s polarised light for an angle of incidence of 70° is noteworthy since the experimental values of R_s were, within experimental error, equal to the predicted Drude value. They reported however, a significantly lower value for R_p compared to the Drude result. The dielectric function calculated from the measured values of R_p and R_s were in reasonable agreement with ellipsometric results which would seem to indicate that the differences between normal incidence reflectance and ellipsometric data is not due solely to experimental error. There would appear to be a fundamental difference in the nature of the interaction of p and s vector fields with a free electron gas. While inhomogeneous optical properties have been introduced to describe the surface of mercury it would seem more realistic to describe the surfce layer interms of an anisotropic dielectric function. However, these models have been shown to be only low order approximations when the surface region of metals and their interaction with electromagnetic fields are analysed from a microscopic point of view. The microscopic or non-local approach to the optical properties of metals is described in section 2.9.

2.8. Optical models for the electrified interface

Phenomenologically, the simplest model that can be used to account for the changes that are observed in reflectance or polarimetric techniques when a metal-electrolyte interface is perturbed by an external field is that of a four-layer model shown in Fig. 2.8.

In ellipsometric studies of the electrical double layer only the combined optical effect of the system as a whole is observed experimentally*.

However, if individual layers in the simple model are assumed to be homogeneous isotropic with sharp boundaries and that there are no specific interactions between adjacent layers, then the optical effects can be divided into two categories and modeled independently. The optical effect of modulating the electrode potential has been assumed to arise from

1. Changes in the concentration of species on the solution side of the interface; which may include contributions from ionic concentration changes in the diffuse and inner layers and density and orientation changes of the solvent in the inner layer[16,22,45].

2. Changes of the electron density in the selvedge caused by the excess surface charge on the metal[55-61].

2.8.1. Optical models for the solution side of the double layer

If a change is injected into a metal, then in the simple case where only electrostatic interactions are considered, ions in the solution of opposite charge will be attracted towards the metal surface and ions of similar charge will be repelled. Experimental evidence suggests that there is a layer of solvent, about one molecule thick, in intimate contact with the surface so that the distance of closest approach of an ion is determined by the solvent layer thickness and an additional distance imposed by the solvation sheath associated with the ion. The electrostatic forces are unable to hold all of the ions required to balance the charge on the metal at the distance of closest approach because thermal motion will disperse the ions away from the

---

*McIntyre and Aspnes[52,53] have shown that if the refractive index changes in the surface region are small and real, then at an angle of incidence of 45° $(\Delta R/R)_p \simeq 0$ and $(\Delta R/R)_s$ is small. If there are changes in a strongly absorbing layer (i.e., the metal selvedge) then $(\Delta R/R)_p \simeq 2(\Delta R/R)_s$.

Bulk electrolyte n_1

Film (diffuse and compact layers) n_2

Metal selvedge $\hat{n}_3 + \delta\hat{n}_3 = n_3 + \delta n_3 - i(k_3 + \delta k_3)$

Bulk metal $\hat{n}_3 = n_3 - ik_3$

Figure 2.8. Simple four layer model for the metal-aqueous electrolyte interface. The selvedge is a region extending inward from the metal surface where the optical properties of the metal deviate from bulk values due to the surface charge on the metal.

electrode to form a space charge region called the diffuse layer. The excess concentration of ions in the diffuse layer is predicted by the Gouy-Chapman theory[62] to decrease exponentially from a maximum value close to the electrode surface. The thickness of the diffuse layer is characterised by a distance $1/\kappa$, where κ is the Debye-Huckel reciprocal length, and is the distance to a plane parallel to the electrode surface which accomodates the total charge giving the same electrical effect as the diffuse charge. Figure 2.9 gives a schematic representation of the structure of the electrical double layer.

The concentration profiles in the diffuse layer which vary continuously in a direction normal to the electrode surface constitute a film of inhomogeneous refractive index. McCrackin and Colson[63] have shown that the optical properties of an inhomogeneous film can be accurately represented by a series of homogeneous films. The ellipsometric parameters are directly related to the integral $\int \Delta n dt$, where dt is the thickness of a layer and Δn is the difference between the refractive index of a film element and that of the ambient phase. Further, it has been shown by Stedman[54] that the effect of ions in the diffuse layer is determined by their surface concentrations and is essentially independent of the nature of the concentration profile. The method adopted by Stedman for computing the variation in optical behaviour of the diffuse layer (for a z:z electrolyte) with charge is outlined below.

In the absence of specific adsorption the diffuse layer charge must be equal and opposite to the charge on the metal which can be obtained from experimental capacitance-potential data by integration:

$$q_m = \int_{E_{q_m}=0}^{E} C dE \quad \text{and} \quad q_d = -q_m \ \mu C \ cm^{-2}$$

From Stern's modification of the Gouy-Chapman theory

$$\Gamma_{-,d} = \frac{(2RT\varepsilon c_b)^{1/2}}{zF}[\exp(zF\phi_2/2RT) - 1]$$

$$\Gamma_{+,d} = \frac{(2RT\varepsilon c_b)^{1/2}}{zF}[\exp(-zF\phi_2/2RT) - 1]$$

where $\Gamma_{-,d}$, and $\Gamma_{+,d}$ are the surface excesses of anions and cations in the diffuse layer respectively (mol cm^{-2}), c_b is the bulk electrolyte concentration, ε the dielectric permittivity and ϕ_2 is the potential drop across the diffuse layer. For dilute aqueous electrolytes at 25°,

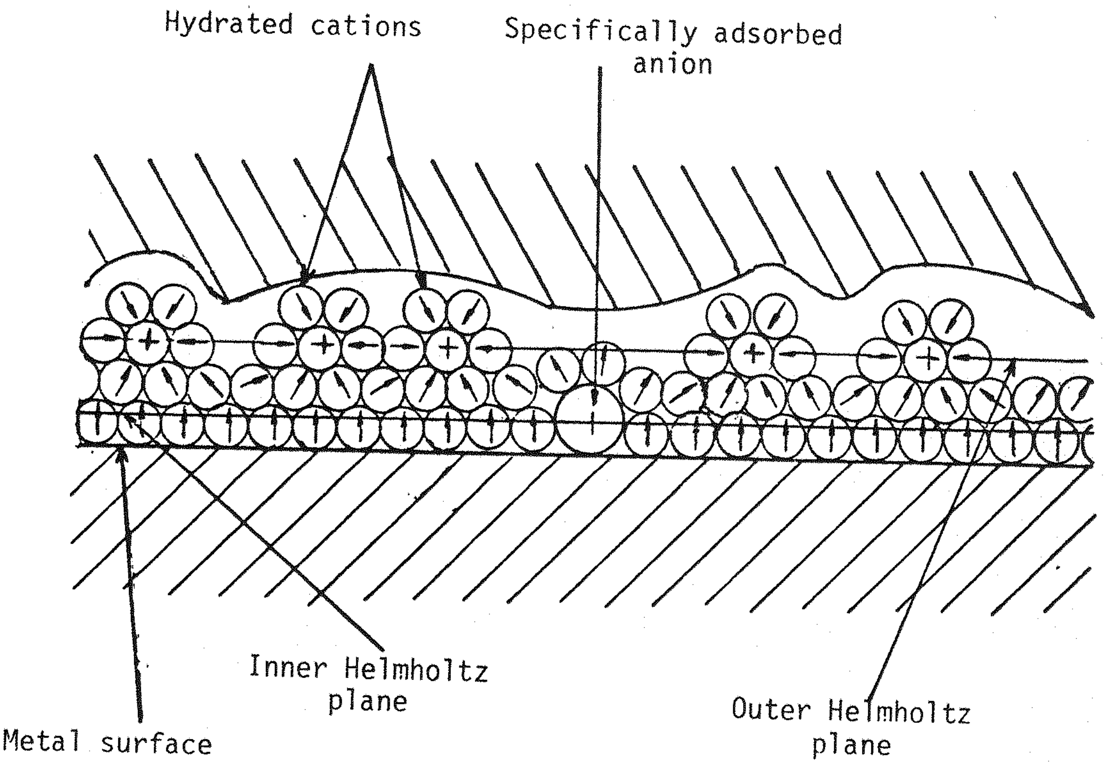

Figure 2.9. Schematic representation of the electrical double layer.

the constants can be evaluated to give

$$\Gamma_{\pm,d} = 6.081 \times 10^{-11} c_b^{1/2}[\exp(\mp 19.47\phi_2) - 1]$$

The ϕ_2 potential can evaluated from

$$q_m = (8RT\varepsilon c_b)^{1/2}\sinh \frac{zF\phi_2}{2RT} \qquad \mu C\, cm^{-2}$$

or

$$\phi 2 = \frac{\sinh^{-1}}{19.47} (-q_d/11.74 c_b^{1/2})$$

The surface excess of anions and cations is converted into a volume concentration by assuming that the ions are uniformly distributed in an element of thickness $2/\kappa$ and the total concentration of ions in the equivalent layer is then

$$c_+ = c_b + (\Gamma_{+,d} + q_{+,i}/F\times 10^{10})10^3\kappa/2 \qquad mol\, dm^{-3}$$

$$c_- = c_b + (\Gamma_{-,d} - q_{-,i}/F\times 10^{10})10^3\kappa/2 \qquad (2.149)$$

where $\kappa = (8\pi F^2/\varepsilon RT)zc^{1/2} = 3.29 \times 10^7 c^{1/2}$ (for $z=1$) and the terms $q_{\pm,i}$ are the contributions from specifically adsorbed ions which must be taken from data presented in the literature in this treatment. Stedman then used the Lorenz-Lorentz equation (Eq. 2.130) to calculate the refractive index of the equivalent layer calculating the density of the layer required in Eq. (2.130) from,

$$\rho = \rho_0 + (M_+ - \rho_0 V_+)c_+/1000 + (M_- - \rho_0 V_-)c_-/1000 \qquad g cm^{-3}$$

where ρ_0 is the density of water, $V_\pm$ are the apparent metal volumes of ions and $M_\pm$ the ion molecular weights. The refractive index of the equivalent layer is then from Eq. (2.130)

$$n = [(\bar{M} + 2\rho\bar{A})/(\bar{M} - \rho\bar{A})]^{\frac{1}{2}}$$

where the mean molar refractivity and the mean molecular weight are calculated from $A = \Sigma X_i A_i$ and $M = \Sigma X_i M_i$ with X_i the mole fraction of species i. In assessing the optical effect of specifically adsorbed ions Stedman[54] simply added the concentration of ions in the inner layer to those of the diffuse layer (Eq. 2.149) to form a single layer for optical calculations. The results computed for aqueous potassium chloride is given in Fig. 5.7 (section 5.1.1.) using capacitance data from Payne[64].

Chiu and Genshaw[65] have adopted a slightly different approach in calculating the refractive index of the inner layer. Starting with the Lorenz-Lorentz equation, they first calculated the 'refractive index' of an ion from molar volumes and refractivities. They then calculated the refractive index of an adsorbed layer by assuming it to be a linear combination of the refractive index of the ion and water

$$n_{film} = n_{H_2O}\ (1 - \theta) n_{ion}\theta$$

where θ is the fraction of surface covered by the ion. Value of n_{film} were calculated as a function of θ and used to produce calibration curves of Δ and Ψ . However, only the experimentally determined values of Δ (at one wavelength) were applied to the calibration curve to obtain the surface coverage of thiocyanate and bromide ions as a function of potential. The agreement between the ellipsometrical determined surface coverage and that obtained by electrocapillary measurements was good for bromide, particularly at the more cathodic potentials but rather poor for thiocyanate where the agreement can only be considered qualitative except for potentials cathodic of the pzc.

Stedman also calculated the optical effects due to volume changes of water in the inner layer based on the surface excess volumes reported by Hills and Payne[66]. Using bulk compression-refractive index data, Stedman demonstrated that inner layer contributions could account for a large fraction of the overall optical effects.

In the above treatments the models for the solution side of the double layer have assumed that the refractive indices of the inner and diffuse layers are real and can be estimated from bulk properties. The refractive index of these layers has been assumed isotropic, which in the case of water adsorbed in the inner layer, is contrary to the accepted model of solvent dipole orientation.

The possibility of interactions between the adsorbed layer and the metal surface, neglected in the above treatments, has been included in the work of Lazorenko-Manevich, *et al.*[67] in the form of a relaxation time modulation of the free electrons close to the metal surface. In their model they suggest that adsorbed ions distort the equipotential surface of the metal and these distortions act as scattering centres for free electrons incident on the surface from within the metal. The agreement they obtained between experiment and theory which included free electron electroreflectance effects and inner layer concentration changes was however, only qualitative.

Compared to the optical studies of ionic adsorption there has been relatively little published regarding the adsorption of organic molecules from electrolyte solutions. Barrett-Gultepel6 has studied the adsorption of benzene onto platinum from sulphuric acid and reported that no reasonable isotropic refractive index could be found to account for the results obtained. Solutions were found however, for uniaxially anisotropic films with n_p (refractive index parallel to the plane of incidence) > n_s (perpendicular to the incidence plane). These findings were in agreement with the interpretation based on double layer capacitance measurements that the benzene molecules are adsorbed with the plane of the ring parallel to the surface.

The adsorption of two isomeric quinolines at the mercury aqueous sodium hydroxide interface has been studied by Humphreys and Parsons[22] using a manual ellipsometer. Their results clearly show that re-orientation of mono-molecular layers can be observed and provide an analysis of the data in terms of a film with anisotropic optical constants which is in accord with the interpretation of double layer capacitance studies made by Buess-Herman et al.[68]

The Fresnel reflection coefficients for an anisotropic film on an isotropic substrate have been derived by Dignam, et al.[69] for a uniaxial optical medium with the optic axis oriented normal to the surface.

Polarised light incident on an uniaxial medium gives rise to two refracted waves since the refractive index of the medium is a tensor quantity whose principal components are n_o and n_e for components parallel and normal to the optic axis. The two refracted waves are called the ordinary and extraordinary rays where the ordinary wave is linearly polarised in the s direction and the extraordinary wave, so called because the vector normal to the plane of constant phase and that normal to the planes of constant amplitude do not coincide, is linearly polarised in the p direction. Associated with the two refracted waves are the angles of refraction $\emptyset_o$ and $\emptyset_e$ (see Fig. 2.10)

The relevant equations, given by Dignam et.al.[69], are:-

$$r_{s1,2} = (n_1\cos\emptyset_1 - n_o\cos\emptyset_o)/(n_1\cos\emptyset_1 + n_o\cos\emptyset_o)$$

$$r_{p1,2} = (n_o\cos\emptyset_o - n_1\cos\emptyset_e)/(n_o\cos\emptyset_e + n_1\cos\emptyset_e)$$

$$r_{s2,3} = (n_o\cos\emptyset_o - n_3\cos\emptyset_3)/(n_o\cos\emptyset_o + n_3\cos\emptyset_3)$$

$$r_{p2,3} = (n_3\cos\emptyset_e - n_o\cos\emptyset_3)/(n_3\cos\emptyset_e + n_o\cos\emptyset_3)$$

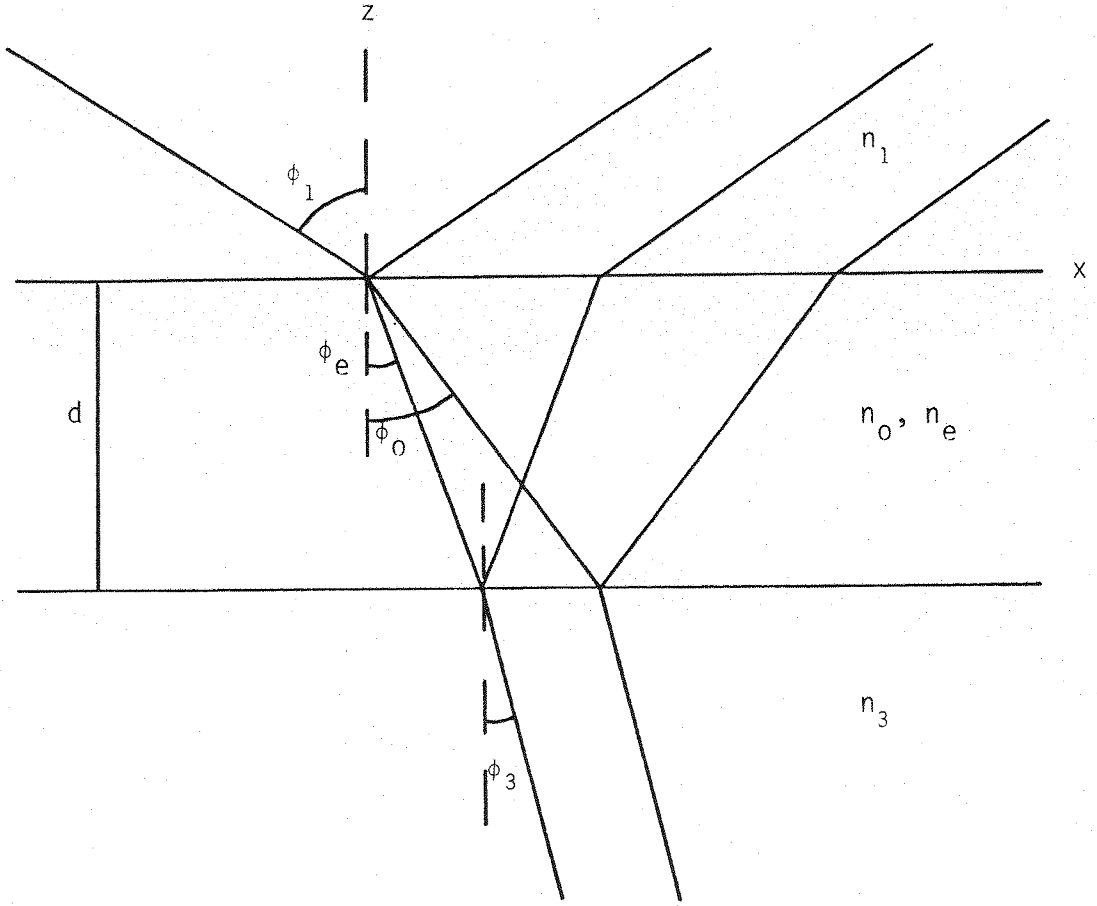

Figure 2.10. Reflection and refraction from a film exhibiting uniaxial anisotropy on an isotropic substrate.

$$R_v = [r_{v1,2} + r_{v2,3}\exp(-i\beta_v)]/[1 + r_{v1,2}r_{v2,3}\exp(-i\beta_v)]$$

where $\beta_v = (4\pi d/\lambda)n_o\cos\phi_v$, $v = r,s$ and the terms n_o, n_e ϕ_o and ϕ_e can be expressed in the p,s coordinate frame by

$$n_s = n_o,\ \phi_s = \phi_o$$

and

$$n_p\cos\phi_p = n_e\cos\phi_e$$

With the aid of Snell's law,

$$n_1\sin\phi_1 = n_o\sin\phi_o = n_e\sin\phi_e = n_3\sin\phi_3$$

the term $\cos\phi_e$ can be written

$$\cos\phi_e = (n_p^2 - n_1^2\sin^2\phi_1)^{1/2}/n_s$$

The above equations apply also to absorbing anisotropic films in which case n_p and n_s become complex.

2.8.2. The electroreflectance effect

When a semiconductor is exposed to a modulated electric field sharp structure in the relative reflectivity spectrum is often observed[70]. This effect, known as electroreflectance, is due primarily to a distortion of the band structure in the space charge region caused by the applied field (the Franz-Keldysh effect). The space charge region in a semiconductor and the penetration depth of light (in the visible region) are often both about 1 µm, whereas the field penetration depth in metals, given by the Thomas-Fermi screening length, is approximatly 0.1 nm for most metals owing to the much higher carrier density. Since the penetration depth of visible light in metals is about 10 nm, the field modulation effects on the band structure of metals are expected to be very much smaller than the corresponding effects in semiconducors. Nevertheless, the electroreflectance effect for metals in contact with electrolyte solutions has been observed to be at least as large as the contribution from the diffuse layer on the solution side of the interface.

The first observation of an electroreflectance spectum of a metal was made by Feinleib[55], by applying a 2 V peak-to-peak signal at 35 Hz to a gold electrode in aqueous KCl (under non-potentiostatic conditions), although because of the small field penetration depth he assumed that the effect was due to changes in the optical properties of the electrolyte. In subsequent papers, Hansen and Prostak[56,57] showed that no reasonable modulation of the electrolyte optical constants occuring in the double layer could account for the peak observed by Feinleib. They did show, however, that if the free electron concentration in a 5 nm surface layer was modulated the plasma frequency, ω_p, might also be modulated (see Eq. 2.146), and the calculated shift of ω_p to lower frequencies was sufficient to qualitatively describe the predominant peak near the plasma edge of gold. However, McIntyre and Aspnes[58] showed that the simple free electron model led to the wrong sign for the electroreflectance effect for metals such as silver and gold, and that experimental spectra contained additional structure at energies far removed from the main peak which was not predicted by the Hansen and Prostak model.

A model proposed by McIntyre and Aspnes[53] has successfully predicted the overall structure and approximate magnitude of electroreflectance spectra of silver and gold at low bias potentials. The model assumes that two semi-infinite phases with homogeneous dielectric functions K_1 and $\hat{K}_3$ are separated by a region of thickness d << λ which has a dielectric function $\hat{K}_2(z)$ which varies continuously between K_1 and $\hat{K}_3$ in a direction normal to the surface plane (Fig. 2.11).

In regions of frequency sufficiently removed from an interband transition the dielectric function of a metal can be separated into free electron, $\hat{K}_f$, and bound electron, $\hat{K}_b$, contributions[11].

$$\hat{K}_3 = \hat{K}_{3f} + \hat{K}_{3b}$$

Assuming that a charge on the metal surface causes a change, ΔN, in the free electron concentration in the selvedge, the resulting change, $\Delta\hat{K}(z)$, in the free electron contribution to the dielectric function may be expressed as

$$\hat{K}_{3f} + \Delta\hat{K}(z) = 1 + \frac{e^2(N + \Delta N)/m\varepsilon_0}{\omega^2 - i\omega/\tau} \qquad (2.150)$$

from which

$$\Delta\hat{k}(z) = (\hat{K}_{3f} - 1)\Delta N/N \qquad (2.151)$$

Further, assuming that the mean value $\langle\Delta\hat{K}\rangle$ is defined by averaging the change $\Delta\hat{K}(z)$ over the transition region

$$\langle\Delta\hat{K}\rangle = \frac{1}{d}\int_{-d}^{0} \Delta\hat{K}(z)dz \qquad (2.152)$$

and if the variation of $\Delta\hat{K}(z)$ between K_1 and $\hat{K}_3$ is linear then from Eq. (2.247)

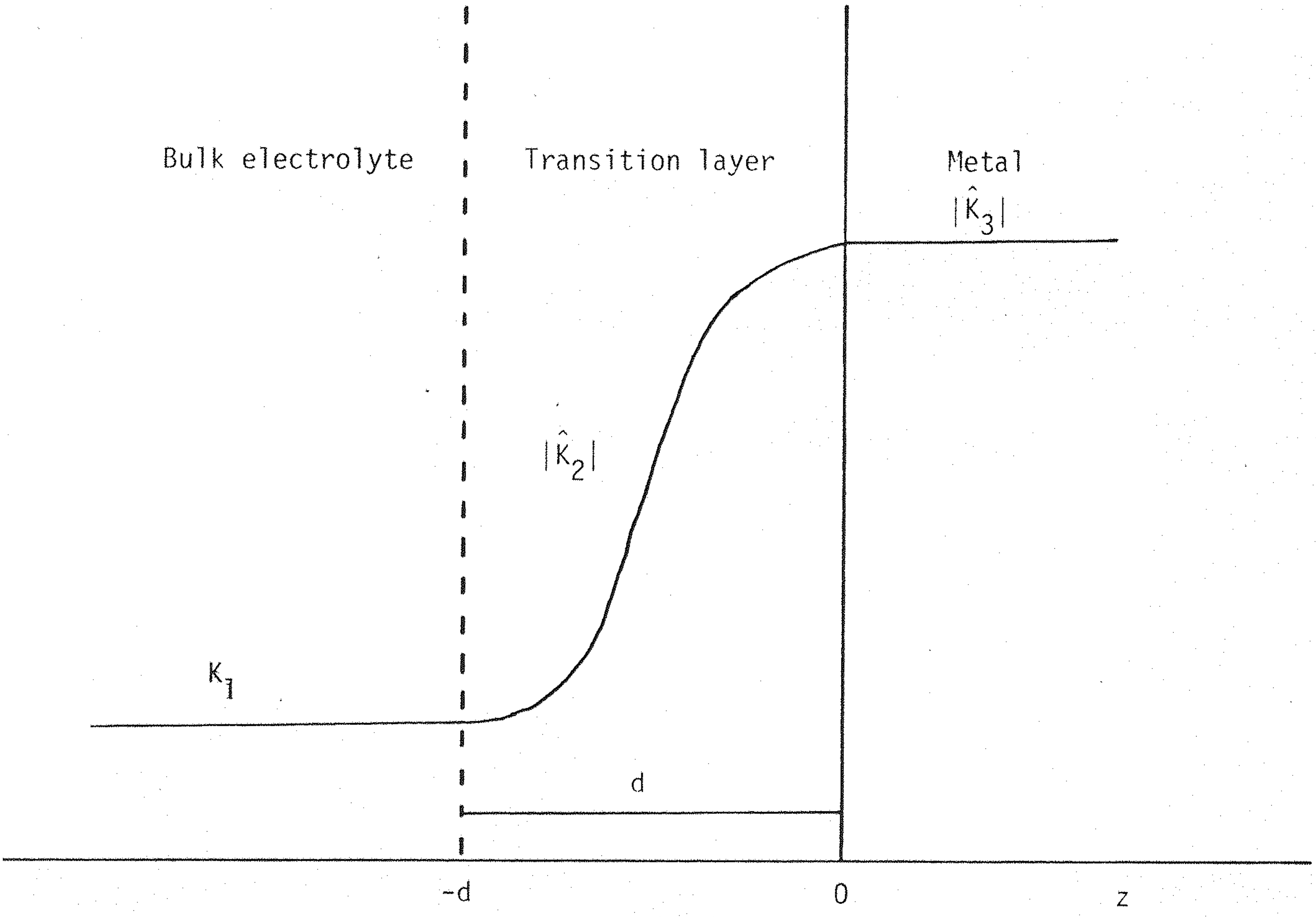

Figure 2.11. Schematic representation of the transition layer model illustrating the optical properties of a metal-electrolyte interface.

$$\langle\Delta\hat{K}\rangle = \frac{(\hat{K}_{3f} - 1)}{d}\frac{\Delta N_s}{N} \qquad (2.153)$$

where ΔN_s is the excess of free electrons per unit surface area required to balance the charge, q_m, on the surface of the metal. The mean local value of the selvedge dielectric function, $\hat{K}_2$, is then

$$\hat{K}_2 = \hat{K}_3 + \langle\Delta\hat{K}\rangle = \hat{K}_3 + \frac{(\hat{K}_{3f} - 1)}{d}\frac{\Delta Ns}{N} \qquad (2.154)$$

and equating real and immaginary parts,

$$K_2' = K_3' + \frac{(K_{3f}' - 1)}{d}\frac{\Delta N_s}{N} \qquad (2.155)$$

$$K_2'' = K_3'' + \frac{K_{3f}''}{d}\frac{\Delta N_s}{N} \qquad (2.156)$$

where $\hat{K} = K' - iK''$ and ΔN_s is related to q_m by $\Delta N = -q_m/e$. The free electron contribution, $\hat{K}_{3f}$ is given by

$$\hat{K}_{3f} = 1 - \frac{Ne^2/m\varepsilon_0}{\omega^2 - i\omega/\tau}$$

where

$$\tau = \sigma_0 m/Ne^2$$

and σ_0 is the dc conductivity.

From a knowledge of the substrate optical constants the above equations can be used to calculate Δ and Ψ from the charge on the electrode. The effect that the predicted changes in the transition layer dielectric function has on ellipsometric parameters is shown in Fig 5.6 (section 5.1.1.).

Several other models have been proposed[59,60] to account for the electroreflectance effect and, where compared with experimental data, give reasonable agreement. All of the treatments mentioned above rely on simple stratified models using local dielectric functions. However, it has been strongly emphasised in two recent review articles[61,71] that a non-local description of the interface must be considered in order to gain an improved understanding of the interaction of light with metals.

2.9. Non local effects at metal surfaces

The classical, and most sensitive method for determining the optical constants of metals is by ellipsometry. However, these instruments require extensive alignment and calibration before optical constants can be evaluated accurately. The accessible spectral range is usually limited to 200 nm - 3000 nm by the transmission of polarisers and retarders, and data is usually collected at a few isolated wavelengths. Reflectance spectrometers, on the other hand, are usually less sophisticated, require less critical alignment and calibrations, and measurements can be made while the wavelength is scanned continuously. In the determination of the optical constants by reflection measurements one has the choice of measuring the reflectivity for p or s polarised light incident on the sample, or of making measurements at normal incidence (polarisation vector always parallel to the surface). Two parameters are required to determine n or K, the options being to measure R_p or R_s at two angles of incidence, R_p and R_s at one angle or, if the normal incidence reflectivity is measured over a sufficiently wide range of frequencies, the optical constants may be evaluated by use of the Kramers-Kronig relationships*.

All of the above methods should, of course, lead to the same value of $n(\omega)$ or $K(\omega)$. However, inconsistency between the dielectric functions obtained from measurements with p and with s polarised light[72], and those obtained at different angles of incidence[73] have been observed. Attempts to reconcile these differences have been made by assuming surface anisotropy or inhomogeneity. These models account for the observed differences, but only by the introduction of fitting parameters which lack direct physical significance.

Prompted by an unexpected strong absorption in the imaginary part of the complex dielectric function, determined by non-normal reflectivity measurements, of the alkali metals[75] between the Drude absorption region and the absorption due to interband transitions, Kliewer and Fuchs[76] re-examined the theory of reflectance from a jellium solid. The assumptions made in using the jellium model is that the positive charged from the ion core is spread out into a uniform background charge and the conduction electrons are allowed to move more or less freely. Kliewer and Fuchs assumed also that any electron impinging on the surface of the metal from within would be specularly

---

*The Kramers-Kronig dispersion relations form a set of integro-differential equations that link the real and imaginary parts of a complex function, provided that the complex quantity is a linear response function which is causal and finite[74].

reflected. The validity of this assumption is difficult to establish, but the specular scattering model provides a more understandable picture of the fundamental physics than do the more rigorous treatments. The principal features obtained with the specular scattering model do however, appear in rigorous approaches.

In the classical treatment of the interaction of light with a metal, it was seen that the divergence of the electric field at the metal surface is zero (Eq. 2.92), i.e. $\nabla.E = 0$. Simply restated, there are no charge fluctuations in the metal, and in the case of normal incidence or s polarised light incident on the surface one would expect a zero divergence since the electric vector is always parallel to the surface. However, for p polarised light there is a component of the electric vector that is perpendicular to the surface, and if non-zero values for the divergence of the electric field are permitted, then there can exist charge fluctuations within the metal. The interaction of free electrons with the charge would give rise to an additional absorption mechanism. It has been shown that if $\nabla.E \neq 0$ for p polarised light then the electric field component inside the metal has a rapidly varying component in a direction normal to the surface plane[71,77]. Since both the direction of propagation of the field and the electric vector are co-linear, the response of the system to the field must be considered as a longitudinal response function.

The dielectric function was introduced phenomenologically to relate the displacement $\mathbf{D}$ within a medium with the electric field, E, causing the displacement. Assuming that $\mathbf{D}$ and $\mathbf{E}$ are linearly related and causal, the classical relationship connecting them is simply $\mathbf{D} = \varepsilon\mathbf{E}$. The actual field in the metal will be a combination of the externally applied field and any fields induced within the medium. The induced fields result from all field effected perturbations that alter the ground state of the system, such as induced polarisations an charge densities.

To determine the displacement, $\mathbf{D}$, at any space-time point, P,t inside a jellium when an electromagnetic field is incident on the surface requires a knowledge of the field in the region of the point P. Fig. (2.12) shows, in a very simple way, that free electrons travelling towards the point P and arriving at a time t will contain energy contributions transfered to them by the field through which they moved in getting to P. The field, and hence the system's response near P at time t will be affected by the field at earlier times in the spatial region around P. Therefore, there are both spatial and temporal regions about P,t which must be considered in determining the field and

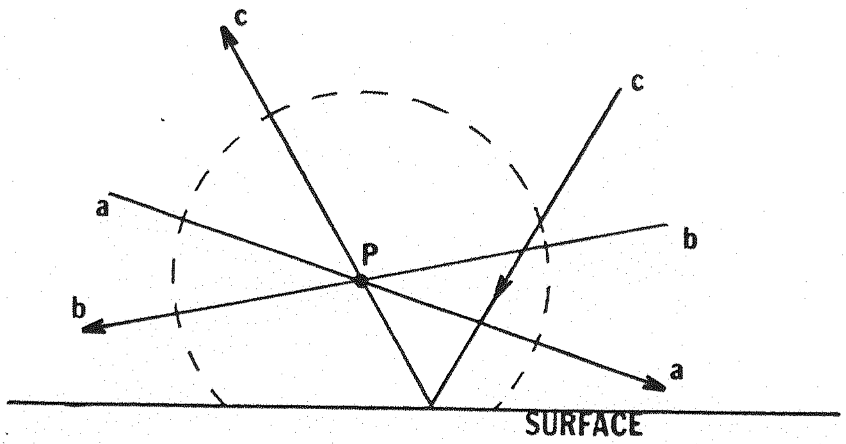

Figure 2.12. Free electrons in the surface region of a metal that intersect at the point P. The region that influences the field at P is indicated schematically by the dashed circle.

response at the space-time point P,t. The inclusion of the temporal region in the dielectric function is implicit because its origin stems from the time representation of Maxwell's equations. The extension of the treatment to include spatial variation is not standard and this extension to the classical formulation leads to the field of non-local optics.

The dielectric function is a response function or linear integral operator that connects the field $\mathbf{D}(\mathbf{r},t)$ with the field $\mathbf{E}(\mathbf{r},t)$. In general

$$\mathbf{D}(\mathbf{r},t) = \int d^3\mathbf{r}'\int_{-\infty}^{t} \varepsilon(\mathbf{r},\mathbf{r}',t-t')\mathbf{E}(\mathbf{r}',t')dt' \qquad (2.157)$$

where $\mathbf{D}(\mathbf{r},t)$ describes the response of the system at location $\mathbf{r}$ and time t to the stimuli $\mathbf{E}(\mathbf{r}',t')$ acting at all times t' and places $\mathbf{r}'$. The system response function is non-local since the displacement at a space-time point $(\mathbf{r},t)$ depends upon conditions in the region of the point $\mathbf{r}$ (represented by $\int d^3\mathbf{r}'$) and at times prior to t (represented by $\int dt'$).

For monochromatic light of frequency ω, the Fourier transform of the above equation may be obtained. If f(t) is some arbitrary function of time the Fourier transform of the function is given by

$$F(\omega) = \int f(t)\exp(i\omega t)dt$$

and for a time shifted quantity h(t-t')

$$H(\omega) = \int h(t-t')\exp[-i\omega(t-t')]dt'$$

The Fourier transform of Eq.(2.157) is therefore

$$\mathbf{D}(\mathbf{r},t) = \int d^3\mathbf{r}'\varepsilon(\mathbf{r},\mathbf{r}',\omega)\mathbf{E}(\mathbf{r}',\omega) \qquad (2.158)$$

which reduces to the classical form when spatial dispersion is neglected, that is when the wavelength of the stimulating field is much larger than interatomic distances. Neglecting spatial dispersion is tantamount to making the local field approximation. The dielectric function, within the framework of the local field approximation may be expressed as

$$\varepsilon(\mathbf{r},\mathbf{r}',\omega) = \delta(\mathbf{r},\mathbf{r}')\varepsilon(\omega)$$

where δ is the Dirac delta function. Substituting into Eq.(2.158) gives

$$\mathbf{D}(\mathbf{r},t) = \int d^3\mathbf{r}'\ \varepsilon(\omega)\delta(\mathbf{r}-\mathbf{r}')\mathbf{E}(\mathbf{r}',t)$$

and since $f(x)\delta(x)dx = f(0)$, the displacement may be written

$$D(\mathbf{r},t) = \varepsilon(\omega)E(\mathbf{r},\omega)$$

which is identified as the classical description of the **D**-**E** relationship and is clearly local in form since **D** at a point **r** is determined completely by E at the same point.

In dealing with the interaction of electromagnetic radiation with a medium it is usual to define field effected quantities with respect to the wave vector of the incident field, hence the Fourier transform of the general response function is $\Sigma(\mathbf{q},\mu)$ where **q** is a wave vector (parallel to the direction of propagation).

For a homogeneous and isotropic medium, the system response to a field $\mathbf{E}(\mathbf{q},\omega)$ is

$$\mathbf{D}(\mathbf{q},\omega) = \varepsilon(\mathbf{q},\omega)E(\mathbf{q},\omega) \qquad (2.159)$$

The dielectric response function is tensorial and requires two independent functions to describe the total response to longitudinal and transverse fields. These two functions are usually the longitudinal and transverse dielectric response functions $K_l(\mathbf{q},\mu)$ and $K_t(\mathbf{q},\mu)$ respectively.

Based on the specular scattering model, Kliewer[71] has calculated the electric field strength normal to the surface plane for a vacuum-jellium interface using electron gas parameters representing those of aluminium, and compared the result to the classical, local field, case. It appears from these and other calculations[77] that, even in the case of the vacuum-jellium interface, the system response cannot always be characerised by a bulk response function, nor can the function be assumed local but anisotropic because of the spatial variation of the longitudinal field.

To illustrate the complexity of the equations required in non-local treatments the longitudinal dielectric function for the free electron gas is given below[71]:

$$K_l(\mathbf{q},\omega) = 1 + \frac{(1 + i/\omega\tau)[\varepsilon^L(\mathbf{q},\omega + i/\tau]}{1 + (i/\omega\tau)[\varepsilon^L(q,\omega + i/\tau) - 1]/[\varepsilon^L(q,0) -1]}$$

where

$$\varepsilon^L(q,\omega) = 1 + (3\omega_p{}^2/q^2/v_F{}^2)f_1$$

$$f_1 = \frac{1}{2} + \frac{1}{8z} \quad [1 - (z - u)^2]\ln\frac{z - u + 1}{z - u - 1} \quad + [1 - (z + u)^2]\ln\frac{z + u + 1}{z + u - 1}$$

$z = q/2k_F$, $u = /qv_F$, k_F is the magnitude of the wave vector at the

Fermi surface, v_F is the magnitude of the Fermi velocity, and $q = |\mathbf{q}|$.

The validity of the McIntyre-Aspnes model[53], in which a metal is covered by a thin selvedge layer of uniform thickness with a local dielectric function (Fig. 2.11), has been analysed from a microscopic point of view by Feibelman[77]. The treatment involved a quantum mechanical evaluation of the electron dynamics in the selvege region of a flat surfaced jellium solid. The main conclusions from this work appear to be that for s-polarised light, where the electric field is parallel to the surface and varies slowly as the field penetrates the selvedge, the McIntyre-Aspnes result turns out to be essentially correct. For p-polarised light, the electric field component is normal to the surface and changes rapidly across the surface layer. However, the displacement vector cannot respond infinitely quickly, and the system is therefore best described in terms of a longitudinal response function. The surface thus responds in a fundamentally different manner to electric fields that are normal than those that are parallel to it, and it is desirable therefore to describe its response by an anisotropic dielectric tensor.

There have been several methods used in calculating the electric field near a metal surface[76-79] and in calculating how these fields contribute to the reflectivity. Although different approaches have been employed, they all arrive at essentially the same conclusions as those outlined by Feibelman.

The application of microscopic treatments to the metal-electrolyte interface does not appear to have gained much attention. Brodskii and Urbakh[78] have included a non-local dielectric function in the transition region between bulk metal and bulk electrolyte which is perturbed by the potential drop across the Gouy-Chapman layer. However, they did not include any contributions arising from the metal side of the double layer, and offered no experimental comparisons. The work of Kof man <u>et al</u>.[80] appears to be the only case in which a free electron electroreflectance effect has been included into a microscopic scheme, but demonstrated only a qualitative agreement between theory and the experimentally measured modulated relative reflectance spectrum (Au(111), normal incidence).

There is substantial evidence, both theoretical and experimental, which suggests that p-polarised light incident on a metal surface produces a selvedge electric field that is more complex than the classical descriptions allow. The presence of an electrolyte, oriented dipoles and specifically adsorbed ions all need to be considered in a determination of the actual field and non-local effects are expected to be more pronounced than for the same metal in vacuum. The difference between classical and microscopic approaches, however small, may be significant in optical studies of the electrical double layer where the changes in the parameters describing the free surface and the perturbed surface are often small. However, no such comparison between classical and non-local contributions to experimentally observable parameters appears to have been given except for theoretical calculations of idealised jellium-vacuum interfaces (see for example Ref.[77]). It is clear that much additional work is needed before optical studies yield anything more than qualitative verification of established models.

CHAPTER 3: INSTRUMENTAL.

3.1 Introduction.

The ellipsometer was built by I.B.M. at the Manufacturing Technology Centre, Southampton, and was originally interfaced to an I.B.M. 1130 computer for automatic operation. It is designed to enable both solid and free liquid surfaces to be studied. Consequently, the sample surface is horizontal and positioned at the common horizontal axis about which the polariser and analyser arms can be rotated.

The ellipsometric parameters, Δ and Ψ are determined by measuring the azimuths of the polariser and analyser that give extinction of light at the photo-detector. The null condition is achieved when plane polarised light incident on a linear quarter wave retarder produces a polarisation state which upon reflection from the sample surface is restored to a linear state. An analysing prism, whose transmission axis is crossed with the plane of polarisation of the reflected beam, extinguishes the light falling on the detector. The nulling process is automated by the inclusion of four Faraday rotation devices, two of which operate under dc conditions and rotate the plane of polarised light entering the retarder and polarisation plane entering the analyser by an amount proportional to the current flowing through the rotation devices. The two dc Faraday compensators produce additional angular offset of the plane of polarisation produced by the polariser and by reflection from the sample surface by currents generated in feed-back loops. The null condition is detected by phase sensitive analysis of an oscillating waveform produced at the photo-detector by the other two Faraday devices operating under ac conditions each of which is placed directly after the dc Faraday compensators. The polarisation angles producing the null condition are then the sum of the prism azimuths and the contribution of angular offset produced by the Faraday dc compensators.

The ellipsometer has been interfaced with a Motorola M6800 based microprocessor system which controls data acquisition and the wavelength of light incident on the sample. The microprocessor replaces the I.B.M. 1130 computer which was not supplied with the ellipsometer.

3.2 Mechanical components.

The ellipsometer is supported on a 4 foot square by a 6 inch thick granite block which stands on 3 leveling feet. The arms containing the polarising prism, quarter wave retarder and Faraday compensators, are of a welded steel fabrication secured through double set of ball races onto a welded steel table. The arms have machined slideways into which supports for the optical components are mounted. Two counter-balance arms, also welded steel and on separate bearing assemblies, are connected to the main arms to reduce the load on the main arm bearings. The centre of gravity of the main and counter-balance arm assemblies coincide with the axis of rotation.

The arms are elevated to the required angle by rotation of a stepper motor (Superior type SS50) meshing with teeth on a disc coaxial with the axis of rotation. Two angular measuring tapes (Heidenhain) fixed to either side of the disc enable the angle of incidence to be set to within 0.003° with a maximum error of 0.01°.

The sample stage is mounted on a heavy steel base by means of three cylindrical support pillars which allow vertical adjustment of the sample stage. The stage is micro-positioning and capable of X and Y translation, rotation about the Z axis by 360° and can be tilted about the X and Y axes by ±1.5°. The height of the sample stage is adjusted by means of a hydraulic jack. Mechanical isolation of the sample stage, essential when studying free liquid surfaces, has been achieved by placing six sorbo rubber balls between the granite block and the steel base of the sample stage. This effectively damps out vibrations transmitted through the floor on which the ellipsometer stands, vibrations produced by the circulation of cooling water and by manipulation of the optical components.

3.3 Optical components.

The optical layout of the ellipsometer is shown in Fig. 3.1. The light source is a 75 watt high pressure xenon arc (osram) mounted in a steel housing (Oriel type C-32) fitted with an adjustable condensing lens assembly (Fig. 3.2). The arc is powered by a stabilised dc supply (Oriel C-72-20-1). Light from a He/Ne laser (R.C.A. 1mW), λ = 632.8 nm, mounted on the polariser arm, can be selected by interrupting the light from the xenon source by a sliding assembly containing two totally internally reflecting (TIR) quartz prisms.

Light from the xenon arc is focused onto a quartz prism monochromator (Schoeffel Instruments QPM 30S). A micrometer screw is used to adjust the wavelength which can be driven by a stepper motor (Superior type SS25) for automatic wavelength scanning. The monochromator has a calibrated wavelength range from 190 nm to 1500 nm and an adjustable slit width of 0.1 mm to 2.0 mm. The half intensity bandwidth ranges from 5 nm at 280 nm to 40 nm at 680 nm for a 0.4 mm slit.

The polarising prisms are quartz Rochon polarisers (I.C. Optical

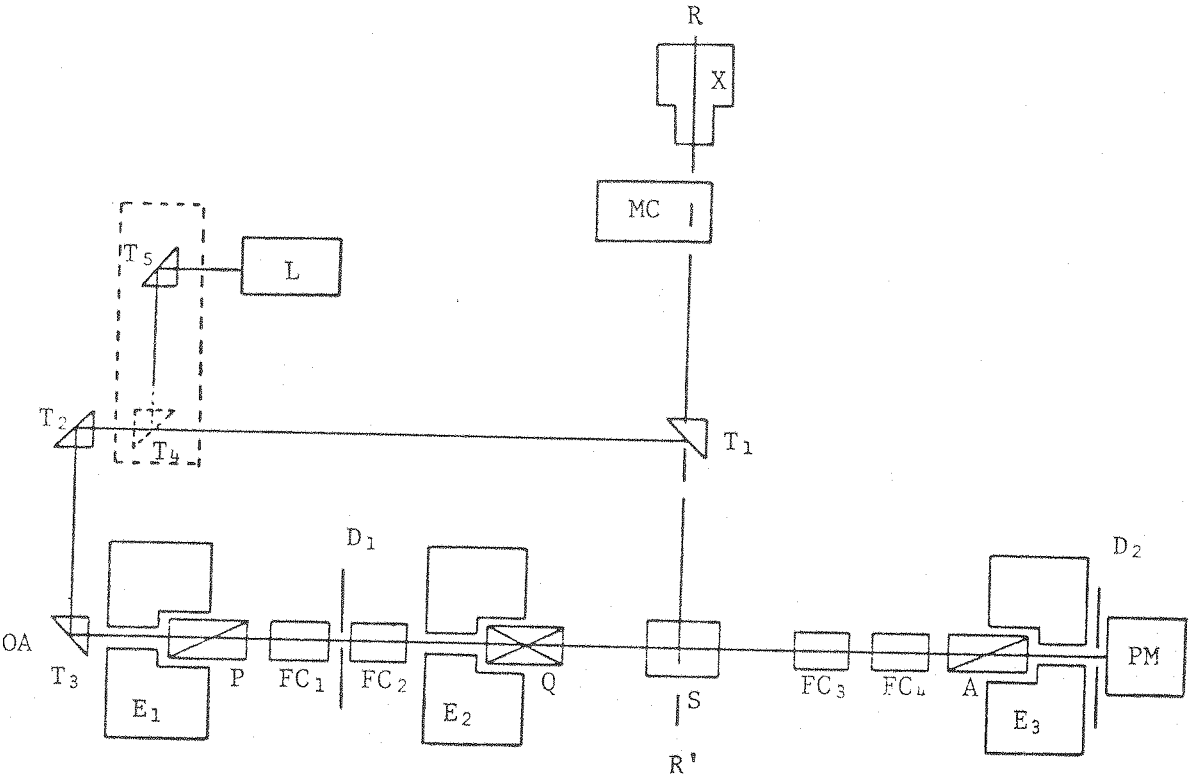

X, 75W dc Xe arc and condenser lens assembly; MC, prism monochromator; T_{1-5}, total internal beam folding prisms; E_{1-3}, servo-driven Moire encoders; FC_{1-4}, Spectrosil 'A' Faraday cores; $D_{1,2}$, stops to eliminate extraordinary rays transmitted by quartz Rochon polarisers P and A respectively; Q, achromatised three-reflection rhomb λ/4 retarder; PM, photomultiplier; S, surface; OA, optic axis; RR', rotation axis of the arms; L, He/Ne laser.

Figure 3.1. Optical layout of the ellipsometer

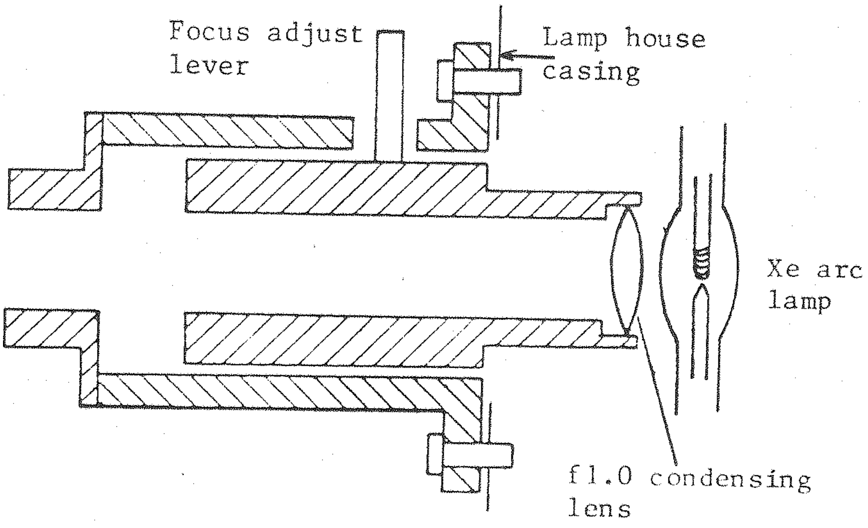

Figure 3.2. Condensing lens assembly

Services). Beam deviation through these prisms have been measured by I.B.M. at 3.5 and 9.2 seconds of arc for the polariser and analyser respectively. Ellipticity in the transmitted beam has been measured at the N.P.L. and has been found consistent over the whole face of both prisms at about 0.135° (= $\tan^{-1}$ b/a).

The quarter wave retarder is an achromatised three-reflection rhomb[81] (Bellingham and Stanley) with a stated beam deviation of < 0.0001°. The retardation has been stated to be 90 - 90.2° for wavelengths in the range 200 to 900 nm. A mica quarter wave plate (for λ = 632.8 nm) is also available.

The polarising and retarding prisms are mounted in three-armed 'spiders'. These assemblies are held by means of spring clips to steel flanges which are fixed to the arm mounts through bearings. Also mounted on the steel flanges are large glass divided circles which are used to measure the prism azimuths (Optical Measuring Tool Ltd., Helston, England). The divided circles comprise a glass disc onto which radial lines have been scribed. Rotation of the glass circles produce Moire fringes when the radial lines on the disc are viewed through a second, fixed, grating. A light beam passing through the rotating disc and reference grating cause fringes to be produced which are observed by means of photo-diodes. Two diodes sense each fringe sequentially so that the direction of rotation can be determined from the phase relation of the two pulse trains. The pulses produced are squared and counted in the angular display unit (Newall electronics), and subsequently encoded as parallel binary coded decimal (BCD) data. The divided circles have internal zero markers, and offset facilities in the display unit enable the relevant prism axis to be set to a known angle. This enables absolute azimuth angles to be measured with a resolution of 1 second of arc with an overall accuracy of ±2 seconds in 360°. The angles are displayed as degrees, minutes and seconds on Nixie tubes. The circles may be set manually or motor driven via dc motors (Ether type 955L for P and A, Evershed and Vignoles type 133/2/C for Q) with friction drive to the periphery of the glass disc.

Two Faraday rotation devices on each arm provide offset and modulation of the plane of polarisation. The cores, made at N.P.L. from Spectrosil synthetic silica (Thermal Syndicate), have end faces parallel to ±0.001° producing a beam deviation of about 0.0005°. The current carrying coils surrounding the silica cores are cooled by a Churchill closed loop water circulator. Flow sensing switches disable the power supply to the current producing circuitry if the water flow rate drops significantly.

The detector is a photomultiplier (EMI type 9659 Q.A.M.) with an extended S-20 photocathode (Centronix 94283 SA) and quartz window.

A detailed analysis of the theoretical limits of precision determined by the mechanical properties and by the defect properties of the optical components for this instrument has been reported by Lowe[82].

3.4 Ellipsometer electronics.

The main function of the ellipsometer electronics is to automate the nulling process, data acquisition and wavelength changes. The electronics system is housed in a 6 foot by 19 inch rack (F.T. Davies type EPP6-19), which contains power supplies for the laser, photomultiplier, arm elevation reader lamps, internal logic, servo loop requirements, stepper and servo-motors. The xenon arc lamp power supply is separate from the rack in order to minimise noise pick up by the other components. A diagram of the electronics system housing is shown in Fig 3.3.

The electronics systems provides the following functions:

1. Servo loops for polariser and analyser control.
2. Digital readout of the prism settings.
3. Null testing and data transfer control.
4. Interface for passing data to the M6800 microprocessor.
5. Stepper motor control for setting the monochromator position either from front panel switches or under computer control.
6. Stepper motor control for manually setting the elevation of the polariser and analyser arms.
7. Variable speed drives for the quarter wave retarder and analyser setting under manual control.
8. Oscilloscope for continuous monitoring purposes.

3.4.1 Servo loops.

The nulling method employed relies on the Faraday or magneto-optic effect. The plane of polarised light incident on a material medium is rotated when a strong magnetic field is applied in the propagation direction. The angle of roatation is proportional to the magnetic flux density and the length of medium traversed. The constant of proportionality, called the Verdet constant, is a characteristic of the medium and varies with the wavelength of incident light.

The rotation is given by $\theta = VBl$ where V = Verdet constant, B = magnetic flux density and l = length of medium traversed.

Two Faraday modulators on each arm provide modulation and offset

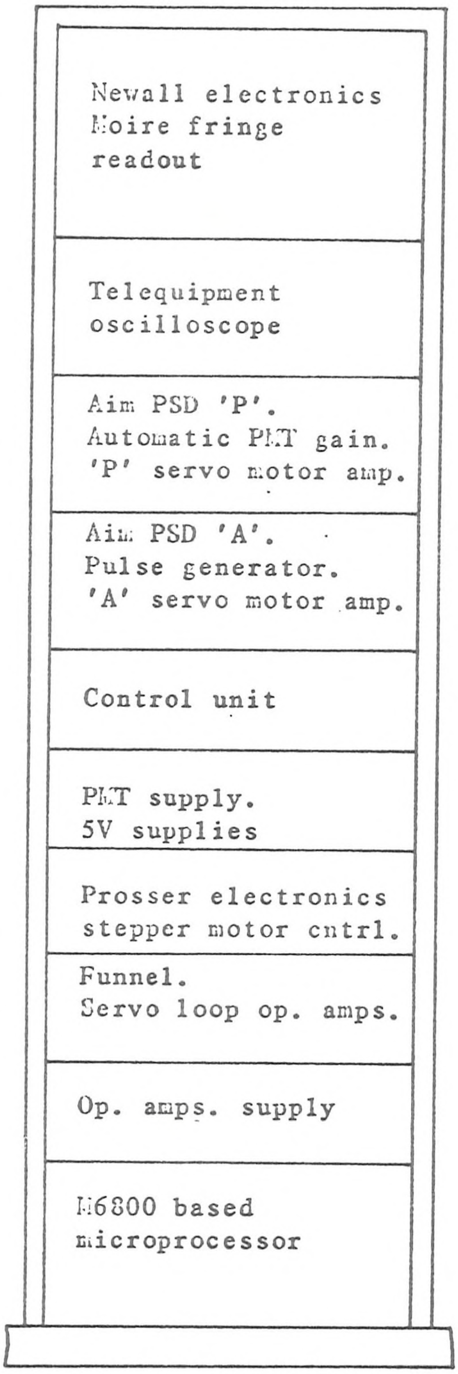

Three separate nixie tube displays for P, A, and Q angles.

Pulse generator used for setting time interval between data set measurements

Front panel switches for controling data acquisition and lamps for monitoring purposes

Front panel switches for monochrom. and arm elevation

Figure 3.3. Ellipsometer electronics unit housing details

of the plane of polarisation. A detailed discussion of the Faraday effect in terms of both classical and quantum mechanical approaches has been given by Partington[83].

The servo loops control the position of the polariser and analyser prisms and the amount of dc Faraday compensation to maintain the system in a null condition. The two loops are similar electronically but the ac Faraday modulators operate at different frequencies (about 830 and 1170 Hz) which have no common harmonics. An outline of the analyser loop is given in Fig 3.4.

Polarised light reaching the photo-multiplier is adjusted to null by the action of the dc Faraday compensators and the motor driven Rochon prisms. The plane of polarisation reaching the analyser is modulated about the point of extinction by the ac Faraday modulators. Light transmitted through the analyser produces a signal at the photo-multiplier output whose shape depends on the sign and magnitude of any null error. This signal is fed to two phase sensitive detectors (AIM PSD 122D) along with reference signals derived from the ac modulators. The phase sensitive detector (PSD) output, which indicates the distance from null, is amplified and fed back to the dc Faraday compensators in such a sense as to maintain the system close to null. If the current flowing through either of the dc Faraday compensators exceeds a preset level, (i.e., the system is approaching maximum compensation) a pulse generated by a dc coupled monostable (see section 3.4.6), after amplification, is applied to the relevant prism drive motor which drives the prism towards the null balance position. The ac modulator coils operate in series resonance with a capacitor to overcome the effect of impedance of the inductor at the modulation frequency.

3.4.2 Phase sensitive detector response.

The intensity of light transmitted through a polariser is proportional to $\sin^2(\theta - \theta_0)$ where θ is the orientation of the plane of polarised light incident on the polariser and θ_0 is the extinction plane of the polariser. The ac component of the signal appearing at the photo-multiplier can be shown to be of the form

$$2AB\sin(\omega t) - A^2\cos(2\omega t)$$

where B is the angular offset from null (i.e., $\theta - \theta_0$), A is the peak rotation of the plane of polarisation produced by the ac modulator and ω is the frequency of modulation.

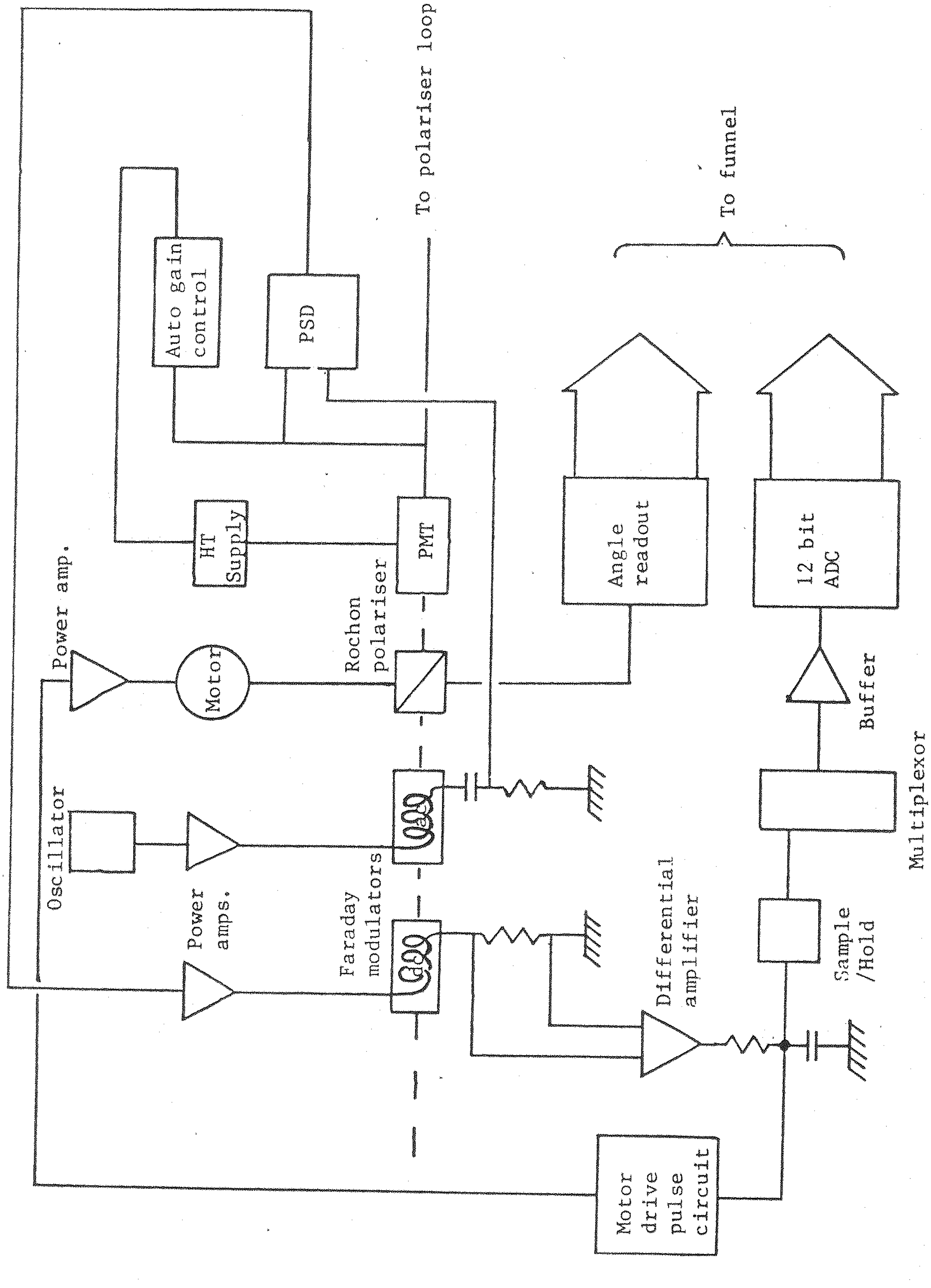

Figure 3.4. Analyser servo loop.

The photo-multiplier output consists of a superposed signal of frequencies ω and 2ω, the relative amounts of each being related to the null error. The amplitude of any fundamental frequency present gives a measure of the angular offset from null and the phase of the signal relative to that of the ac Faraday modulation will give the direction of offset. The ac Faraday modulation frequency is therefore, used as the reference signal for the phase sensitive detector. The PSD output will indicate the magnitude and direction of any null error. If the error is less than about 1° at 650 nm or less than 4° at 300 nm the dc Faraday compensator current will be adjusted by the amplified PSD signal to maintain the null condition. The waveforms given in Fig. 3.5 show the effect of null errors in polariser and analyser azimuths separately and the combined signal produced at the photo-multiplier output.

3.4.3 Angular read-out.

When the system is nulled the information on the polarisation angles producing the null condition is contained in two parts. One of these is obtained from the Moire fringe counters and is in digital form. The other is the rotation caused by the dc Faraday compensator current and is in analogue form initially. The Faraday modulation component and its subsequent conversion into digital form is discussed in the control unit description (section 3.4.7). A block diagram of the data control system is shown in Fig. 3.6 and explained in the following sections.

3.4.4 Angular encoder read-out.

This unit (Newall Electronics Ltd.) provides storage and display of the polariser and analyser azimuths and the quarter wave retarder fast axis. The information received by this unit from the Moire fringe encoders (explained in section 3.3) is used to update a buffer store. On receipt of a data request signal, initiated by the microprocessor, the buffer is isolated from updating and after a settling time of 1 μs this data is available on the data bus. The data is at TTL level and consists of seven 4-bit bytes in binary coded decimal form for each of the polarising and retarding prisms. This data is then transferred sequentially to the microprocessor's 8-bit data input ports via a digital multiplexor in the funnel circuitry. For details of the microprocessor and data format see section 3.4.10.

Signals produced by 'A' null errors

Signals produced by 'P' null errors

Combined PMT signal

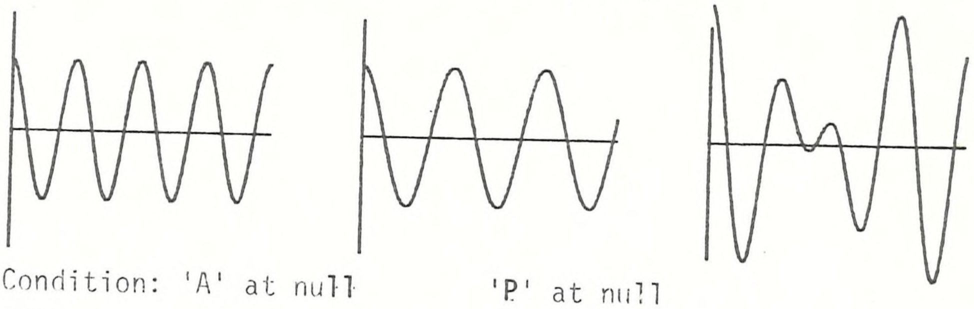

Condition: 'A' at null

PSD o/p = 0

'P' at null

0

Signals contain only 2ω component.

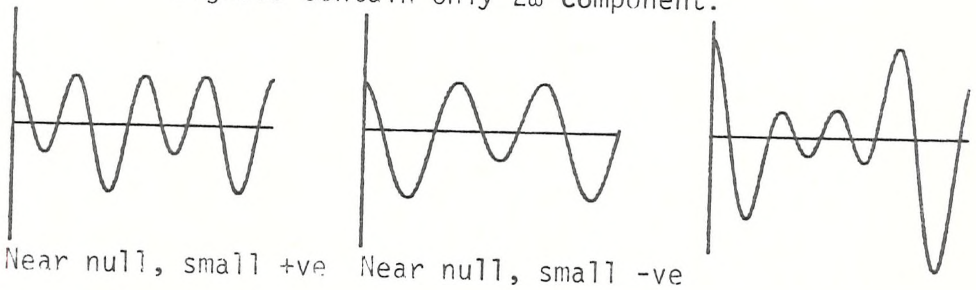

Near null, small +ve error, $B_A > 0$

PSD o/p > 0

Near null, small -ve error, $B_P < 0$

PSD o/p < 0

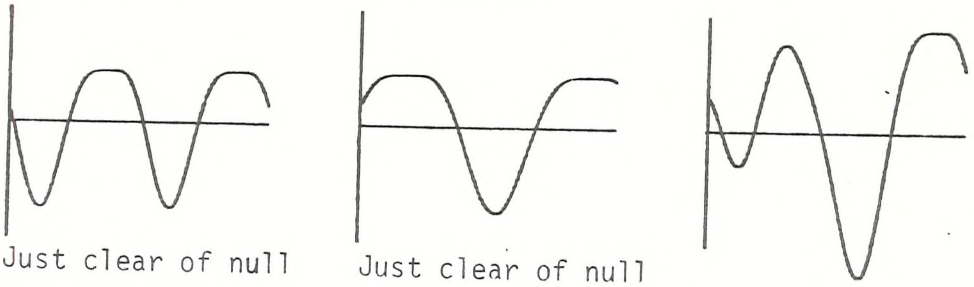

Just clear of null (-ve error) signal is out of phase. PSD >>0

Just clear of null (+ve error) signal in phase with reference

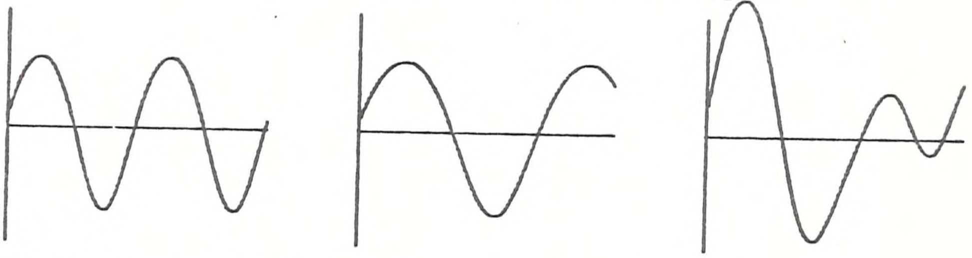

'A' and 'P' well clear of null, both signals produced by positive null errors. Signal is dominated by the fundamental frequency.

Figure 3.5 Effects of null errors on the ac component of the photomultiplier output.

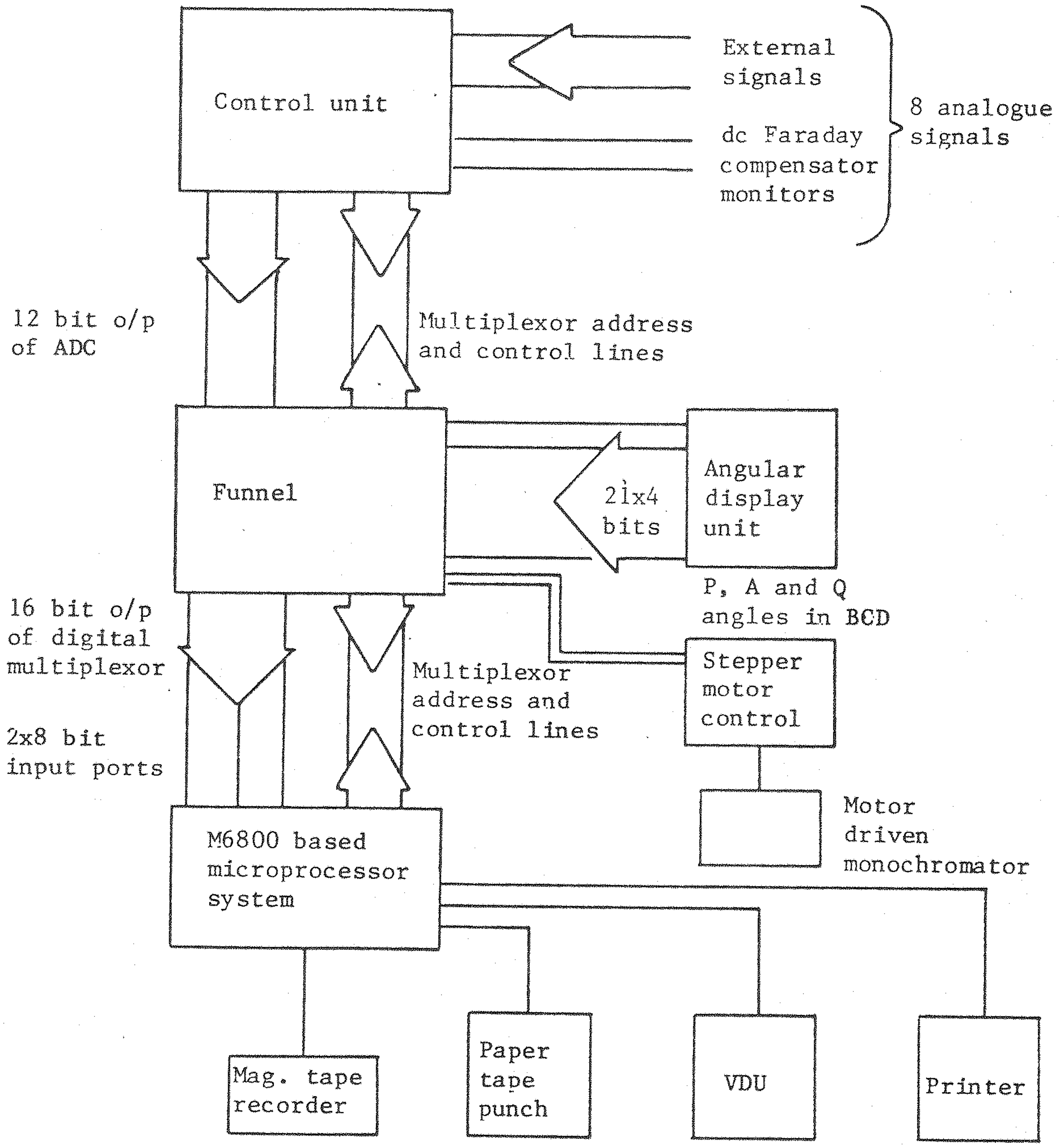

Figure 3.6. Data control system.

3.4.5 Control unit.

This unit provides a wide range of functions to control the flow of digital and analogue data. The unit accepts signals from the microprocessor for controlling the analogue data flow, provides switches to initiate and control data transfer and contains indicator lamps to show the status of the data handling process. Analogue signals from amplifiers monitoring the Faraday compensation current (see next section) together with externally generated analogue signals (e.g., from the electrochemical cell) are stored in sample/hold amplifiers for subsequent conversion into digital form. The null testing circuits and pulse generators for automatic control of the polarising prism motors are included in the unit. The unit also contains the power supplies for the arm angle reader lamps, the quarter wave retarder drive motor (manual control) and the analyser motor (when not under automatic control).

3.4.6 Control unit nulling circuitry.

Current flowing through the dc Faraday compensators is monitored as a voltage drop across 0.5Ω resistors connected in series with the compensator coils. These voltages are amplified by a factor of 2.5 by means of conventional differential amplifiers, and fed via low pass filters (33 ms time constant) to the sample/hold amplifiers. The filtered outputs of the differential amplifiers are also available at the front panel for driving a chart recorder.

One of the necessary conditions that has to be satisfied before data can be transferred to the microprocessor is that the system is nulled. If the current flowing through each of the dc Faraday modulators is less than the maximum available from the driving power amplifiers, then the system is nulled and the PSD outputs are zero. When the compensation current nears one extremity of the compensation range, a pulse is generated by a dc coupled monostable (Fig. 3.7) which is fed to the prism motor drive amplifiers. This turns the motor through a fixed angle, further pulses being produced if the current flowing is not reduced to lie within pre-defined limits. The null sensing and motor drive circuit is shown in Fig. 3.7. The circuit contains facilities for adjusting the pulse width and threshold level beyond which the pulses are produced.

The pulse width is determined by the minimum compensation range which is about ±0.45° at 650 nm. The pulse width is set to step the polarising prism through less than 0.5° to ensure that the drive motors are not sent through and beyond the null point. The threshold level is

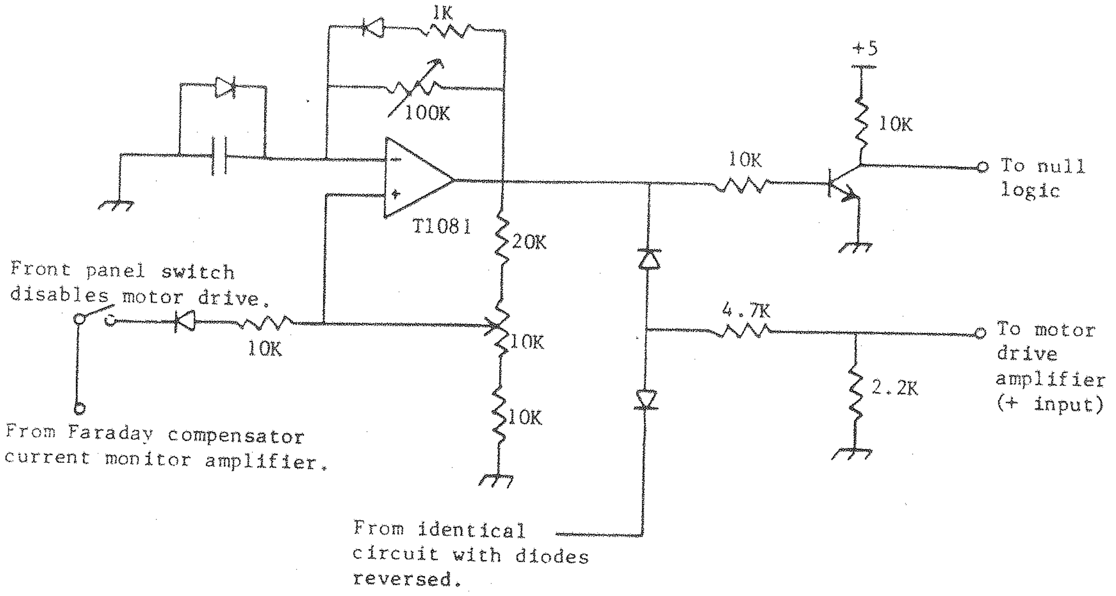

Two symmetrical (counter acting) circuits for each motor.
All diodes 1N914.

Figure 3.7. Null sensing and motor pulse circuitry.

determined by the maximum current available for driving the dc modulators which is about ±10A producing a voltage drop of ±5 V across the monitoring resistor. The threshold level is set at ±3.5 V which, when exceeded, will trigger the monostable to produce one or more positive or negative pulses depending on the sign and magnitude of the monitored voltage. The output of the monostables is fed to an amplifier (AIM WPA 116) the output of which drives the polarising prisms in such a sense as to decrease the compensation current and since the output is pulsed, the prism drive motors are either on or off.

3.4.7 Analogue data handling.

Up to eight analogue signals can be handled by the central unit, only two of which are usually monitored. Once the system is nulled, conversion of the analogue data to digital form can take place. Signals from the amplifiers monitoring the Faraday compensator current (two channels) together with a maximum of six external analogue signals from external sources (e.g. electrode potential and cell current) are stored in sample/hold amplifiers upon receipt of a hold signal. The hold signal is generated by logic circuitry in the control and funnel units and is discussed in the next two sections. The output of the eight sample/hold amplifiers are fed to a multiplexor (Analog Devices MPX 8A). On receipt of the relevant addresses, the eight analogue signals are sequentially transferred to an analogue to digital convertor (Analog Devices ADC 12-u) via a unity gain buffer amplifier. The signal is converted into a 12-bit, two's complement, binary number. The data is then available for transfer to the 2 x 8 bit data bus via the digital multiplexor in the funnel unit. The control unit multiplexor addresses and the digital data word format are described in section 3.4.11.

3.4.8 Control unit logic circuitry.

A large section of the logic circuitry required for automatic data acquisition is contained in the control unit. A 'start data block' signal is required by the funnel logic to hold data in the analogue sample/hold amplifiers and the digital data buffers in the angle encoder unit. The 'start data block' signal can be produced at constant time intervals by using an external signal generator or can be produced when required by the user, by pressing a front panel push button. When using the ellipsometer in its automatic wavelength scanning mode, the start signal can be generated by the computer as soon as the drive to the monochromator motor stops. The 'start data block' signal is inhibited if the system is not nulled. A 'reset' function (push button) is also provided which drops the 'hold' signal and resets all other logic levels to their initial state.

Front panel lamps indicate the status of the data transfer process. A 'hold' lamp is illuminated when data is ready for transfer and a 'steady' lamp is lit by a signal from the computer when the monochromator motor is not active. An 'out of balance' lamp is on when the system is nearing an off null condition.

A circuit diagram of the control unit logic is shown in Appendix A1. The control signals and their interaction with the funnel logic and microprocessor are discussed in more detail in the data acquisition section (3.4.11).

3.4.9 Funnel unit logic circuitry.

The funnel, so called because if its ability to multiplex up to sixteen channels of data onto a single data highway, provides a means of communication between the ellipsometer and the microprocessor. It accepts control and addressing information from the microprocessor and routes this data to the appropriate unit along with signals to drive the control unit front panel lamps. The funnel passes polariser, analyser and quarter wave retarder settings plus signals generated within the control unit to the microprocessor.

The logic is implemented at TTL level and comprises two sections. One section contains a multiplexor which handles the six originally digital words (P, A and Q) and the output of the analogue to digital convertor situated in the control unit. The multiplexor output forms the 16-bit data bus which transfers data to two of the microprocessors 8-bit input ports. The other section contains logic gates which complement the control unit logic circuitry to control and monitor the data acquisition and transfer processes. This logic section also routes information to the stepper motor via the Prosser control unit which controls the monochromator position. The funnel unit logic circuitry is shown in Appendix A1.1 and A1.2.

The ellipsometer was originally interfaced to an IBM 1130 computer which was located in a separate room. The only means of comunication between the ellipsometer operator and the computer (in their original location) was by means of push buttons and switches mounted on the front panel of the ellipsometer electronics housing. Much of the logic circuitry in the control and funnel units was designed for operating with a remote computer.

The ellipsometer was not supplied with a computer, so a suitable microprocessor based controller had to be designed and built.

3.4.10 Microprocessor and interfacing details.

Full automation of the ellipsometer is achieved through the use of a controlling microprocessor. The microprocessor issues the commands required by the funnel and control logic to read and temporarily store data which may be subsequently transferred to the microprocessor for storage and further processing. The microprocessor can also be used to issue the commands necessary to change the wavelength of light incident on the sample.

The microprocessor system was built by the Department of Electronics, Southampton University, and is based on a Motorola M6800 central processor unit (CPU) operating a 1MHz. The CPU board is housed in a card rack (Eurocard International size card (114 x 203 mm)) along with several other component cards to be described below. The card rack provides direct connection between the component cards and the CPU address, data and control lines.

The system contains an RT/68 monitor program (Microware Systems Corp., Iowa) supplied as a 1024 byte program stored in read only memory (ROM) and is required for communication between the terminal (visual display unit - Hazeltine 2000), and the CPU. The monitor program is required for initial machine code program development, saving these programs, Basic language programs and data onto magnetic tape and for loading previously saved programs back into memory. The system also contains a Basic interpretor (Computerware Software Services, California), supplied as an 8K program stored in ROM.

The Basic language master program, the machine language subroutines and data generated by the ellipsometer, are stored in the 32K bytes of available read/write memory (commonly called random access memory - RAM).

The machine language program (listed in Appendix A1.3), required to access the data originating from the ellipsometer or to transmit the required (logic level) control signals to the ellipsometer, was written in the Chemistry Department, Southampton Univesity. To make the automatic operation of the ellipsometer flexible, <u>i.e.</u>, to enable the user to select initial and final wavelength limits in a wavelength scanning experiment or to select 1, 2 or 4 zone data collection, required a high level (BASIC) program in which parameters such as wavelength or the number of zones over which the data was to be collected could be varied from experiment to experiment. Several programs were written during the course of this investigation, for both calibration and data collection purposes. These programs used portions of the machine code program and hence before they could be written, a knowlege of machine code programing was required. The most general of the Basic programs written is given as Appendix A1.4 and the interaction between programs and between the microprocessor and the ellipsometer is described below.

A hard copy of stored data or programs can be obtained on a dot matrix line printer (Dolphin BD80) or may be saved on punched paper tape (Facit 4070). Interfacing of these peripheral devices and of the ellipsometer is achieved through two distinct types of interface circuits. The system contains four interfaces known as peripheral interface adaptors (PIA's), two of which are used for controlling the printer and paper type punch and a third by the RT/68 monitor. A circuit diagram of one of these interfaces is given in Appendix A1.5

The microprocessor has been configured with four input and four output memory mapped latched ports, each port comprising an 8-bit word. Two of the output ports are used for sending instructions and addressing information to the funnel circuitry. A block diagram of these ports and what information they convey is given in Fig. 3.8. Two of the input ports are used for receiving the 16-bit data word from the digital multiplexor. Another of the input ports along with the two output ports described above form what is called a 'hand shake' between the microprocessor and the ellipsometer.

3.4.11 Data acquisition.

The digital multiplexor in the funnel unit receives 21 x 4 bit data words from the angular display unit and the 12-bit output from the analogue to digital convertor housed in the control unit. The 16-bit output from the digital multiplexor forms the data word which is ultimately received by the microprocessor. Individual data words are selected by sending a 4-bit address to the digital multiplexor. The three least significant bits are also sent to the analogue multiplexor to select one of the eight analogue signals for conversion into digital form. The most significant bit is used to select either the originally analogue data when the funnel address bit 4 is '1' or the originally digital data when bit 4 is '0'. Figure 3.9 shows the funnel address codes associated with each of the data words and the format of that data.

The process of data acquisition and subsequent transfer to the microprocessor is controlled via machine and Basic language routines

Output ports

Memory address	7	6	5	4	3	2	1	0	Bit
$7000	LED's on computer front pannel								
$7001		SEQ END		λ STEADY	Monochromator Dir.	Pulse motor	START TRANS.	END OF BLOCK	
$7002				DATA REQ.		Funnel address			
$7003	Not use								

Input ports

	7	6	5	4	3	2	1	0	Bit
$7004	Switches on computer front pannel								
$7005							HOLD	DATA READY	

2 x 8 bit data bus

$7006	3rd most significant char.				Least significant char.			
$7007	Most significant char.				2nd most significant char.			
Decimal value	128	64	32	16	8	4	2	1

Figure 3.8. 8 bit latched input/output port configuration.

Funnel address binary	Computer input port at $7007		input port at $7006		Memory allocation Hex
Data in binary coded decimal					
0001	–	Q^{o} hundreds	Q^{o} tens	Q^{o} units	A3FD, A3FC
0010	Q' tens	Q' units	Q'' tens	Q'' units	A3FB, A3FA
0011	Status	P^{o} hundreds	P^{o} tens	P^{o} units	A3F9, A3F8
0100	P' tens	P' units	P'' tens	P'' units	A3F7, A3F6
0101	–	A^{o} hundreds	A^{o} tens	A^{o} units	A3F5, A3F4
0110	A' tens	A' units	A'' tens	A'' units	A3F3, A3F2
0111	–	–	–	–	A3F1, A3F0
Data in 12 bit 2's complement					
1000	–	P Faraday compensator			A3EF, A3EE
1001	–	A Faraday compensator			A3ED, A3EC
1010	–	External channel 1			A3EB, A3EA
1011	–	External channel 2			A3E9, A3E8
1100	–	External channel 3			A3E7, A3E6
1101	–	External channel 4			A3E5, A3E4
1110	–	External channel 5			A3E3, A3E2
1110	–	External channel 6			A3E1, A3E0

Figure 3.9. Funnel address and data structure.

which are listed and explained in Appendices A1.3 and A1.4 respectively. The function of the logic circuitry in the control and funnel units and the computer to funnel transactions are described below. The Appendix numbers on the right hand side of the page refer to the relevant logic circuit diagram and the (hexadecimal) numbers refer to the memory address of the relevant section of the machine language routine (appearing as the leftmost column in Appendix A1.3).
ju0

1)	Computer to funnel: 'start of transfer'	Appendix A1.1
	+ 'lambda steady'	A111 and A113
2)	Wait for 'hold' = 1 (funnel to computer)	A116 to A11B
	'start' (push button, control front panel)	
	gives the signal 'commence'	Appendix A1
	'commence' and 'start' are gated in the funnel	
	unit to produce 'go'. Once 'go' has been set	Appendix A1.1
	no further 'start' signals are required,	
	unless 'go' is reset by 'reset'	Appendix A1
	(push button, control front panel) or	
	'sequence end' (computer to funnel)	Appendix A1.1
	Before 'hold' is set a 'start data block'	
	signal must be generated in the control logic.	Appendix A1
	This signal is produced by either the	
	'start data' push button or from an external	
	pulse generator (using the 'external start data	
	input). 'go' and 'start data block' then gives a	
	'hold' signal which is used to hold analogue	Appendix A1.2
	data in the sample/hold amplifiers located in the	
	control unit. After a de lay of 5 μs	
	(data acquisition time for S/H amps.) 'hold dig',	
	'hold ADC' and 'holdtim' signals are sent to the	Appendix A1.2
	Newall display unit to prevent further changes,	
	to the analogue sub-system and to the computer	
	respectively	
3)	A funnel address is issued by the computer	A10F to A120
	followed by a 'data request' signal.	A141, A143
	If the most significant bit of the address is '0'	
	then originally digital data is selected and the	
	data selected by the funnel address can be	

	transfered to the computer as soon as the computer recieves the 'data ready' signal.	Appendix A1.2
	If the most significant bit of the funnel address is '1' then the signal 'hold'+'FADD3'+'data request' when gated together produce a 'convert' pulse to the ADC. When the ADC recieves 'convert' it sets the 'status' to '1' and resets it to '0' when the converted data is available. 'data ready' is then set and the computer can read the originally analogue data.	Appendix A1.2
4)	Data word passed from funnel to computer	A14D to A155
5)	Computer drops 'data req.' which resets analog. data rdy.' and therefore 'data rdy.' and 'hold'	A157, A159 Appendix A1.2
6)	Next funnel address selected by the computer	A128
7)	Test to see if all 16 channels of data have been read. If more data required then goto step 3.	A12B
8)	Computer issues 'end of block' to funnel which resets 'hold'. The ellipsometer is then free to acquire a new data set, for example, at a different electrode potential or wavelength of incident light.	A12D, A12F

CHAPTER 4: EXPERIMENTAL.

4.1 Ellipsometer alignment

Extensive alignment procedures performed by the manufacturers (I.B.M.), have been reported by Lowe[81]. Precession of the polariser and analyser arm rotation axis (ideally defined by RR' in Fig. 3.1) has been measured by means of an auto collimator (by I.B.M.) and stated to be less than 0.05°. The optic axis of the polariser arm is defined by the axis of rotation of the polariser and retarder encoders (E_1 and E_2 in Fig 3.1) and since the retarding rhomb, Q, has an axis of symmetry about which it must be rotated to prevent beam deviation, the rotation axes of E_1 and E_2 have been adjusted, by the manufacturers, to intersect normally with RR'. It has been found necessary to perform only minor adjustments of the totally internally reflecting (TIR) prisms mounted at the extremity of the polariser arm (labeled T_2 and T_3 in Fig. 3.1) to bring the incident beam down on the optic axis. The prisms, mounted on 'spiders' are held in place by springs attached to the polariser arm. The three pivot pins, forming the prism mount are threaded to provide adjustment of the prism attitude.

With the arms set at 70° and a wavelength in the green selected, the beam reflected from a front surfaced aluminum mirror (on Chance-Pilkington Float glass parallel to ±0.0003°) was observed on a disk with a central pin hole mounted into the analyser arm. The sample stage was leveled and the height of the stage adjusted to minimise the distance between the central pin hole and the centre of the reflected beam. With the motor drive to the quarter wave encoder engaged, the precession of the reflected beam was minimised by adjustments to T_2 and T_3. The height of the sample stage was adjusted and if necessary T_2 and T_3 were readjusted until the reflected beam rotated centrally on the pin hole with minimum precession. The position of T_2 and T_3 were secured (locking nuts) and the alignment checked.

To ensure maximum light intensity output from the xenon arc lamp, the lamp house unit was removed from its mount on the ellipsometer and the image of the arc focused on a suitable distant surface. The lamp position and concave reflector were adjusted until the arc and its image reflected from the concave mirror coincided. The unit was returned to its mount on the ellipsometer and the position of the unit, with respect to the rotation axis, RR', adjusted until the signal observed on the oscilloscope monitoring the photomultiplier output of a nulled system (reflection from aluminium) was maximised. The position of the monochromator assembly was similarly adjusted with respect to the rotation axis, again until the monitored signal of the photomultiplier output was maximised

To facilitate the alignment of an electrode in an electrochemical cell an attachment has been added to the analyser arm which can interrupt the reflected beam and direct it through a TIR prism to a roughened pespex screen. After the above alignment procedure was completed, the position of the beam on the screen was marked and served as a reference position for sample surface alignment. The alignment device is shown in Fig. 4.1.

4.1.1. Prism azimuth alignment.

Azimuthal angles of polarising and retarding prisms are conventionally measured with respect to the plane of incidence and are zero when the plane of transmission of the polarising prisms or fast axis of the retarding prism is parallel to the place of incidence. Alignment procedures, described by McCrackin *et. al.*[84], have been used for setting the angular read-out displays to measure absolute azimuth angles conforming with the above convention. The method relies on the fact that pure s or p polarisations incident on a metal remains linearly polarised on reflection and linearly polarised light parallel to the slow or fast axis of a linear retarder remains linear upon transmission through it.

With the quarter wave retarder removed, the ellipsometer was set for observing the reflection from pure water at the principal angle of incidence (Brewster angle). One of the ac Faraday modulators was switched on and the polariser prism rotated until the null signal was observed on the monitoring oscilloscope. The transmission axis of the polariser was then parallel to the plane of incidence. The water reflecting surface was replaced by a front surfaced aluminium mirror and the angle of incidence set to 70°. Again with only one of the ac Faraday modulators on, the analyser was adjusted to give a near null signal (analyser transmission axis approximately in the s direction) and then both polariser and analyser azimuths finely adjusted until a null condition was obtained. The polariser angle display was then adjusted to zero using the offset facilities incorporated into the display unit. Reflection from the metal surface enabled the polariser angle to be set with greater precision because the photomultiplier signal, produced by ac Faraday modulation about extinction, was much larger than for dielectric reflection. The ellipsometer arms were then set in the straight through position, the polariser azimuth set accurately to 0° (the plane of incidence), the analyser adjusted to give null, and the analyser angle displayed was then set to 90°.

The quarter wave retarder used in the present study was a three

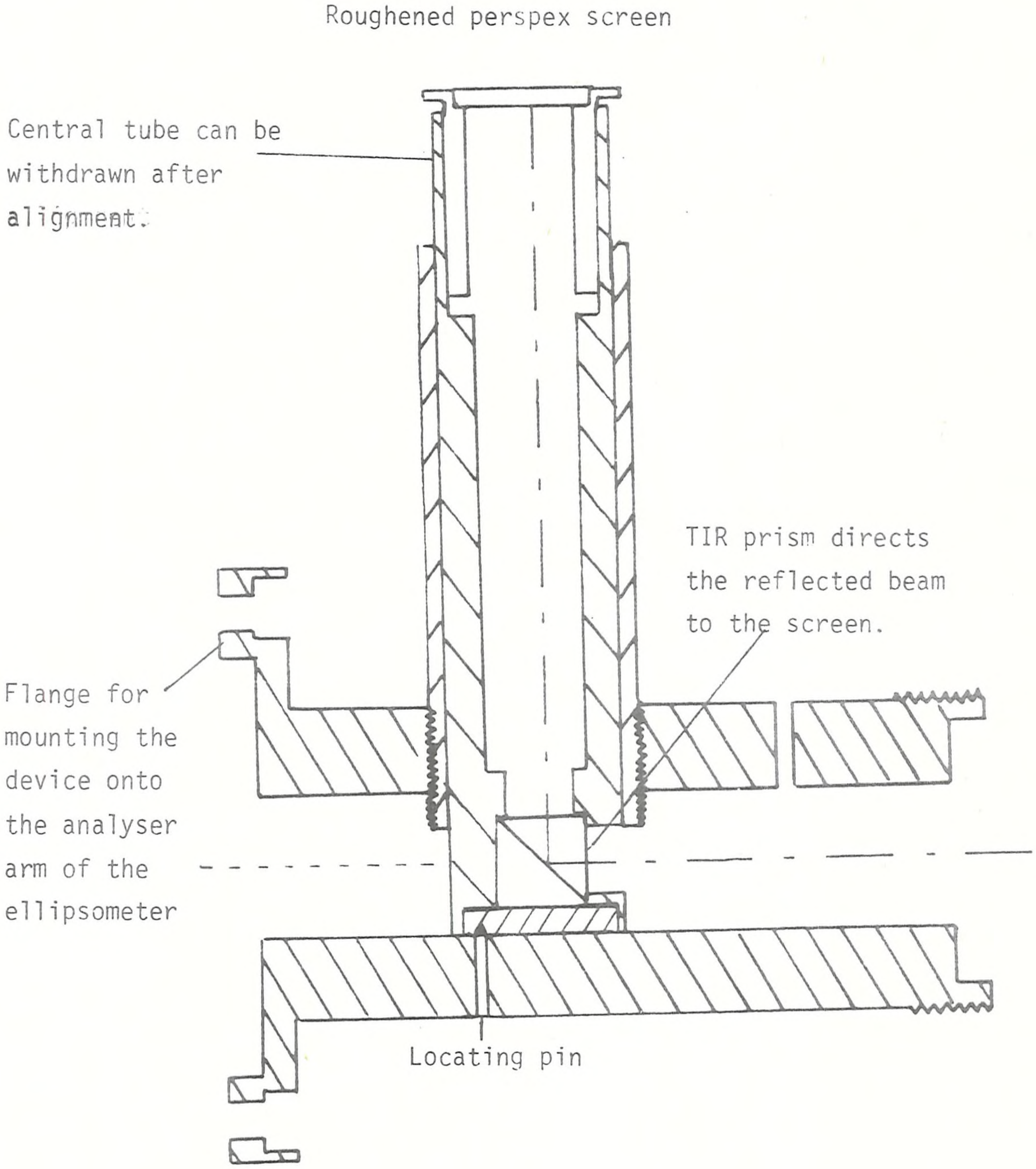

Figure 4.1. Sample alignment device.

reflecton rhomb, made of synthetic silica, with one surface coated with magnesium fluoride to produce an almost constant retardation throughout the visible and near ultra-violet spectrum. The construction and principles of the three reflection rhomb, and other retarders based on the Fresnel rhomb, has been extensively discussed by King and co-workers[81,85].

From a knowlege of the principles of operation of rhomb type retarders, the fast axis of such devices can be found by inspection. Rhomb retarders derive their phase retardation from the difference in phase change on reflection for the p and s components when light undergoes two or more internal reflections. A sketch of a three reflection rhomb is shown in Fig. 4.2.

From Snell's law, $n_1\sin\phi_1 = n_2\sin\phi_2$, where n_2 is the refractive index of the rhomb material and ϕ_2 is the angle of incidence for reflection within the material. It follows that for $n_2 > n_1$ the angle of refraction, ϕ_1, is greater than ϕ_2. There exists an angle ϕ_2 for which $\phi_1 = 90°$, that is, the transmitted wave runs along the interface between the two media. The angle at which this occurs is called the critical angle, ϕ_c. For angles of incidence, ϕ_2, greater than ϕc all light is totally internally reflected. It was shown in section 2.2 that, for external reflection, the phase changes introduced into p and s components vary with angle of incidence. A similar effect is observed for internal reflection and the relationships between phase angle and angle of incidence are[86]:

$$\tan\delta_p/2 = [n(n^2\sin^2\phi - 1)^{1/2}]/\cos\phi$$

$$\tan\delta_s/2 = (n^2\sin^2\phi - 1)^{1/2}/n\cos\phi$$

$$\tan\Delta/2 = \tan(\delta_p/2 - \delta_s/2) = [\cos\phi(n^2\sin^2\phi - 1)^{1/2}]n\sin^2\phi$$

where n is the refractive index of the material, ϕ is the internal angle of incidence, the phase changes introduced into p and s components on reflection are given by δ_p and δ_s, and the phase difference is $\Delta = \delta_p - \delta_s$. Fig. 4.3 shows the variation in phase as a function of the internal angle of incidence for n=1.511 (crown glass). Since the s component is retarded by the least amount, the fast axis of the retarder is defined by a plane perpendicular to the plane of incidence (normal to the plane of the paper in Fig 4.3)

For precise alignment, the quarter wave retarder axes were

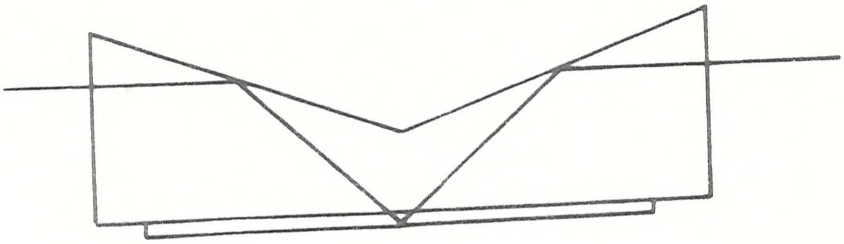

Figure 4.2. Coated three reflection rhomb retarder

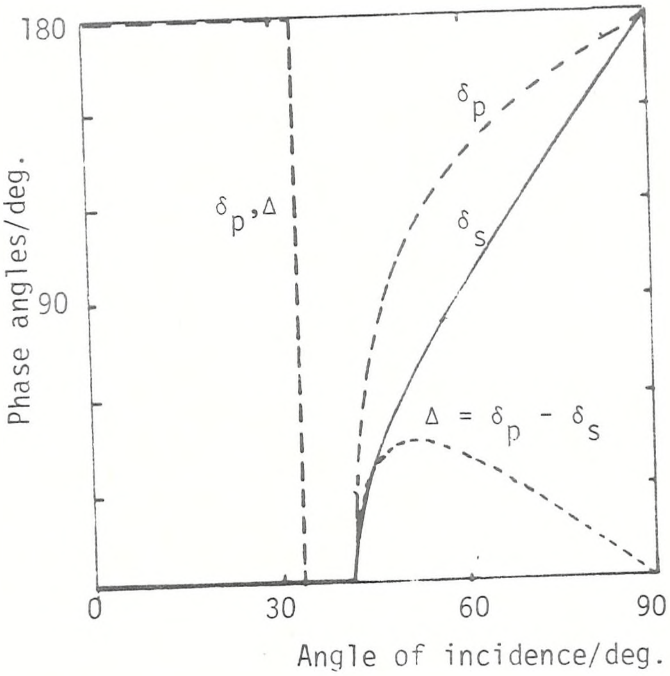

Figure 4.3. Phase changes as a function of angle of incidence for internal reflection

determined by rotating the device to give the null condition with the polariser and analyser azimuths set in the p and s planes respectively and the ellipsometer arms in the straight through position. A total of four null positions are possible since extinction of the light will occur when the fast or slow axis of the retarder is in the plane of incidence. Any ambiguity can be resolved by determining the two null values of P and A for reflection from a metal surface with the retarder set at +45° and -45° from the angle determined in the 'straight through' experiment. The actual quarter wave fast axis azimuth (45° or 135° with respect to the plane of incidence) can be determined by comparing the value of P at each null with the range of values given in Table 2.1 (section 2.4) simply from a knowlege of the prism's attitude inside its mounting.

4.2 Automatic wavelength selection - Micrometer position to wavelength conversions.

The wavelength of light emerging from the quartz prism monochromator is selected by rotation of the prism which moves the spectrum across a fixed slit. The prism is rotated by a cam coupled to a precision micrometer screw, calibrated in mm, and since the dispersion of light is strongly wavelength dependent, so is the curve relating wavelength to monochromator screw position. The monochromator position *vs.* wavelength dispersion curve is similar in form to the dispersion of refractive index of the prism material, *i.e.*, the refractive index of the prism changes rapidly at shorter wavelengths.

The monochromator has been supplied with a calibration table relating the monochromator micrometer screw position (mm) to the wavelength of light transmitted. A stepper motor which is directly coupled to the micrometer can be controlled by commands issued by the computer to the stepper motor control unit or manually by front panel switches on the control unit. Each drive pulse sent from the controlling unit moves the micrometer position by 0.0025 mm. and up to 400 pulses/second can be issued. For automatic control of the wavelength, the number of 0.0025 mm. steps required to drive the micrometer from one wavelength position to another must be known or calculated. The calibration data could be stored in memory and the distance through which the micrometer must be moved to change wavelengths easily calculated and converted into the required number of motor drive pulses. However, if the optical properties of a sample were to be studied over a large range of closely spaced wavelengths, then an equally large range of calibration data would be required which would restrict the memory space available for ellipsometric data storage. An alternative method, which has been implemented, is to find an empirical relationship between wavelength and micrometer position and to use this relationship to calculate the position required for a new wavelength and hence, the number of drive pulses required to derive the micrometer to the new position. Two simple relationships have been found to cover the near ultra-violet and visible regions. For wavelengths less than 300nm the expression

$$\text{Micrometer position(mm)} = \frac{1328.3526}{\lambda - 121.4} + 1.46714 \qquad (4.1)$$

has been found to give excellent agreement with the supplied calibration. For wavelength > 300 nm the expression

$$\text{Micrometer position/mm} = \frac{965.6028}{\lambda - 147.2} + 2.5969 \qquad (4.2)$$

is used. Two simple equations, rather than a single more complex equation were used because Eqs. (4.1) and (4.2) could be inverted enabling the wavelength to be found from the monochromator position. From the form of the calibration curve it is probable that the Selmeyer or Cauchy dispersion equations (Eqs. (2.141) or (2.143)) could be used but since these equations use terms in λ^2 and possibly λ^4 they would take longer to evaluate than Eqs. (4.1) and (4.2)

The calculated calibration curve along with selected points taken from the supplied calibration is shown in Fig. 4.4. The error in the calculated micrometer position is very small and negligible by comparison with the half intensity band width.

4.3 Dc Faraday compensator calibration.

The rotation of the plane of polarised light passing through a Faraday cell depends on the magnetic flux density along the cell core and on the Verdet constant associated with the core material (see section 3.4.1). The amount of current flowing through the coils producing the magnetic field is monitored as a voltage drop across a measuring resistor. This analogue voltage is converted into a 12 bit, 2's complement number so that data received by the computer will be in integer format within the range ±2047 ($2^{11} = 2048$, the 12th bit conveys the sign information). These numbers must then be converted into an equivalent angle and then applied to the measured prism azimuth angles, P and A, to give the true polarisation angles describing the null condition.

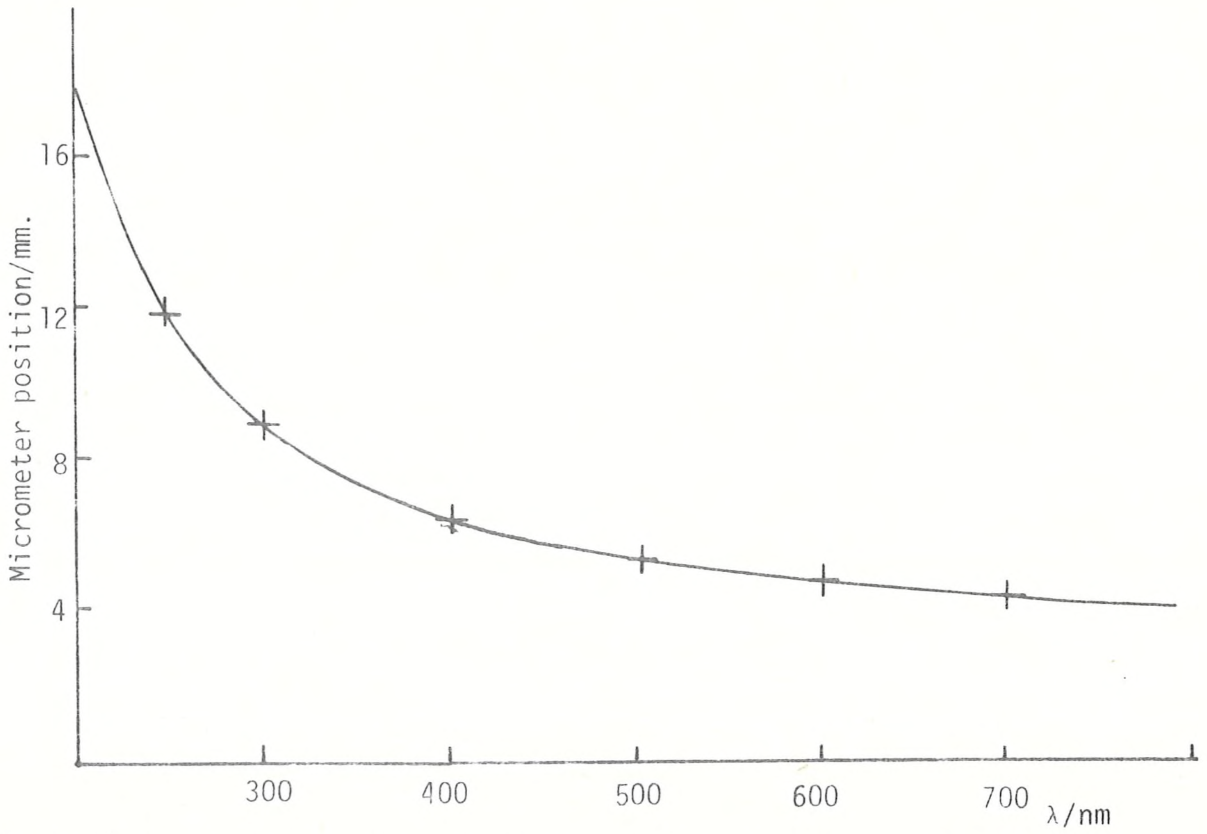

Figure 4.4. Monochromator-micrometer calibration. Curve calculated from Eqs. (4.1) and (4.2); +, points from supplied calibration table.

In principle, the Verdet constants could be evaluated at each wavelength employed, the binary number representing the current flowing converted into an actual current value, the magnetic flux density calculated and hence, the rotation calculated (using the equation in section 3.4.1). However, the equations for calculating the Verdet constant as a function of wavelength[3] are cumbersome and contain empirical constants which would need prior evaluation at each wavelength.

4.3.1 Calibration procedure.

The ellipsometer arms were each set to 90° ("straight through" position) and the quarter wave retarder removed. To calibrate the polariser dc Faraday compensator, for example, the analyser was set to an arbitrary angle and the polariser set to an angle different by approximately 90°. Power was applied to the polariser Faraday cells (both ac and dc) and the current flowing through the dc coil monitored for 5 different polariser prism azimuth angles, ranging from near maximum positive compensation to near maximum negative compensation. A BASIC program, written to automate the calibration procedure as much as possible, was used to read and store the azimuth angles and the binary data representing the current flow. Making use of the automatic wavelength scanning facility, a wavelength was selected under computer control and after a suitable delay (necessary for manually setting the prism angle), the dc current equivalent was logged by the computer. The polariser angle was manually changed and the data acquisition repeated. For each prism setting the analogue data was averaged over 40 samples. When a complete set of data had been obtained at one wavelength, a linear regression analysis of the data was performed and the slope, giving the Faraday cell specific rotation in degrees/unit of digital data, and intercept, corresponding to the polarisation angle yielding the null condition, were recorded. The computer then issued the commands required to change the wavelength of incident light and the process repeated. The Faraday cell specific rotation was determined at 20 nm intervals from 300 to 680 nm for the polariser arm Faraday cell and at 40 nm intervals from 300 to 660 nm for the analyser cell with a monochromator slit width of 0.4 nm and using the photomultiplier auto gain facility.

For reasons mentioned earlier, empirical equations relating the specific rotation to wavelength rather than storing the calibration data in memory, were sought. Both the Faraday effect and dispersion have similar wavelength dependence and since the computer selects micrometer position (and is accurately known), rather than absolute wavelengths, it was decided to find equations relating the specific rotation to micrometer position. Expressions of forms similar to Eqs. (4.1) and (4.2) were found to predict satisfactorily the Faraday cell specific rotation units of degrees/unit of digital data in terms of the monochromator micrometer position. Again, two equations were required to cover usable wavelength range and are given below:

For $\lambda < 380$ nm

$$\text{Specific rotation /deg./digit} = \frac{0.2276}{\text{micrometer position/mm} - 28.45} + 0.00905 \qquad (4.3)$$

and for $\lambda > 380$ nm

$$\text{Specific rotation /deg./digit} = \frac{2.1903}{\text{micrometer position/mm} - 75.00} + 0.0306 \qquad (4.3)$$

The analyser Faraday cell was found to be consistently less sensitive than the polariser cell by a mean factor of 0.9796 (standard deviation 0.0028).

The experimentally determined specific rotations, the values calculated from Eqs. (4.3) and (4.4) and the maximum expected errors are shown in Table 4.1. The maximum error has been calculated from the expression:

$$\text{Error} = (\text{experimental rotation} - \text{calculated}) \times 1400$$

The value of 1400 (corresponding to 3.5V drop across the current monitoring resistor) was taken because currents above this digitally equivalent value will cause the relevant prism motor to be activated (see section 3.4.6) to reduce the Faraday component. The sensitivity of the Faraday cell specific rotation in °/digit is 0.00248 at 300 nm and 0.00042 at 660 nm, giving a maximum compensation range of ±3.5° at 300 nm and ±0.6° at 600 nm

4.1. Mercury electrodes for optical studies.

The difficulty in producing a vibration free mercury pool is exemplified by the work of Smith[87]. Preliminary studies of the reflection from a mercury pool indicated that the granite block (some 2 tons), on which the ellipsometer stands, was not sufficient to damp out the vibrations transmitted through the structure of the building. Attempts were therefore made to produce a mercury thin film electrode on a platinum substrate. Such an electrode was succesfully used by Robinson[88] in modulated reflectance studies of the mercury aqueous electrolyte interface.

The platinum used as a substrate for the mercury thin film electrode was 5 mm in diameter and was initially sealed into Kel-F rod by a method described in section 4.5. Attempts to produce an electrode

Table 4.1

Faraday cell specific rotations

λ/nm	Measured 10^3deg/digit.	Calculated 10^3deg/digit.	Error 10^3deg/1400 digit.
360	-1.6126	-1.6267	19.67
380	-1.4336	-1.4348	1.64
400	-1.2774	-1.2789	2.08
420	-1.1506	-1.1492	-2.46
440	-1.0408	-1.0395	-1.69
460	-0.9472	-0.9464	-1.04
480	-0.8677	-0.8647	-4.14
500	-0.7954	-0.7950	-0.54
520	-0.7337	-0.7326	-1.54
540	-0.6743	-0.6772	4.02
560	-0.6263	-0.6275	1.69
580	-0.5817	-0.5834	2.48
600	-0.5421	-0.5438	2.44
620	-0.5059	-0.5076	2.38
640	-0.4712	-0.4759	-2.14
660	-0.4464	-0.4437	-3.72
680	-0.4233	-0.4161	-10.13

sealed into soda glass were frustrated by repeated cracking of the glass adjacent to platinum. The mercury thin film electrode was prepared by a method described by Hartley et.al[89]. Mercury was deposited onto the platinum substrate under galvanostatic condition and following a rinse in distilled water the electrode was polarised cathodically in nitric acid (0.1 M) causing the mercury to spread out forming a flat surface. However, on transfering the electrode to the optical cell, the film invariably broke resulting in an uneven surface and some of the platinum substrate exposed. No pre-treatment of the platinum substrate prior to mercury deposition or post-treatment (varying degrees of hydrogen evolution) remedied the situation. The problem was ultimately traced to a thin layer of material, adsorbed around the edge of the platinum, between the platinum and the Kel-F. Several other methods of sealing the platinum into a suitable support (platinum sealed in glass with various types of epoxy resin) were also unsuccessful.

Attention was therefore redirected to finding a suitable method of producing a vibration free mercury pool. Many methods were tried, placing synthetic rubbers and foams of various types between the cell and sample table, placing the same materials between the sample table and ellipsometer base, but success was ultimately found by placing six sorbo rubber balls between the sample stage and the base of the ellipsometer. Using this method, all vibrations were largely damped and the monitored photomultiplier signal was only slightly influenced by residual vibrations.

4.4.1 The mercury optical-electrochemical cell.

Most of the ellipsometric measurements were conducted using a free mercury pool contained in a pyrex cell giving an electrode area of about 9.5 cm^2. The cell was equipped with two side arms angled at approximately 20^o to the base into which fitted the cell window tubes. The tubes holding the cell windows (2 mm thick fused quartz) had open flanges at one end which fitted snugly into shallow barrels machined into the polariser and analyser arms and were held in place by means of threaded collars. A diagram of the cell, cell window assembly and auxiliary glassware is shown in Fig. 4.5. The counter electrode used was a palladium rod saturated with hydrogen prior to inclusion into the cell by cathodic evolution. This formed a non-contaminating electrode provided that the hydrogen dissolved in the palladium was not completely depleted by electrochemical oxidation. As a further precaution against contamination, the counter electrode was housed in a compartment separated from the main compartment by a sintered glass

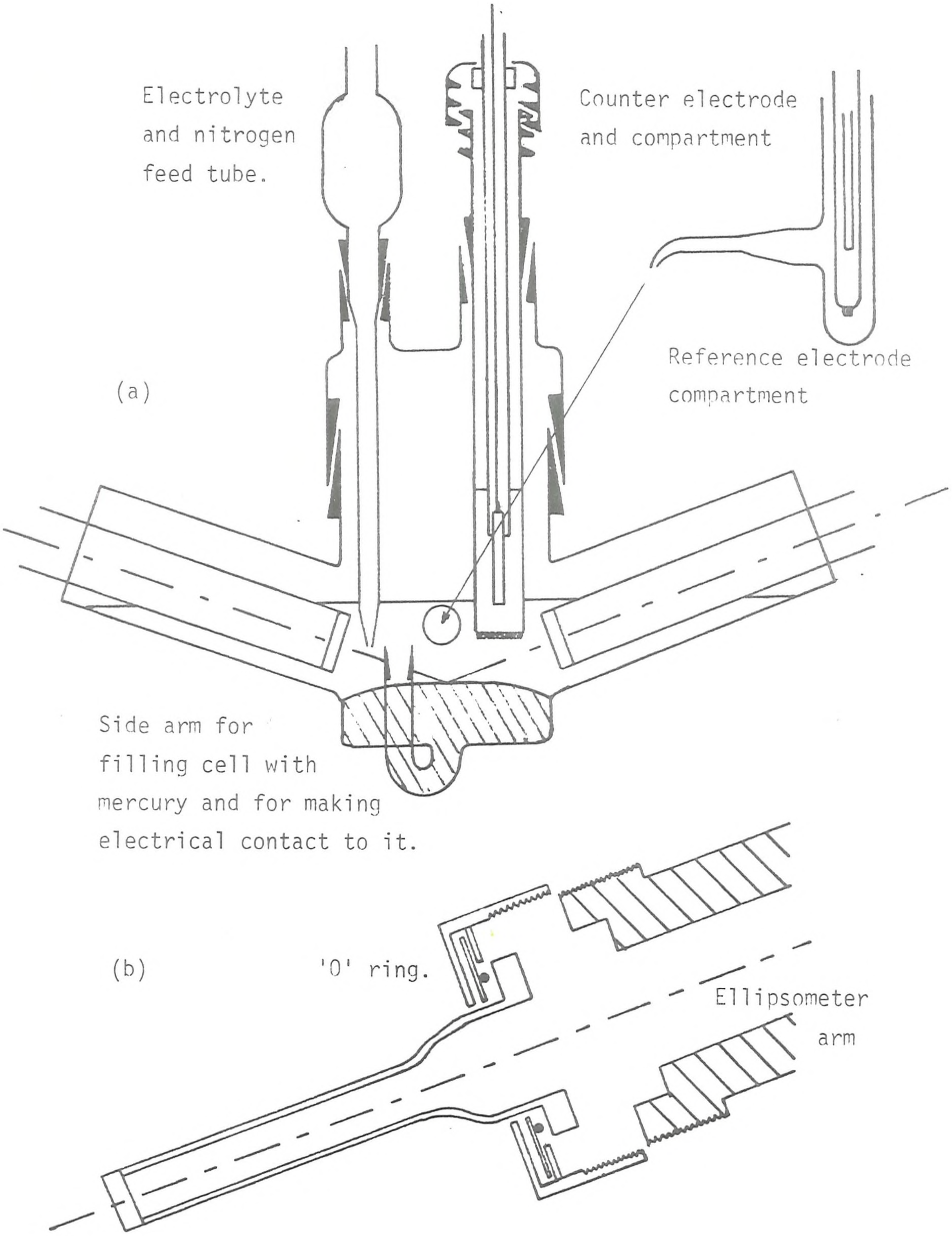

Figure 4.5. (a) The 70° mercury pool cell.
(b) Cell window and collar.

disc. Electrical contact to the mercury pool was made via a platinum wire, sealed in glass, placed in a 'U' tube which connects to the base of the cell. The 'U' tube was also used for introducing mercury into the cell. The reference electrode, used throughout, was a commercial saturated calomel electrode and was housed in a compartment separated from the main cell body by a bridge which formed a Luggin capillary.

4.5 The optical-electrochemical cell for solid electrodes.

An open trough cell made of PTFE , has been constructed for use with specially mounted solid electrodes and is shown in Fig. 4.6. The electrodes used in this cell were prepared by first spot welding a connecting wire to the back surface of the metal and then sealing the electrode into Kel-F rod. The rod was first cut to the required length and a hole drilled centrally through the rod to house the connecting wire. The Kel-F rod and positioned electrode were placed into the base of a barrel and piston assembly and the base entrance closed with a close-fitting, flat surfaced plug. The whole assembly was placed in an oven at 200°C for 30 minutes then transfered to a hydraulic press where moderate pressure was applied to the piston and the assembly allowed to cool to room temperature. A hole was drilled into the back of the Kel-F rod to expose the connecting wire, a fine insulated extension wire was soldered to the exposed wire and finally, the metal/solder contact was covered with epoxy resin. The electrodes were then polished to a mirror finish with either diamond impregnated polishing wheels or alumina slurries following standard procedures.

In an attempt to maintain an oxygen free atmosphere above the electrolyte, a cell enclosure was constructed out of perspex sheet. The counter electrode used was either a Pd/H_2 rod or a platinum ring sealed into glass. The method by which the counter and reference electrodes were supported in the cell is illustrated in Fig. 4.6 along with diagrams of the cell and cell enclosure. The cell enclosure was secured to the sample table by means of clamps which fit into slideways machined into the surface of the table.

4.6 Electrochemical equipment.

Electrode potentials were controlled by a battery powered potentiostat of conventional summing type design and mounted directly above the cell to minimise the length of leads connecting to the cell. This arrangement was found necessary because the much larger commercial potentiostats had to be set up several feet away from the cell and noise pick-up (presumably by the reference electrode and connecting wire) when amplified by the potentiostat, caused mechanical

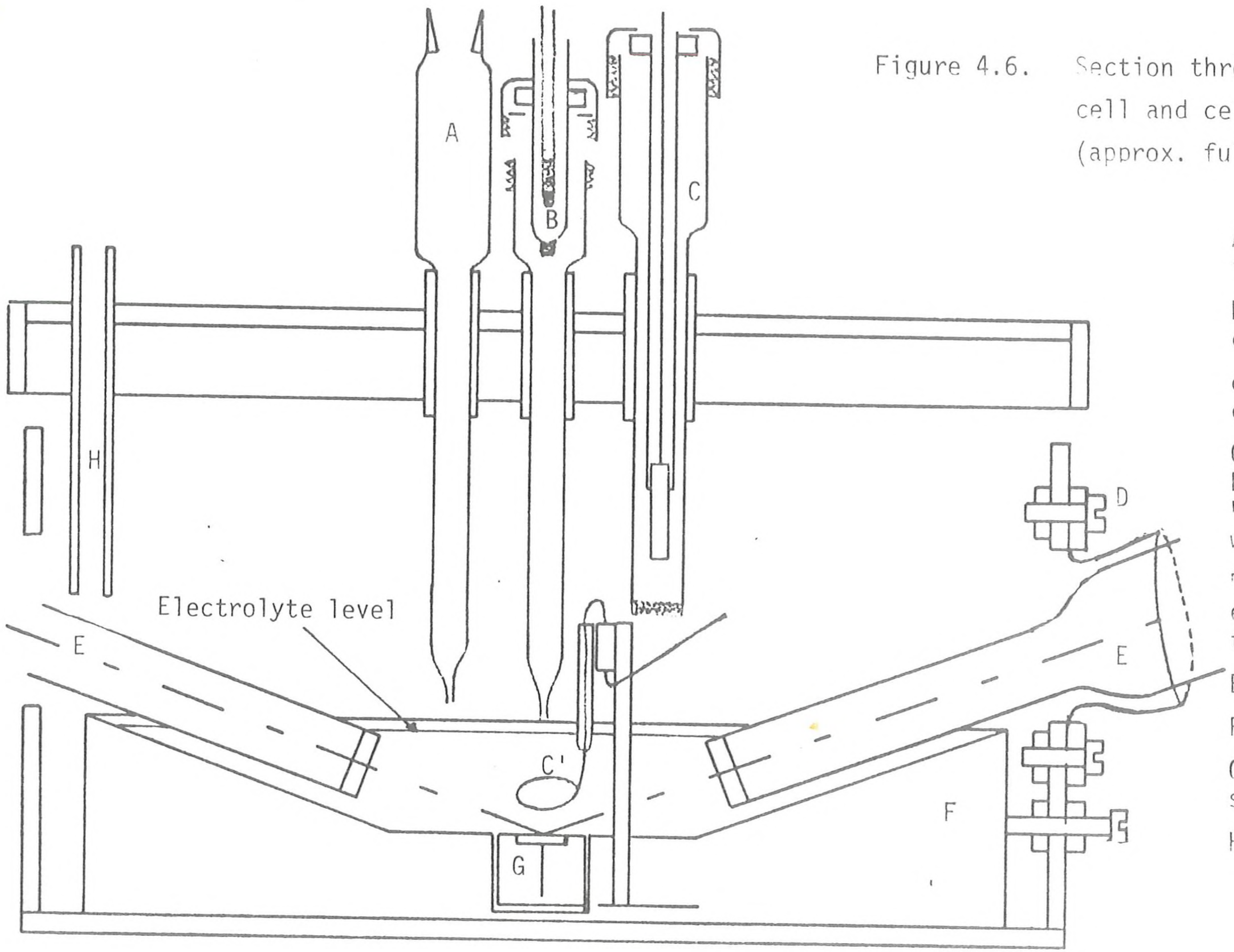

Figure 4.6. Section through the solid electrode cell and cell enclosure. (approx. full scale)

A. Electrolyte and nitrogen inlet.

B. Reference electrode compartment

c. Counter electrode compartment (Pd/H_2 electrode)

C! Alternate counter electrode Pt loop sealed in glass and held in position by stout Cu wire fixed to perspex stand.

D. Flange for securing polyethylene tube to cell enclosure to form an air tight seal.

E. Cell window assembly.

F. PTFE cell.

G. Working electrode sealed in Kel-F

H. Nitrogen feed to cell.

oscillations of the mercury pool which were observed in the photomultiplier output. Bias potentials and potential sweeps were obtained from a Wenking waveform generator (VSG 72).

4.7 Reagents.

All electrolytes were prepared from analytical grade reagents without further purification. The water was four times distilled. Distilled water from a large throughput still was transfered to the first reservoir of a three stage, all-pyrex still. The first two reservoirs contained dilute solutions of potassium permanagate and orthophosphoric acid, respectively. The mercury was rigorously purified before each experiment by a chemical cleaning procedure (prolonged agitation with sodium hydroxide solution, nitric acid (both 4M) and water) followed by double distillation under partial vacuum.

4.8 Experimental procedures.

Two types of experiments have been carried out:

1. A study of the potential dependence on the adsorption of F^-, Cl^-, SO_4^{2-} and isoquinoline at the mercury/electrolyte interface at several wavelengths of incident light.

2. To study the spectral properties of rhodamine B adsorbed at the mercury-electrolyte and platinum-electrolyte interfaces by monitoring the ellipsometric parameters as a function of wavelength at fixed electrode potential.

The procedures common to both types of experiment will be discussed in this section; data collection and more specific experimental details will be described in the following sub-sections.

Ellipsometric measurements were conducted in a temperature controlled room (21°C ±1°C). It was necessary to cover the cell with a dark cloth to exclude stray light entering the analyser arm by reflection from the sample surface. The angle of incidence was set at 70.00° for all experiments.

The nitrogen used (B.O.C. "white spot") for removing dissolved oxygen from the electrolytes was purified to remove traces of oxygen by bubbling it through a solution containing a vanadium (II) complex (ammonium meta-vanadate (2g), dissolved in hydrochloric acid (25 cm^2, conc.) and diluted to 200 cm^3 with water), standing over zinc amalgam. The nitrogen was passed through a second flask containing distilled water before being used to purge the electrolytes. The electrolytes were purged for about 30 minutes before being introduced into the cell.

The ellipsometer electronics, and in particular the Xe arc lamp, were switched on at least one hour before any data collection was attempted. With the cell and electrode correctly aligned (see the following two sub-sections) and the cell windows in place, all electrical connections were completed. A suitable electrode potential was selected and the potentiostat switched on. Sufficient electrolyte to cover the cell windows was then added to the cell and the electrolyte purged for about 10 minutes. An initial wavelength was selected and the monochrometer exit slit adjusted to 0.4 mm.

4.8.1 Mercury cell: Preparation and alignment.

The glass cell components were cleaned by prolonged immersion in a freshly prepared mixture of nitric and sulphuric acids (conc., equal volumes) then thoroughly rinsed with tap water, distilled water and a final rinse with triply distilled water. The components were oven dried at 80°C, assembled and all cell openings sealed with ground glass stoppers or "fingers" cut from polyethylene gloves to exclude airborn impurities from entering the cell.

The ellipsometer sample stage was mounted on six sorbo rubber balls and the table leveled. The cell was clamped in position on the sample table and its position roughly adjusted to coincide with the rotation axis of the ellipsometer arms. The cell window assemblies were fixed in place and the cell arms and window tubes loosely wrapped with lightweight polyethylene sheets to form a seal as air tight as possible but without producing significant mechanical coupling to the ellipsometer. Mercury was added to the cell through the side arm used for making electrical contact to the mercury. The level of mercury was adjusted in conjuction with x-y translations of the sample table until the incident beam was reflected from the central portion of the mercury surface and the alignment judged satisfactory by viewing the reflected beam in the alignment device. The reference and counter electrode compartments were filled with degassed electrolyte, the appropriate electrical connections made, a suitable potential selected and the potentiostat switched on. Sufficient electrolyte to cover the cell windows was added to the cell and a nitrogen feed connected.

4.8.2 The solid electrode cell: Preparation and alignment.

The PTFE cell was cleaned by overnight immersion in a surfactant solution (Decon, 2% v/v in distilled water) followed by thorough rinses with tap and distilled water. The platinum electrode was polished with successively finer grades of alumina powder slurries down to 0.05 µ particles. The electrode was carefully rinsed and placed into the well in the base of the cell. The platinum ring counter electrode was fixed to its mount inside the perspex enclosure and the connecting wires fed through a tube mounted into the lid of the enclosure. The Luggin capillary tube was inserted through another tube in the lid and lightweight polyethylene tubes were fixed in position around cell window entrance holes. The assembly was clamped in position on the sample table, a disc with a central pin hole was fixed in position at the exit of the polariser arm and a mirror, normal to the analyser arm optic axis was mounted at the entrance to the analyser arm. The monochromator exit slit was opened fully and a wavelength in the green region selected. The sample table was then adjusted for height and tilt until the incident beam and beam reflected back from the mirror mounted on the analyser arm coincided. The pin hole and mirror were replaced by the cell window assemblies, electrolyte was added to the reference electrode compartment, and the reference electrode inserted and the compartment sealed to stop the electrolyte draining out of the vertically mounted compartment. All electrical connections were completed, a suitable potential selected and the potentiostat switched on. Electrolyte was then added to the cell and nitrogen bubbled through the solution. Usually a sulphuric acid electrolyte was used to clean the electrode surface by repeated potential sweeps into the hydrogen evolution and oxygen evolution regions. When voltammograms indicative of a clean surface were achieved, the electrolyte was removed by suction and the cell repeatedly rinsed with distilled water and then with the electrolyte to be used in the experiment.

4.8.3 Data acquisition: Potential sweeps at fixed wavelengths.

The changes in the polarisation angles producing the null condition as the potential was swept within the double layer region were typically less than 0.05°. Attempts to record the optical data using the ellipsometer in its fully automatic mode were not satisfactory owing to the level of noise present in the monitored dc Faraday cell signals. The problem was partially overcome by using a stepped electrode potential waveform and averaging the monitored Faraday components at each potential level by the computer. However, this procedure lengthened considerably the data acquisition time and did not reduce the scatter of recorded data to an acceptable level. The noise level became more significant as the wavelength decreased because the current required by the Faraday cells to rotate the plane of polarisation by a fixed amount decreased rapidly with decreasing wavelength.

The procedure adopted was to apply a linear ramp potential profile to the working electrode and monitor the dc Faraday compensator currents (amplified voltage drop across the measuring resistor - see section 3.4.6) directly on an x-y recorder. Additional filtering of the monitored signals was provided by a low pass filter (0.1 s time constant) connected at the recorder input. A comparison of the data collected by the two methods outlined above for pentan-1-ol adsorption-desorption on mercury is shown in Fig. 4.7.

After selecting the required wavelength of incident light manually, adjusting the monochromator slit width and removing the nitrogen feed to the cell, the ellipsometer was manually nulled (dc Faraday compensators off, ac modulators on) by adjusting the P and A azimuths until the PSD outputs were zero. Power to the dc Faraday compensators was applied and the zero current reference position marked on the x-y recorder trace along with the angles indicated on the angular read-out display unit. This served as the reference angle from which the record of the dc Faraday compensator current could be converted into absolute angles. The potential sweep was initiated and the current flowing through the polariser Faraday compensator was recorded as a function of the programmed potential. On completion of the potential sweep the record was calibrated by manually rotating the polariser azimuth through small angles and noting both the new angles and the corresponding change in the Faraday compensation current. The procedure was repeated to record the analyser Faraday compensator contribution and finally a conventional cyclic voltammogram was recorded to monitor the condition of the electrochemical system. The data recorded for a potassium chloride (0.01M) electrolyte for wavelengths of incident light at 300 and 637.8 nm, giving the worst and best cases in terms of noise and sensitivity are shown in Fig. 4.8 and 4.9, respectively.

The ellipsometric parameters were determined for wavelengths in the range 300 to 600 nm in steps of 50 nm and at the He/Ne laser wavelength, 632.8 nm. The process of data acquisition and calibration took about 90 minutes to complete which included approximately 10 mins. nitrogen purge between every second wavelength change.

4.8.4 Data acquisition: Automatic wavelength scanning.

Single zone ellipsometric data has been obtained for rhodamine B adsorbed on mercury and platinum under potentiostatic conditions over the wavelength range 300 to 650 nm in 5 nm intervals. For these experiments, the ellipsometer was used in its fully automatic mode

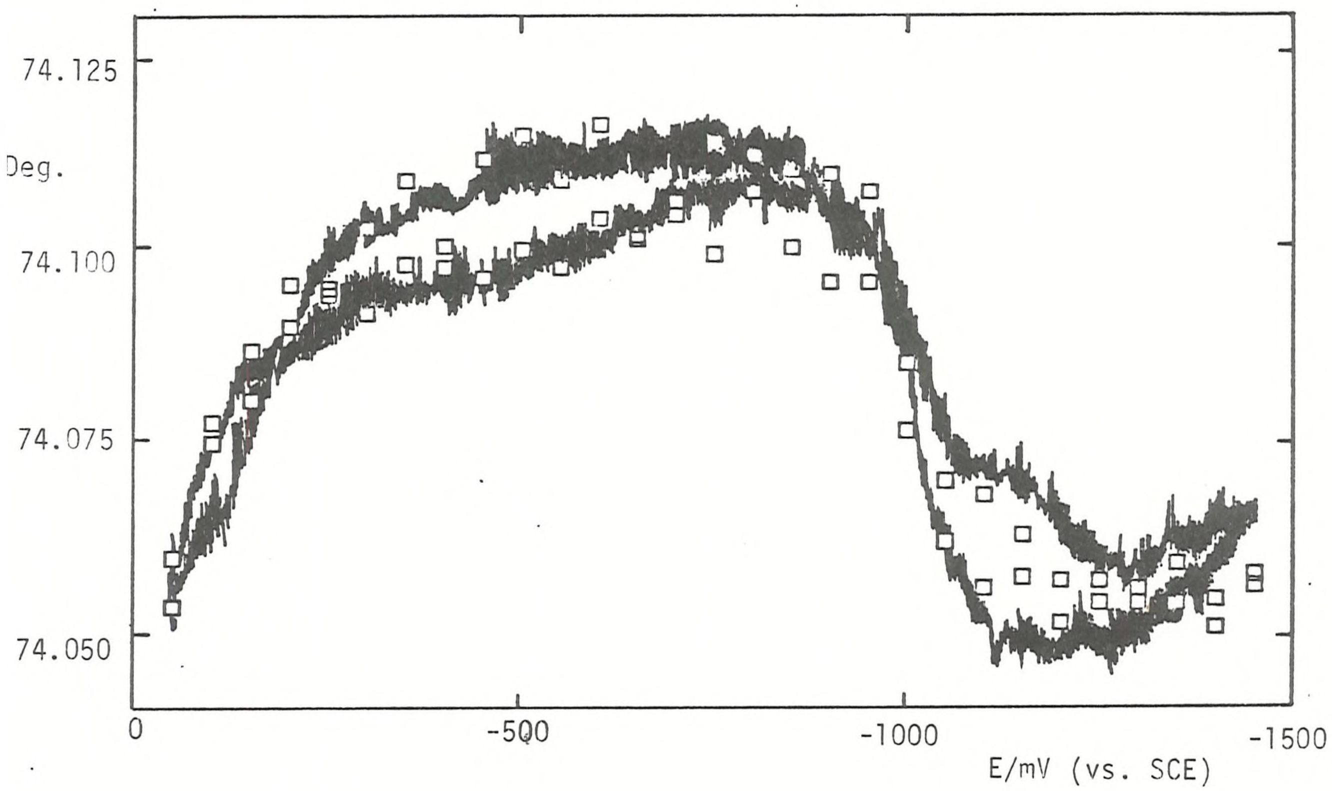

Figure 4.7. Change in null angle as a function of electrode potential for pentan-1-ol (0.02 M) in potassium fluoride(0,1 M)

□ , data collected by the computer (full automatic control). Potential stepped in 50 mV intervals. Continuous trace, analogue data (Faraday compensator current) monitored continuously on an X-Y recorder λ = 632.8 nm, ϕ_1 = 70°, mercury electrode.

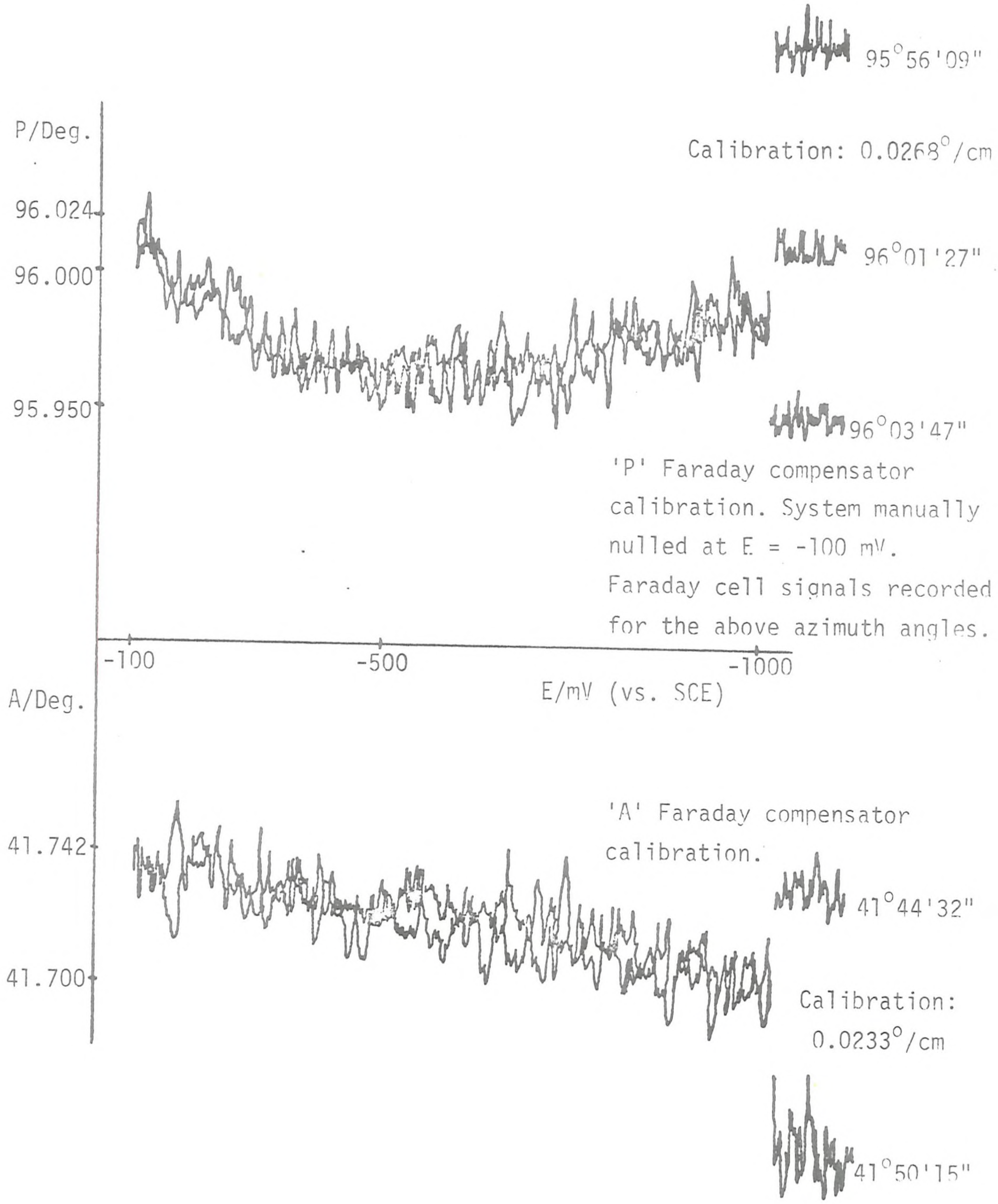

Figure 4.8. Monitored dc Faraday compensator signals as a function of electrode potential for potassium chloride (0.01 M). λ = 300 nm, $\phi_1 = 70°$, cyclic potential sweep at 20 mV/s.

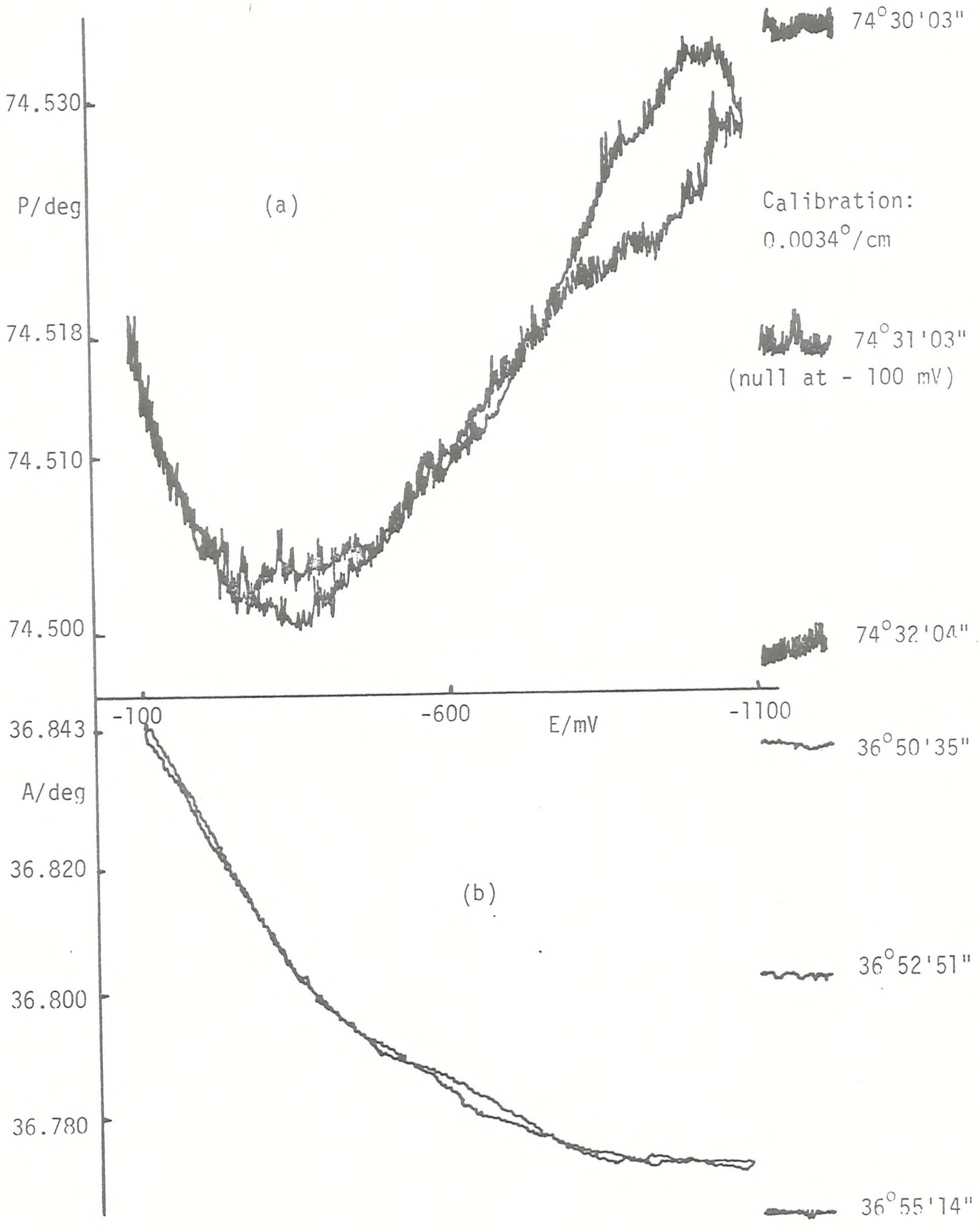

Figure 4.9. Monitored dc Faraday compensator signals as a function of electrode potential for mercury-potassium chloride (0.01 M). λ = 300 nm, ϕ_1 = 70°, cyclic potential sweep at 20 mV/s.

because of the large number of data sets required. The errors in the null angles recorded produced by noise in the dc Faraday compensator component was reduced somewhat by averaging the data recorded at each wavelength over 32 data samples. The changes in the ellipsometric parameters were, in general, much larger than those previously described for ionic adsorption so that any remaining Faraday compensator noise was less significant. Initial measurements were made, in the absence of adsorbed dye, for the mercury surface in contact with base electrolyte at a potential near to the p.z.c. at 5 nm intervals in the 300nm to 650nm. A known amount of dye was added to the cell and the ellipsometric measurements repeated for several electrode potentials.

In these experiments, and indeed any experiments conducted using the ellipsometer as an automated instrument, requires the use of the controlling computer and two programs:

1. A high level language program (Basic) which enables the user to set up the information required by the ellipsometer logic circuitry to perform functions that change the wavelength of incident light and make available to the computer the data describing the null condition.

2. A machine language program that relays the information set up in the Basic program in a form compatible with the ellipsometer logic circuitry and to convert the data transmitted by the ellipsometer into an easily understandable form.

The sequence of operations required for automatic wavelength scanning is described below:

1. When power is applied to the ellipsometer electronics, the angles displayed on the read-out unit are not the true azimuth angles. The prism angles are set by rotating them in a counter-clockwise direction (the observer looking towards the light source) until the zero reference marker on the glass-divided curcles has been sensed by the display unit (see section 3.3). At this point, a discontinuous change in the displayed angle will be observed and the measured angles are then absolute. The quarter wave retarder fast axis is then set to 45°.

2. With the optical cell mounted in position and correctly aligned, the initial wavelength of incident light is selected and the power to the monochromator drive circuitry switched on.

3. The friction drives to the polariser and analyser circles are engaged and micro-switches, situated on the encoder housings which connect the motor drive amplifier outputs to the motors, are switched on.

4. Power to the ac and dc Faraday cells is applied and the photomultiplier tube voltage increased until a signal is observed on the monitoring oscilloscope.

5. The output of the motor pulse circuitry (section 3.4.6) to the motor drive amplifiers is switched on which enables the ellipsometer to perform the auto nulling sequence.

6. Once nulled, the PMT voltage is adjusted to give a near overload condition at the PSD's. The motor drives are then disabled, the light beam interrupted and the PSD's zeroed. The auto gain PMT voltage facility is then selected and adjusted to give near overload signals to the PSD's.

7. The 'stop' and 'reset' push buttons on the control unit front panels are pressed to ensure that all control and funnel unit logic levels are initialised.

8. The 'lambda sets timer' and 'timer starts data' functions are selected (control unit front panel switches) and the output of the pulse generator (set to a high frequency pulse rate) fed to the 'external timer' input socket.

9. The Basic program is then run and data requested by the program (wavelength range, number of the analog data samples to be accumulated and averaged at each wavelength, etc.) is input.

10. The 'start' and 'start data' push buttons on the control unit front panel are pressed and the first data set is gathered, transfered to the computer and converted into decimal format.

11. The routine in the Basic program calculates the number of pulses required by the monochromator motor to select the next wavelength and sends a series of logic signals via the funnel to the motor drive circuitry along with a 'λ not steady' signal which inhibits data acquisition while the monochromator motor is active. When the new wavelength has been selected, the computer issues 'λ steady' followed by 'data request' and the data acquisition process continues when a trigger pulse is received by the timer.

12. When the complete spectrum has been recorded, the computer issues an 'end of block' signal which inhibits further data collection. The data stored in memory can be saved on magnetic tape or paper tape for future processing and a hard copy of the data recorded on paper via the printer. The required changes to the cell can be made, such as selecting a new electrode potential or adding dye solution to the cell, and the data acquisition procedure repeated from step 9.

4.8.5 Measurement of solution refractive indices.

The refractive indices of the non-absorbing solutions (F^-, Cl^-, SO_4^{2-} and isoquinoline) were measured with an Abbe-60 refractometer (Bellingham and Stanley) using a sodium vapor lamp source and were converted to values at other wavelengths assuming the dispersion correction to be the same as that for pure water.

The refractive index of the rhodamine B solution was determined by ellipsometry for wavelengths at 20nm intervals in the range 300nm to 660nm and at 5nm intervals from 500nm to 595nm. Since absolute values of Δ and Ψ were required to calculate the refractive index, four zone averaged values of Δ and Ψ were recorded for reflection from the air solution interface with the solution contained in the mercury cell without cell windows.

4.9 Computations.

Most of the computations performed were simulations producing theoretical values of Δ and Ψ , or changes in these values for a given range of input variables such as wavelength, optical constants of the substrate and film and film thickness. A number of programs have been written in Fortran IV for the ICL 2970 and Honeywell (6080) and in Basic for the PDP 1145 computers at Southampton University. Many of the programs were formally identical to sections of the general ellipsometric data analysis program written by McCrackin[90] and were checked against this program.

CHAPTER 5: RESULTS AND DISCUSSION

5.1. Ionic adsorption studies.
    5.1.1. Mercury-sodium fluoride.
    5.1.2. Mercury-potassium chloride.
    5.1.3. Mercury-sodium sulphate.
    5.1.4. General discussion on the ionic adsorption data.
    5.1.5. Conclusions.

5.2. The adsorption of isoquinoline on mercury.
    5.2.1. Adsorption from 0.3 mM isoquinoline solutions.
    5.2.2. Adsorption from 10 mM isoquinoline solutions.
    5.2.3. Conclusions.

5.3. Spectroscopic ellipsometry.
    5.3.1. Spectroscopic ellipsometry of rhodamine B adsorbed on mercury.
    5.3.2. Spectroscopic ellipsometry of rhodamine B adsorbed on platinum.
    5.3.3. Conclusions

5.1. Ionic adsorption studies.

5.1.1. Mercury - sodium fluoride

The ellipsometric parameters, Δ and Ψ, have been determined for two concentrations of sodium fluoride (0.01 and 0.1 M) as a function of electrode potential and for wavelengths in the range 300 to 600 nm in 50 nm intervals. The electrode potential was cycled between -100 and -1000 mV using a triangular ramp of 20 mVs^{-1}. Outside of these limits the changes in Δ and Ψ became large and irreversible while within the limits the changes were reversible with no hysteresis between cathodic and anodic half cycles. The cyclic voltammograms recorded for these solutions showed a slowly rising cathodic current starting at about -600 mV and an overall cathodic charge imbalance, both effects being caused presumably, by residual dissolved oxygen in the electrolyte. The excess cathodic charge for the first few sweeps was about 16 μCcm^{-2} and was observed to increase as the experiment progressed but could be reduced to values close to those observed for the initial sweeps by purging the electrolyte with nitrogen.

At each wavelength employed, three potential sweeps were performed in order to obtain sequentially, the changes in P, A and cell current as a function of electrode potential. This procedure of data acquisition and of angular calibration (see section 4.8.3) required at least 21 cycles of the electrode potential and took about 2 hours to complete. The values of Δ and Ψ were obtained by a single zone measurement of the nulling angles P and A and will be in error due to component imperfections mentioned earlier (section 2.6). However, for small changes in Δ and Ψ these errors are expected to be constant and since the data has been presented in terms of the changes in Δ and Ψ to facilitate comparisons of data obtained at different wavelengths and with existing theories, these errors become unimportant. The data obtained for 0.01 and 0.1 M sodium fluoride are shown in Figs. 5.1 and 5.2 respectively. The data is presented in terms of $\delta\Delta$ and $\delta\Psi$ as a function of q_m, the charge on the metal, where

$$\delta\Delta = \Delta - \Delta_0 \quad \text{and} \quad \delta\Psi = \Psi - \Psi_0 \qquad (5.1)$$

Δ_0 and Ψ_0 are the values of Δ and Ψ at the pzc. Electrode potentials were converted to charges by integration of the capacitance data given by Hsieh[91].

In view of the faradaic processes that were observed in the voltammetry of these electrolytes, a series of experiments was performed at a fixed wavelength of incident light, 450 nm, where the changes in P and A were monitored for several potential sweeps. The

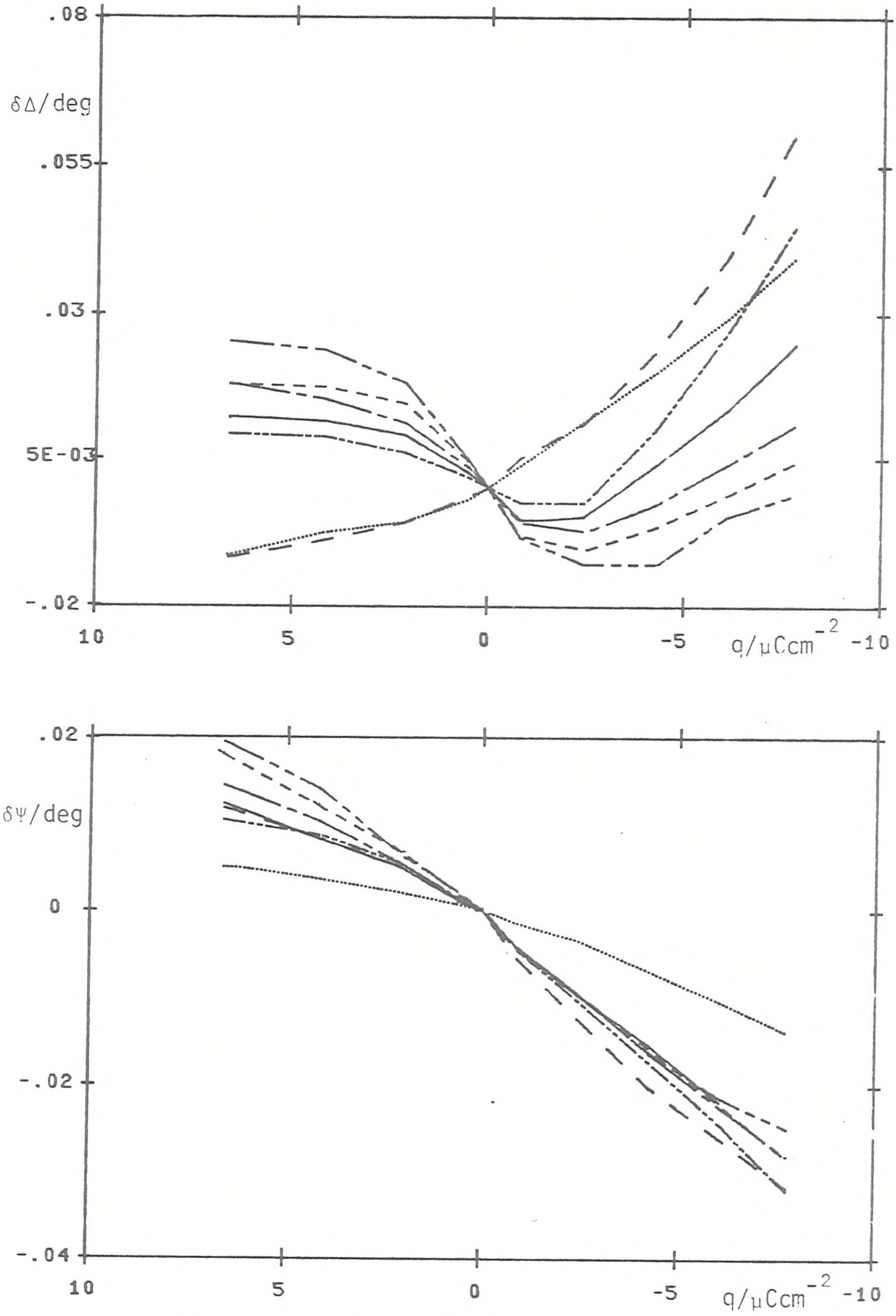

Figure 5.1. Changes in ellipsometric parameters as a function of charge for mercury-sodium fluoride (0.01 M).
Wavelengths: 300 nm ·········· ; 350 nm — — — -
400 nm —·-—·- ; 450 nm ————
500 nm ------ ; 550 nm ——·——
600 nm ———-—.

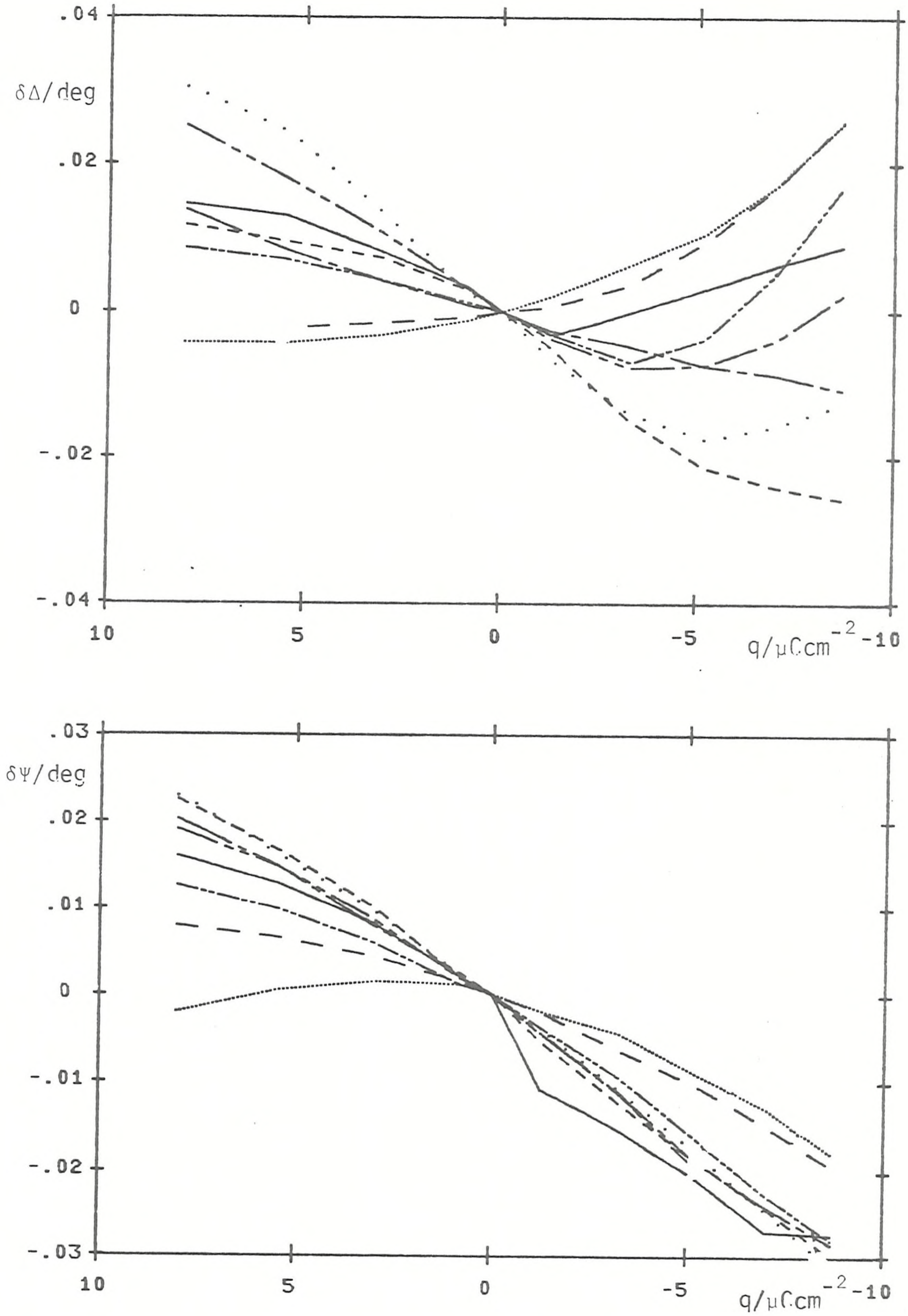

Figure 5.2. Changes in ellipsometric parameters as a function of charge for mercury-sodium fluoride (0.1 M).

Wavelengths: 300 nm ·············· ; 350 nm — — — —

400 nm —·—·—·— ; 450 nm ————————

500 nm ———— —— ; 550 nm - - - - - - - - -

600 nm ——— — — — ; 632.8 nm · · · · · · · ·

changes in the ellipsometric parameters were reproducible for up to about 5 potential sweeps and Δ and ψ were both observed to decrease with increasing cathodic potential. However, as the number of sweeps increased, the changes in Δ became less pronounced and ultimately an increase in Δ was observed at potentials more cathodic than about -700 mV and no amount of purging returned the system to its original condition. The changes in Ψ were reproducible throughout the course of the experiment but both the initial null values of P and A (absolute angles) were observed to change with each re-determination of these angles as the experiment progressed. To illustrate these effects, the data obtained are given in Fig. 5.3. Since the initial values of the nulling angles were observed to change, the data has been presented using the values of P and A recorded for the first sweep at the anodic limit of the potential range to define the zero reference values of Δ_o and Ψ_o.

It is interesting to note that reactions were clearly visible in the optical data, and while it was not intended to collect this data to gain information concerning faradaic processes, an attempt has been made to show that the optical data comprised effects other than simply double layer charging phenomena. Insufficient data was collected to present a full analysis of the charge transfer processes occuring but the data can be qualitatively interpreted in terms of the changing refractive index of the diffusion layer caused by the products of oxygen reduction.

The reduction of oxygen at mercury electrodes is observed to occur as a two step process, each step being clearly seen in dc polarograms of air saturated electrolytes as distinct reduction waves[92]. The overall reactions for the two steps are:

1st step: $O_2 + 2H_2O + 2e^- \quad H_2O_2 + 2OH^-$ (5.2)

2nd step: $H_2O_2 + 2H^+ + 2e^- \quad 2H_2O$ (neutral solutions) (5.3)
or $H_2O_2 + 2e^- \quad 2OH^-$ (alkaline solutions) (5.4)

The characteristic polarographic reduction potential (half wave potential, $E_{1/2}$) for the first step is reported to be practically independent of the solution pH, and in many electrolytes is -0.1 V[93]. The $E_{1/2}$ for the second step is more pH dependent but for air saturated potassium chloride (0.05 M) a value of -0.9 V has been given[92].

The electrode potential was held at -0.1 V while the necessary calibrations of the optical signals were performed and while the

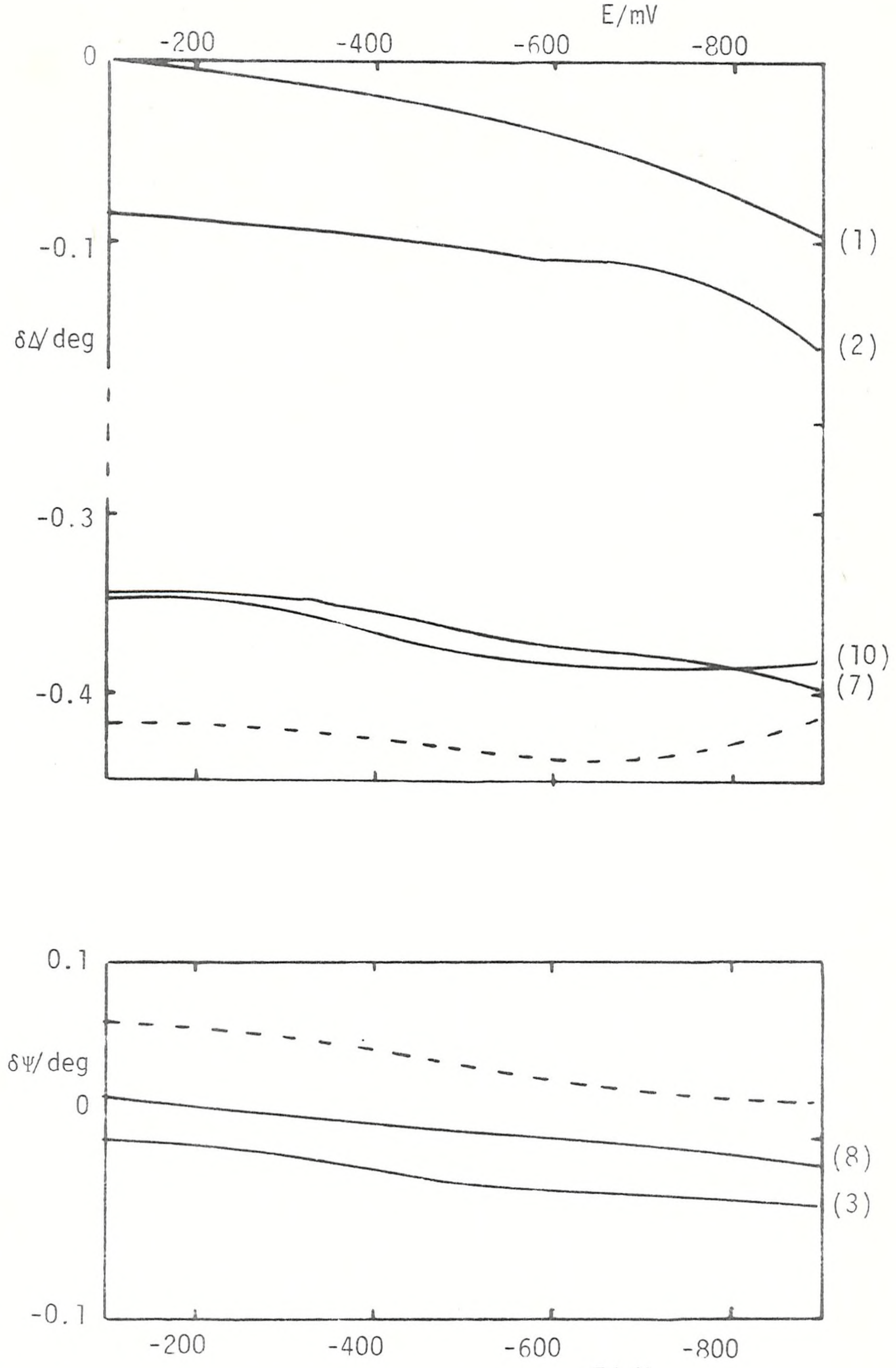

Figure 5.3. Variation of δΔ and δΨ with number of potential sweeps for mercury/NaF (0.01 M) at 450 nm. The number of times the potential was swept between limits before optical data was acquired is indicated. The dased line refers to data from Fig. 5.1. Their position, relative to the solid curves are not known because the data was collected at different times and small alignment differences (particularly cell windows) causes small differences in the null angles.

electrolyte was periodically purged with nitrogen. At this potential, the reduction of dissolved oxygen can occur resulting in the formation of hydrogen peroxide and hydroxyl ions via reaction (5.2). The refractive index of H_2O_2 at 450 nm has been estimated to be 1.42 on the basis of the reported value of 1.41 determined at 589.3 nm[94] by assuming the dispersion correction to be the same as that for pure water. This is considerably higher than either the bulk electrolyte refractive index of 1.339 or the refractive index of the diffuse layer of 1.343 if assumed to result from the excess of ions in the diffuse layer required to balance the electrode charge (see section 5.2 for details of diffuse layer refractive index calculations). Ignoring for the moment the variation of Δ and ψ with electrode potential, the overall temporal effect is that values of Δ progressively decrease and the corresponding values of ψ increase. The magnitude of the changes in Δ are roughly an order of magnitude greater than the changes in ψ. It will be shown in the following section that these effects are consistent with an increasing refractive index of a transparent film on a metal substrate. Simple calculations using the Drude equation (Eq. 2.32 in section 2.4), with mercury optical constants calculated from data given by Arakawa[51] and an assumed film refractive index of 1.42, have been performed to predict the changes in Δ and ψ, with respect to film free mercury, for different film thicknesses. The decrease in Δ by -0.26° and the increase in ψ by 0.03°, obtained from a comparison of curves 2 and 7 for Δ and curves 3 and 8 for given in Fig. 5.3, can be accounted for by an 0.8 nm film. The actual values computed were -0.268° and +0.032° for $\delta\Delta$ and $\delta\Psi$ respectively. Similar changes are predicted for a lower film refractive index and a larger film thickness, e.g., for a 2 nm film of refractive index 1.37 the changes in $\delta\Delta$ and $\delta\Psi$ were -0.264° and +0.032° respectively.

The finer detail contained in the variation of Δ and ψ with potential cannot be accounted for by such a simple model. Thus, if the changes in Δ of nearly -0.1° recorded for the initial sweeps (curves 1 and 4 in Fig. 5.3) were the result of an increase in the film refractive index, then Ψ would be expected to increase by about 0.01°.

The reduction of hydrogen peroxide to water or hydroxyl ions becomes apparent at about -0.6V (from polarographic data), but since the cathodic limit of the potentials used in thse studies was -0.9V, the reaction never becomes diffusion limited ($E_{1/2}$ = -0.9V) and hence, the production of H_2O_2 is expected to be the major contribution to changes in the diffusion layer refractive index. As the experiment progressed however, for the more cathodic potentials Δ was observed to increase. This effect, in part at least, may be explicable by the reduction of H_2O_2 to H_2O or OH^- which will have the effect of reducing the refractive index of the diffusion layer because of their lower refractivities[18].

Since the concentration of oxygen in the electrolyte was not known it has not been possible to assign a diffusion layer thickness and because of the limited amount of data collected, no quantitative analysis regarding the optical properties of the diffusion layer has been attempted. It would appear however, that most of the results obtained are explained by optical effects arising from the reduction of dissolved oxygen.

5.1.2. Mercury-potassium chloride.

Ellipsometric data obtained for potassium chloride (0.01 and 0.25 M) were recorded as a function of electrode potential for several wavelengths in the range 300 to 632.8 nm. The data is presented as a function of charge on the electrode using capacitance data[91], the difference quantities $\delta\Delta$ and $\delta\Psi$ calculated using Eq. (5.1) are shown in Figs. 5.4 and 5.5. Again a slight cathodic charge imbalance was observed in the cyclic voltammograms for both chloride concentrations (a cathodic charge excess of about 15 μCcm^{-2}) but no time dependent effects such as those described in the previous section were observed. The current flowing during the cathodic sweep did increase slowly with time, but could be reduced to values close to those observed in the initial sweeps by periodically purging the electrolyte with nitrogen. The changes in the null angles, P and A, measured in sequence, were monitored continuously as the electrode potential was swept between -100 mV and -1100 mV using a triangular waveform of 20 mVs^{-1}.

Trends common to both chloride concentrations for the $\delta\Delta$ and $\delta\Psi$ vs. q_m data have been observed. On the anodic side of the pzc Δ decreases with increasing charge and this decrease becomes more pronounced with decreasing wavelength. The trend is reversed on the cathodic side of the pzc where larger decreases in Δ are evident as the wavelength increases. The most significant difference between these two sets of data lies in the values of Δ recorded for the cathodic branch, i.e., the decrease in Δ with increasing cathodic charge is much more pronounced for the 0.01 M electrolyte.

The changes in Δ observed for both chloride and sulphate electrolytes (section 5.3) bear some resemblance to the surface tension changes observed as a function of potential. If the surface area of the mercury pool was not sufficiently large, then there would be the

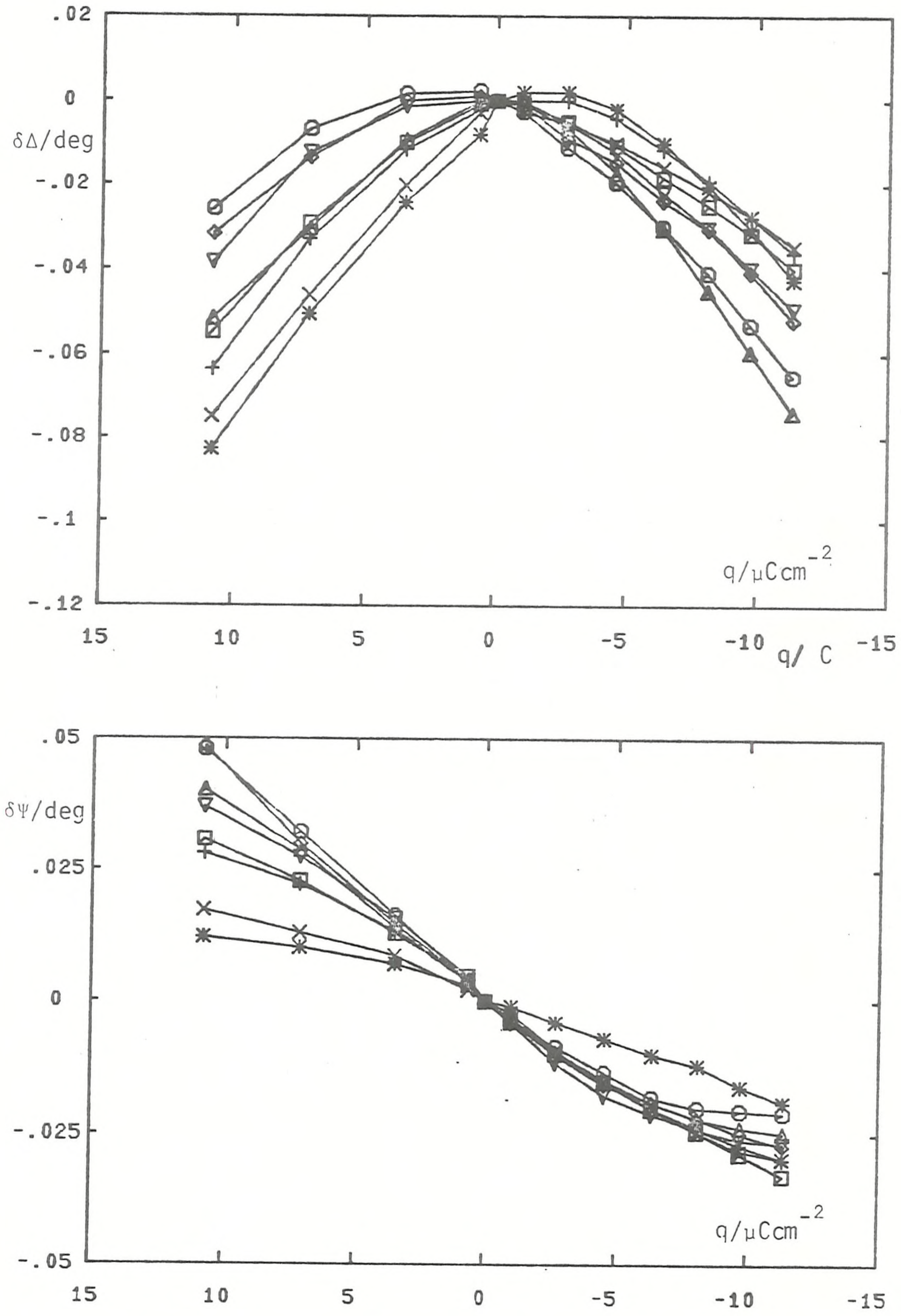

Figure 5.4. Changes in ellipsometric parameters as a function of charge for mercury-potassium chloride (0.01 M). Wavelengths: *, 300 nm; x, 350 nm; +, 400 nm □, 450 nm; △, 500 nm; ▽, 550 nm ◇, 600 nm; ○, 632.8 nm.

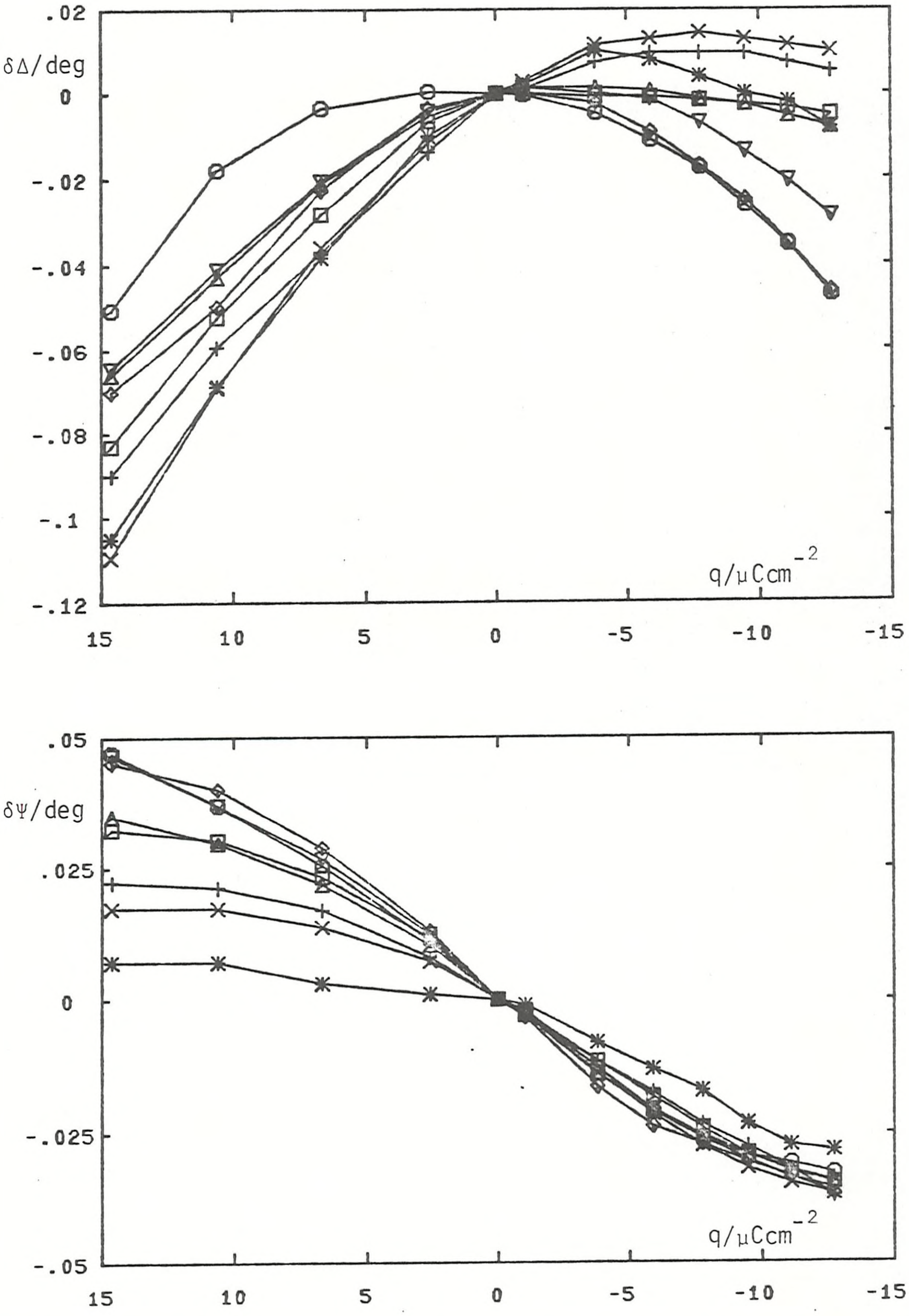

Figure 5.5. Changes in ellipsometric parameters as a function of charge for mercury-potassium chloride (0.25 M)
Wavelengths: *, 300 nm; x, 350 nm; +, 400 nm
□, 450 nm; Δ, 500 nm; ▽, 550 nm
◇, 600 nm; ○, 632.8 nm.

possibility of an optical effect arising from a changing surface curvature with potential. The effects of a changing angle of incidence, a likely effect of curvature changes, on the values of Δ and Ψ predicted for mercury in contact with potassium chloride (0.01 M), assuming the absence of a surface film, are given in Table 5.1. In these calculations and all other similar calculations in this section, use has been made of the full Drude equation to predict the values of Δ and Ψ for given values of the optical constants defining the simple three layer model. The mercury optical constants were calculated from values of the dielectric function given by Arakawa[51] and are tabulated in appendix B.1. The refractive indices of the bulk electrolytes were measured at 589.3 nm using an Abbe refractometer and were corrected for use at other wavelengths by assuming the dispersion correction was the same as that of pure water.

Table 5.1

Changes in Δ and Ψ* predicted for small changes in the angle of incidence

λ/nm	Ø/°	Δ/°	Ψ/°
300	70.01	-0.033	0.001
	70.02	-0.067	0.001
450	70.01	-0.035	-0.001
	70.02	-0.070	-0.001
600	70.01	-0.032	-0.001
	70.02	-0.065	-0.002

*The absolute values of Δ and Ψ for $Ø_1$ = 70° have been taken as the reference zero.

No wavelength dependence in Δ and essentially no angle dependent changes in Ψ are predicted for angle of incidence changes within the range required to produce changes in Δ of a magnitude similar to those observed experimentally. To produce a positive change in Ψ of 0.04° (similar to the val ues observed at the anodic limit for λ = 450 nm), would require an angle of incidence decrease of 0.4° which would cause Δ to change by +1.2°.

The ellipsometric parameters obtained for both chloride concentrations at 550 nm are quantitatively similar to the data obtained by Humphreys[95] using sodium chloride (0.1 M) and potassium chloride (0.5 M) electrolytes at 546.1 nm and a mercury pool of more than twice the area of the pool used here. From the above discussions it would seem reasonable to assume that curvature changes are not a source of error.

Changes in the optical properties of the double layer have been considered to result from several contributing factors, (1) the electroreflectance effect[52,57,59], (2) refractive index changes due to surface excesses of ions in the diffuse and inner layers[18,54], and (3) to optical effects caused by orientation, compression and concentration changes of water molecules in the inner layer[19-21,54].

For many liquid metals, the dielectric function can be calculated on the basis of the free electron model, and the electroreflectance effect, assumed to arise from perturbations of the free electron concentration in the selvedge, can be calculated by the method proposed by McIntyre and Aspnes[52]. The model considers the metal-electrolyte interface as a region of thickness $d \ll \lambda$ whose dielectric function, $\hat{K}_2$, varies continuously in a direction normal to the metal surface between $\hat{K}_3$, the bulk metal dielectric function, and K_1, the ambient dielectric function. The model further assumes that a change, ΔN, in the free electron concentration in this transition layer produces a change, $\Delta\hat{K}(z)$, in $\hat{K}_2$ and that a mean value $\langle\Delta\hat{K}\rangle$ can be defined by averaging the local change, $\Delta\hat{K}(z)$, over the transition region. This model leads to the expression

$$\langle\Delta\hat{K}\rangle = (\hat{K}_{3f} - 1)\Delta N/N \qquad (5.5)$$

where N is the free electron concentration of the bulk metal, ΔN is the change in the number of electrons in the selvedge required to maintain electro-neutrality and $\hat{K}_{3f}$ is the free electron component of the bulk metal dielectric function. ΔN can be related to the charge on the metal by

$$\Delta N = -q_m/ed \qquad (5.6)$$

where e is the electronic charge and d the thickness of the selvedge. The dielectric function of the transition layer is then given by

$$\hat{K}_2 = \hat{K}_3 + (\hat{K}_{3f} - 1)(-q_m)/Ned \qquad (5.7)$$

Eqs. (5.5) to (5.7) were used to calculate Δ and Ψ as a function of the charge on the electrode for several wavelengths of incident light, an assumed transition layer of 0.5 nm, and K_{3f} calculated using Eqs. (2.147) and (2.148). Fig. 5.6 shows the change in Δ as a function of the electrode charge, relative to an uncharged electrode, for the mercury electrolyte interface along with some experimental data for comparision. Essentially no change in Ψ is predicted by this model. The predicted changes in Δ and Ψ were not sensitive to the transition layer thickness or to the value of the refractive index of the electrolyte. It appears that the McIntyre-Aspnes model is not applicable to the mercury-aqueous electrolyte interface. Apart from a qualitative similarity between the free electron electroreflectance predictions and the changes in Δ on the anodic side of the pzc, there is no correspondence between theory and experiment. Further discussion of the electroreflectance effect is presented in section 5.1.4.

Several methods have been proposed for estimating the refractive index of the solution in the double layer region as a function of the charge on the metal[18,54]. These methods, yielding essentially the same optical effect[54], involve calculation of excess ionic concentrations from double layer capacitance data and conversion of the ion concentrations to an equivalent refractive index using the Lorenz-Lorentz equation (see section 2.9.1).

As a first step, the diffuse layer refractive index was calculated using the Stedman model[54]. The diffuse layer charges were taken from a plot of Grahame's data given by Payne[64] and the surface excess of anions and cations in the diffuse layer estimated from the Gouy-Chapman theory. The surface concentrations were converted into volume concentrations by assuming that the optical effect of an inhomogeneous film (n varying continuously in a direction normal to the surface) could be approximated by a film of thickness 2/κ of homogeneous refractive index, where κ is the Debye-Hu^c^kel reciprocal length. After calculating the density of the layer and the mole fraction of all species in this layer, using apparent molal ion volumes[96], the Lorenz-Lorentz equation was used to compute the refractive index of the equivalent layer using ion refractivities given by Waddington[97]. The outcome of these calculations for both chloride concentrations employed is given in Fig. 5.7. The reason for the small changes in refractive index with charge on the metal lies in the fact that the diffuse layer charge is always positive which suggests that the layer consists mainly of potassium ions, whose ionic refractivity and molal ion volume are smaller than those of water.

The effect of such refractive index changes on Δ and Ψ can be easily calculated for a wavelength of 589.3 nm where the ionic

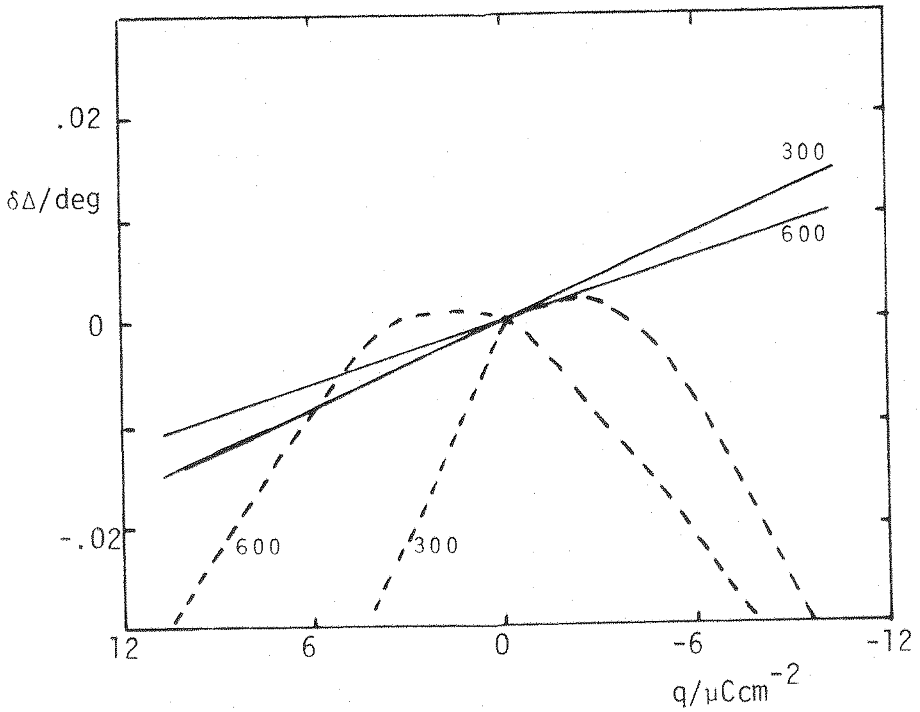

Figure 5.6. Electroreflectance effect predicted from a free electron model at the wavelengths indicated, 0.5 nm selvedge ——— ; experimental data (KCl, 0.01 M) - - - - - .

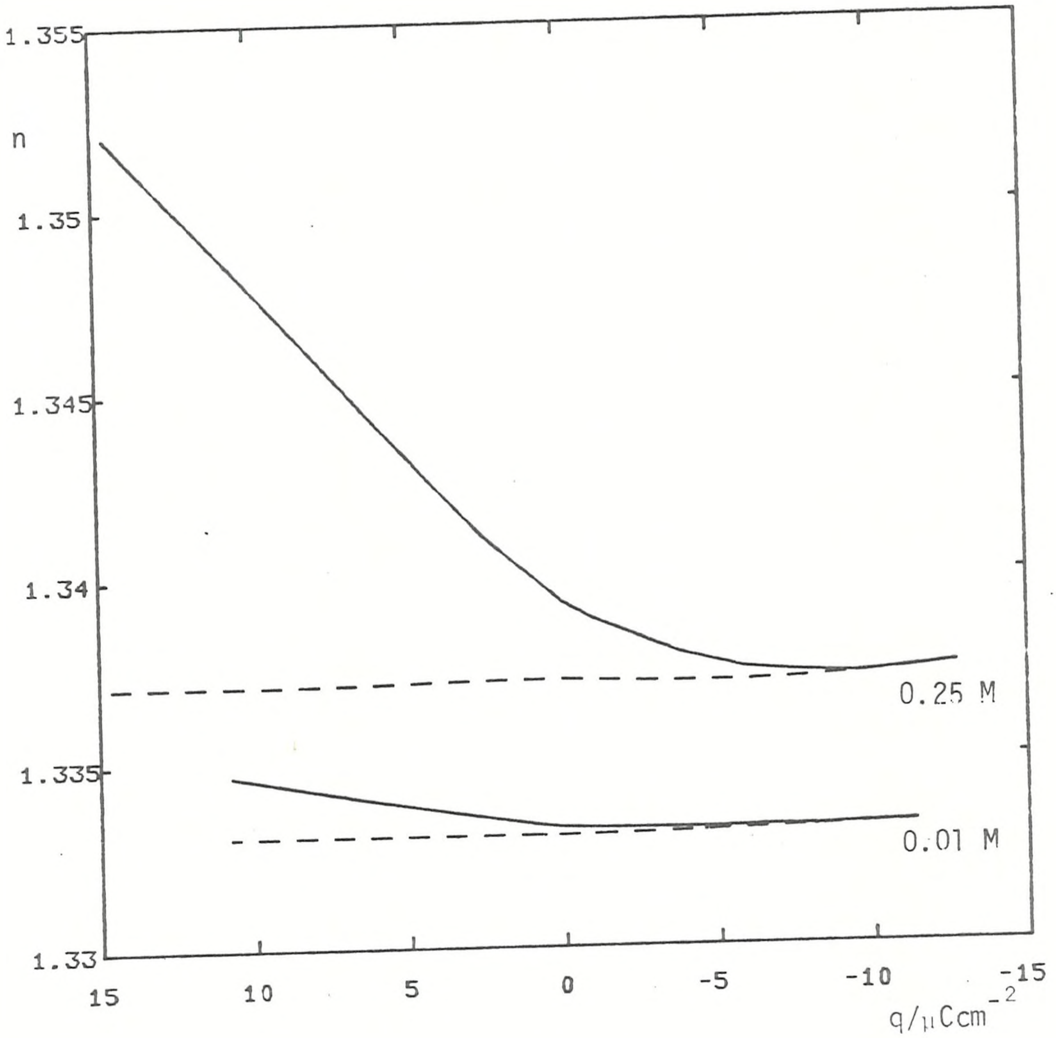

Figure 5.7. Equivalent layer refractive index for potassium chloride solutions at λ= 600 nm.

- - - - - diffuse layer only.

——— combined inner and diffuse layers.

refractivity data is readily available[97]. The effect of wavelength dispersion on the calculated diffuse layer refractive index has been estimated by assuming that the dispersion correction is the same as that for pure water. The concentration of chloride ions in the inner layer was calculated from the inner layer charge ($q_i = -q_m - q_d$) and was simply added to the concentration calculated for the diffuse layer to form a single equivalent layer for optical calculations. The computed refractive indices are given in Fig. 5.7 along with the diffuse layer predictions, and the variation of the calculated ellipsometric parameters are shown in Figs. 5.8 and 5.9 along with some experimental data for comparison. For positive charges, the predicted negative change in Δ and the positive change in Ψ are observed experimentally but the predicted wavelength dispersion is small and does not correspond to the dispersion observed. The negative changes in both Δ and ψ on the cathodic side of the pzc are not predicted by this approach.

Stedman[54] has calculated the optical effects of changes due to volume changes of water in the inner layer based on surface excess volumes measured by Hills and Payne[66]. From their estimate of ca 17% compression of the water layer for the mercury-sodium fluoride (0.1 M) interface as the surface charge increases from -10 to +20 μC cm^{-2}, Stedman has calculated a refractive index of 1.405 (from bulk compression - refractive index data) resulting in changes of Δ and ψ of -0.120° and 0.013° respectively. It will be shown below that increasing the refractive index of a thin transparent film produces negative changes in Δ and positive changes in ψ with respect to a film free reference state, but it does not alter the wavelength dispersion. Inclusion of the contribution from the inner layer water compression, assuming the values mentioned above are reasonable estimates for the electrolytes used here, to the already predicted changes would overestimate the changes in Δ on the anodic side of the pzc but the corresponding changes in ψ would still be underestimated.

It is clear from the above discussions that the simple three layer model using refractive indices based on bulk properties does not explain the experimental data. It is, intuitively, reasonable to suppose that the intensive properties of chemisorbed molecules and ions are altered from the properties of the species in solution by, for example, partial charge transfer or by induced dipole moments. It is not too surprising then, that the simple models, using parameters derived from bulk properties, do not predict the changes in ellipsometric parameters satisfactorily.

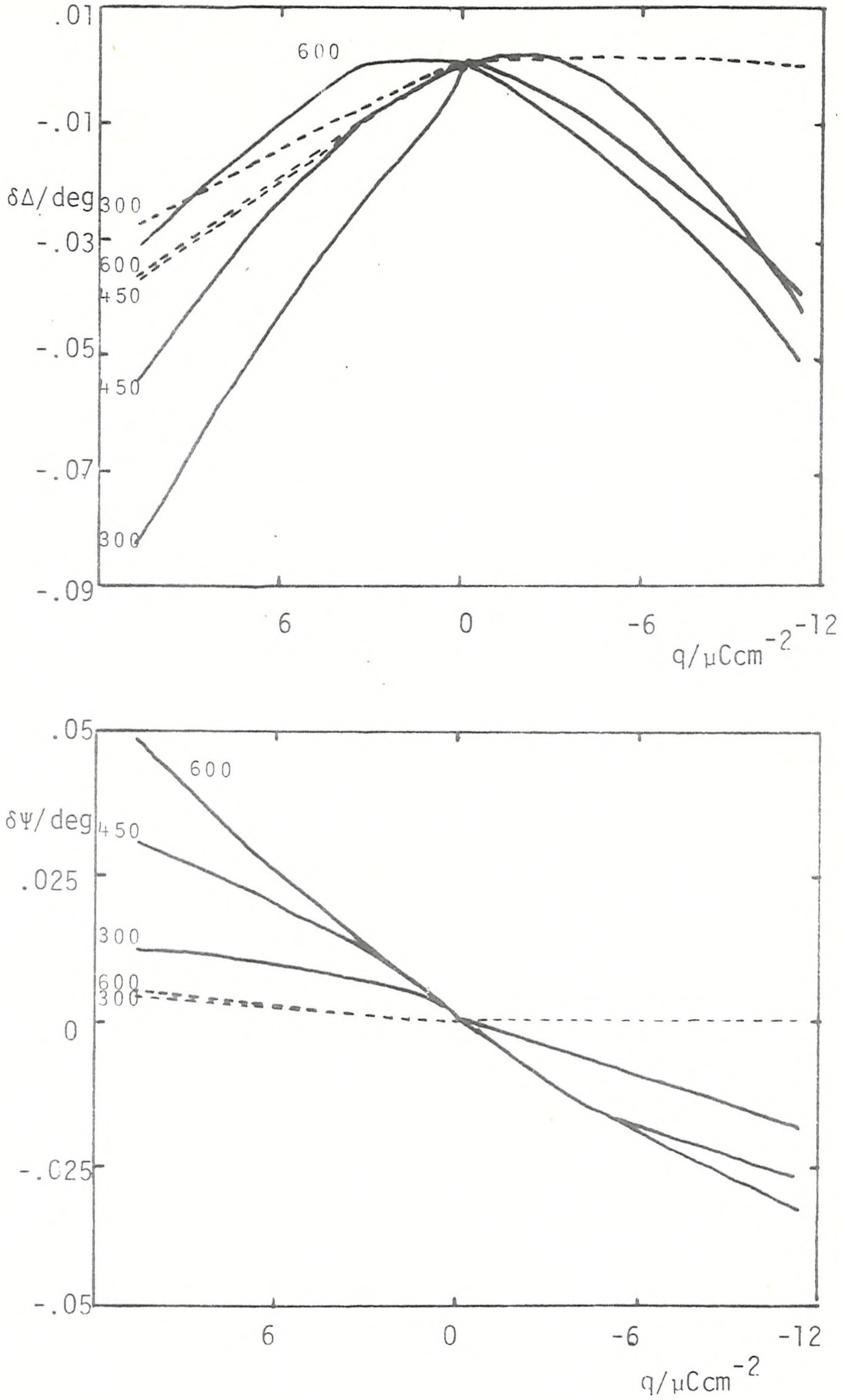

Figure 5.8. Predictions, based on the Stedman model, for the diffuse + inner layer contributions to changes in Δ and Ψ for KCl (0.01 M) at the wavelengths indicated - - - - - ; experimental data ———— .

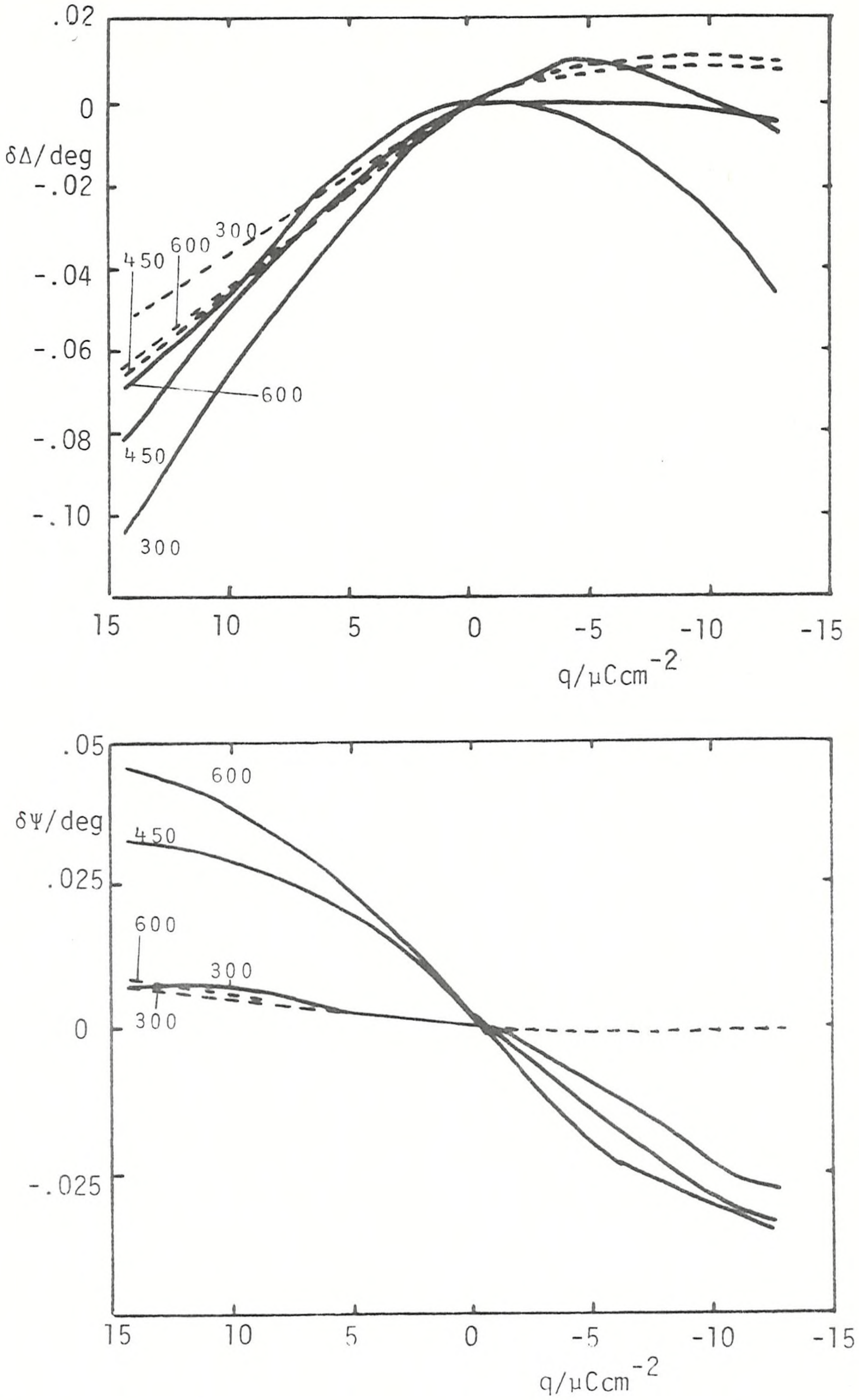

Figure 5.9. Predictions for the diffuse and inner layer contributions to changes in Δ and Ψ for KCl (0.25 M) - - - - ; experimental ——— .

In an attempt to make some generalisations concerning the optical properties of the double layer, the simple three layer model has been used to predict the changes in Δ and Ψ for a wide range of film optical constants. The simulations have been repeated for a number of wavelengths to enable some generalisations concerning the dispersion of the experimental results to be made.

The effect of changing the refractive index ($k_2=0$) for a 0.5 nm film on mercury for a number of wavelengths is shown in Fig. 5.10. The film refractive indices chosen ranged from near bulk electrolyte values (0.01 M KCl) up to 1.9 and the reference values, Δ_0 and Ψ_0, were taken as the values calculated for film free mercury in contact with electrolyte. The changes in Δ for a given change in n_2 become increasingly more negative as λ increases up to 400 nm and then become progressively less negative as λ increases from 450 to 632.8 nm. The critical angle (similar to the Brewster angle for a transparent substrate) varies with wavelength, and for mercury is close to 70° for λ = 450 nm. The changes in Δ are most sensitive to changes in film properties at the critical angle. The predicted dispersion for a transparent film is, for the most part, opposite to the experimentally observed dispersion on the anodic side of the pzc. The changes in Δ are consistently an order of magnitude larger than the changes in Ψ which again, is not the case for the experimental results. Increasing the film thickness used in the above calculations merely increases the rate of changes of Δ and Ψ with n_2 but does not affect the wavelength dispersion or the relative change in Δ with respect to Ψ.

For an absorbing film on mercury, the wavelength dispersion becomes much more pronounced. Computed changes for films of constant extinction coefficient (k_2 = 0 to 1.2) and refractive index varying over the range used in the previous simulation are shown in Fig. 5.11. The reference values, Δ_0 and Ψ_0, were taken as the values calculated for a 0.5 nm film of complex refractive index $n_2 = 1.33 - ik_2$, $k_2 = 0 \cdot\cdot 1.2$. The refractive index is shown decreasing from right to left in these figures for comparison with the anodic branch of the experimental data. For these films the changes in Δ become less negative as k_2 increases and as the wavelength increases, while the changes in Ψ become more positive as k_2 increases to about 0.4 but then become progressively less positive as k_2 continues to increase. Particular values of k_2 can be found that yield qualitatively similar wavelength dispersion behavior to those observed on the anodic side of the pzc experimentally. Selected curves from Fig. 5.11 have been replotted on an expanded scale in Fig. 5.12 along with some values of

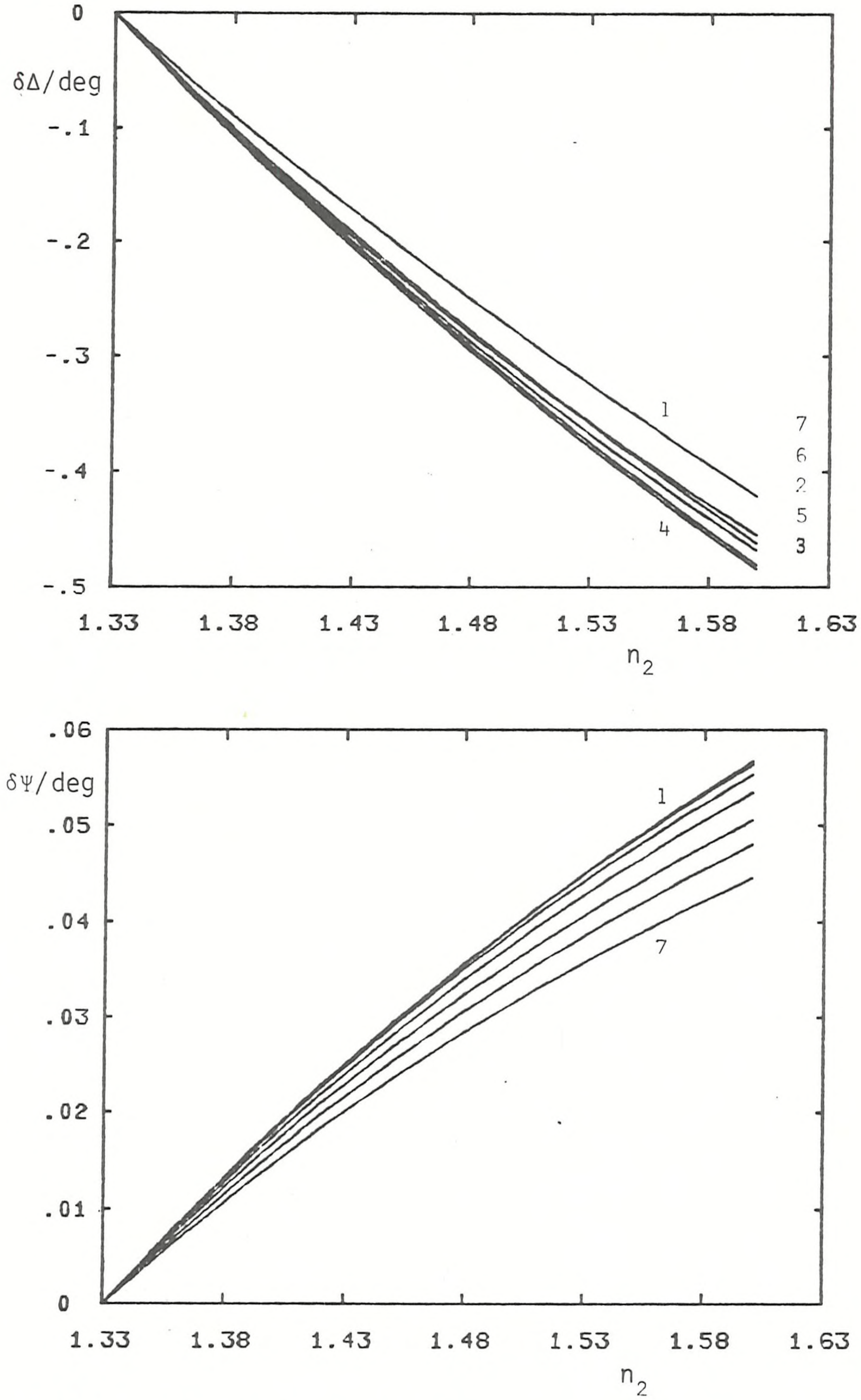

Figure 5.10. Effect of changing film refractive index, n_2 ($k_2 = 0$) on Δ and Ψ for a 0.5 nm film on mercury. Curve 1, $\lambda = 300$ nm to curve 7, $\lambda = 600$ nm in steps of 50 nm.

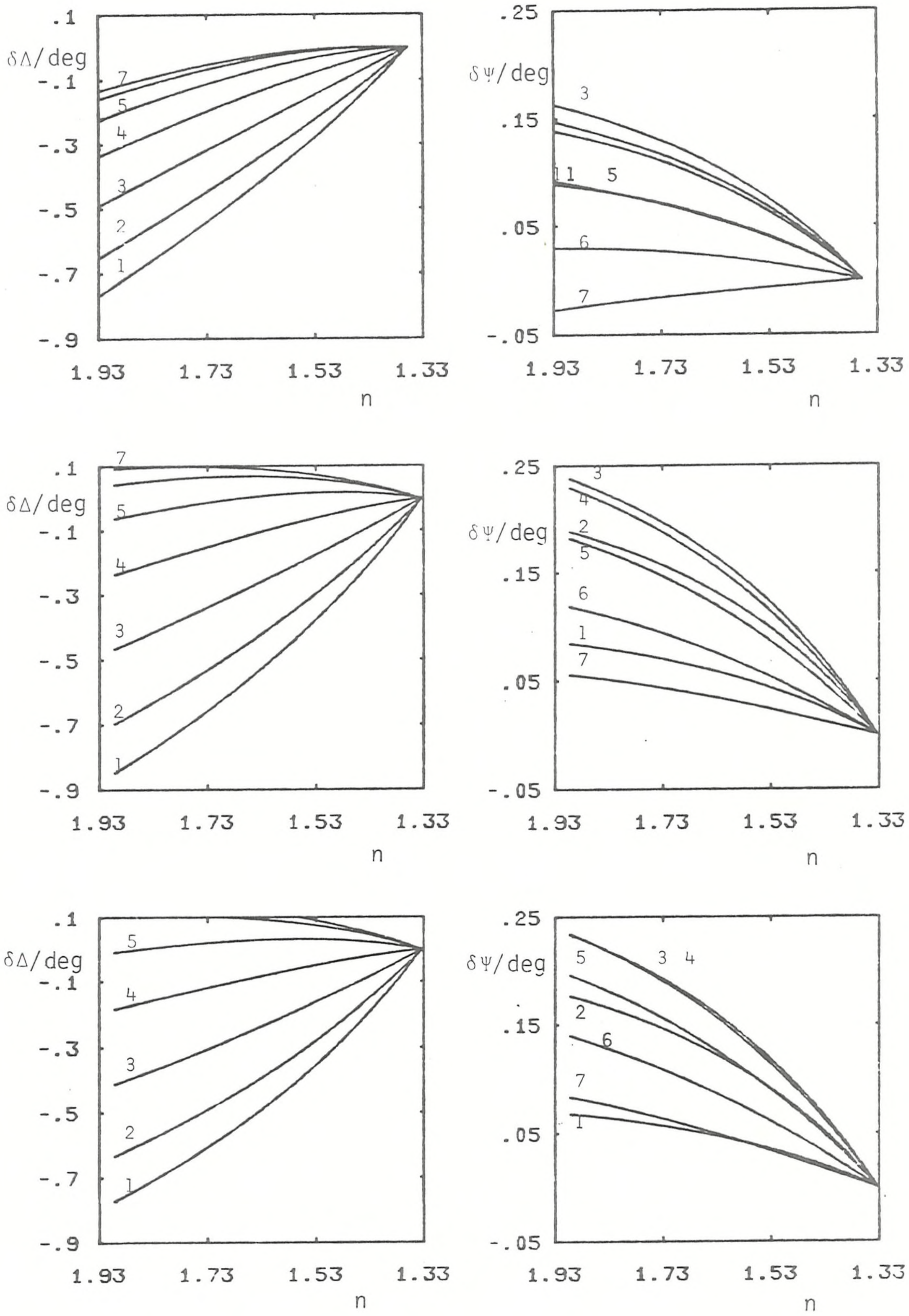

Figure 5.11. Effect of changing film refractive index, n_2 on Δ and Ψ for a 0.5 nm film on mercury.
Curve 1, k_2 = 0 to curve 7, k_2 = 1.2 in steps of 0.2.
(a) 300 nm, (b) 450 nm, (c) 600 nm.

Δ and Ψ recorded at the anodic limit in the experimental data to show more clearly the dispersion effects. From these computations, it appears that if k_2 is in the range 0.4 to 0.9 then the overall wavelength dispersion of the anodic branch of the experimental data is qualitatively predicted. Outside of these limits either the dispersion is not accounted for or the changes in $\delta\Delta$ or $\delta\Psi$ are of the wrong sign.

To account for the changes in Δ and Ψ observed for the cathodic branch of the data where only changes in a surface film on the substrate are considered, it has been found that k_2 must increase while n_2 is held relatively constant. Computed changes in Δ and ψ for films of constant refractive index ($n_2 = 1.33$ to 1.93) and k_2 varying in the range 0 to 1.2 are shown in Fig. 5.13. The reference Δ_0 and Ψ_0 values were taken as the values calculated for $n_2 = n_2 - ik$, $k = 0$ and $n_2 = 1.33 \cdot\cdot 1.93$.

By allowing both n_2 and k_2 to vary, the values of Δ and Ψ can cover a wide range of values and since for an absorbing film these values are not linearly related to changes in the film constants, the choice of the reference values Δ_0 and Ψ_0 can have a pronounced effect on the relative changes $\delta\Delta$ and $\delta\Psi$ If the inner or diffuse layers contained optically absorbing species, then it becomes difficult to find unique solutions for the film properties if only the relative quantities $\delta\Delta$ and $\delta\Psi$ are known accurately. It would seem probable that a multitude of solutions exist within the range of film optical properties studied that would qualitatively simulate the observed experimental results. A set of related solutions would also exist for each assumed film thickness.

To complete these simulations, the effect of a 0.5 nm film of mercury-like optical constants on mercury has been considered. The range of metal-like refractive indices used is given by $n_2 = (n_3 + \Delta n_3) - i(k_3 + \Delta k_3)$ where Δn_3 and Δk_3 ranged from -0.2 to +0.2. The reference zero was calculated for film free mercury in contact with electrolyte and the generated data is given in Figs. 5.14 and 5.15 as plots of Δ vs. Ψ. Shown also on the figures are the values of $\delta\Delta$ and $\delta\Psi$ recorded at the anodic and cathodic limits of the experimental data. If the changes in the ellipsometric parameters were to depend only on films of these types, then for the anodic branch n_2 and k_2 would both have to decrease with increasing charge. The cathodic branch of the data would require that n_2 increases while k_2 decreases with increasing cathodic charge.

A further discussion of these three layer model calculations is presented in section 5.1.4.

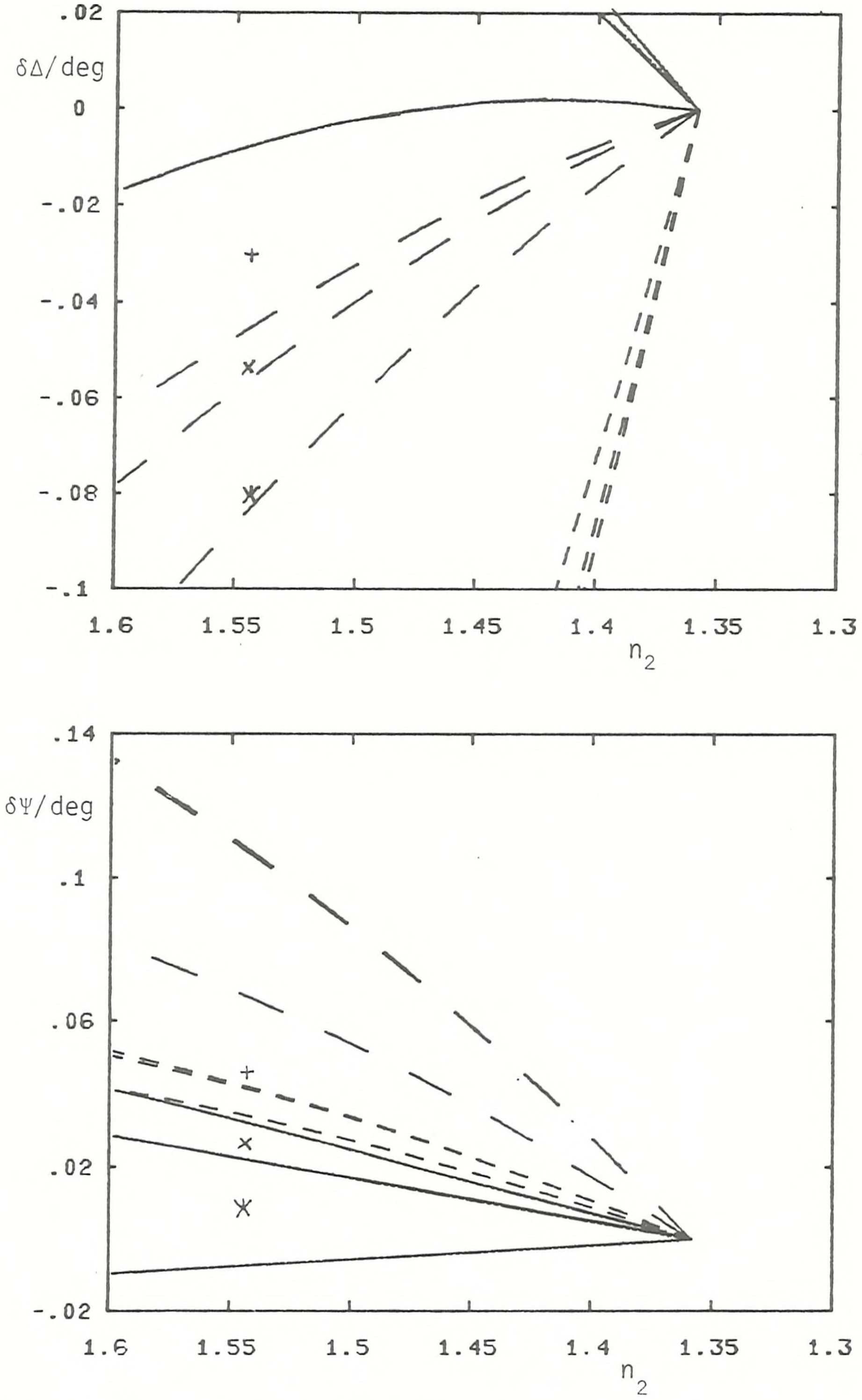

Figure 5.12. Effect of film extinction coefficient, k_2, on the wavelength dispersion of Δ and Ψ for a 0.5 nm film.

- - - - - $k_2 = 0$

—— —— $k_2 = 0.6$

———— $k_2 = 1.2$

Experimental values recorded at anodic limit in KCl (0.01 M); *, 300 nm; x, 450 nm; +, 600 nm.

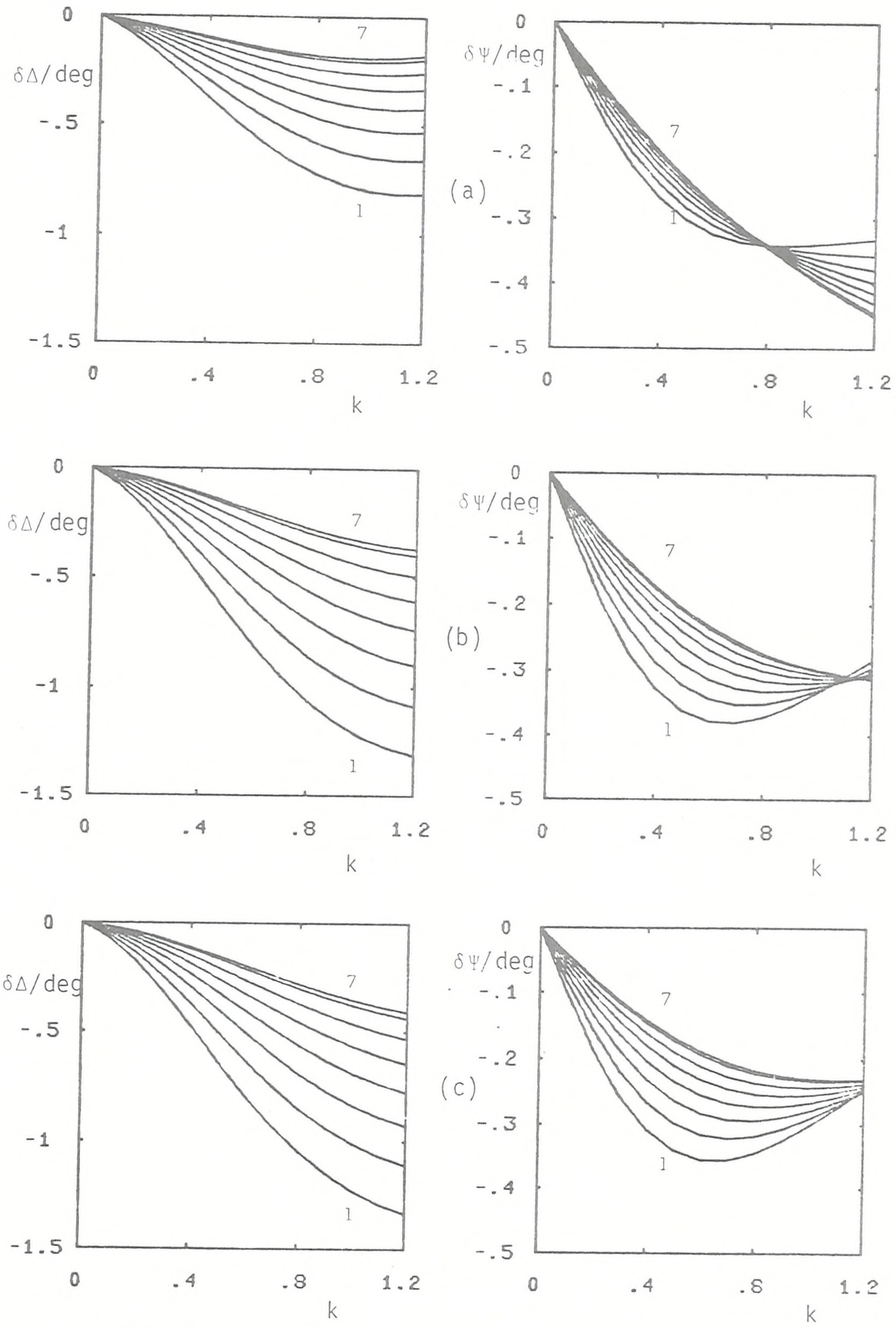

Figure 5.13. Effect of changing film extinction coefficient, k_2, on on Δ and Ψ for a 0.5 nm film on mercury.
Curve 1, n = 1.33 to curve 7, n = 1.87 in steps of 0.09.
(a) 300 nm, (b) 450 nm, (c) 600 nm

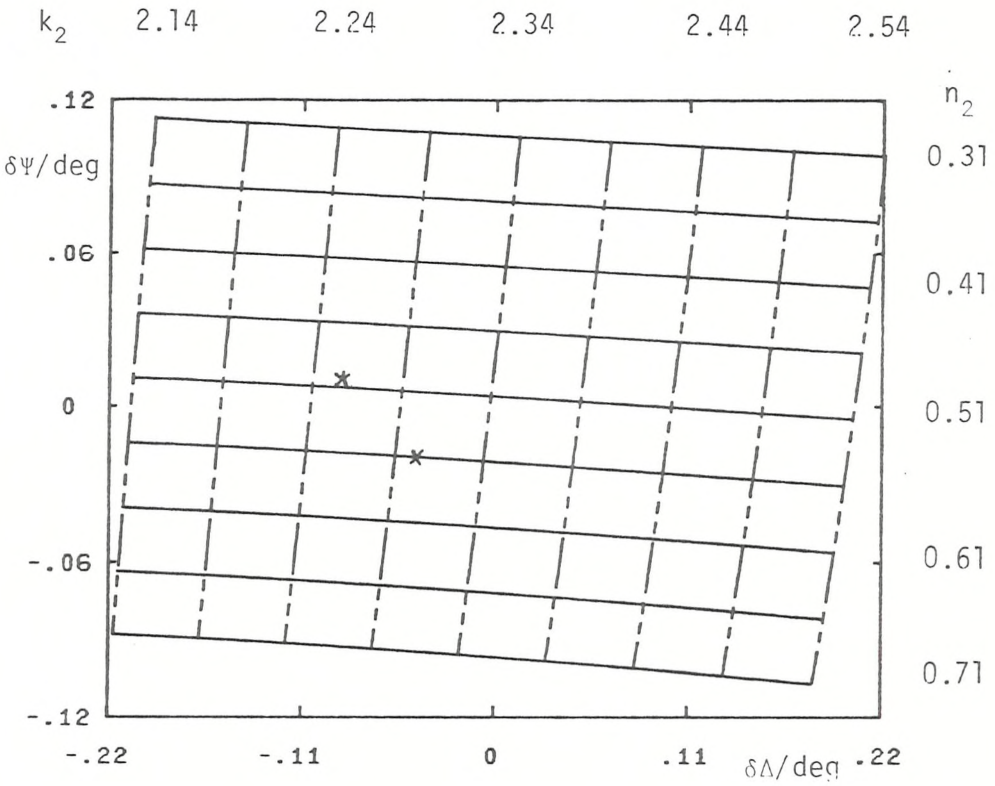

Figure 5.14. Plot of δΨ vs. δΔ for a 0.5 nm film of metal-like optical constants on mercury at λ = 300 nm.

——————— lines at constant n_2

—— - - —— lines at constant k_2

*, experimental values of δΔ vs. δΨ recorded at -100 mV for potassium chloride (0.01 M)

x, experimental values of δΔ vs. δΨ recorded at -1100 mV.

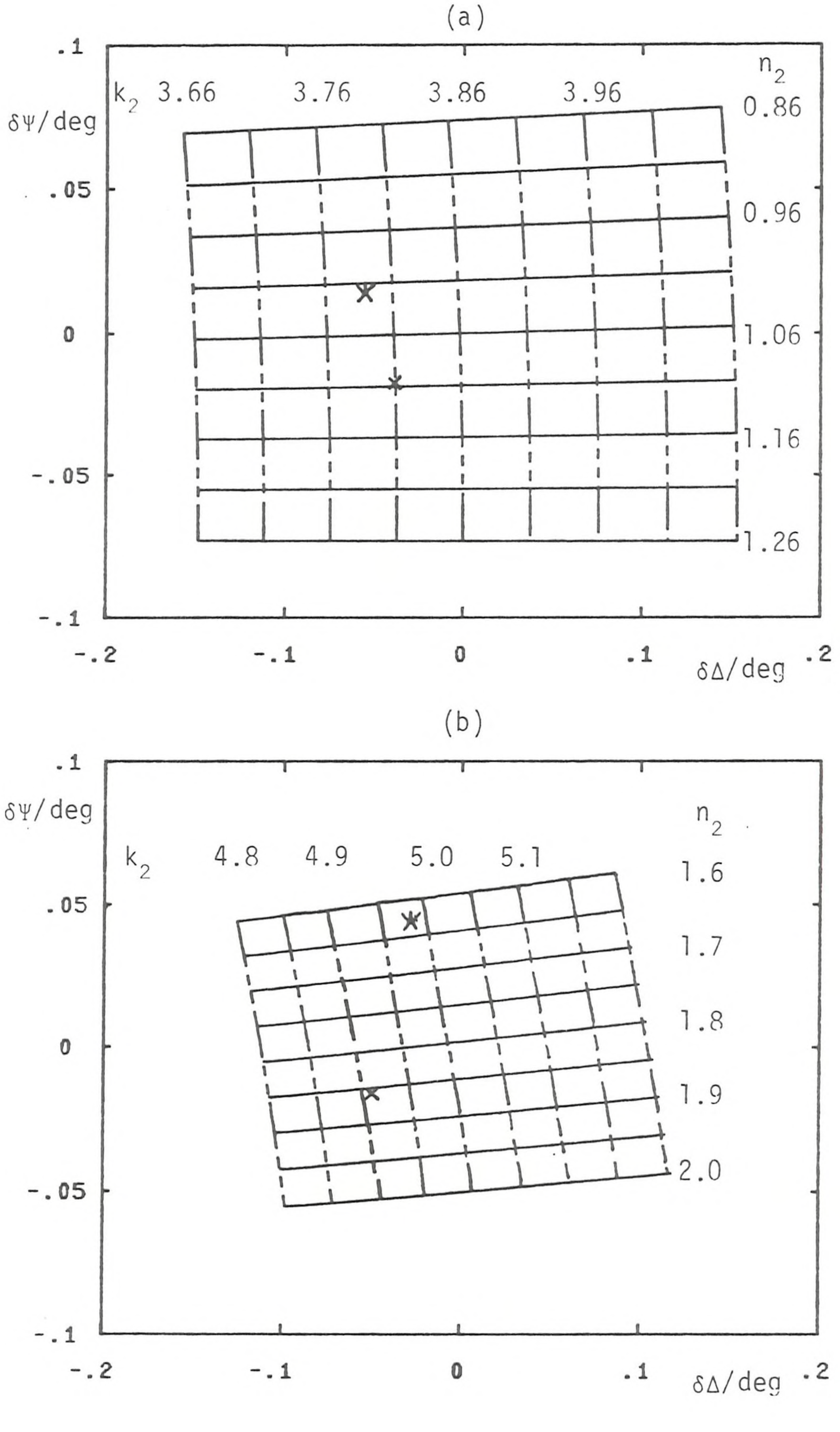

Figure 5.15. Plot of δΨ vs. δΔ for a 0.5 nm film of metal-like optical constants on mercury.
(a) λ = 450 nm, (b) λ = 600 nm.
*, experimental values of δΔ and δΨ recorded at -100 mV for potassium chloride (0.01 M)
x, experimental values of δΔ and δΨ recorded at -1100 mV

5.1.3. Mercury-sodium sulphate.

The ellipsometric data obtained for sodium sulphate (0.5 M) in the wavelength range 300 to 632.8 were recorded in the same way as described for the fluoride and chloride electrolytes. A small cathodic charge imbalance of about 6 μCcm^{-2} was observed in the cyclic voltammogram recorded immediately before optical data collection and again the level of current flowing in the cathodic half cycle was observed to increase with time but much more slowly than in the case of the other electrolytes. The data is presented in Fig. 5.16 as a function of charge using the capacitance data given by Grahame[98]. There is a close similarity for both ellipsometric parameters between the sulphate and chloride data (particularly for 0.01 M KCl). The observations made in the discussion of the chloride data concerning the simple three layer models for electroreflectance and solution side effects are equally applicable here.

5.1.4. General discussion on the ionic adsorption data.

Some of the results obtained for the different electrolytes studied have been plotted on the same graphs using the rational potential scale, E - Epzc, (Figs. 5.17 to 5.20) rather than a charge abscissa because of the much larger charge range accessible in the sulphate electrolyte. An almost linear decrease in Δ with increasing charge or potential has been observed for the sulphate and chloride electrolytes. The magnitude of the slopes are relatively insensitive to wavelength changes and for both chloride concentrations the slope is approximtely $0.006^{\circ}\ \mu C^{-1}$ whereas for the sulphate electrolyte, the slope is about $0.0015^{\circ}\ \mu C^{-1}$. Qualitatively, the data on the anodic side of the pzc for the chloride and sulphate solutions reflects the amount of specifically adsorbed ions since for a particular charge on the mercury the observed changes in Δ increase in the order Cl^- (0.25 M) > Cl^- (0.01 M) >> SO_4^{2-} (0.5 M).

The computations based on the three layer model presented in section 5.1.2 show clearly that the wavelength dependence of the chloride data cannot be explained in terms of a transparent or slightly absorbing layer on the mercury surface. This is true also of the sulphate data since a similar wavelength dispersion has been observed. The inclusion of a fourth layer whose optical properties are defined by the free electron electroreflectance effect and the McIntyre-Aspnes model for this transition layer, does not improve matters except for qualitative similarities in Δ observed on the anodic side of the pzc.

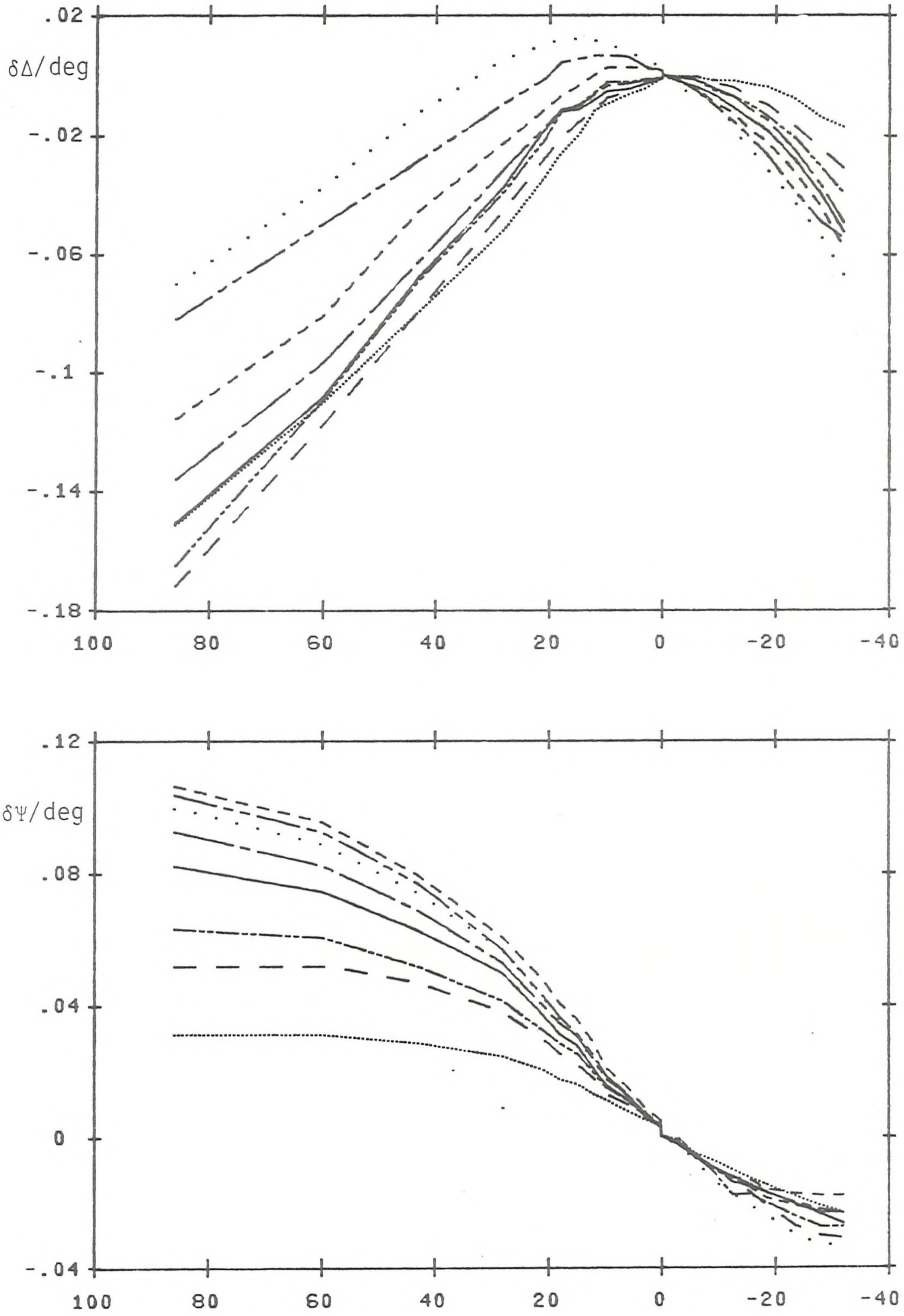

Figure 5.16. Changes in the ellipsometric parameters as a function of charge for mercury-sodium sulphate (0.5 M).

Wavelength: 300 nm ··········· ; 350 nm — — — — —

400 nm —·-—·- ; 450 nm ————

500 nm ——— — — ; 550 nm - - - - - -

600 nm —- - - — ; 632.8 nm. · · · · · ·

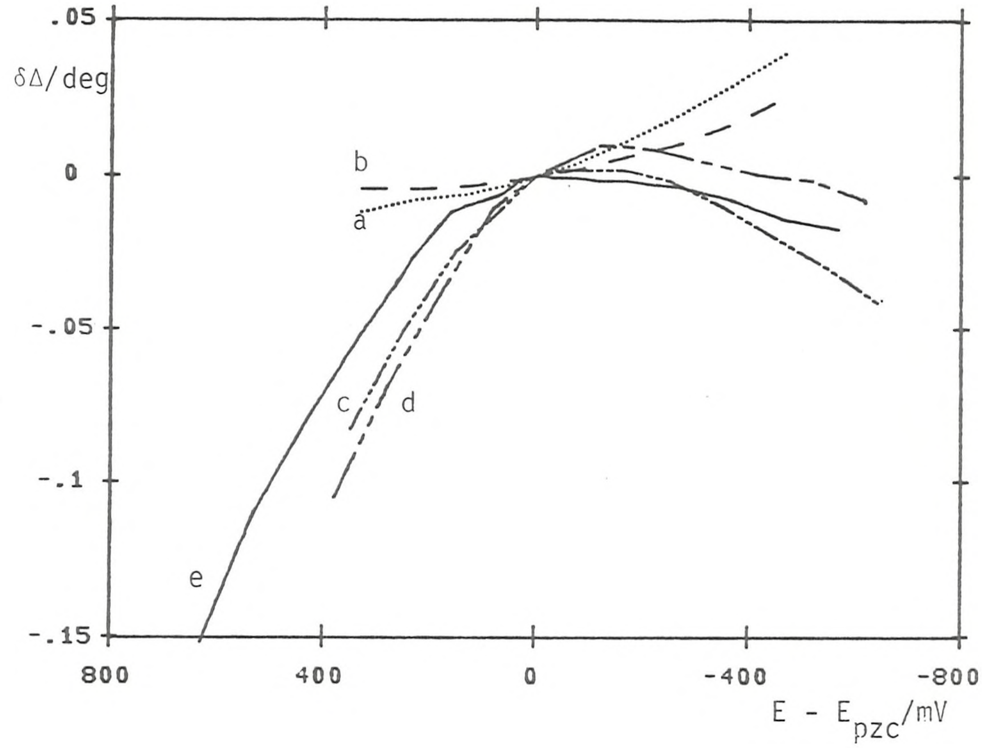

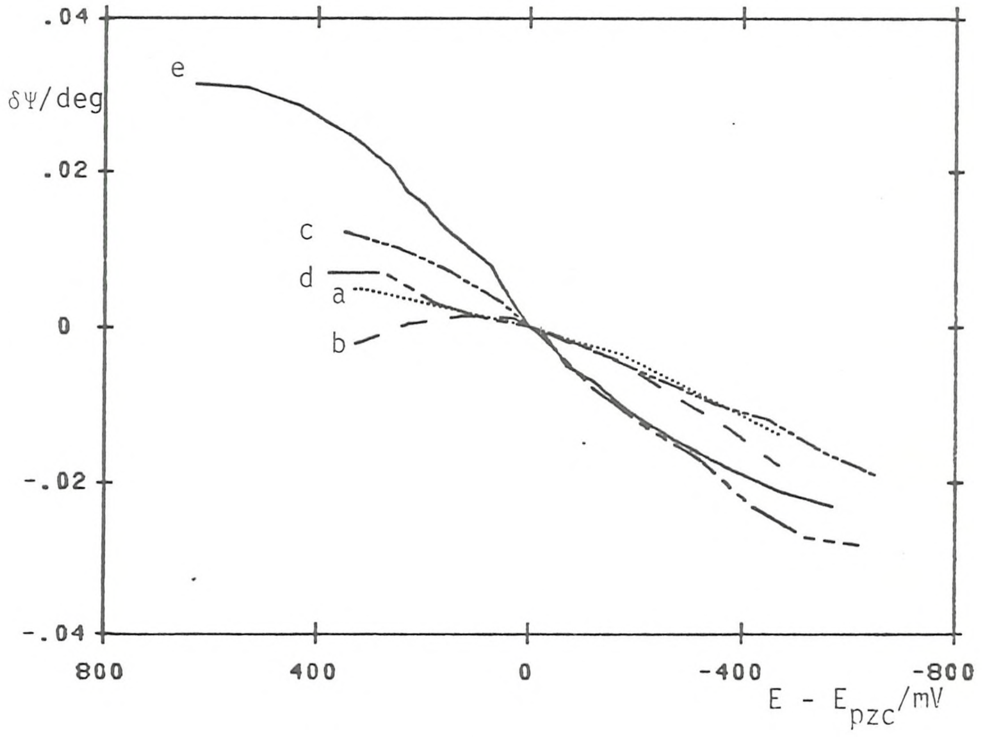

Figure 5.17. Summary of results obtained at 300 nm.

a, Sodium fluoride (0.01 M).

b, Sodium fluoride (0.1 M).

c, Potassium chloride (0.1 M).

d, Potassium chloride (0.25 M).

e, Sodium sulphate (0.5 M)

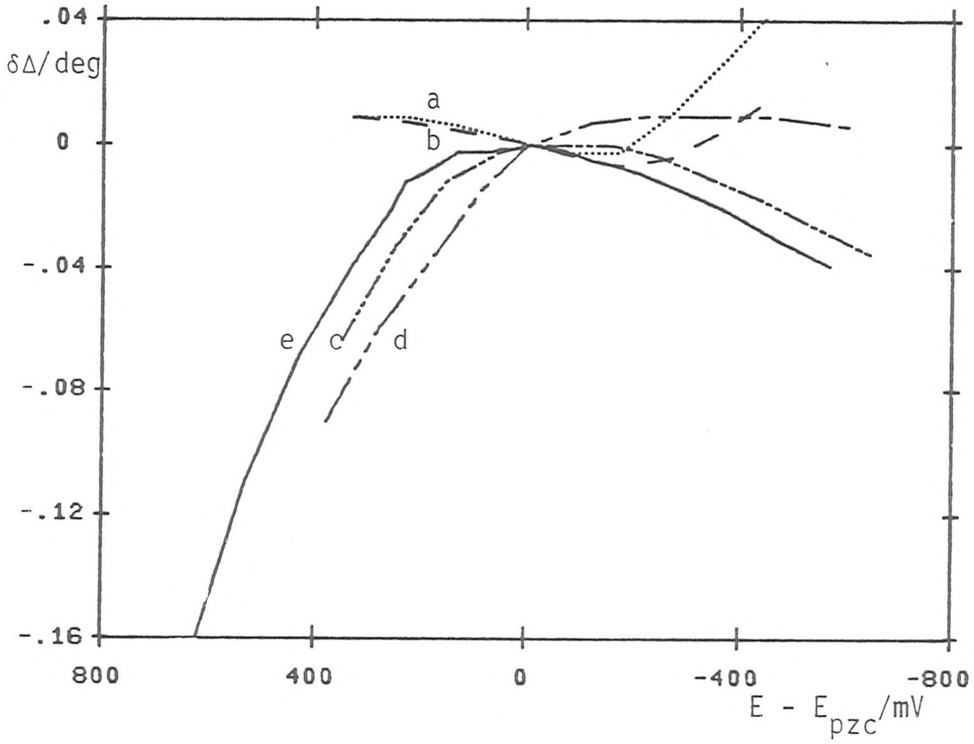

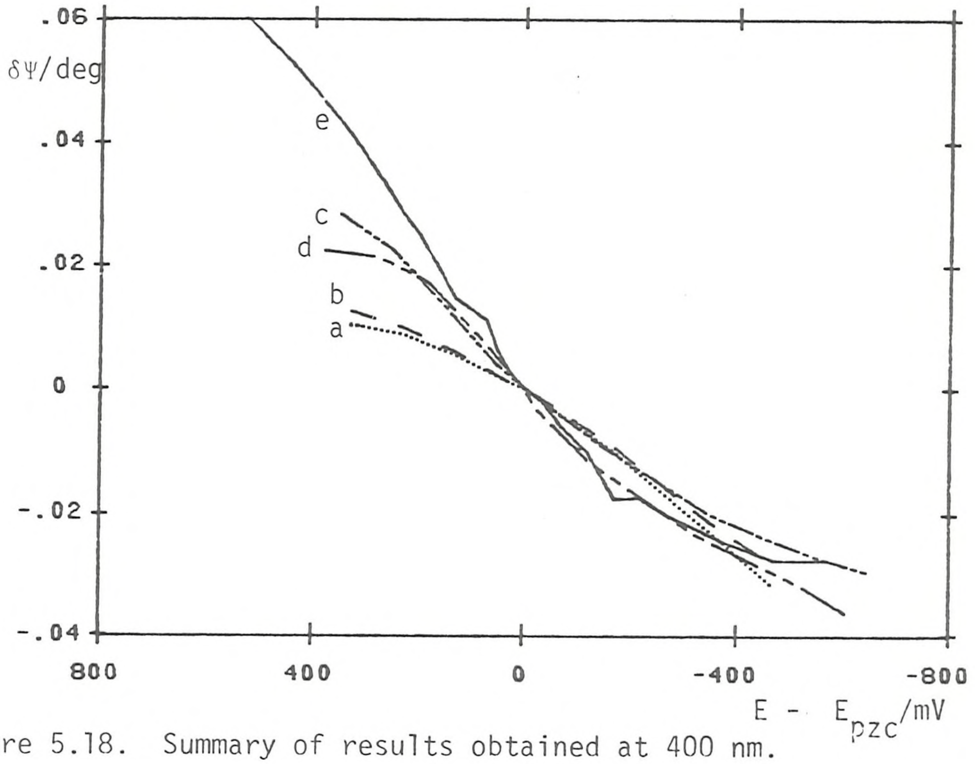

Figure 5.18. Summary of results obtained at 400 nm.

a, Sodium fluoride (0.01 M).

b, Sodium fluoride (0.1 M).

c, Potassium chloride (0.1 M).

d, Potassium chloride (0.25 M).

e, Sodium sulphate (0.5 M).

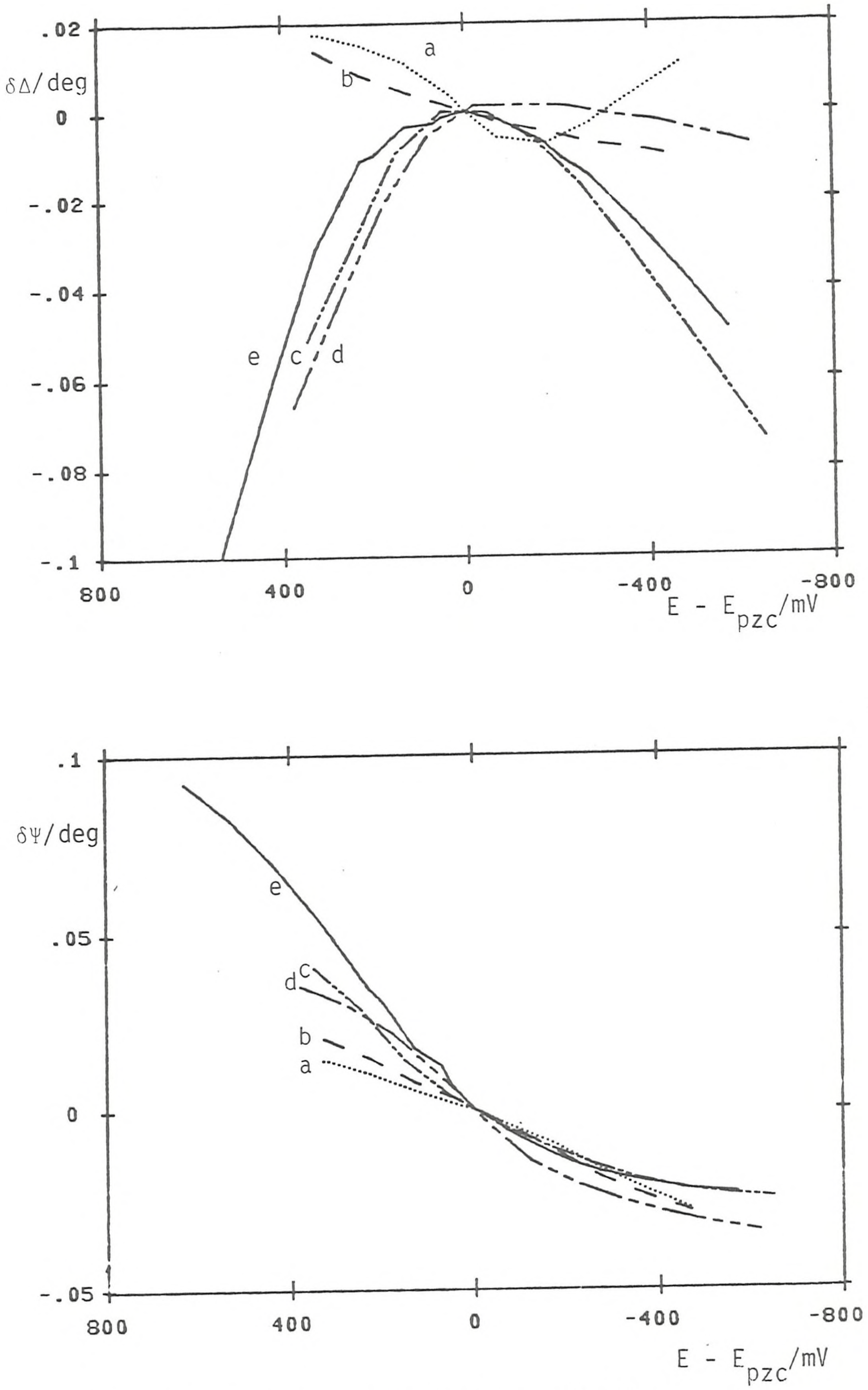

Figure 5.19. Summary of results obtained at 500 nm.

a, Sodium fluoride (0.01 M).

b, Sodium fluoride (0.1 M).

c, Potassium chloride (0.1 M).

d, Potassium chloride (0.25 M).

e, Sodium sulphate (0.5 M).

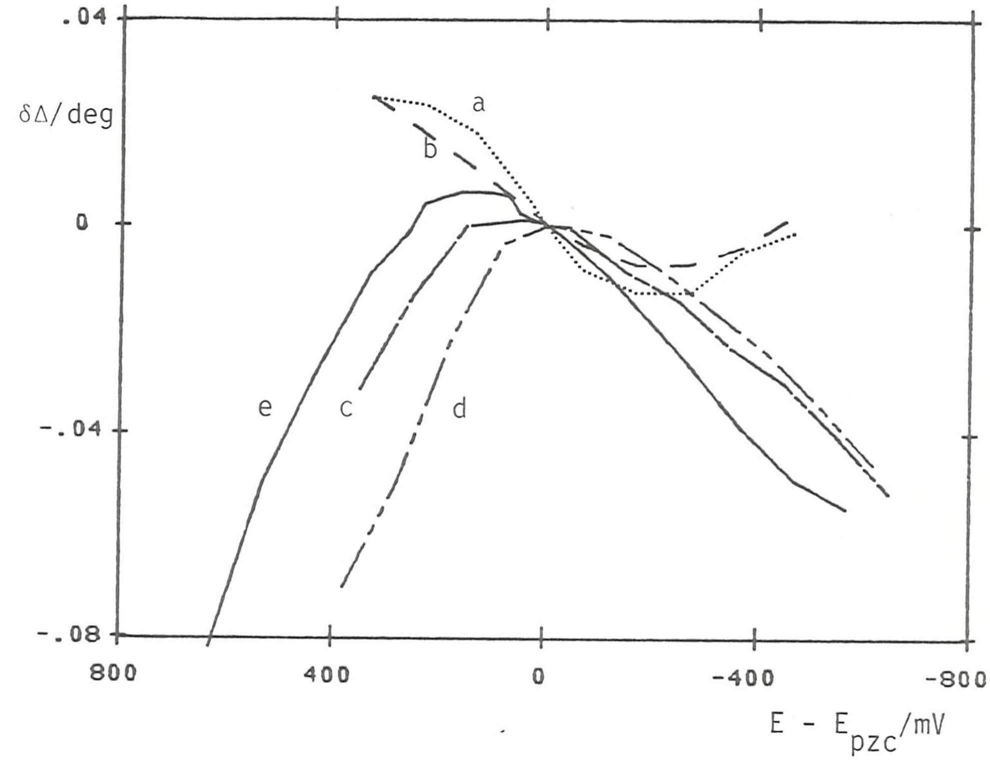

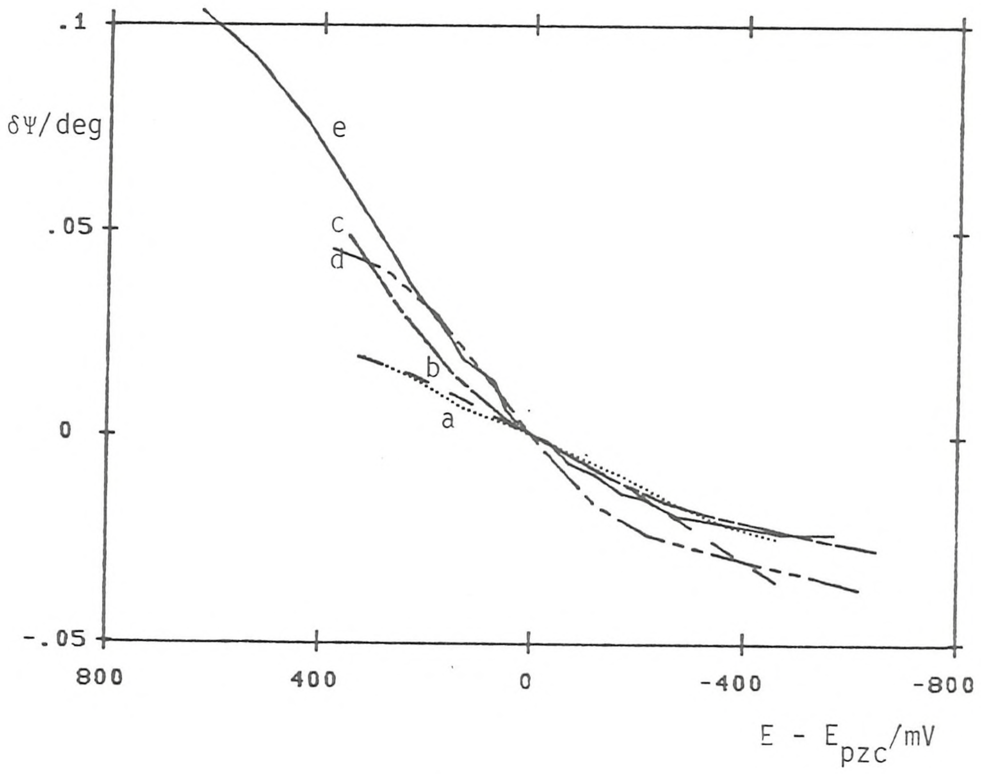

Figure 5.20. Summary of results obtained at 600 nm.
a, Sodium fluoride (0.01 M).
b, Sodium fluoride (0.1 M).
c, Potassium chloride (0.1 M).
d, Potassium chloride (0.25 M).
e, Sodium sulphate (0.5 M).

If the changes in the solution side of the double layer were to be considered solely responsible for the observed changes, then from the simulations, the film representing the double layer would need to be optically absorbing with a relatively constant extinction coefficient over the whole of the charge range studied of 0.4 or greater. However, the high absorbance index required to give a reasonable fit to the experimental data would suggest a high concentration of charge carriers in the adsorbed layer. Dignam et.al.[69] have shown that if data for a thin anisotropic film on a metal is analysed assuming the film to be optically isotropic, the values for the extinction coefficient similar to those for semiconductors are obtained. In view of the high field strength which exists across the double layer, it would seem reasonable to suppose that dipole orientation or induced dipoles in otherwise spherical ions would result and give rise to anisotropic optical properties.

Films with metal-like optical constants have also been found that give rise to optical effects similar to those observed experimentally. It is appropriate to treat films of this type as resulting from an electroreflectance effect. To simulate the overall decrease in Ψ as the charge on the metal decreases and the increase in Δ (on the anodic side of the pzc), requires that both n_2 and k_2 for the film decrease. However, such an empirical electroreflectance effect would predict an increase in Δ on the cathodic side of the pzc which would mean that the effects due to the solution side of the double layer are much larger than solution side effects at anodic potentials. This would be difficult to account for because the diminishing amounts of specifically adsorbed anions of high ionic refractivities would lead to a decrease in solution refractive index and hence, a further increase in Δ.

The four layer model - metal/selvedge/adsorbed layer/electrolyte - would undoubtably yield many solutions for the unknown quantities defining the intermediate layers that would quantitatively explain the experimental data recorded. It would not be possible to decide which of the solution, if any, is most applicable without much more additional information. Before any quantitative information concerning the solution side of the double layer can be extracted from optical data, the question of the electroreflectance effect must be addressed.

Of the various modes proposed for the electroreflectance effect[57,59] the free electron model[52] has had the most success in explaining semiquantitatively early experimental results on polycrystalline silver and gold[99,100] from modulated specular reflectance studies. However, using the same technique, Bewick and Robinson[19] reported significant differences between the model and their results for mercury in aqueous fluoride electrolytes. Similar differences have been reported by Hinnen et.al.[21] for several electrolytes on polycrystalline gold. Although the techniques of ellipsometry and specular reflectance differ, (the reflectance technique measures the change in reflectivity for a small sinusoidal perturbation of the electrode potential of linearly polarised light (p or s)), the same Fresnel equations are used to predict the changes observed for the proposed models of the interface.

From a rigorous analysis of the data presented in the literature for the dielectric function of mercury determined by both ellipsometry and reflectance techniques, Arakawa[51] has shown that the dielectric function of mercury is not described by the free electron gas model. This finding does not necessarily invalidate the use of the free electron electroreflectance models if field modulation of the bound electron contribution to the overall dielectric function of the substrate is small. The simple free electron gas model requires that an electron-gas electron which strikes the surface is reflected specularly. The presence of ions in the surface region will destroy the lateral homogeneity of the surface and introduce a scattering centre. Lazorenko-Manevich[101] has attempted to account for such scattering by assuming a potential dependent free electron relaxation time (mean time between collisions) and has demonstrated a semiquantitative agreement between this model (with the inclusion of a classical free electron electroreflectance effect and contributions from surface excess of ions) and experimental data obtained for polycrystalline gold in sulphuric acid.

Feibelman[77] has analysed the McIntyre-Aspnes model of the transition layer from a microscopic point of view. Briefly, the conclusions reached were that for s polarised light the classical model yielded a reasonable approximation to the microscopic theory, but for p polarised light, the use of a local surface dielectric function was in poor correspondence with the microscopic results. Similar microscopic analyses[78,79] have arrived at essentially the same results ie., it is not possible to assign a dielectric function to the transition layer but the layer must be described by an anisotropic dielectric tensor. These findings are more fully described in section 2.9. Kofman[80] has included into a microscopic analysis of the interface, a free electron electroreflectance effect and has found reasonable agreement between theory and experimental findings for gold single crystals in contact with sodium fluoride.

Since specifically adsorbed ions will destroy the homogeneity of the metal surface assumed in the free electron model, it would seem pertinent to study electrolytes containing anions which are not strongly adsorbed onto mercury. Electrolytes containing anions such as F^- and ClO_4^- are obvious candidates but other anions could be used provided that the study is restricted to cathodic potentials where specific adsorption is less likely to occur. Contributions from the inner and diffuse layers to the overall optical effect must also be considered. Lee and Bagchi[102] have suggested that for overlayers that do not interact strongly with the substrate, the adsorbed layer may be regarded as completely decoupled from the substrate but such layers must be treated as optically anisotropic if they are to be incorporated in to the microscopic description.

If it can be assumed that the Stedman approach gives a good approximation to the optical effects of the diffuse layer, then with sufficient data collected for many wavelengths and possibly using angle of incidence variation as an auxillary variable, it would in principle be possible to assess the validity of the non-local description of the selvedge and the incorporated free electron electroreflectance effect. Only after the electroreflectance effect is clearly accounted for could any quantitative data relating to specific adsorption be extracted from optical studies.

5.1.5. Conclusion.

The optical properties of a material is characterised by a complex refractive index or complex dielectric function, the real and imaginary parts of which are interrelated and not independently variable. Thus the absorption of light by a material over a particular wavelength range must invariably be linked to anomolous dispersion of refractive index. By observing the changes in Δ and Ψ as a function of electrode potential for a number of systems and over a wide range of wavelengths it was hoped that the dispersion behavior could be identified (either normal or anomolous) and therefore help in a quantitative analysis of the properties of adsorbed materials.

Although no quantitative conclusions were obtained from the ionic adsorption studies, several interesting qualitative observations can be made. The decrease in Δ with increasing anodic charge observed for the chloride and sulphate electrolytes is to be expected in view of the increasing surface excess of anions in the inner and diffuse layers. The changes in Δ predicted, on the basis of double layer capacitance studies and ionic refractivities (Stedman approach [54]) are in reasonably good agreement with the experimental values for wavelengths of incident light greater than 450 nm, but neither the wavelength dependance nor the magnitude of observed effects is satisfactorily accounted for at shorter wavelengths. There is little correspondence between the observed and predicted changes in Ψ. The theoretical changes in Δ and Ψ caused by changes in the free electron concentration in the transition layer model of McIntyre and Adpnes[52,53] (electroreflectance) appears inappropriate for the mercury aqueous electrolyte interface. An almost wavelength independent linear variation of Δ with charge on the metal is predicted which if viewed in conjunction whith the solution side predictions would yield a good agreement with the data recorded on the anodic side of the pzc but only for short wavelengths. Essentially no change in Ψ is predicted by the free electron model so that the changes in Ψ are not in any way explained by these two models. The complex behavior observed, progresively larger changes in Δ and smaller changes in Ψ with decreasing wavelength on the anodic side of the pzc, and larger changes in Δ with increasing wavelength and essentially no wavelength variation in Ψ on the cathodic side has proved impossible to account for by any change in film refractive index. Approximate solutions were found to account for the data obtained on the anodic side of the pzc but a quite different set of solutions was required to predict the changes observed at cathodic potentials. No smoothly varying isotropic optical properties appear to exist, either transparent or absorbing, that would account for the results obtained.

Specifically adsorbed anions and the water in the inner layer would probably be better described in terms of anisotropic optical properties. There are several reasons why no attempt was made to explore the possibility of anisotropic solutions. The apparent failure of the free electron electroreflectance effect, the uncertainty of a suitable starting point (i.e. film constants) insufficient data and time all conspired against such an analysis.

The fluoride data obtained in this investigation was shown to include effects attributed to a charge transfer process and significant reduction currents were observed in all other electrolytes employed. Clearly a re-designed cell is required, preferably with some easy method of renewing the mercury surface and electrolyte, before an in depth study of ionic adsorption is attempted. By using ions which are not specifically adsorbed to any extent and by an extensive study of not only the wavelength dependence on changes in Δ and Ψ but also the concentration dependence, it may be possible to draw some general conclusions concerning the processes responsible for the changes in ellipsometric parameters. It may then be possible to build, on broad generalisations, a more accurate description of the interface.

It is perhaps pertinent at this point to stress again the work of Kliewer[76], Feibelman[77] and others[78,79] and their theoretical treatments of the interaction of light with metal surfaces. It is clear, in their conclusions if not in the complexity of their arguments, that the macroscopic treatment of the interaction of radiation with metal sufaces, which embodies the local field approximation, does not describe accurately the fields that are set up within a metal when electromagnetic radiation is incident on the surface, particularly when the external field is polarised perpendicularly to the surface. The rigorous analysis, provided by Feibelman, is not in a form that can be incorporated into an analysis of experimental data but the simpler, so called, specular reflection model described by Kliewer has been used by Kofman[80] in his analysis of modulated specular reflectance data (Au single crystals-aqueous fluoride interface). Since no comparison between classical and microscopic treatments of experimental data appears to have been attempted, it is difficult to say at this stage whether the non-local approach will lead to a better understanding of the electrified interface.

5.2. The adsorption of isoquinoline on mercury.

The adsorption of isoquinoline (0.3 mM and 10 mM) from a supporting electrolyte of sodium sulphate (0.5 M) and sodium hydroxide (0.04 M) onto mercury has been studied as a function of electrode potential for several wavelengths in the range 350 to 632.8 nm. The supporting electrolyte was prepared from analytical grade materials (B.D.H., Analar) and reagent grade isoquinoline was used without further purification. A stock solution of the base electrolyte containing a known concentration of isoquinoline was prepared by dissolving an accurately weighed sample of isoquinoline, using a weight pipette, in the electrolyte. All solutions were purged with nitrogen for about 30 minutes prior to introduction into the cell and for a few minutes at regular intervals throughout the course of the experiment. In order to minimise the time required for data acquisition, and hence minimise contamination of the electrode surface, only single zone measurements were performed at each wavelength. The results are presented in terms of relative changes in Δ and Ψ not only to enable data obtained at different wavelengths to be compared but also because of uncertainty in the absolute values determined due to imperfections in the optical components of the ellipsometer. Initial measurements were made for mercury in contact with the adsorbate-free supporting electrolyte in a manner previously described (see section 5.1) and the observed changes in Δ and Ψ with potential were quantitatively similar to those obtained for sodium sulphate (0.5 M) reported in section 5.1.3.

The values of Δ and Ψ in any electrochemical experiment result from a combination of effects and in attempting to gain information on the adsorption process, for example, it is desirable to account for and subtract out the other contributing factors to the overall effect. Adsorption may be quantified by measuring a parameter in the presence and absence of adsorption and subtracting the 'adsorption' curve from the 'base' curve. However, in ellipsometry the measurements made for the adsorbate free solution are the result of optical effects not necessarily the same in the presence of an adsorbed layer. Fortunately in studies of organic adsorption on metals, the changes in Δ and Ψ due to adsorption are generally much larger than other effects and in addition, potential regions are often accesible where the adsorbate is desorbed providing a useful internal reference state. To facilitate at least a qualitative comparison of the adsorption phenomena with the supporting elecrolyte 'base' data, the ellipsometric data for the 0.3 mM isoquinoline solution were obtained immediately after the base data by adding a measured volume of isoquinoline solution, of known concentration, to the known volume of electrolyte already in the cell. The data obtained from the base and adsorption experiments at wavelengths of 350, 500 and 632.8 nm are shown in Fig 5.21. The shapes of the Δ and Ψ adsorption curves for all wavelengths employed were similar although the relative positions on the ordinate axis of base and adsorption curves were somewhat variable. This variation may be due to contamination of the mercury surface or accidental mispositioning of the of the surface during the purging of the electrolyte with nitrogen.

The changes in Δ and Ψ observed at potentials more cathodic than -1300 mV in both base and adsorption experiments were similar, suggesting that the isoquinoline was completely desorbed at about -1300 mV. The reference state, required to enable a comparison of data obtained at different wavelengths, was chosen as the values of Δ and Ψ measured at -1300 mV. The relative changes, $\delta\Delta$ and $\delta\Psi$, obtained for the 0.3 mM isoqinoline solution are given in Figs 5.22 and 5.23. The data obtained in the anodic sweep direction, showing hysteresis of about 100 mV in the re-adsorption of isoq$\underset{\wedge}{\overset{u}{}}$inoline has been omitted for clarity of

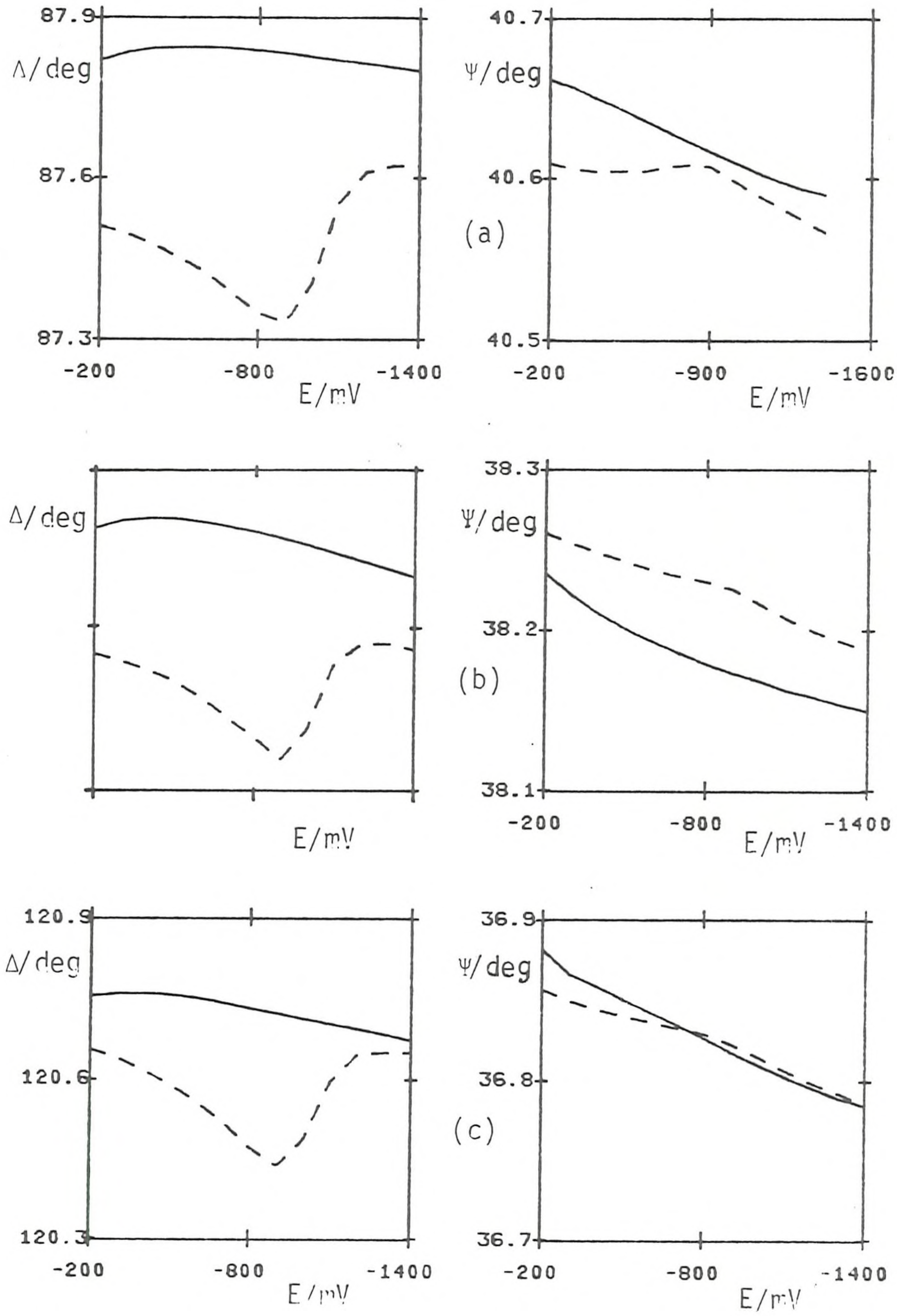

Figure 5.21. Δ and ψ as a function of electrode potential (vs. SCE) for base electrolyte (0.5 M Na_2SO_4 + 0.04 M NaOH), continuous curve; and for 0.3 mM isoquinoline in base, dashed curve. (a) 350 nm, (b) 500 nm, (c) 632.8 nm

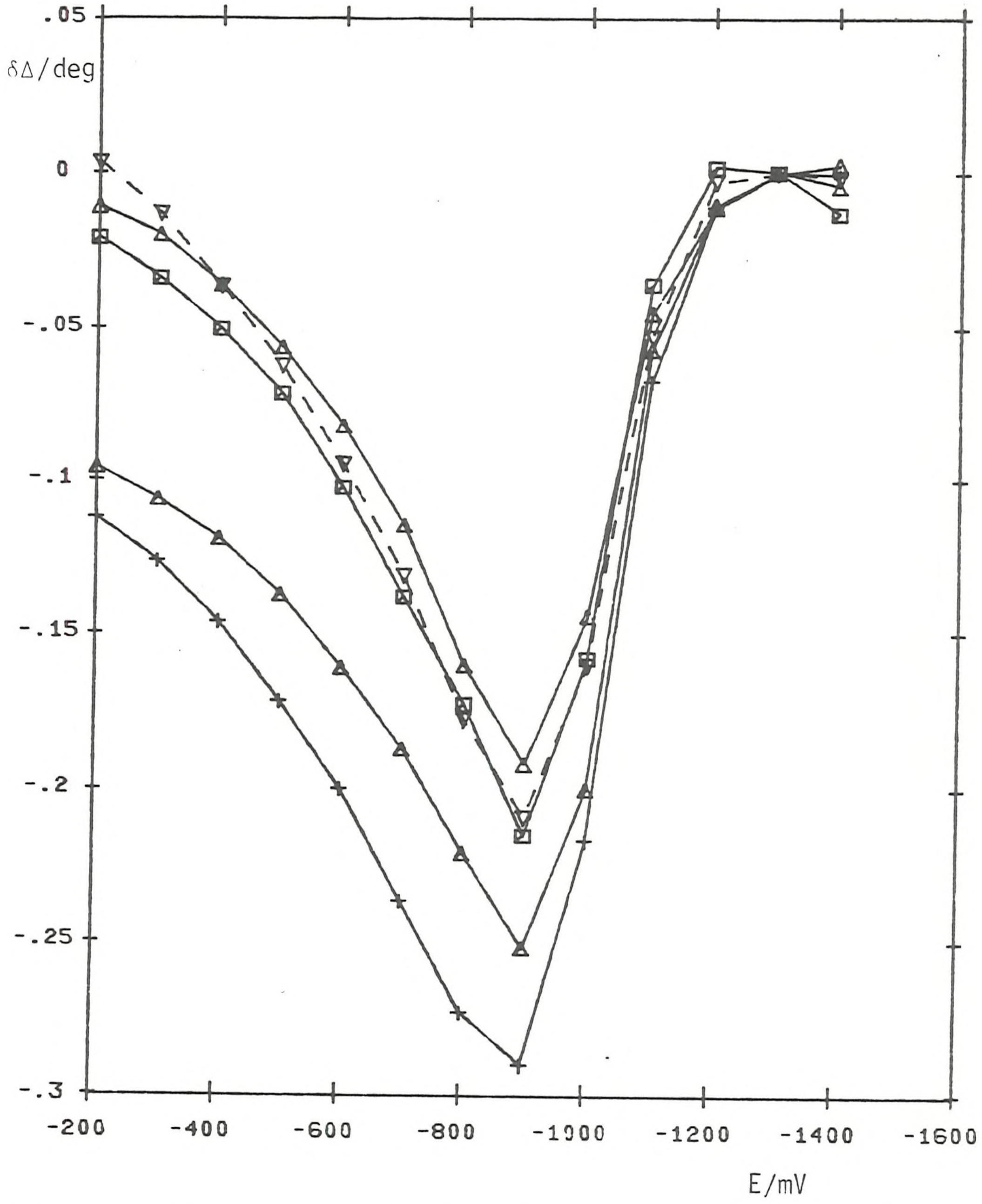

Figure 5.22. Adsorption of isoquinoline at the mercury-aqueous electrolyte interface: δΔ as a function of electrode potential (vs. SCE) for 0.3 mM isoquinoline in Na_2SO_4 (0.5 M) and NaOH (0.04 M).
+, 350 nm; Δ, 400 nm; □, 500 nm; *, 600 nm; ▽, 632.8 nm

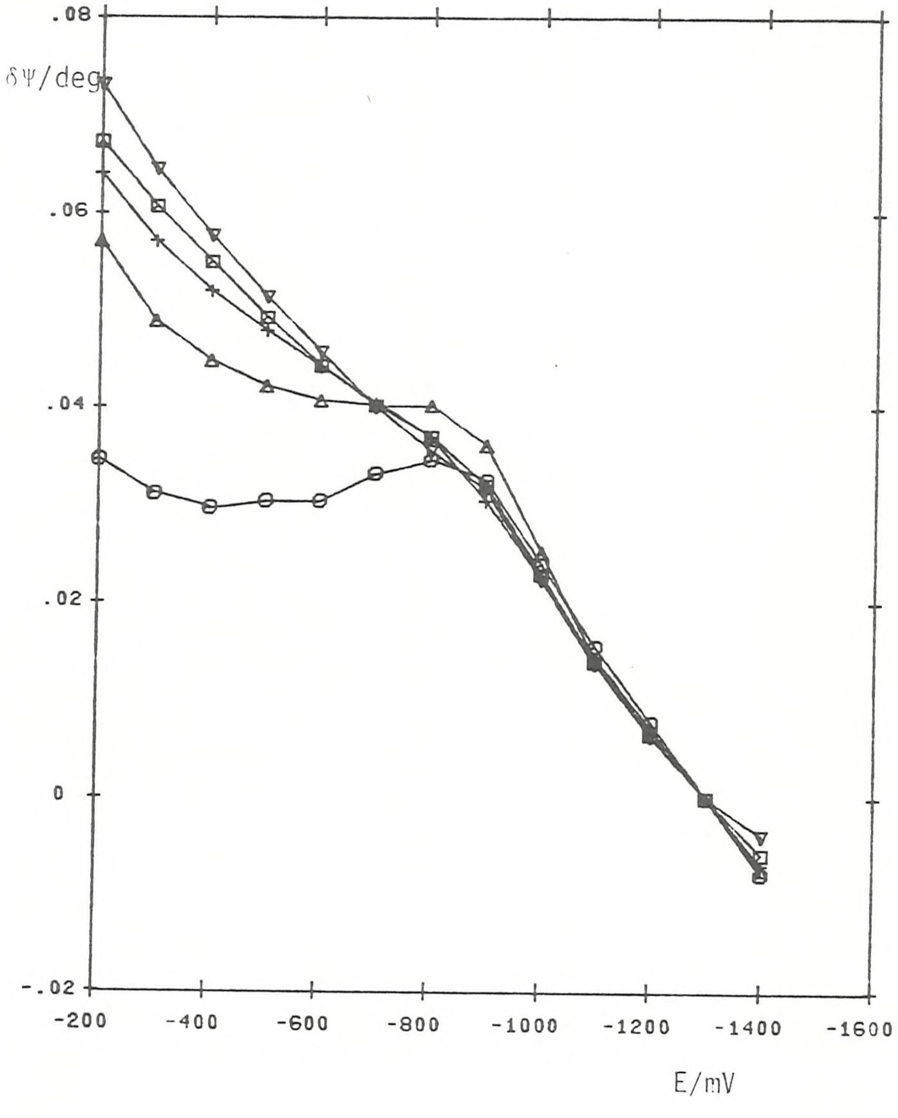

Figure 5.23. Adsorption of isoquinoline at the mercury-aqueous electrolyte interface; δΨ as a function of electrode potential (vs. SCE).

○ , 350 nm; ∆, 400 nm; +, 500 nm; □, 600; ▽ 632.8 nm presentation but will be discussed later.

The changes in Δ and Ψ as a function of the mercury electrode potential for isoquinoline (10 mM) in the same supporting electrolyte are shown in Figs. 5.24 and 5.25. In the absence of a suitable film free reference state an arbitrary reference, corresponding to the data obtained at the anodic limit of -400 mV, has been used. Again, some hysteresis, about 60 mV, was observed in the region of rapid changes of Δ and Ψ with potential (-750 to -850 mV) between data collected in cathodic and anodic sweep directions. The potential range was restricted at the negative end by Faradaic processes involving the isoquinoline. In view of the significant differences between the behavior observed for the two adsorbate concentrations studied each will be discussed separately.

Apart from the hysteresis mentioned above, the data collected for both isoqinoline concentrations was reversible with potential. The hysteresis was probably the result of several contributing factors. Slow mass transfer, reported by Buess-Herman et al[103] to interfere with the reliability of electrocapillary measurements made for isoquinoline concentrations below 1.5 mM, was probably compounded by the much larger electrode surface area used in the present investigation. Accurate potential control over the whole of the electrode surface was not possible because of the compromise in cell design required to enable both optical and electrochemical studies to be performed. The current distribution was certainly not uniform and the equipotential surface, therefore, would not be parallel to the electrode surface, particularly at the edges of the mercury pool. Changes in surface excess in a region of well defined electrode potential, following a potential excursion, may well have been offset by surface diffusion to or from regions of less well defined potential.

The adsorption of isoquinoline has been examined in sodium hydroxide by Silva[104] and in sodium sulphate by Buess-Herman et al.[103] using capacity measurements at the dropping mercury electrode. Adsorption from sodium hydroxide solution has also been studied by Humphreys and Parsons[22] using ellipsometric measurements at a mercury pool electrode and light of 546.1 nm wavelength. The conclusion drawn from the above investigations is that isoquinoline adsorbs in three orientations depending on electrode potential and concentration of the adsorbate in solution. In dilute solutions, less than 1.5 mM, the molecules are adsorbed with the plane of the rings parallel to the electrode surface. For more concentrated solutions and as the potential is made more cathodic the molecule takes up an upright position and at

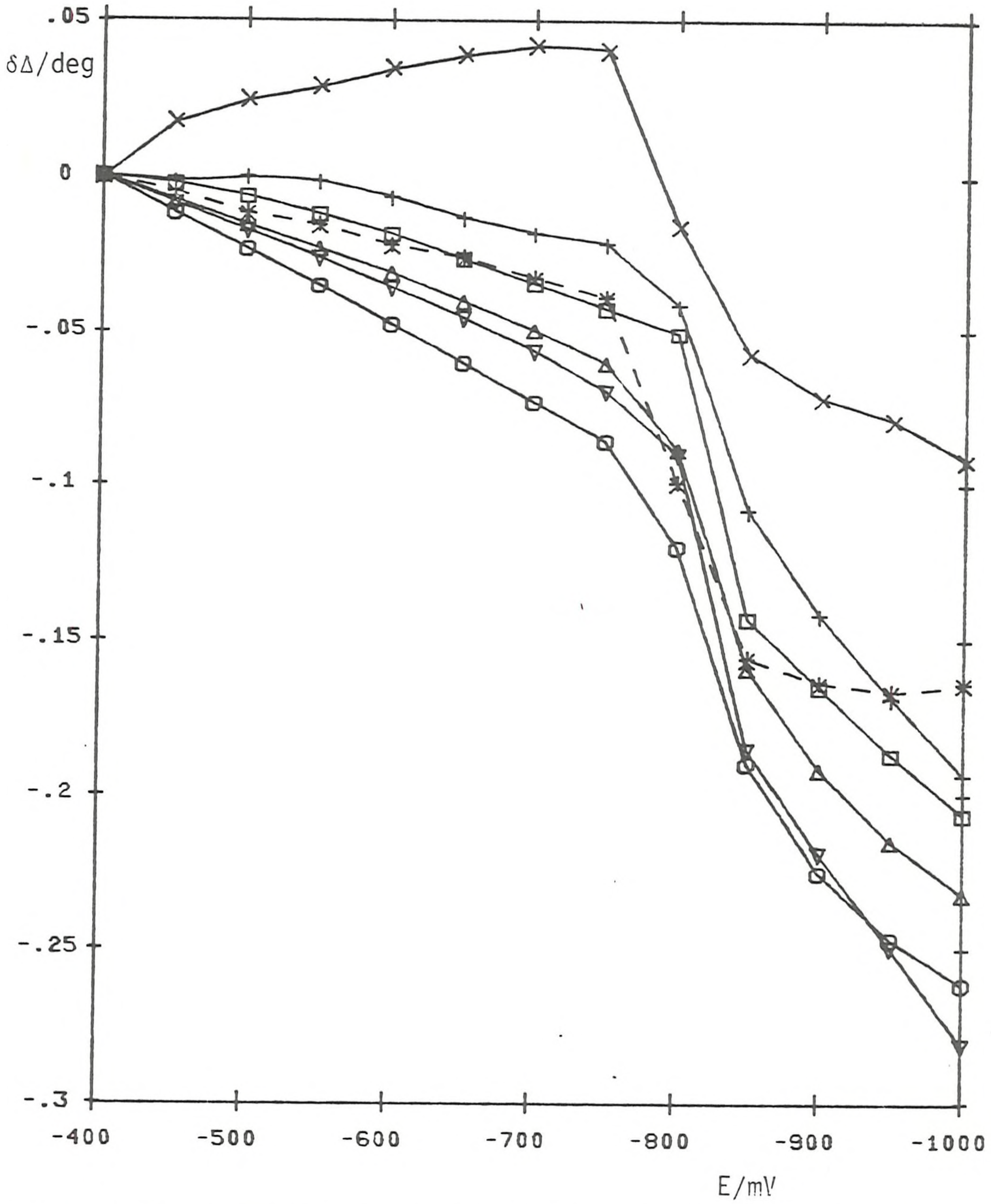

Figure 5.24. Adsorption of isoquinoline at the mercury-aqueous electrolyte interface: δΔ as a function of electrode potential (vs. SCE) for 10 mM isoquinoline in Na_2SO_4 (0.5 M) and NaOH (0.04 M)
x, 350 nm; +, 400 nm; □, 450 nm; Δ 500 nm; *, 550 nm; ∇, 600 nm; ○, 632.8 nm.

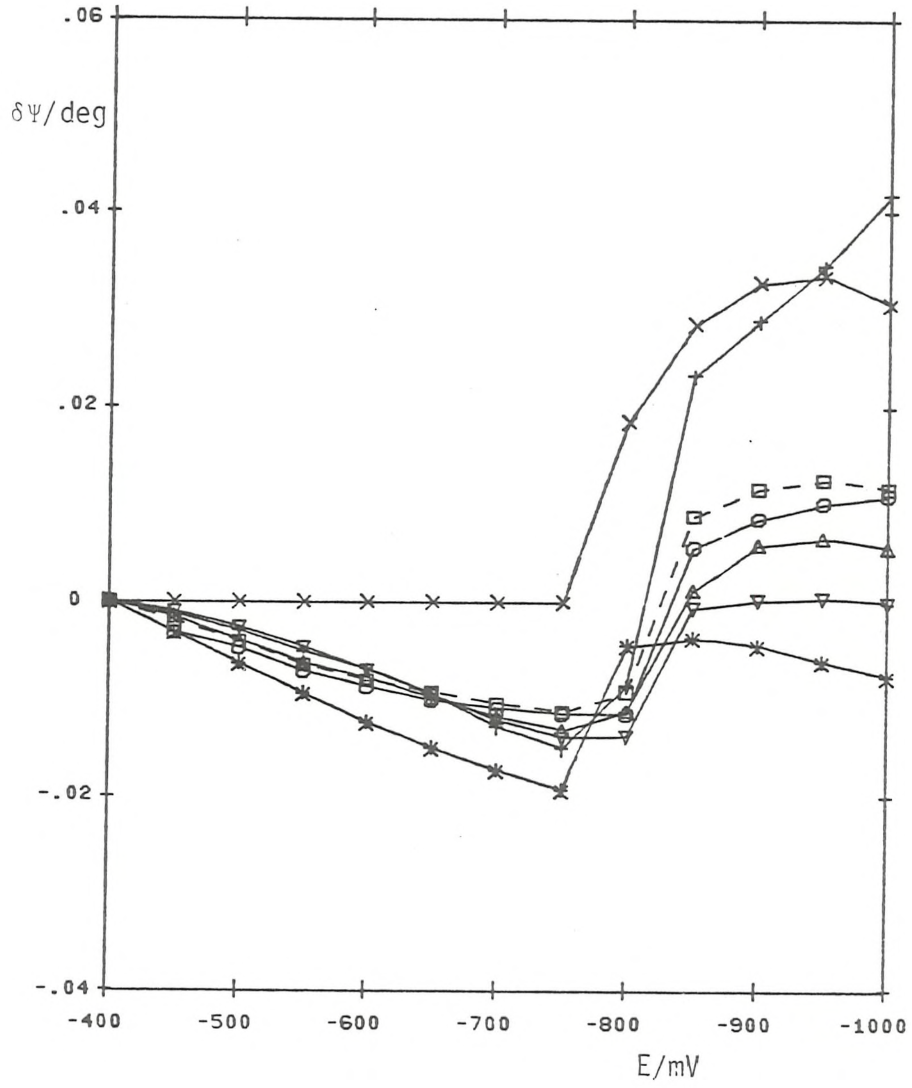

Figure 5.25. Adsorption of isoquinoline at the mercury-aqueous electrolyte interface: δΨ as a function of electrode potential (vs. SCE) for 10 mM isoquinoline in Na SO (0.5 M) and NaOH (0.04 M).

x, 350 nm; +, 400 nm; □, 450 nm; Δ, 500 nm;

*, 550 nm; ∇, 600 nm; O, 632.8 nm.

sufficiently negative potentials a sudden re-orientation is observed. From an analysis of the data presented in this investigation, the conclusions of the previous investigations and in particular the optical models proposed by Humphreys and Parsons are supported.

Some physical properties and molecular orientations of isoquinoline are given in Table 5.1

5.2.1. Adsorption from 0.3 mM isoquinoline solutions.

For an adsorbate of refractive index greater than that of the surrounding medium decreasing values of Δ and increasing values of Ψ are expected with increases in the amount of material adsorbed. The pronounced minimum in $\delta\Delta$ and the change in slope of $\delta\Psi$ at about -900 mV suggests that the surface concentration of isoquinoline is at a maximum at this potential. For a transparent isotropic film, in the absence of complicating factors such as electroreflectance effects, the changes in Ψ would be expected to be about an order of magnitude less than the corresponding changes in Δ and of opposite sign (see for example Fig 5.10 in section 5.1.2). The changes in $\delta\Psi$ (Fig. 5.23) are strongly influenced by effects other than simple changes in refractive index of the inner layer due to adsorption since changes in Ψ are similar for electrolyte solutions with and without the isoquinoline present particularly at longer wavelengths. The slopes of the $\delta\Psi$ curves for potentials more anodic than -900 mV are more markedly altered by the presence of the adsorbate, particularly at shorter wavelengths. This effect may be linked to a stronger π electron interaction between isoquinoline and the substrate, if the molecule is lying flat, at the more anodic potentials but it is a matter of conjecture whether an interaction of this type would modify the optical properties of the adsorbate or the substrate. The wavelength dispersion of these curves and the magnitude of the changes are reminiscent of the changes observed in the study of ionic adsorption (see Figs. 5.4, 5.5 and 5.16). Since diffuse layer contributions to the values of Ψ are expected to be small, inner layer or electroreflectance contributions to the optical effects common to both ionic and organic adsorption must be responsible for the similarity in the Ψ data. The chemical nature of the adsorbed species and hence the refractive index of the inner layer are substantially different for the two classes of adsorbate so electronic effects may be the common factor responsible for the overall similarity.

From capacity measurements of the adsorption of isoquinoline at a dropping mercury electrode Buess-Herman _et_ _al_.[103] have obtained surface

Table 5.1

Some physical properties and orientations of isoquinoline.

		Reference
Dipole moment/D	2.2	103
Solubility in Na_2SO_4 (0.5 M)/M	3.1×10^{-2}	103
Bulk refractive index, 434.1 nm	1.6648	105
486.2 nm	1.6443	105
589.3 nm	1.6223	105
656.3 nm	1.6141	105

			Dipole moment/D	
Orientation	Carbons on surface	Thickness/nm	Perpendicular to surface	Parallel to surface
	All	0.3	-	-
	4,5	0.7	0.88	2.44
	5,6	0.73	1.99	1.67
	7,8	8.7	2.44	0.88

excesses with the aid of the Gibbs equation which closely parallel the changes in Δ observed here for similar adsorbate concentrations. They have concluded that for dilute solutions of isoquinoline the molecules are adsorbed with the plane of the rings parallel to the mercury surface and that the maximum surface excess of molecules in this orientation is reached at potentials close to the minimum in $\delta\Delta$ obesrved in this investigation.

By adjusting the base and adsorbtion curves for $\delta\Psi$ to equal zero at -1300 mV it has been possible to obtain rough estimates of effect of adsorption on the changes in $\delta\Psi$ by subtracting the base from the adsorption curve. The subtracted curves, shown in Fig 5.26, show a maximum at the same potential as the minimum found in the $\delta\Delta$ curves. By assuming that the adsorbed layer has bulk optical properties predicted changes in Δ and Ψ have been calculated as a function of film thickness. The refractive index of the bulk isoquinoline, at the required wavelength, was calculated from the Cauchy dispersion formula (Eq. 2.143) with required constants calculated from refractive index data given in Table 5.1. The film thicknesses that gave the observed changes in Δ are given in Table 5.2. The predicted changes in Ψ are about a factor of 2 larger than the adjusted values shown in Fig 5.26. but the film thicknesses calculated to give the changes in Δ observed are close to the value expected for isoqinoline adsorbed flat on the electrode.

Barrett-Gultepe[16] has found that an adsorbed layer of benzene at the platinum electrolyte interface, where the molecules are oriented with the plane of the ring parallel to the electrode surface, can be interpreted in terms of an anisotropic film with $n_s > n_p$. However, because of the strong influence of double layer effects on the values of ψ it has not been possible to obtain more than a very rough estimate of the effects of adsorption on the measured values of Ψ and hence it was not possible to examine an anisotropic film as a model for the data obtained here. From the rather limited analysis presented it appears that the properties of the adsorbed isoquinoline, from dilute solutions, are not substantially altered, apart from probable orientation, from bulk properties.

5.2.2. Adsorption from 10 mM isoqinoline solutions.

At sufficiently large cathodic potentials and isoquinoline concentrations an abrupt change in capacity or ellipsometric parameters was observed in the previously mentioned investigations. These observations have been linked to a sudden re-orientation of close

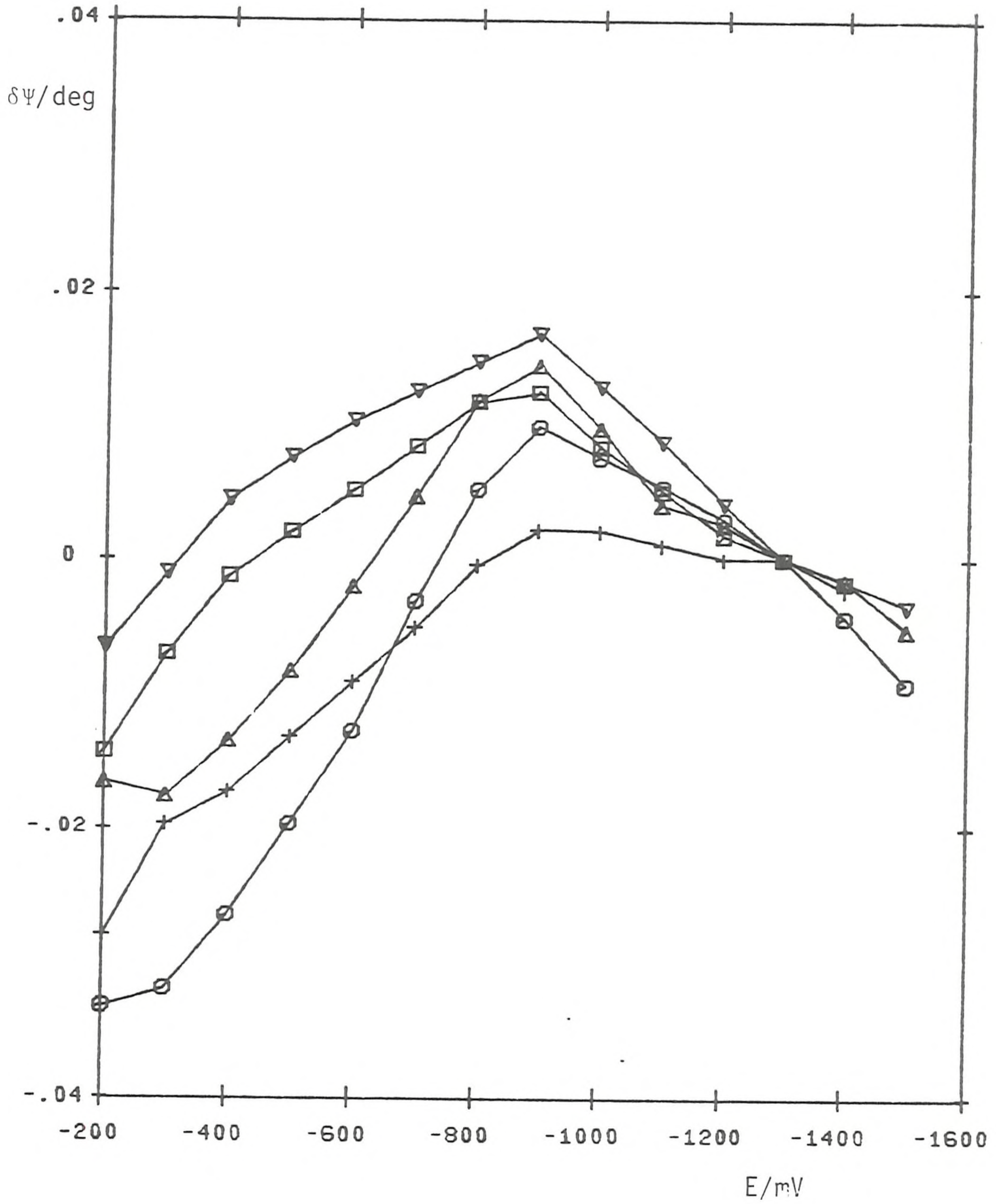

Figure 5.26. Adsorption of isoquinoline at the mercury-aqueous electrolyte interface: Curves produced by subtraction of the base from the adsorption curves after adjustment of curves for coincidence at - 1300 mV. δψ as a function of electrode potential (vs. SCE) for 0.3 mM isoquinoline in 0.5 M Na_2SO_4 and 0.4 M NaOH.

○, 350 nm; Δ, 400 nm; ▢, 500 nm; ▽, 600 nm; +, 632.8 nm.

Table 5.2

Film thickness calculations assuming bulk refractive index of isoquinoline. Computed values of film thickness giving rise to the observed changes in Δ for the 0.3 mM isoquinoline solution

λ/nm	Assumed index	$\delta\Delta_{obs}$	$\delta\Psi_{obs}$	Film thickness/nm	Error in Ψ $\Psi_{obs} - \Psi_{cal}$
350	1.708	-0.291	0.001	0.26	-0.034
400	1.677	-0.252	0.014	0.23	-0.015
500	1.641	-0.215	0.012	0.21	-0.011
600	1.621	-0.192	0.017	0.21	-0.002
632.8	1.616	-0.209	0.002	0.23	-0.018

Table 5.3

Film thickness calculations assuming bulk refractive index of isoquinoline. Computed values of film thickness giving rise to the observed changes in Δ for the 10 mM isoquinoline solution

λ/nm	Assumed index	$\delta\Delta_{obs}$	$\delta\Psi_{obs}$	Film thickness/nm	Error in Ψ $\Psi_{obs} - \Psi_{cal}$
350	1.708	-0.108	0.019	0.1	0.005
400	1.667	-0.088	0.035	0.08	0.025
450	1.656	-0.086	0.020	0.08	0.010
500	1.641	-0.102	0.019	0.1	0.008
550	1.629	-0.118	0.018	0.12	0.006
600	1.621	-0.100	0.014	0.11	0.004
632.8	1.616	-0.104	0.018	0.12	0.008

packed mono-molecular layers of isoquinoline from an orientation with carbon atoms 4 and 5 in contact with the mercury surface to an orientation with carbons 6 and 7 adjacent to the mercury. From the molecular dimensions given in Table 5.1 such a re-orientation would be accompanied by an increase in film thickness of 0.17 nm. The abrupt changes in Δ and at potentials centred on -850 mV shown in Figs. 5.24 and 5.25 are typical of the changes expected for an increase in film thickness and/or increase in refractive index of a transparent film. By assuming that the observed changes in this transition region result, simply, from an increase in film thickness, and further assuming that the adsorbed layer has bulk optical properties then the change in film thickness required to give rise to the changes in $\delta\Delta$ are easily calculated. The program used simply calculated Δ and Ψ as a function of film thickness from the optical constants describing the substrate, film and electrolyte using the Drude equation. Table 5.3 reports the outcome of these calculations for film thicknesses that gave rise to the observed change in Δ and the difference between observed and calculated changes in Ψ. Although the film thickness required to give rise to the observed changes in λ are close to the value expected for re-orientation they are consistently smaller. Also, the predicted changes in $\delta\Psi$ are consistently larger than those observed experimentally which suggests, in agreement with Humphreys and Parsons[22], that a model assuming isotropic adsorbate properties is not completely satisfactory. A more appropriate model, suggested by the above authors, was to treat the adsorbed layer in terms of anisotropic optical properties, and in analysing their data on this basis they obtained optical properties of the adsorbed layer which were consistent with the proposed orientation changes.

In the most general case of anisotropy there a three refractive indices, n_x, n_y, and n_z associated with the three directions in the Cartesian frame. In a bulk liquid the molecules are randomly oriented so that

$$n_b = (n_x + n_y + n_z)/3$$

For an adsorbed molecule the situation may be simplified if free rotation about the axis normal to the electrode surface is allowed, in which case

$$n_b = (n_p + 2n_s)/3$$

where $n_p = n_z$ and $n_s = n_x = n_y$

A program was written that generates tables of $\delta\Delta$ and $\delta\Psi$ for a range of values of n_s and n_p describing a final state from given values of n_s, n_p and film thickness of an initial state. From the dipole orientation of isoquinoline in the [4,5] orientation (Table 5.1) it could be expected that n_s would be larger than n_p and for the [6,7] orientation the reverse might be expected ($n_p > n_s$). The initial values chosen to describe the adsorbed layer at potentials anodic of the transition were such that

$$n_b(\lambda) = (n_p + 2n_s)/3$$

where $n_b(\lambda)$ was taken as the bulk isoquinoline refractive index and that n_s should be greater than n_p, a film thickness of 0.7 nm was assumed. The final film thickness was assumed to be 0.87 nm and tables of $\delta\Delta$ and $\delta\Psi$ covering a wide range of n_p and n_s were generated for each wavelength studied. The parameters found describing the initial and final properties of the adsorbed layer that gave rise to the changes in Δ and Ψ observed experimentally (to within ± 0.005^o) are given in Table 5.4. Although the values of n_s and n_p computed for a wavelength of 550 nm differ from the values obtained by Humphreys and Parsons (at 546.1 nm) the form of the solutions are identical i.e the values of (n_p - n_s) for the [4,5] orientation were smaller than the values for the [6,7] orientation and both were negative. In the absence of absolute values of Δ and Ψ it has not been possible to assign unique values of n_s and n_p to the adsorbed film. Further computations have indicated that a range of values of n_s and n_p give rise to very similar changes in Δ and Ψ provided that the values of (n_p - n_s) for both orientations remain the same as those mentioned above. The solutions found show an overall increase in n_p with decreasing wavelength, i.e. normal dispersion behavior, although almost constant values of n_s were found.

Apart from the quite different behavior observed at 350 nm, changes in $\delta\Delta$ and $\delta\Psi$ at potentials anodic of the transition region are both negative and decrease almost linearly with increasing cathodic potential. Qualitatively the effect observed at wavelengths greater than 350 nm could be accounted for by an isotropic film with increasing extinction coefficient as the potential is made more cathodic (see Fig. 5.13 in section 5.2). The solution for the data obtained at 350 nm would however, be quite different, requiring a significant decrease in refractive index and almost constant extinction coefficient (see Fig. 5.11). However, by assuming an anisotropic model with adsorbate properties at a potential immediately anodic of the transition ([4,5] orientation) defined by the values used in the previous computations a set of solutions has been found that accounts for the changes observed

Table 5.4

Anisotropic film calculations for oriented monolayers of isoquinoline. Computed values of n_p and n_s for the transition region (-750 to -850 mV) for the 10 mM isoquinoline solution

λ/nm	Assumed properties prior to transition Thickness 0.7 nm		Computed properties after transition Thickness 0.87 nm		Equivalent bulk refractive index $n_b=(n_p+2n_s)/3$
	n_p	n_s	n_p	n_s	
350	1.6	1.8	1.59	1.70-1.75	1.68
400	1.55	1.75	1.52	1.50-1.52	1.51
450	1.53	1.73	1.51	1.58-1.60	1.56
500	1.51	1.71	1.50	1.59-1.69	1.59
550	1.50	1.70	1.49	1.56	1.54
600	1.49	1.69	1.48	1.57-1.58	1.54
632.8	1.48	1.68	1.47	1.54-1.55	1.52

Table 5.5

Anisotropic film calculations for oriented monolayers of isoquinoline. Computed values of n_p and n_s for potentials anodic of the transition region for the 10 mM isoquinoline solution

λ/nm	Assumed properties prior to transition Thickness 0.7 nm		Computed properties at anodic limmit Thickness 0.7 nm		Equivalent bulk refractive index $n_b=(n_p+2n_s)/3$
	n_p	n_s	n_p	n_s	
350	1.6	1.8	1.60	1.80	1.74
400	1.55	1.75	1.52	1.53	1.53
450	1.53	1.73	1.49-1.50	1.52-1.63	1.51-1.59
500	1.51	1.71	1.44-1.45	1.43-1.50	1.43-1.48
550	1.50	1.70	1.45	1.46	1.46
600	1.49	1.69	1.42	1.41-1.42	1.42
632.8	1.48	1.68	1.40	1.36-1.38	1.37

for potentials anodic of the transition. A constant film thickness of 0.7 nm was assumed. The computed values of n_s and n_p, summarised in Table 5.5 are the values found to give the same change in Δ and Ψ as the changes observed experimentally between potentials of -400 and -750 mV. The computed values for wavelengths greater than 350 nm of n_p and n_s at each wavelength are very similar and show normal dispersion behavior. These computations suggest that the adsorbed layer at potentials close to -400 mV is isotropic ($n_p \simeq n_s$) and that with increasing cathodic potentials more material is adsorbed and the adsorbate undergoes a slow orientation resulting in a small increase in n_p and a larger increase in n_s. A mixture of flat and upright orientations would account for the isotropic properties of the film found from the above computations.

5.2.3. Conclusions.

Under conditions where close packed, oriented mono-molecular layers are formed, the changes in Δ and Ψ appear to be dominated by the optical properties or the inner layer. Under conditions where the isoquinoline adsorbs with the rings parallel to the mercury surface (0.3 mM solution) it appears that saturation coverages are observed only over a narrow range of potential. The changes in Ψ with electrode potential are, for the dilute solutions, strongly influenced by effects other than the refractive index of the inner layer. The changes in Δ however, appear to be dominated by the changes in refractive index accompanying adsorption. The data was analysed, assuming that the film was characterised by bulk, isotropic refractive indices, and yielded a film thickness for the adsorbed isoquinoline close to that expected for the proposed co-planar orientation.

Except for the data obtained at 350 nm (where the isoquinoline became optically absorbing) all of the data obtained for the adsorption of isoquinoline (10 mM) were successfully analysed and gave properties of the layer that were uniaxially anisotropic, transparent and with a normal dispersion behavior connecting the solutions obtained at the various wavelengths of incident light employed. At the cathodic limit of the potential range employed, the inner layer optical properties were found to be isotropic, indicating a disordered layer which became progressively more oriented with increasing cathodic potential. Inner layer optical properties consistent with a rapid reorientation of the adsorbed isoquinoline were found at higher cathodic potentials.

5.3. Spectroscopic ellipsometry.

5.3.1. Spectroscopic ellipsometry of rhodamine B adsorbed on mercury.

The adsorption of rhodamine B (2.3×10^{-6}M) from a supporting electrolyte of sodium sulphate (0.5 M) and sulphuric acid (0.05 M) onto mercury, under potentiostatic conditions, has been studied by single zone measurements of Δ and Ψ for wavelengths in the range 300 to 650 nm at 5 nm intervals. The method adopted was to first determine Δ and Ψ for the base electrolyte at -400 mV (close to the pzc for 0.5 M Na_2SO_4) at each wavelength, then a measured volume of a solution containing rhodamine B dissolved in the base electrolyte was added to the cell and the ellipsometric parameters were re-determined. The Δ and Ψ spectra were recorded at several electrode potentials in the range +240 to -800 mV. Some of the data collected in the wavelength range 450 to 650nm, covering the main absorance band of rhodamine B in solution, is shown in Fig. 5.27 along with the data recorded for mercury in the supporting electrolyte. Beside a general shift to lower values of Δ and higher values of Ψ, on addition of the dye to the base electrolyte, pronounced structure was observed in the wavelength region of strong absorption of the dye in solution.

In ultra-violet visible spectrophotometry the absorbance of a compound is quantified by determining the difference between an absorbing material disolved in a suitable solvent and the pure solvent. However, in ellipsometry the changes Δ and Ψ that result when a strongly absorbing material is added to a transparent electrolyte are not solely due to the presence of an adsorbed layer on the substrate but also to changes in the refractive index of the medium, diffuse layer, and possibly electroreflectance effects. A simple subtraction of the data collected for the base electrolyte from that obtained in the presence of the absorbing material to quantify the changes in Δ and Ψ due to the adsorbed layer only would therefore be in error. To determine the optical effect caused by only the adsorbed dye layer the ellipsometric parameters should ideally be measured for the electrolyte containing the dye solution under conditions where the dye is not adsorbed on the surface of the substrate and subtract these results from the re-determined values of Δ and Ψ under conditions where an adsorbed layer is formed. A 'filmless' reference state was not observed in the potential range employed here. It was necessary therefore, to predict what effect a strongly absorbing medium might have on the measured values of Δ and Ψ in the absence of an adsorbed layer on the mercury surface and to use these corrected values as the reference state for comparison with the data collected in the presence of an

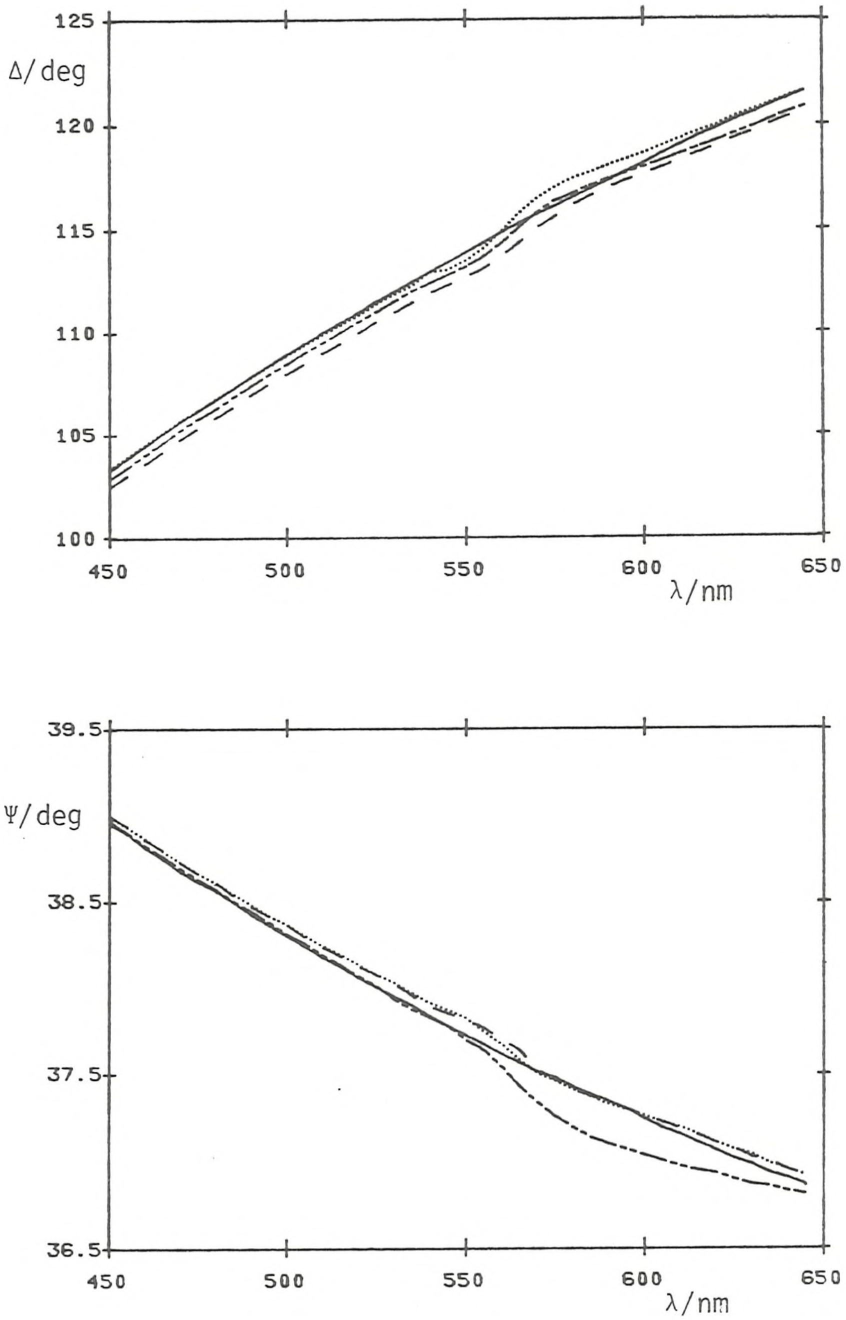

Figure 5.27. Δ and Ψ spectra for the mercury-aqueous electrolyte interface

——— , base electrolyte (0.5 M Na_2SO_4 + 0.05 M H_2SO_4) at - 400 mV (vs. SCE).

·········· , base + rhodamine B (2.3×10^{-6} M) at + 240 mV.

—··— , base + rhodamine B at - 400 mV.

— — — - , base + rhodamine B at - 800 mV.

adsorbed layer. The method adopted for adjusting the values of Δ and ψ measured for the mercury in base electrolyte to those that would be obtained for changes in the refractive index of the medium on addition of the dye solution is as follows:

The mercury substrate optical constants were calculated from the values of Δ and ψ recorded in the presence of the base electrolyte. The refractive index of the electrolyte needed in these calculations was taken from a value measured at 589.3 nm and corrected for use at other wavelengths by assuming the dispersion correction to be the same as that for pure water. From these calculated values of n and k for the mercury substrate and the measured refractive index of the rhodamine B solution used (see below) new, hypothetical values of Δ and Ψ were calculated for the mercury in contact with the dye solution. The values of Δ and ψ corrected for the dye solution refractive index were then subtracted from the experimental values obtained with the dye actually present. The difference spectra obtained by this method are shown in Figs. 5.28 and 5.29.

The values for n and k obtained for the mercury substrate from the single zone determination of Δ and ψ will be in error due to optical component imperfections, contributions from the solution side of the double layer, and electroreflectance effects, but since difference quantities are presented, the errors in $\delta\Delta$ and $\delta\psi$ are anticipated to be small by comparison with the large effects observed in the spectral region covering the major absorption band of the dye.

The optical constants of the rhodamine B solution used were determined by measuring Δ and Ψ at the air solution interface, in four zones, at 20 nm intervals in the range 300 to 660 nm and then at 5 nm intervals in the range 500 to 600 nm to cover the main absorption bands of the dye. The refractive index dispersion curve for the rhodamine B solution is given in Fig. 5.30 along with the dispersion curve for sodium sulphate (0.5 M), also determined by a four zone ellipsometric analysis, for comparison. The values of refractive index calculated for the sodium sulphate solution are, incidentally, in very good agreement with calculated indices based on a literature value determined at 589.3 nm[a] and assuming the dispersion correction to be the same as that for pure water. The extinction coefficients, k, determined for the rhodamine B solution were subject to some scatter, due, presumably, to the low intensity of the reflected beam. The values of k obtained in the wavelength region corresponding to the absorption maximum in the uv-visible absorption spectrum (Fig. 5.31) were about 0.009 which is considerably larger than value calculated using Eqs.(2.122) and (2.123)

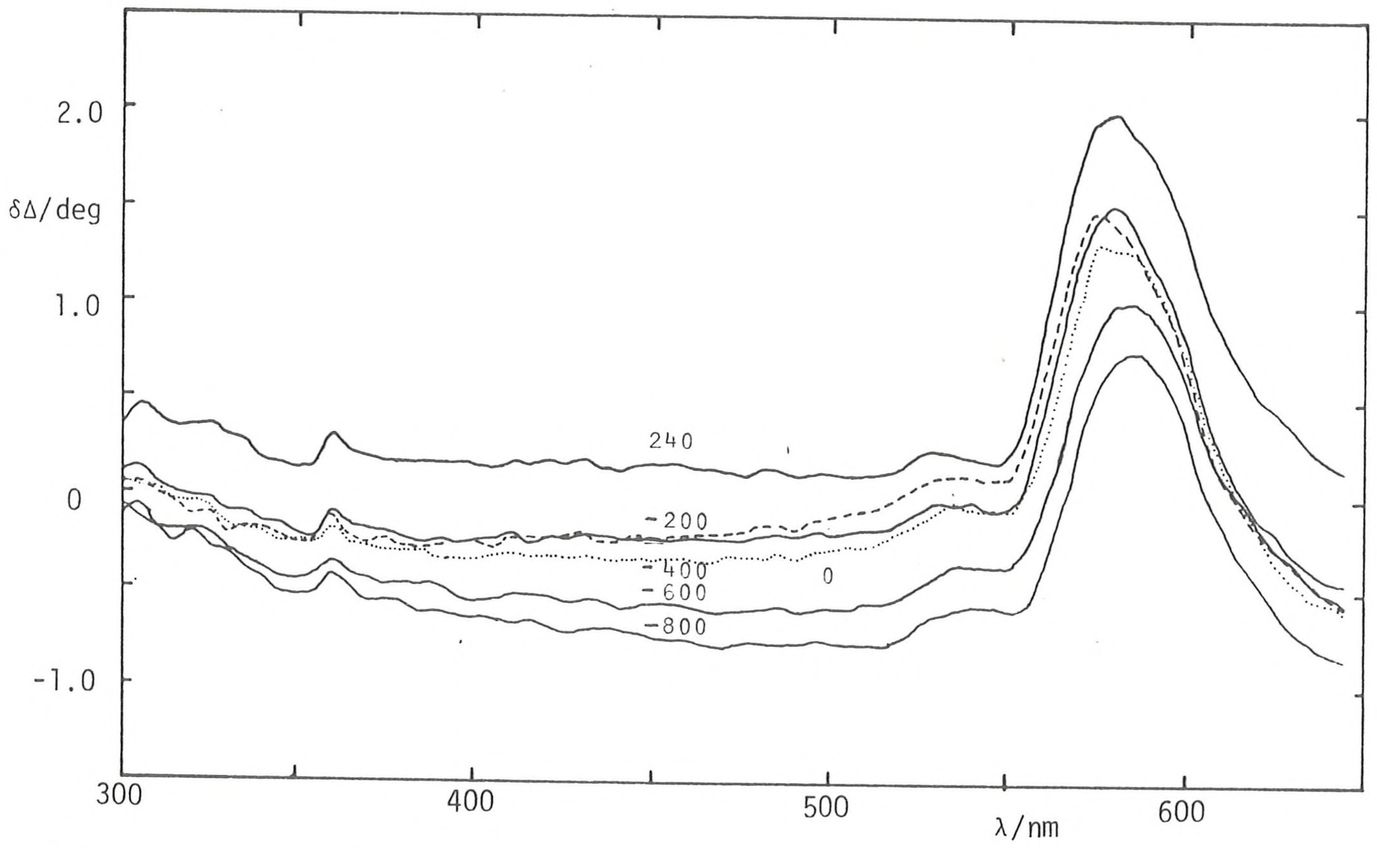

Figure 5.28. Difference spectra, δΔ, corrected for the effects of an absorbing medium. Data collected for the mercury-rhodamine B system at the potentials indicated.

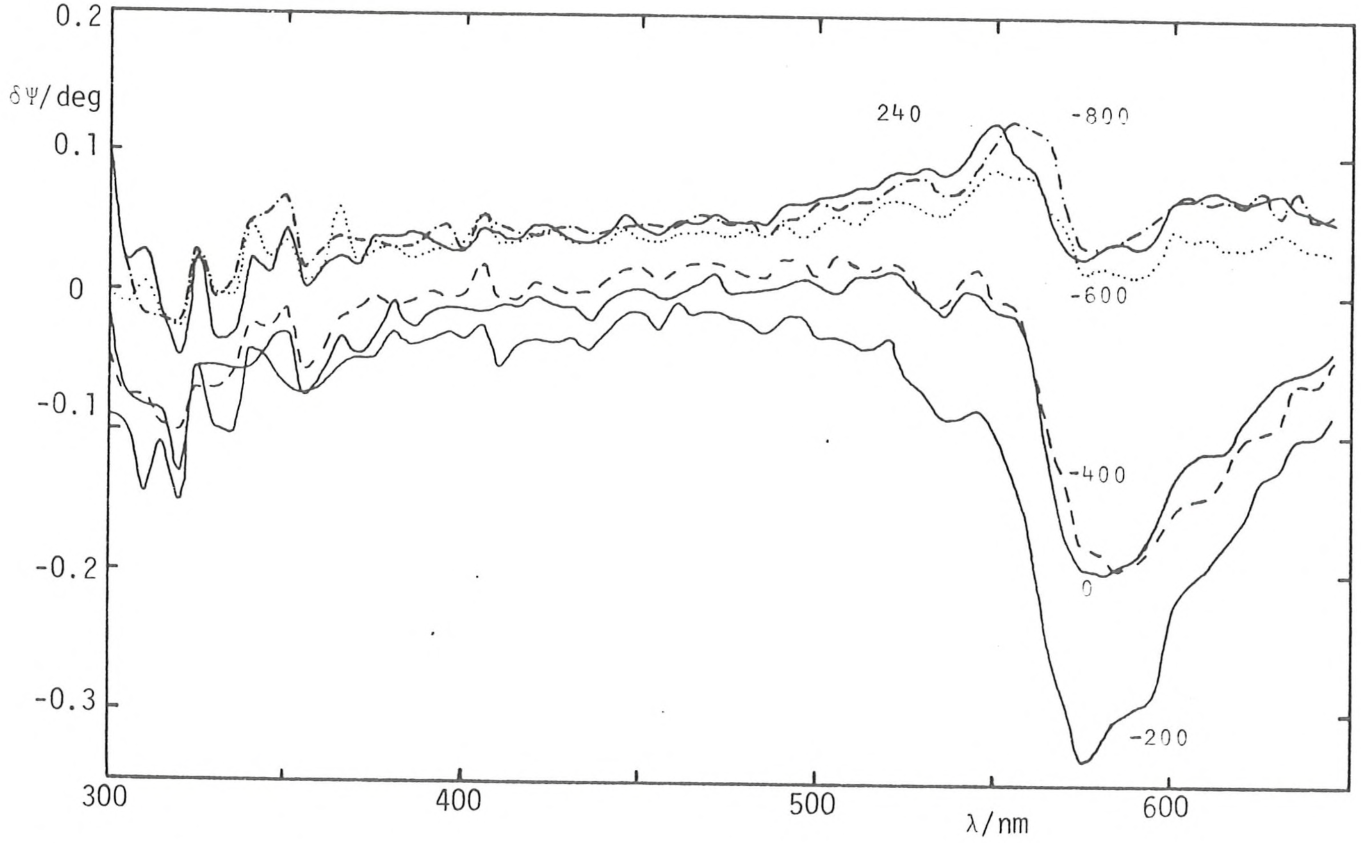

Figure 5.29. Difference spectra, δψ, for the mercury-rhodamine B system at the potentials indicated (mV vs. SCE).

Figure 5.30.

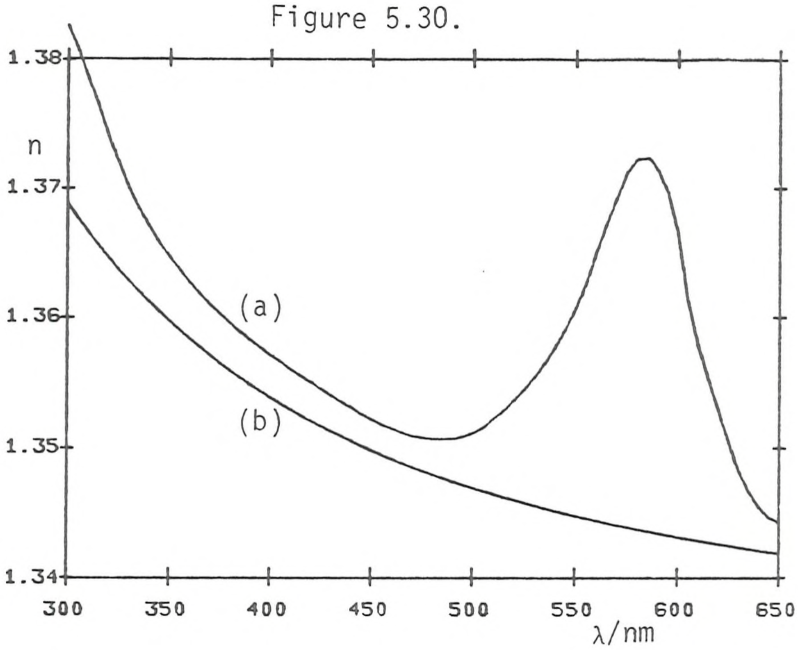

Figure 5.31.

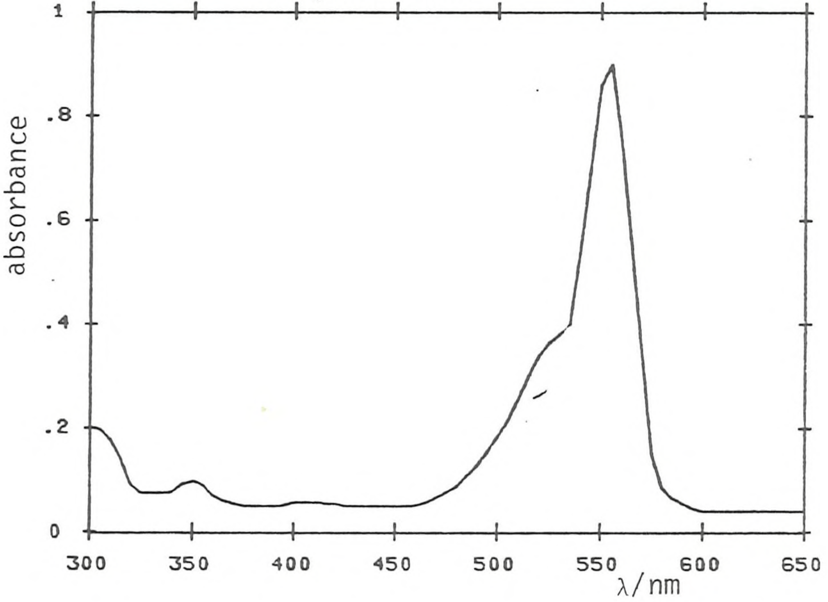

Figure 5.30. (a) Refractive index of rhodamine B (2.3×10^{-6} M) in Na_2SO_4 (0.5 M) and H_2SO_4 (0.05 M) determined by ellipsometry.

(b) Refractive index of Na_2SO_4 (0.5 M) determined by ellipsometry.

Figure 5.31. Absorbance spectrum of rhodamine B (10^{-5} M) in Na_2SO_4 , 1 cm cell.

considerably larger than value calculated using Eqs.(2.122) and (2.123) of 3×10^{-6}. The discrepancy is almost certainly due to a surface excess of the dye at the air solution interface since the ellipsometric data was averaged over four zones and should be free of most errors due to component imperfections.

The effect that an absorbing medium on a film free mercury substrate has on the values of Δ and Ψ has been calculated because of the discrepancy between the measured and calculated extinction coefficient. The refractive indices of the medium used in these simulations were those determined experimentally and the extinction coefficient profiles were calculated from the uv-visible absorbance spectrum of the dye solution using Eqs. (2.122) and (2.123) and were multiplied by factors to obtain maximum k values, at the wavelength corresponding to the absorbance maximum of the dye in solution, ranging from 0 to 0.27. The spectra given in Fig. 5.32 represent the difference between the values calculated using the optical constants of the mercury previously calculated, the measured refractive index of the dye solution used and the extinction coefficients calculated from the absorbance spectrum and the experimentally observed parameters for mercury in the sulphate electrolyte. The effect that k has on Δ is very small, compared to the overall effects caused by changes in n of the medium, until k is ≈ 0.03, the effect on Ψ however, becomes apparent when k is greater than $\simeq 0.003$. A solution with an extinction coefficient of 0.003 would have an absorbance ($\log_{10}I_0/I$) of ≈ 4000 for a 1 cm path length and clearly light would not propagate through such a medium. It can be shown that for k as small as 3.5×10^{-6} the transmittance ($100I_x/I_0$) would be $\simeq 20\%$ per cm and hence insufficient light would propagate through the 2 cm path between entrance and exit windows of the cell arrangement used in this study to enable a meaningful analysis of the reflected beam. The value of k for the solution was therefore assumed to be zero over the entire wavelength range studied for the correction of the base electrolyte values of Δ and Ψ.

The optical constants of a solid rhodamine B film deposited on glass have also been determined by ellipsometric measurements in four zones. The film was produced by dropping a saturated solution of the dye in acetone onto a glass slide and allowing the solvent to evaporate at room temperature. By a process of repeated additions of the dye solution onto previously dried films a highly reflecting smooth surface was obtained. The film was opaque to visible light and assumed to be thick enough to enable a determination of the optical constants without

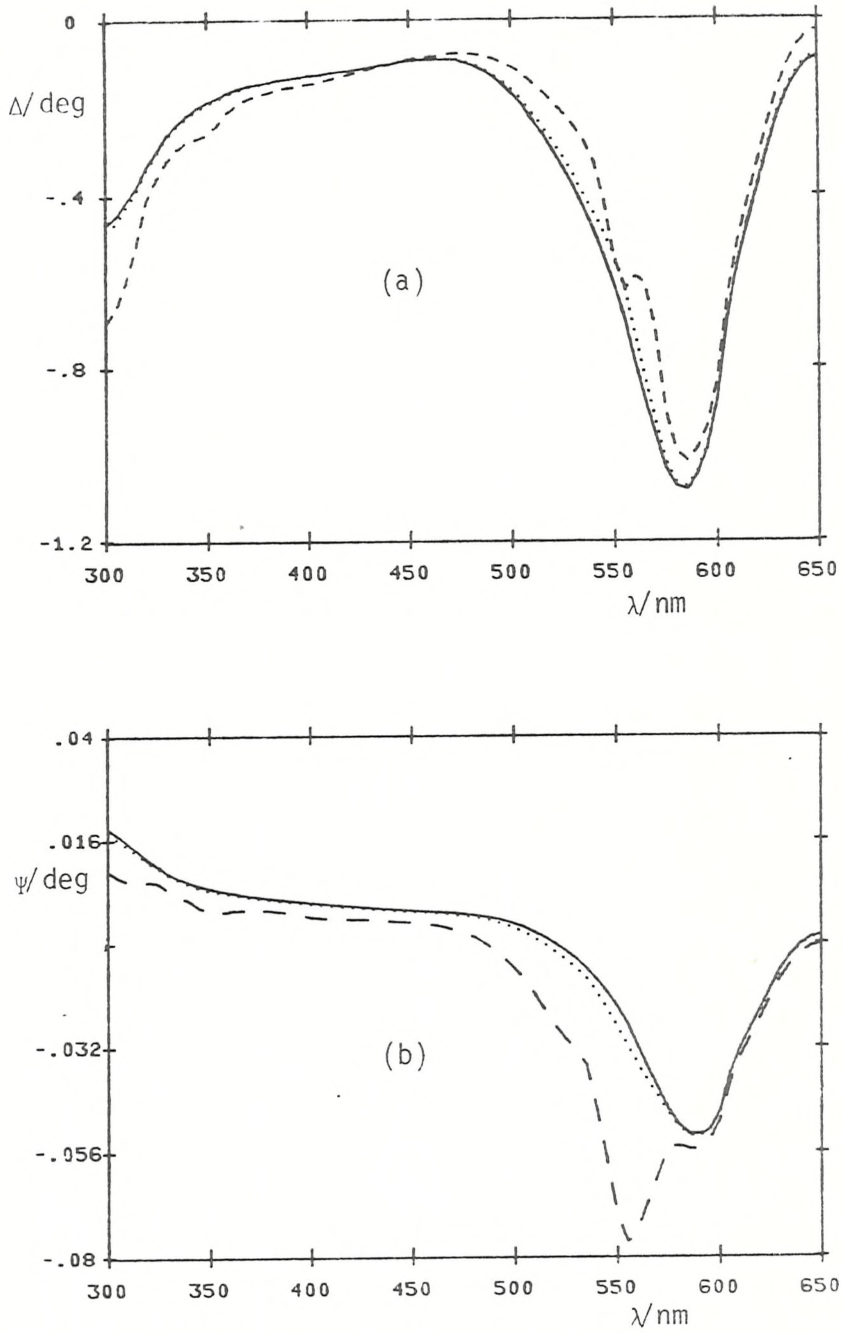

Figure 5.32. Effects of an absorbing medium on a film free substrate. Reference state: Δ and Ψ obtained experimentally for mercury in Na_2SO_4/H_2SO_4. Refractive index of medium from ellipsometric data (Fig. 5.30a) and extinction coefficient profiles calculated from the absorbance spectrum (Fig 5.31)

(a) ——— $k = 0$
········ $k = 10^{4}$ x value calculated from absorbances.
- - - - - - $k = 10^{5}$ x calculated value.
(b) ········ $k = 10^{2}$ x calculated value
- - - - - $k = 10^{3}$ x calculated value

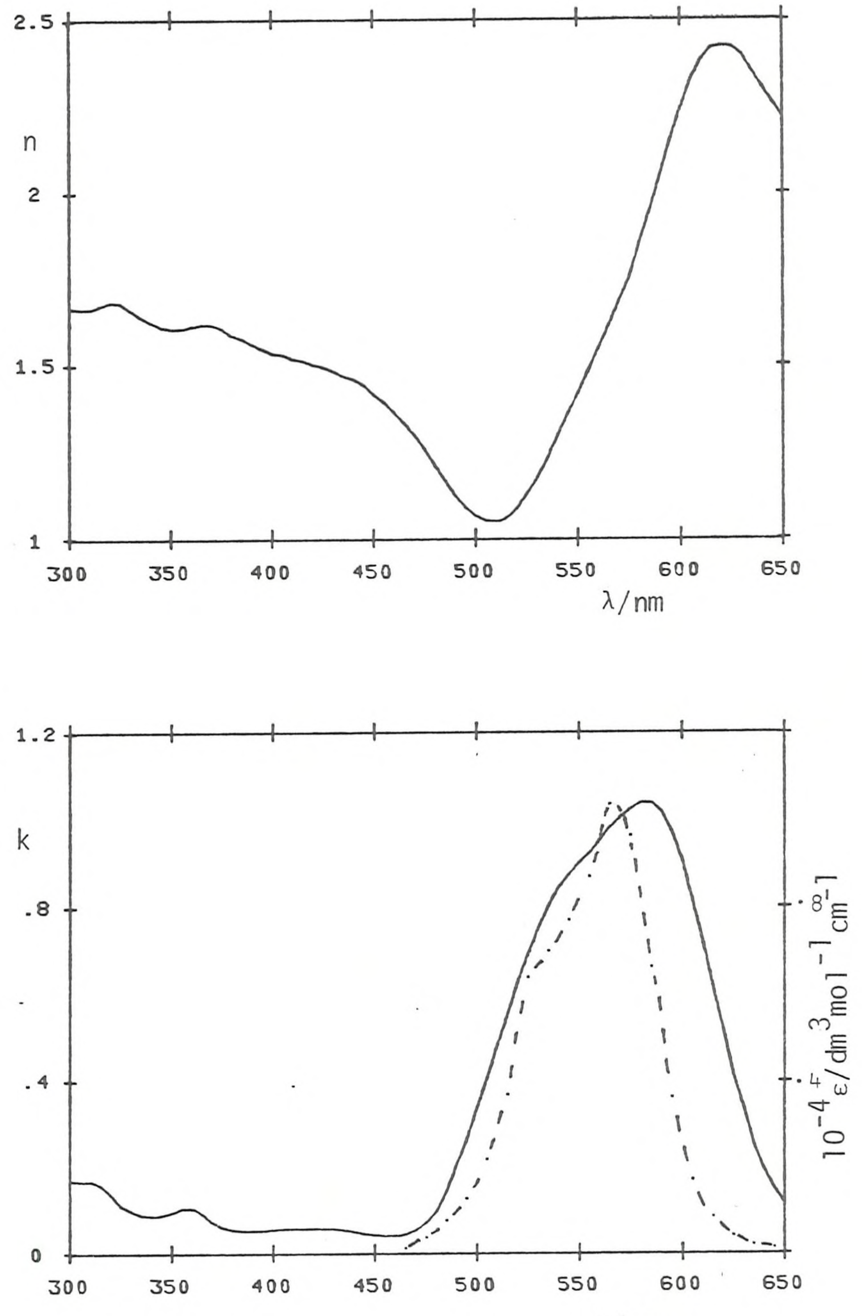

Figure 5.33. (a) Refractive index (b) extinction coefficient of solid rhodamine B on glass. (b) also shows the molar extinction coefficient data of Ref. 106, - - - - - - .

influence from the underlying glass substrate. The values of n and k determined by analysis of the ellipsometric data are given in Figs 5.33. By comparison with the solution phase absorbance, the solid phase absorption spectrum is much broader. The broadening of absorption bands in the solid phase has been observed by Weigl[106] who reported that the bands in solid films were about twice as broad as the corresponding solution bands for a number of photoconductive films of cationic dyes including rhodamine B. A significant decrease in the molar extinction coefficient of these solid films was also reported. For comparison, the molar extinction coefficients given in Ref. 106 for solid rhodamine B have been plotted along with the extinction coefficient obtained here in Fig. 5.33. The broader spectrum obtained by ellipsometry is probably due to the larger band width of the incident light at longer wavelengths, but surface roughness and crystal structure may also influence the determined constants.

The overall structure observed in the $\delta\Delta$ spectra (Fig. 5.28) is largely independent of electrode potential. Small peaks are observed at 360 and 535 nm and the larger peaks centered around 580 nm correspond closely to the extinction coefficient maxima observed for the solid dye film at 360 and 585 nm and to the shoulder observed in the region of 545 nm (Fig. 5.33). The larger peaks recorded at electrode potentials of -600 mV and -800 mV appear to be red shifted by about 5 nm and there is an general shift to lower values of $\delta\Delta$ as the electrode potential is made more cathodic. The $\delta\Psi$ spectra are more potential dependent i.e. minima are observed around 580 nm for all potentials but a maximum develops in the spectra at the anodic and cathodic extremities of the potential range employed.

Differential double layer capacitance and cyclic voltammetry curves for rhodamine B solutions are given in Figs. 5.34 and 5.35 respectively. A step in the capacitance curve and a peak in the cyclic voltammogram occur at approximately the same potential, about -550 mV. No anodic peaks in the voltammogram were observed which suggests that the dye undergoes an irreversible reduction. Interestingly, the changes observed in the $\delta\Psi$ spectra are observed at potentials more cathodic than the reduction peak observed in the voltammogram. The changes observed in the $\delta\Delta$ spectra in the same potential region were less pronounced, i.e. a red shift of 5 nm of the peak position and a vertical displacement of the spectra.

In an attempt to explain the observed spectra the changes in Δ and Ψ for a film of rhodamine B of bulk optical properties on a mercury substrate were calculated using the Drude equation (Eq. 2.32). Using the values of n and k determined for the solid dye and the mercury

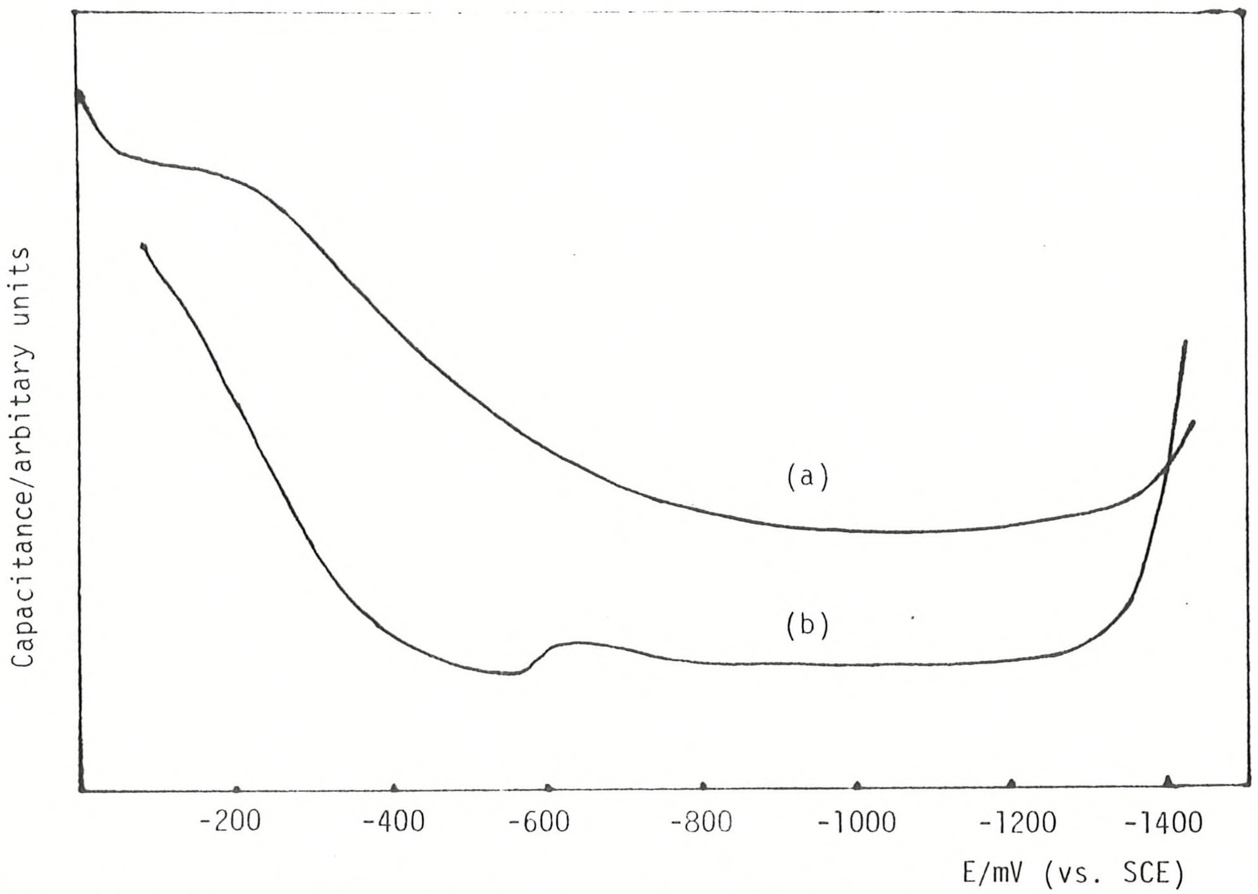

Figure 5.34. Capacity-potential curves for Na_2SO_4 (0.5 M) + H_2SO_4 (0.05 M), (a); and Na_2SO_4+H_2SO_4+rhodamine B (10^{-4} M), (b).

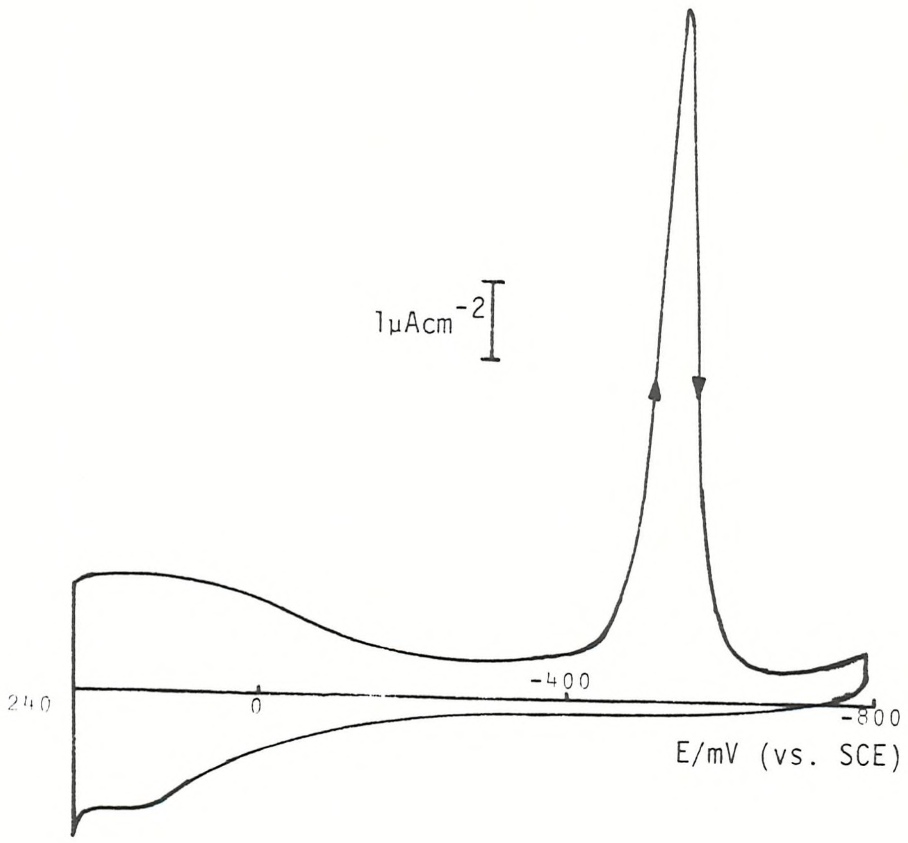

Figure 5.35. Cyclic voltammogram for rhodamine B (2.3×10^{-6} M) in Na_2SO_4 (0.5 M) and H_2SO_4 (0.05 M). Sweep speed 20 mVs^{-1}, mercury pool electrode (9.5 cm^2).

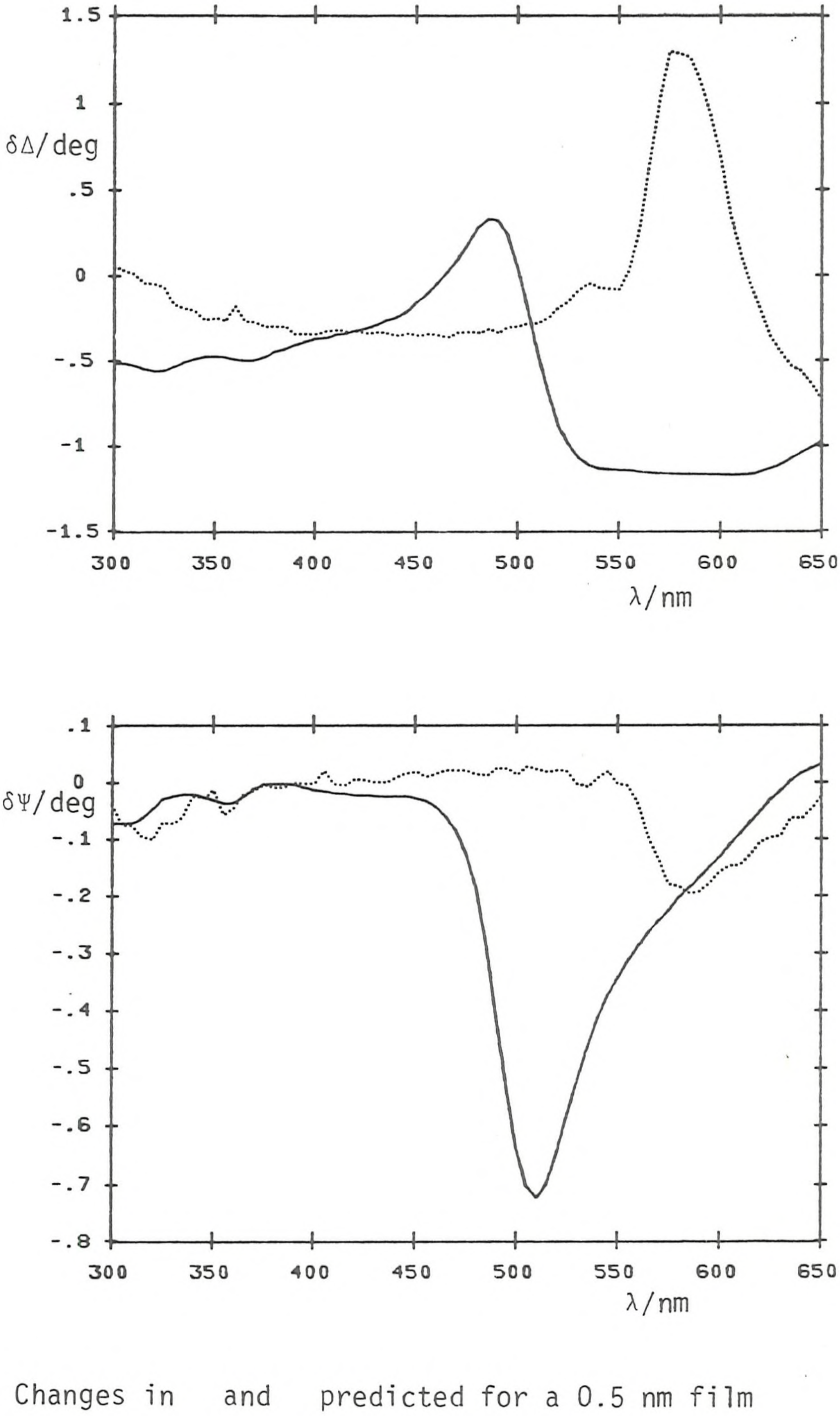

Figure 5.36. Changes in and predicted for a 0.5 nm film of rhodamine B (bulk properties) on mercury.
——————— , simulation.
··················· , experimentally observed changes.

optical constants calculated from the ellipsometric parameters obtained for the base electrolyte at -400 mV, $\delta\Delta$ and $\delta\Psi$ spectra have been calculated for a 0.5 nm film. The outcome of these calculations is shown in Figs. 5.36 along with the experimental data obtained for mercury in rhodamine B solution at -400 mV. The figure shows that there is no correspondence between the observed and predicted data although a red shift of about 100 nm of the bulk dye optical properties would simulate the overall structure but not the magnitude of the experimentally observed effects. A shift in the absorption spectrum of rhodamine B adsorbed on silver of about 40 nm to longer wavelengths has been observed by reflectance spectroscopy[23] and similar shifts have been observed by Campbell _et al_.[107,108], using surface Raman spectroscopy, for several dyes also adsorbed on silver.

Using a computer program described by Cahan[109] to find possible values for the optical constants of a film from values of Δ and Ψ describing the film free substrate, the values $\delta\Delta$ and $\delta\Psi$ recorded experimentally for the film covered surface and the refractive index of the ambient phase, solutions for n and k of the adsorbed layer were found for a series of assumed film thicknesses. The solutions found, for an assumed 0.5 nm layer on mercury are shown in Fig. 5.37 along with the bulk dye spectra for comparison. It can be seen that a shift in the absorption spectrum of about 60 nm to longer wavelengths is sufficient to account for the observed changes. There is however, a significant decrease in the strength of the absorption band, an effect not reported in previous optical studies of dye adsorption. From the two parameters measured ellipsometrically it is not possible to find unique values for the three unknown quantities required to characterise a film of isotropic optical properties (n,k and film thickness). However, as the assumed film thickness, required in the above computations, was increased the structure in the n and k spectra became progresively less pronounced. A film thickness of 1 nm decreased the maximum extinction coefficient by a factor of 3 and it continued to decrease with increasing film thickness. For a multi-layer film, one might expect the properties of the film to approach those of the bulk phase and hence find significantly larger values of the extinction coefficient than were actually computed. These results suggest that the dye is adsorbed at monolayer (or less) coverages and that the presence of the substrate shifts the wavelength of maximum absorption. The smaller value of k computed from the experimental results suggests that the dye does not form a close packed layer.

Some insight into the electronic transitions responsible for the

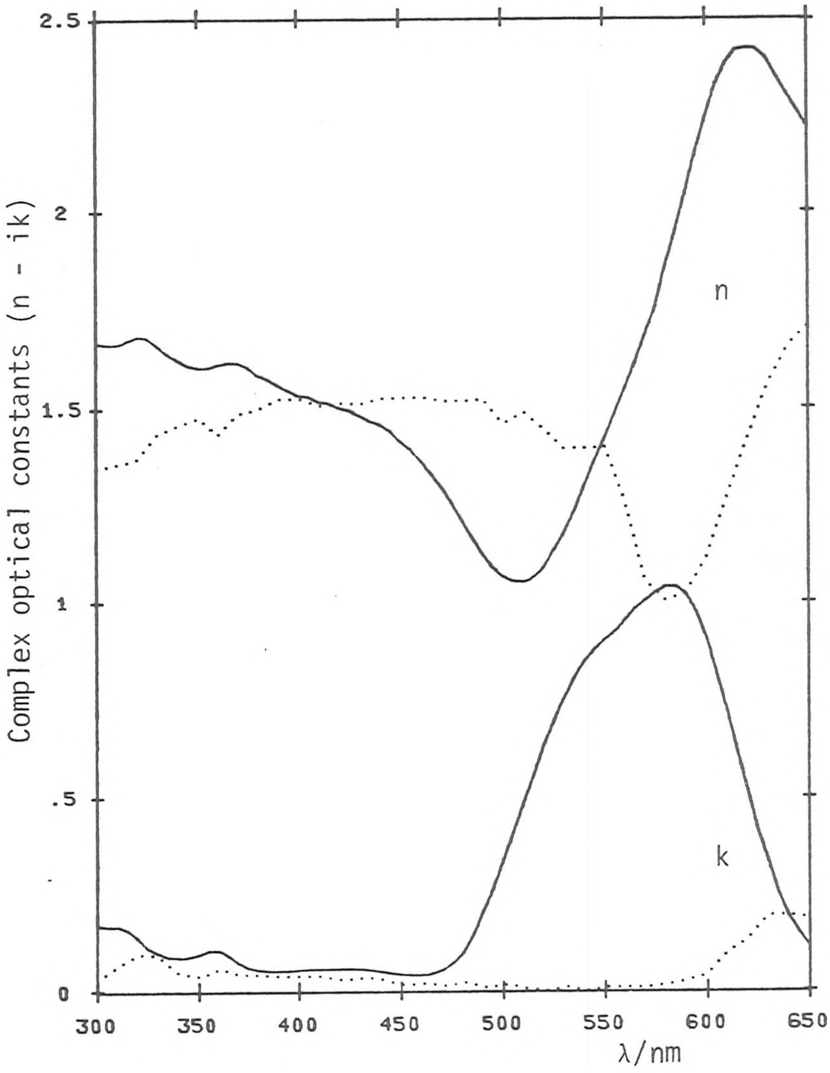

Figure 5.37. Optical properties of bulk rhodamine B, ———— ; optical constants for an assumed 0.5 nm film on mercury from an analysis of the data collected at -400 mV, ⋯⋯⋯ .

absorption process can be gained from the Lorentzian oscillator model (see section 2.7.1). The dielectric function is, according to this model is given by

$$K = 1 + \frac{e^2}{\varepsilon_0 m} \sum_j \frac{N_j f_j}{\omega_j^2 - \omega^2 + i\omega\Gamma} \qquad (5.8)$$

where N_j is the density of bound electrons with resonance frequency ω_j and f_j is the transition probability of j^{th} Lorentzian transition. The maximum value of K'' occurs at the resonance frequency, the half width of the K'' peak is Γ, and the height of the maximum in K'' can be shown to be

$$K''_{max} = \frac{N_j f_j e^2}{m\omega_j \Gamma_j \varepsilon_o} \qquad (5.9)$$

The complex dielectric function ($K = K' - iK''$) for bulk rhodamine B, calculated from the experimentally determined values of n and k obtained from the solid dye deposited on glass is plotted as a function of photon energy in Fig. 5.38. The absorption centred on 2.1 eV is known to be the sum of two oscillators and could, by deconvolution, be resolved into two Lorentzian profiles. Although deconvolution programs were not available a simple estimate yielded approximate values for for each of the major transitions of about 0.15 eV each. These values, after some adjustment, were used with trial values of K''(max) for each oscillator to reconstruct the dielectric function for comparison with experiment. A good agreement between the Lorentzian model and experimental data was achieved using the following parameters:

$$K''(\text{max1}) = 3.5,\ \hbar\omega_1 = 2.1\ \text{eV},\ \hbar\Gamma_1 = 0.18\ \text{eV}$$
$$K''(\text{max2}) = 1.5,\ \hbar\omega_2 = 2.25\ \text{eV},\ \hbar\Gamma_2 = 0.2\ \text{eV}$$

and for the absorption at shorter wavelengths;

$$K''(\text{max3}) = 0.25,\ \hbar\omega_3 = 3.47\ \text{eV},\ \hbar\Gamma_3 = 0.3\ \text{eV}$$
$$K''(\text{max4}) = 0.5,\ \hbar\omega_4 = 4.1\ \text{eV},\ \hbar\Gamma_4 = 0.7\ \text{eV}$$

The reconstructed spectra are shown in Fig. 5.38 along with the experimental values. The experimental values of $K'(\omega)$ are consistently greater than the values calculated by an almost constant value of 2. This is almost certainly due to contributions from the glass substrate to the overall value of $K'(\omega)$ since the dye is only slightly absorbing

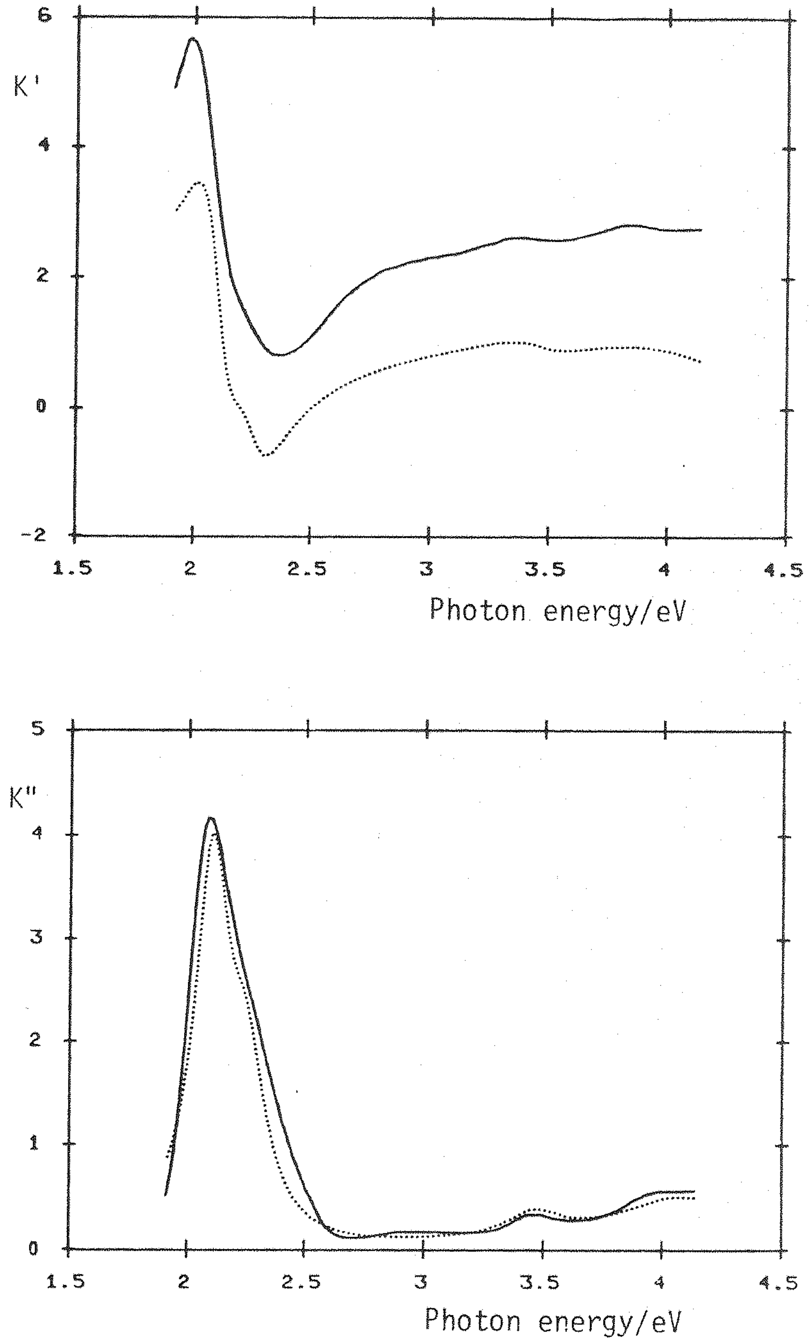

Figure 5.38. Real and imaginary parts of the complex dielectric function spectrum for rhodamine B solid on glass.

———— , experimental data;

………… , calculated from the Lorentz oscillator model.

at photon energies greater than 2.5 eV (450 nm).

From Eq. (5.9) and the values listed above the maximum value of the product N_jf_j for the corresponding oscillators were found to be 9.6×10^{20} and 4.9×10^{20} cm^{-3} for oscillators 1 and 2 respectively. If only one oscillator was assumed responsible for the absorption process then a value of 1.9×10^{21} cm^{-3} was obtained for the product Nf *i.e* close to the sum of the individual values. The above procedures were repeated for the values of n and k found to describe the experimental observations, however, it was not possible to assign a value to Γ with any certainty because the long wavelength side of the absorption peak had been shifted outside of the experimental range (see Fig 5.39). A value of $h\Gamma = 0.1$ eV was sufficient to describe the high energy side of the $K''(\omega)$ peak which results in a value of 8.8×10^{19} cm^{-3} for Nf. Since the surface excess (and hence N) of the dye was not known, it has not been possible to make any predictions concerning the oscillator strength. The solutions found for the optical properties of the adsorbed dye layer resulted from single zone measurements of ellipsometric parameters and are therefore likely to be in error. While these errors may possibly account in part for the low value calculated for the transition probability they would not affect the wavelength position of any observed effects.

Red shifts in absorption maxima are frequently observed in the solution phase absorbance spectra of molecules exhibiting $\pi \rightarrow \pi^*$ transitions when the solvent is made more polar. Most transitions result in an excited state which is more polar than that of the ground state and dipole-dipole intractions between the solvent and solute can lower the energy level of the excited state. A similar effect could account for the red shifts observed for some dyes adsorbed on metal surfaces but in these cases image dipoles in the metal would be responsible for the lower energy of the adsorbate's excited state.

5.3.2 Spectroscopic ellipsometry of rhodamine B adsorbed on platinum.

The ellipsometric parameters for rhodamine B adsorbed on platinum have been determined in the same manner as described in the preceding section. The difference spectra, $\delta\Delta$ and $\delta\Psi$, were obtained for electrode potentials ranging from +300 to -1000 mV, using the data recorded at -200 mV for platinum in supporting electrolyte as reference, and are shown in Figs. 5.39 and 5.40. Unlike mercury, no reduction currents associated with the rhodamine B were observed in cyclic voltammograms.

Only one peak has been observed in the $\delta\Delta$ spectra at all potentials studied, but its position and width are very similar to the

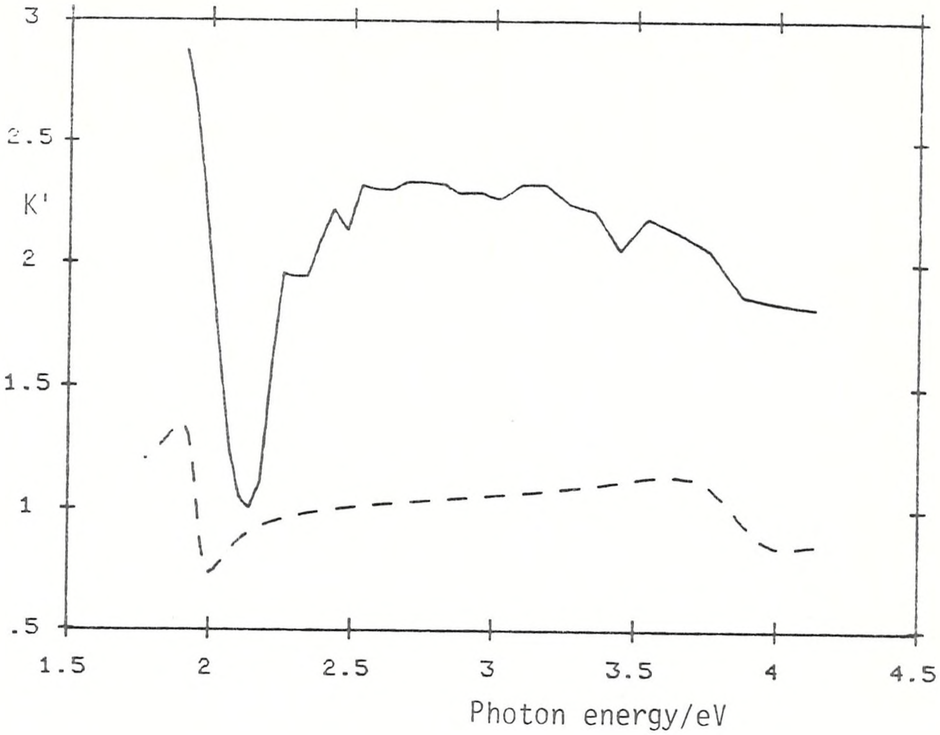

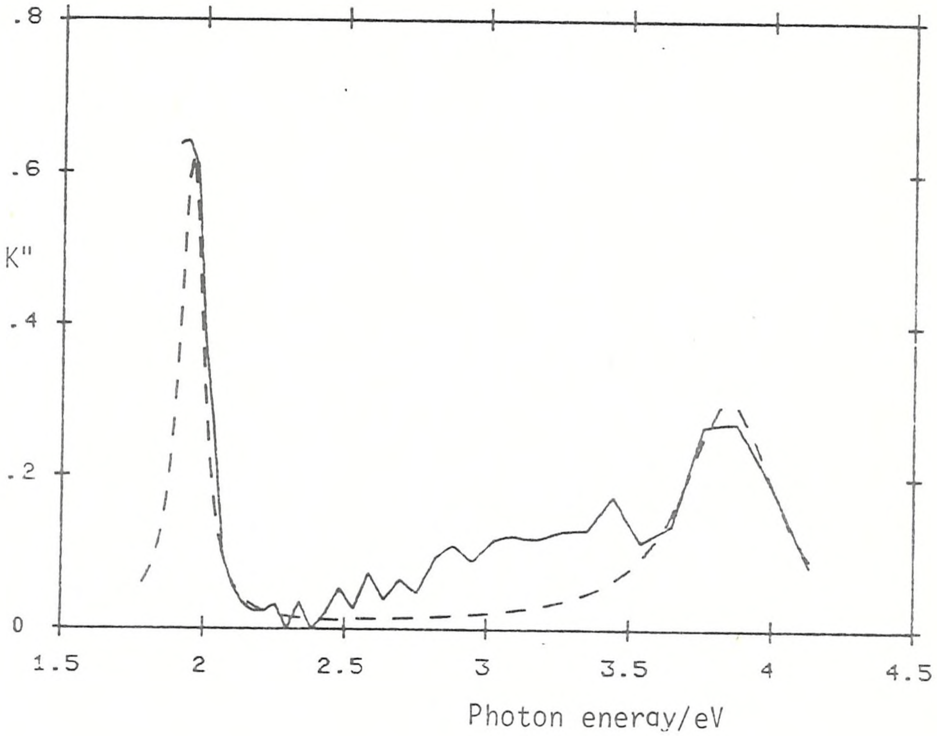

Figure 5.39. Solutions for the optical properties of rhodamine B adsorbed on mercury.

———— , values found by computer analysis;

- - - - , Lorentzian profiles after adjusting parameters to give the best fit to the K" spectrum.

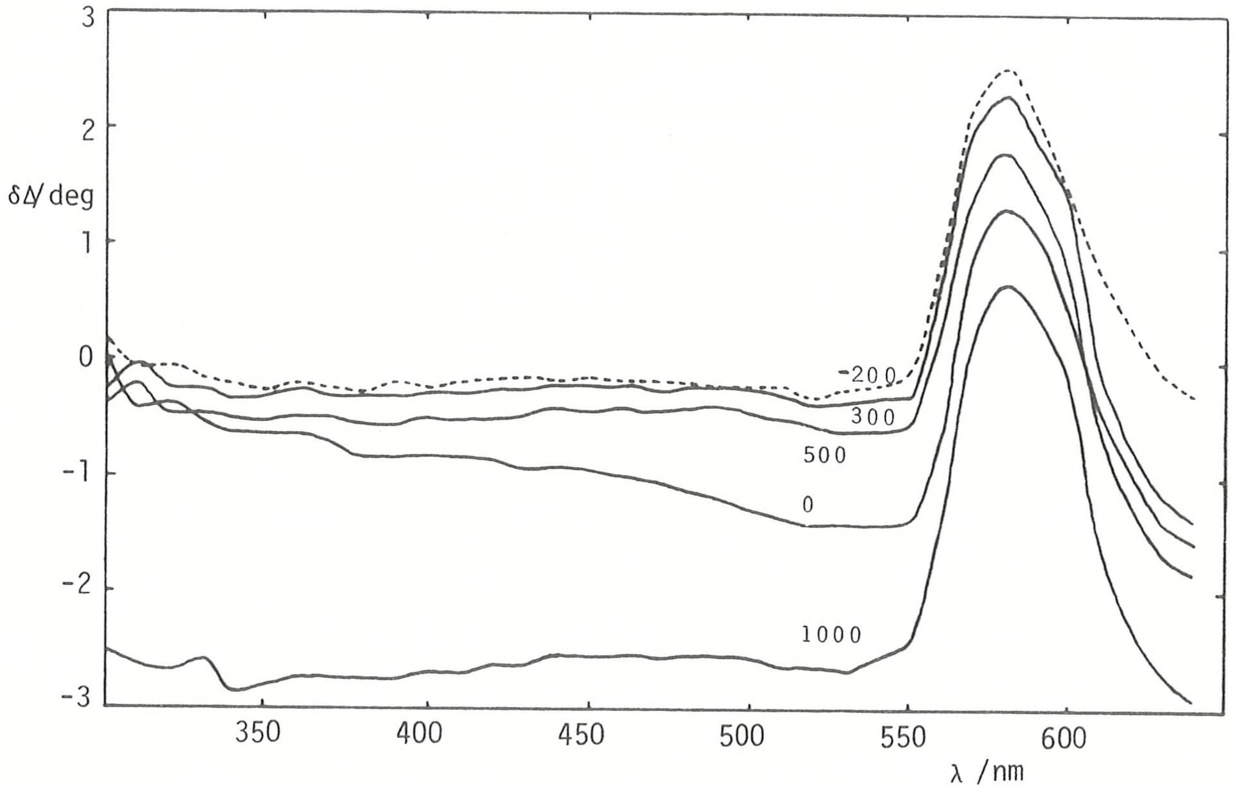

Figure 3.40. Difference spectra, δΔ, obtained after correcting for the effects of an absorbing medium, for rhodamine B adsorbed onto platinum at potentials indicated (mV vs. SCE).

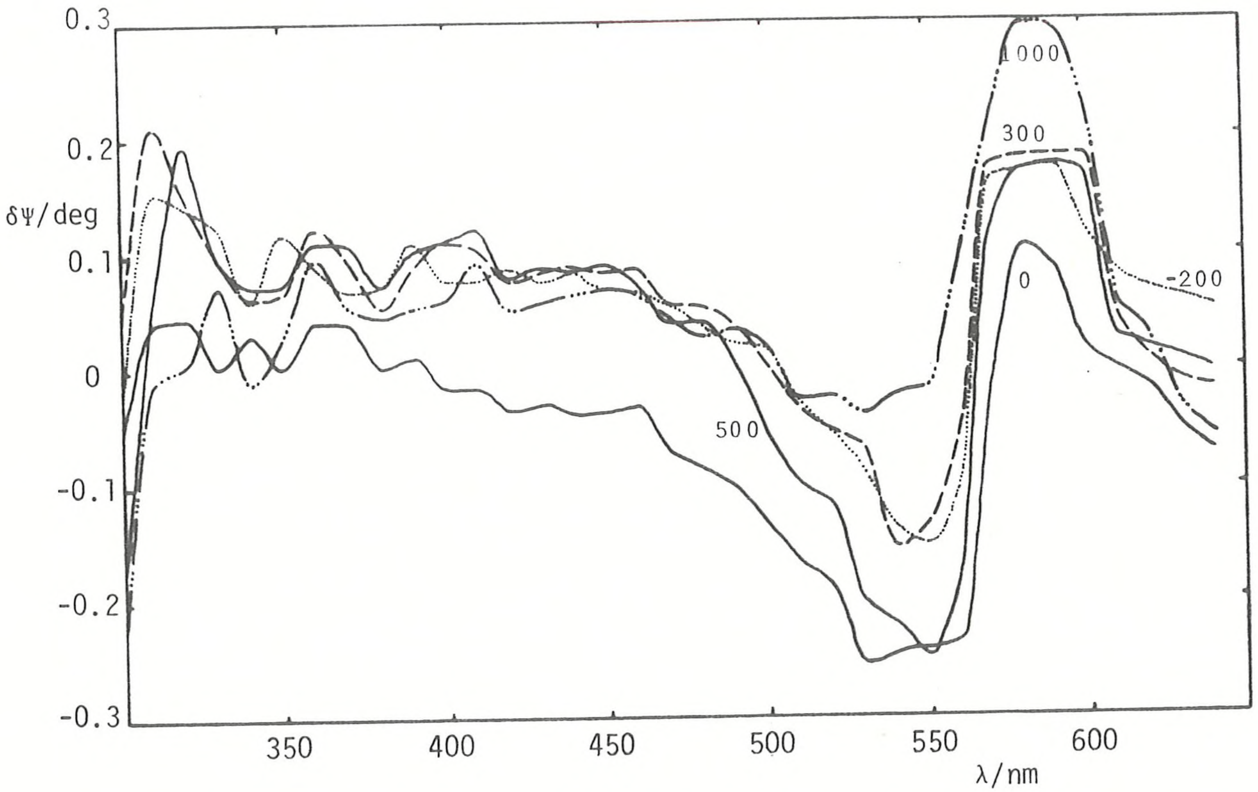

Figure 3.41. Difference spectra, δΨ,obtained after correcting for the effects of an absorbing medium, for rhodamine B adsorbed onto platinum at potentials indicated

major peak observed for the mercury substrate . The $\delta\psi$ spectra however, differ considerably from the corresponding mercury-dye data. A trough is observed at about 540 nm (575 nm on mercury) followed by a peak centred on 580 nm. The magnitude of the changes observed are approximately the same for all potentials in the hydrogen adsorption and double layer regions. The data obtained at 1000 mV (well into the oxide region) differs by having a much smaller trough followed by a larger peak.

The theoretical changes in Δ and Ψ caused by a 0.5 nm film of rhodamine B of bulk optical properties on platinum were calculated and gave very similar results to those calculated for the same film on mercury. Again, as for mercury, a shift in the absorption maximum of the bulk dye to longer wavelengths by about 100 nm would simulate, qualitatively, the observed effect in Δ but such a shift would not at all account for the structure observed in the Ψ spectrum.

Attempts to find solutions for the optical properties or the adsorbed layer on platinum were largely unsuccesful. Solutions were found only over a narrow wavelength range (500 - 550 nm), solutions at all other wavelengths gave negative values for k or very large positive values for n and k.

Plieth[23] has studied the adsorption of rhodamine B on platinum and concluded, from a Kramers-Kronig analysis of reflectivity data, that the wavelength of maximum adsorption of the dye adsorbed on platinum was blue shifted by about 55 nm (λ_{max} = 494 nm). Although no solutions to the three layer model could be found to account for the data obtained in this investigation, the $\delta\Delta$ and $\delta\Psi$ spectra obtained do not support the findings of Plieth, i.e. there is very little structure in the region of 500 nm. It has been suggested that rhodamine B is much more strongly adsorbed on platinum than on silver (in which a red shift was observed by Plieth) and if this is the case then the platinum selvedge properties may be altered. The simple 3 layer model would, under these circumstances, need extending to include effects due to modification of the surface region of the platinum. The possibility of anisotropy in the adsorbed dye layer may also be responsible for the lack of solutions found for the 3 layer model. Such an analysis is beyond the scope of the experimental data obtained in this investigation because 5 or 6 constants would have to be found, by numerical techniques, from only two experimentally observed parameters at each wavelength.

5.3.3. Conclusions.

It has been demonstrated that the optical properties of strongly absorbing dyes adsorbed on metals can be determined by *in situ* spectroscopic ellipsometry. Solutions to the values of n and k for rhodamine B adsorbed on mercury, for an assumed film thickness, were found for all wavelengths in the range 300 to 650 nm, and clearly indicate a red shift in the absorption maximum of the dye of about 60 nm.

These properties were obtained from an analysis of the data collected while the mercury was in contact with the dye solution. By measuring the refractive index of the ambient phase, over a wide range of wavelengths, it has been possible to effect an analysis without the need to replace the dye solution with a transparent medium. The solutions found however, rely heavily on the accuracy with which the complex refractive index of the ambient phase can be measured. The values reported in this investigation are likely to be in error due to a surface excess of dye at the air solution interface.

CHAPTER 6: CONCLUSIONS

Ellipsometry has been applied to the study of electrochemical adsorption at the metal-electrolyte interface. The first two topics of this study are in areas where there is currently a paucity of experimental data and doubt about its interpretation. These concern the optical response of the mercury-electrolyte interface to changing ionic adsorption, and the measurement of the adsorption and reorganisation of organic monolayers at this electrode.

The third topic is a new area and concerns the electrochemical adsorption of coloured materials at mercury and platinum electrodes in the presence of the optically absorbing dye electrolyte.

The instrument used is a nulling ellipsometer with the capability of scanning the wavelength from 280 nm to 650 nm, and incorporates computerised control and data acquisition. The rate at which the data, representing the null condition, can be collected has enabled either the adsorption to be followed continuously as the electrode potential was swept dynamically or the spectral properties of the adsorbed materials to be determined, over a wide range of wavelengths with high resolution.

For ionic adsorption, where the changes in Δ and Ψ are observed to be relatively small, the effects of anion adsorption at anodic charges can be seen clearly although only qualitatively accounted for on the basis of surface excesses and inner layer refractive indices derived from published data. The wavelength dispersion of the changes in Δ observed at anodic charges cannot be accounted for satisfactorily by any change in inner layer refractive index either real or complex. The changes in Δ at cathodic charges and Ψ at any charge, similarly, cannot be explained by any surface layer refractive index. The electroreflectance effect for the mercury-aqueous electrolyte interface is not explained by the macroscopic model based on free electron density changes in the surface layer of the mercury. However, the electroreflectance effect must necessarily be smalland comparable with changes due to inner layer refractive index changes. Clearly, the macroscopic optical models of the double layer, at least in the case of simple ionic adsorption, are inadequate.

The optical properties of many liquid metals have been shown to agree well with the Drude free electron model but no satisfactory models appear to have been applied to those cases where the optical properties deviate from Drude behavior. There is strong theoretical evidence to suggest that the failure is due, not to the Drude model itself but, to the local field approximation used in the macroscopic treatment of the interaction of light with a metal surface. Whether the optical properties of mercury are adequately described by a free electron model awaits further developments of the non-local or microscopic approaches since all but the simplest (specular scattering) model yields descriptions that cannot be used to calculate the optical properties of perfect metals. Similarly, the incorporation of electroreflectance effects into a microscopic description of the field within metals must be postponed until the free mercury surface is adequately modelled.

The adsorption of isoquinoline at the mercury-aqueous electrolyte interface embodies several aspects of organic adsorption which have been clearly identified in this investigation. By observing the changes in ellipsometric parameters continuously as the electrode potential was cycled between limits, the adsorption and subsequent desorption of isoquinoline, from dilute solutions, was clearly seen and characterised by large changes in Δ. The somewhat smaller changes in Ψ were however strongly influenced by effects other than simple inner layer refractive index changes and were observed, at all wavelengths employed, to be similar to the changes observed in the ionic adsorption studies.

For more concentrated solutions of isoquinoline the ellipsometric data was interpreted as resulting from an isotropic film at anodic potentials, which underwent a slow process of re-organisation yielding a close packed, oriented mono-molecular layer as the potential was made more cathodic. At more cathodic potentials large changes in Δ and Ψ were identified with another, more sudden, re-organisation of the adsorbed isoquinoline again resulting in a close packed, oriented mono molecular layer.

Data was obtained at several wavelengths in the near ultra-violet and visible regions, most of which, after allowing for normal dispersion, was satisfactorily explained on the basis of a film of mono layer thickness whose refractive index and orientation depended on the amount of material adsorbed and on the electrode potential. In contrast to the ionic adsorption studies, the changes in ellipsometric parameters observed in these organic adsorption studies were dominated by the changes in inner layer refractive index. The changes in Δ and Ψ must however, include the more subtle changes due to electroreflectance effects and changes in the optical properties of isoquinoline caused by interaction between the adsorbate and substrate. A more detailed analysis than has been possible with the limited amount of data collected is therefore required if information concerning the changes in electronic properties of the adsorbate or substrate are to be examined.

The spectral properties of rhodamine B adsorbed at the mercury-aqueous electrolyte interface have been determined by in situ spectroscopic ellipsometry. The effect of the light-absorbing ambient phase on the measured ellipsometric parameters was accounted for , from using ellipsometric measurements of the complex refractive index of the dye solution at the air-solution interface. After correcting the results for the effects of an absorbing medium, the data was sucessfully analysed to give the optical properties of the adsorbed layer, for an assumed film thickness, at all wavelengths. The wavelength of maximum extinction coefficient of the adsorbed dye was shifted by about 60 nm to longer wavelengths along with a reduction in the extinction coefficient compared to the solid dye spectra.

These results indicate the possibility of studying the electronic properties of strongly absorbing organic materials adsorbed at monolayer coverages on metal surfaces without the need to replace the absorbing medium with dye-free electrolyte.

References

1. A. Rothen in Ref. 5, p. 7.

2. A.C Hall in Ref. 6, p.1.

3. J. Kruger, 'Advances in Electrochemistry and Electrochemical Engineering', Vol. 9, P. Delahay and C.W. Tobias, Eds., (Wiley, N.Y. 1973), p. 227.

4. R. Parsons, Sci. Prog., 64 (1977) 29.

5. E. Passaglia, R.R. Stromberg and J. Kruger, Eds., 'Ellipsometry in the Measurement of Surfaces and Thin Films', Natl. Bur. Stand. Misc. Pub. 256, (U.S. Govt. Printing Office, Washington D.C. 1964).

6. N.M. Bashara, A.B. Buckman and A.C. Hall, Eds., 'Proceedings of the Symposium on Recent Developments in Ellipsometry', Published as Surf. Sci., 16 (1969).

7. N.M. Bashara and R.M.A. Azzam, Eds., 'Proceedings of the Third International Conference on Ellipsometry', Published as Surf. Sci. 56 (1976).

8. R.H. Muller, R.M.A. Azzam, D.E. Aspnes, Eds., 'Proceedings of the Fourth International Conference on Ellipsometry', Published as Surf. Sci., 96 (1980).

9. J.L. Ord, in Ref. 6, p.55.

10. H.P. Layer, in Ref. 6, p.177.

11. B.D. Cahan and R.F. Spanier, in Ref 6. p.166.

12. R. Greef, Rev. Sci. Instr., 41 (1970) 532.

13. C.T. Chen and B.D. Cahan, J. Electrochem. Soc., 129 (1982) 17.

14. A. Bewick and K. Kunimatsu, Surf. Sci., 101 (1980) 131.

15. M.A. Barrett, in Ref. 5, p.213.

16. M.A. Barrett-Gultepe, in Ref.7, p.76.

17. Y.C. Chiu and M.A. Genshaw, J. Phys. Chem., 72 (1968) 4325.

18. W.K. Paik, M.A. Genshaw and J. O'M. Bockris, ibid, 74 (1970) 4266.

19. A. Bewick and J. Robinson, J. Electroanal. Chem., 60 (1975) 163.

20. A. Bewick and J. Robinson, ibid, 71 (1976) 131.

21. C. Hinnen, C. Nguyen Van Huong, A. Rousseau and J.P. Dalbera, J. Electroanal. Chem., 95 (1979) 131.

22. M.W. Humphreys and R. Parsons, J. Electroanal. Chem., 82 (1977) 369.

23. W.J. Plieth, P.Gruschinske, H.J. Hensel, Ber. Bunsenges. Phys. Chem., 82 (1978) 625.

24 B.Z Nikolic, R.R. Azdic, and E.B. Yeager, J. Electroanal. Chem., 103 (1978) 281

25. R.H. Muller in Ref. 6, p14. See also R.H. Muller in Ref. 3, p.167.

26. Z. Knittl 'Optics of Thin Films', (Wiley N.Y. 1976).

27. R.C. Jones, J. Opt. Soc. Amer., 31 (1941) 488.

28. E. Schmidt, ibid., 60 (1970) 490.

29. R.M.A. Azzam and N.M. Bashara, ibid., 62 (1972) 700.

30. F.L. McCrackin, E. Passaglia, R.R. Stromberg and H.L. Steinberg, J. Res. Na tl. Bur. Stand., 67A (1963) 363.

31. W.A. Shurcliff, 'Polarised Light', (D. Van Nostrand, Princeton, N.J., 1964).

32. R.M.A. Azzam and N.M. Bashara, 'Ellipsometry and Polarized Light', (North Holland, Amsterdam, 1977).

33. H. Mueller, J. Opt. Soc. Amer., 38 (1948) 611.

34. M.C. van de Hulst, 'Scattering of Light by Small Particles', (Wiley, N.Y., 1957) p.44.

35. See for example: Born and Wolf, 'Principles of Optics', 6th ed., (Pergamon, Oxford, 1980).

36. F. Wooten, 'Optical Properties of Solids', (Academic Press, N.Y., 1972).

37. C. Kittel, 'Introduction to Solid State Physics', 5th ed., (Wiley, N.Y., 1976).

38. R.W. Ditchburn, 'Light', (Blackie, London, 1953).

39. H.E. Bennett, M. Silver and E.J. Ashley, Phys. Rev.

40. G.B. Irani, T. Huen and F. Wooten, Phys. Rev., 38 (1971) 2385.

41. F.H. Ehrenrich and H.R. Philipp, Phys. Rev., 128 (1962) 1622.

42. N.R. Comins, Phil. Mag., 25 (1972) 817.

43. N.V. Smith, Adv. Phys., 16 (1967) 629.

44. L. Schultz, ibid., 6 (1956) 102.

45. E.G. Wilson and S.A. Rice in, 'Optical Properties and Electronic Structure of Metals and Alloys', F. Abeles, Ed., (North Holland, Amsterdam, 1966).

46. W.E. Mueller, J. Opt. Soc. Amer., 59 (1969) 1246.

47. J.N. Hodgson, Phil. Mag., 4 (1959) 183: 5 (1960) 272: 6 (1961) 509: 7(1962) 229.

48. E.D. Crozier and E. Murphy, Can. J. Phys., 50 (1972) 1914.

49. N.V. Smith, Phys. Lett., 26A (1968) 126.

50. A.N. Bloch and S.A. Rice, Phys. Rev., 185 (1969) 933.

51. E.T. Arakawa, T. Inagaki and M.W. Williams, in Ref. 8, p. 248

52. J.D.E. McIntyre and D.E. Aspnes, Surf. Sci., 24 (1971) 417.

53. J.D.E. McIntyre in Ref. 3., p. 61.

54. M. Stedman, Chem. Phys. Lett., 2 (1968) 457; Symp. Faraday Soc., 4 (1970) 64.

55. J. Feinleib, Phys. Rev. Lett., 16 (1966) 1200.

56. A. Prostak and W.N. Hansen, Phys. Rev., 160 (1967) 600.

57. W.N. Hansen and A. Prostak, ibid., 174 (1968) 500.

58. J.D.E. McIntyre and D.E. Aspnes, Bull. Amer. Phys. Soc., 15 (1970) 366.

59. B.D. Cahan, J. Horkans and E. Yeager, Symp. Faraday Soc., 4 (1970) 36.

60. W.J. Anderson and W. N. Hansen, J. Electroanal. Chem., 47 (1973) 229.

61. A.M. Brodskii and M.I. Urbakh, Elecktrokhim, 15 (1978) 947.

62. See for example: P. Delahay, 'Double layer and Electrode Kinetics, (Interscience, 1965).

63. F.L. McCrackin and J.P. Colson in Ref. 5, p.61.

64. R. Payne, Trans. Faraday Soc., 64 (1968) 1638.

65. Y.C. Chiu and M.A. Genshaw, J. Phys. Chem., 72 (1968) 4325.

66. G.J. Hills and R. Payne, Trans. Faraday Soc., 61 (1965) 326.

67. R.M. Lazorenko-Manevich and E.B. Brik, Elektrokhim., 11 (1975) 750.

68. C. Buess-Herman, N. Vanlaethem-Meuree, G. Quarin and L. Gierst, ibid., 123 (1981) 1.

69. M.J. Dignam, M. Moskovits and R.W. Stobie, Trans. Faraday Soc., 67 (1971)3306

70. M. Cardona, 'Modulation Spectroscopy', (Academic Press, N.Y., 1969).

71. K.L. Kliewer, Surf. Sci., 101 (1980) 57.

72. A.G. Givtsor, et.al., Opt. Spektrosk, 45 (1978) 738.

73. K. Naegele and W.J. Plieth, Surf. Sci., 61 (1976) 504.

74. W.J. Plieth and K. Naegele, ibid, 50 (1975) 53.

75. H. Mayer and B. Hietel in Ref. 45, p.___.

76. K.L. Kliewer and R. Fuchs, Phys. Rev., 72 (1968) 607.

77. P.J. Feibelman, Phys. Rev. B., 14 (1975) 762.

78. A.M. Brodskii and M.I. Urbakh, Elecktrokhim., 11 (1974) 905.

79. A. Bagchi, R.G. Barrera and A.K. Rajagopal, Phys. Rev. B., 20 (1979) 4824.

80. R. Kofman, R. Garrigos and P. Cheysac in Ref. 71, p. 231.

81. P.B. Clapham, M.J. Downs and R.J. King, Appl. Opt., 8 (1969) 1965.

82. A.C. Lowe in Ref. 7, p.134.

83. J.R. Partington, 'An Advanced Treatise of Physical Chemistry', Vol. IV, p.592.

84. F.L. McCrackin, E. Passaglia, R.R. Stromberg and H.L. Steinberg, J. Res. Natl. Bur. Stand., 67A (1963) 363.

85. R.J. King, J. Sci. Instr., 43 (1966) 617.

86. J.M. Bennett, Appl. Opt., 9 (1970) 2123.

87. T. Smith, Adv. Colloid. Interface Sci., 3 (1972) 161.

88. J. Robinson, Ph.D. Thesis, University of Southampton, 1976.

89. A.M. Hartley, A.G. Hilbert and J.A. Cox, J. Electroanal. Chem., 17 (1968) 81.

90. F.L. McCrackin, 'A Fortran Program for Analysis of Ellipsometer Measurements', Natl. Bur. Stand., Tech. Note 479, (U.S. Govt. Printing Office, Washington D.C., 1969).

91. S. Hsieh, Ph.D. thesis, University of Southampton, 1969.

92. I.M. Kolthoff and J.J. Lingane, Polarography, Vol. 2, (Interscience, N.Y., 1952).

93. I.M. Kolthoff and C.S. Miller, J. Amer. Chem. Soc., 63 (1941) 1013.

94. Handbook of Chemistry and Physics, R.C. West, Ed., CRC Press, 1977.

95. M.W. Humphreys, Ph.D. Thesis, University of Bristol, 1975.

96. H.S. Harned and B.B. Owen, The Physical Chemistry of Electrolytic Solutions, 3rd ed. (Reinhold, 1958) p. 358, 396.

97. T.C. Waddington, Trans. Faraday Soc., 62 (1966) 1482.

98. D.C. Grahame, Chem. Rev., 41 (1947) 411.

99. J.D.E. McIntyre, Symp. Faraday Soc., 4 (1970) 50.

100. J.D.E. McIntyre, Surf. Sic., 37 (1973) 658.

101. R.M. Lazorenko-Manevich, E.B. Brik and Y.M. Kolotyrkin, Electrochim. Acta., 22 (1977) 151.

102. M.H. Lee and A. Bagchi, Phys. Rev. B, 22 (1980) 1687.

103. C. Buess-Herman, N. Vanlaethem-Meuree, G. Quarin and L. Gierst, J. Electroal. Chem., 123 (1981) 21.

104. A.F. Silva, Ph.D. Thesis, University of Southampton, 1981.

105. C.J. West and N.E. Dorsey, Eds., 'International Critial Tables', Vol. VII, p.45, (McGraw-Hill, N.Y.)

106. J.W. Weigl, J. Chem. Phys., 24 (1956) 364.

107. C.G. Blatchford, J.R. Campbell and J.A. Creighton, Surf. Sci., 108 (1981) 411.

108. J.R. Campbell and J.A. Creighton, J. Electroanal. Chem. (Accepted for publication).

109. B.D. Cahan, in Ref 7, p.354.

Appendix A1. Control unit logic circuitry.

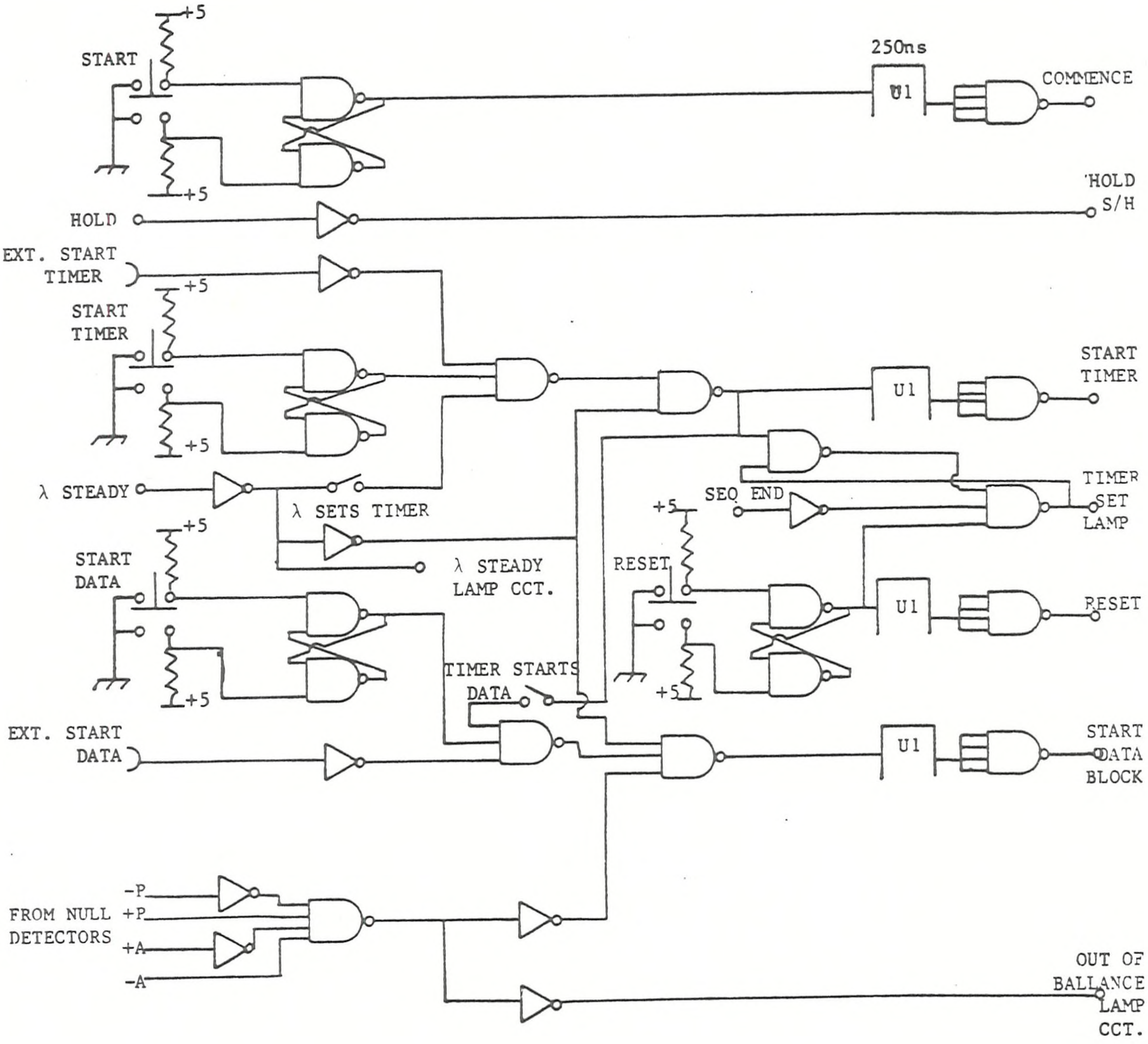

Appendix A1.1. Funnel unit logic circuitry.

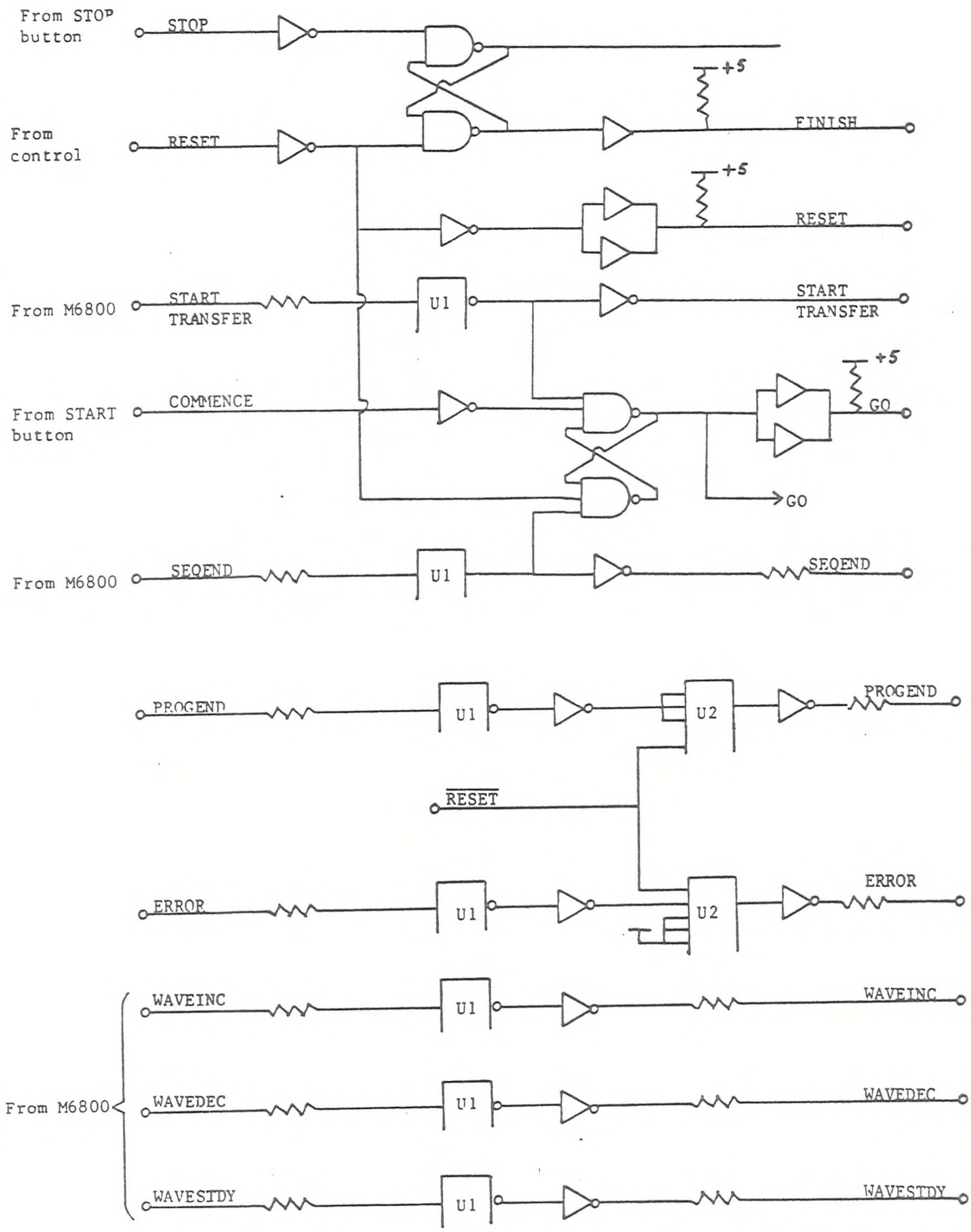

Appendix A1.2 Funnel unit logic - continued.

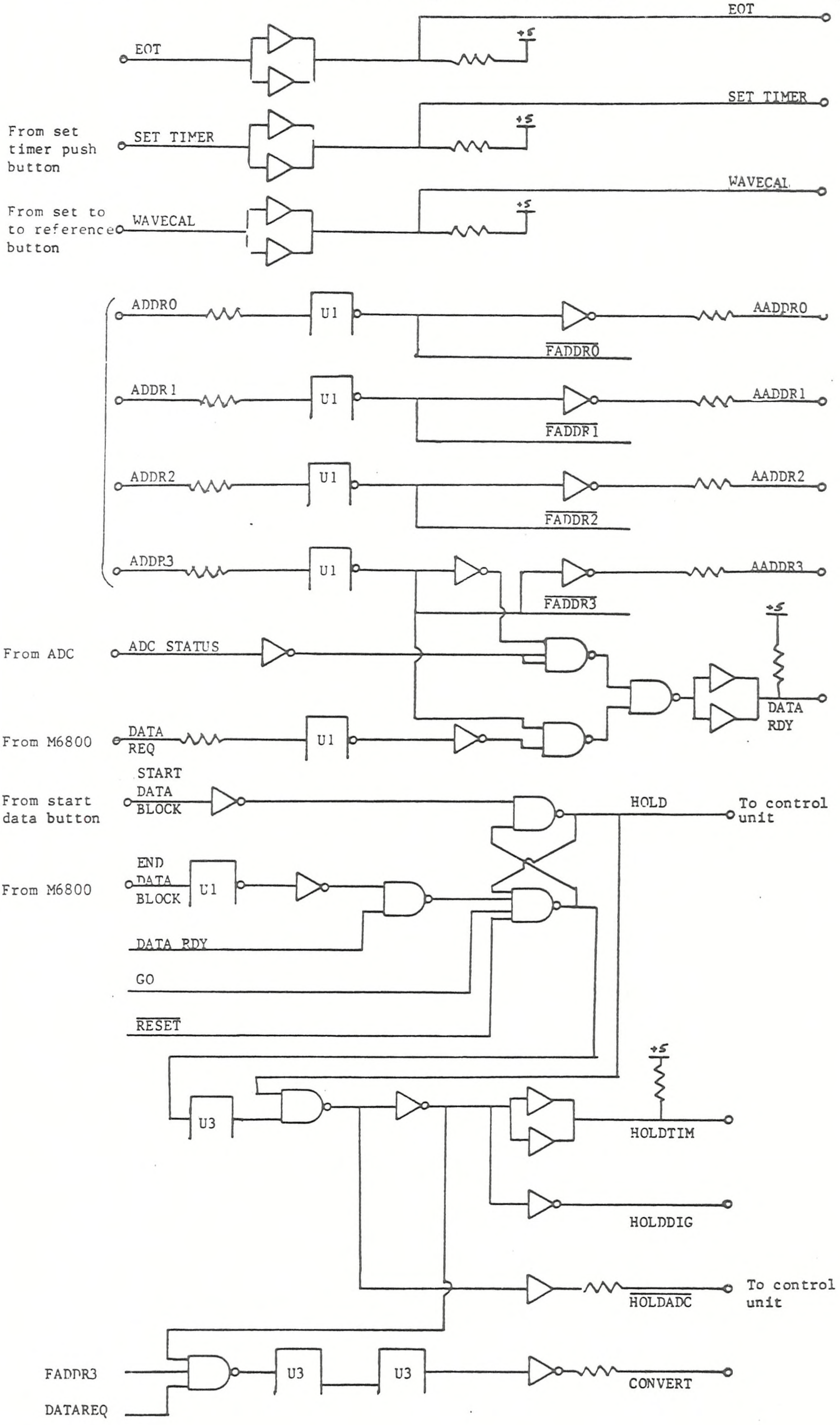

Appendix A1.3 Machine language program.

```
;      ELLIPSOMETER MACHINE CODE ROUTINES
;
;      ACQUIRE ONE DATA SET (16 CHANNELS)
:
A100  CE 7000   INIT    LDX #7000
A103  6F 00             CLR 0,X         ;CLEAR OUTPUT PORTS
A105  6F 01             CLR 1,X
A109  6F 03             CLR 2,X
A109  6F 03             CLR 3,X
A10C  CE A3FE           LDX #$A3FE      ;INITIALISE STORE POINTER
A10F  C6 00             LBAB #0         ;FIRST FUNNEL ADDRESS
A111  86 12             LDAA #$12       ;START TRANSFER + LAMBDA STEADY
A113  B7 7001           STAA $7001      ;OUTPUT IT
A116  B6 7005  HOLDLP   LDAA $7005      ;  ┐
A119  85 02             BIT 02          ;  } WAIT FOR HOLD = 1
A11B  27 F9             BEQ HOLDLP      ;  ┘ HOLD = 0 BACK 7
A11D  F7 7000  SCAN     STAB $7000      ;OUTPUT ADDR. TO LEDS
A120  F7 7002           STAB $7002      ;OUTPUT ADDR. TO FUNNEL
A123  BD A141           JSR GETWRD      ;GET ONE DATA WORD AND STORE IT
A126  09                DEX             ;NEW STORE POINTER
A127  09                DEX
A128  5C                INCB            ;NEW FUNNEL ADDRESS
A129  C1 10             CMPB #$10       ;COMPARE TO 16
A12B  26 F0             BNE SCAN        ;B<16 THEN GET MORE DATA
A12D  86 11             LDAA #$11       ;SET BITS FOR END OF BLOCK +
A12F  B7 7001           STAA $7001      ;LAMBDA STEADY AND OUTPUT IT
A132  7F 7001           CLR $7001       ;CLEAR OUTPUT PORTS
A135  86 08             LDAA #08        ;CYCLE COUNTER
A137  B7 A20F           STAA CYCL       ;STORE CYCLE COUNTER
A13A  7E A210           JMP AVELP       ;JUMP TO DATA AVE. ROUTINE
;
;     SUBROUTINE TO GET ONE DATA WORD AND STORE IT
,
A141  CA 10    GETWRD   ORAB #$10       ;SET DATA REQUEST BIT
A143  F7 7002           STAB $7002      ;OUTPUT IT
A146  B6 7005  LOOP1    LDAA $7005      ;
A149  85 01             BITA 01         ;WAIT FOR DATA READY HI
A14B  27 F9             BEQ LOOP1       ;IF DATA READY LO - BACK 7
A14D  B6 7007           LDAA $7007      ;INPUT MS DATA BYTE
A150  A7 01             STAA 1,X        ;STORE IT
A152  B6 7006           LDAA $7006      ;INPUT LS DATA BYTE
A155  A7 00             STAA 0,X        ;STORE IT
A157  C4 0F             ANDAB #$0F      ;DROP DATA REQUEST BIT
A159  F7 7002           STAB $7002      ;OUTPUT IT
A15C  39                RTS             ;RETURN TO MAIN SEGMENT
;
A16E                                    ;TEMP STORE FOR X REGISTER
A16F                                    ;
;     ENTRY FROM BASIC PROGRAM
:     "USER" SUBROUTINE TO PUT THE CIRCLE
;     VALUE INTO INDIRECT LOCATIONS $30,31
;
A170  FF A16E  STX $A16E                ;SAVE X
A173  FE 0030           LDX $0030       ;POINTER TO USER DATA
A176  E6 00             LDAB 0,X        ;DATA TRANSFERED FROM BASIC
;                                       ;1=Q DATA, 3=P OR 5=A
A178  86 FF             LDAA #$FF       ;LO BYTE OF CIRCLE DATA ADDR.
A17A  58                ASLB            ;MULTIPLY B DATA BY 2
A17B  10                SBA             ;SUBTRACT B FROM A
A17C  B7 A3DF           STAA $A3DF      ;PUT ADDRESS OF FIRST BYTE OF
A17F  86 A3             LDAA #$A3       ;INTO $A3DE
A181  B7 A3DE           STAA $A3DE      ;$A3DE NOW CONTAINS THE STARTING
;                                       ;ADDRESS OF THE SELECTED CIRCLE
A184  FE A3DE           LDX $A3DE       ;LOAD X WITH IT
A187  A6 00             LDAA 0,X        ;LOAD A WITH MSB
A189  84 0F             ANDA $0F        ;KILL LEFT NIBBLE
A18B  FE 0030           LDX $0030       ;STOPE FIRST BYTE
A18E  A7 00             STAA 0,X        ;0.X / 0., DEG. HUNDREDS/
A190  FE A3DE           LDX $A3DE       ;2ND BYTE
A193  09                DEX
A194  A6 00             LDAA 0,X
A196  FE 0030           LDX $0030
A199  A7 01             STAA 1,X        ;1,X / DEG. TENS, DEG. UNITS/
```

```
A19B  FE A3DE            LDX $A3DE       ;3RD BYTE
A19E  09                 DEX
A19F  09                 DEX
A1A0  A6 00              LDAA 0,X
A1A2  FE 0030            LDX $0030
A1A5  A7 02              STAA 2,X        ;2,X / MIN. TENS, MIN UNITS/
A1A7  FE A3DE            LDX $A3DE       ;4TH BYTE
A1AA  09                 DEX
A1AB  09                 DEX
A1AC  09                 DEX
A1AD  A6 00              LDAA 0,X
A1AF  FE 0030            LDX $0030
A1B2  A7 03              STAA 3,X        ;3,X /SEC TENS, SEC. UNITS/
 A1B4  86 07              LDAA #07        ;EXPONENT 07
 A1B6  A7 06              STAA 6,X        ;IN BYTE 6
 A1B8  86 10              LDAA #10
 A1BA  AA 00              ORAA 0,X
 A1BC  A7 00              STAA 0,X
 A1BE  FE A16E            LDX $A16E       ;RESTOR X
 A1C1  39                 RTS             ;RETURN TO BASIC
 ;
 ;   MODIFY A-D OUTPUTS TO 12 BIT INTEGER WITH SIGN
 ;
 A1D1  CE A3E0            LDX #$A3E0      ;FIRST ANALOG DATA ADDR.
 A1D4  E6 01     LOOP2    LDAB 1,X        ;HI BYTE
 A1D6  A6 00              LDAA 0,X        ;LO BYTE
 A1D8  C5 08              BITB #08        ;IS SIGN BIT SET
 A1DA  27 0A              BEQ STORE       ;DO NOT COMPLEMENT DATA
 A1DC  53                 COMB            ;COMPLEMENT DATA
 A1DD  CA 80              ORAB #$80       ;RAISE MSB AS -VE FLAG
 A1DF  43                 COMA            ;COMPL.
 A1E0  8B 01              ADDA #$01       ;2'S COMPLEMENT
 A1E2  24 02              BCC STORE       ;BRANCH IF CARRY CLEAR
 A1E4  CB 01              ADDB #$01
 A1E6  E7 01     STORE    STAB 1,X        ;WRITE DATA BACK
 A1E8  A7 00              STAA 0,X
 A1EA  08                 INX
 A1EB  08                 INX
 A1EC  8C A3F0            CPX #$A3F0      ;COMPARE TO LAST DATA ADDR.
 A1EF  26 E3              BNE LOOP2       ;BACK 29
 A1F1  39                 RTS             ;BACK TO BASIC
 ;   ROUTINE TO DRIVE MONOCHROMATOR AT 400 STEPS/SEC.
 ;   BEFORE ENTRY PUT CONTROL BYTE INTO 41946 (0 FOR FWD,
 ;   8 FOR REV) AND PUT HI BYTE OF NO. OF PULSES INTO
 ;   $A3D9 (41945 DECIMAL) AND LO BYTE INTO $A3DA (41946)
 ;   START ADDRESS $A1F2. USE POKE(40,161):POKE(41,242):
 ;   A=USER(X)
 ;
 A1F2  FE A3D9            LDX $A3D9       ;LOAD X WITH NO. STEPS
 A1F5  B6 A3DB            LDAA $A3DB      ;LOAD A WITH CONTROL BYTE
 A1F8  5F                 CLRB            ;B=0,   8 FOR REV.,0 FWD
 A1F9  8B 04     LP       ADDA #04        ;PULSE BIT. DIR. ALREADY SET
 A1FB  B7 7001            STAA #$7001     ;OUTPUT IT
 A1FE  80 04              SUBA #04        ;DROP PULSE BIT
 A200  B7 7001            STAA #$7001     ;OUTPUT IT
 A203  09                 DEX             ;DECREMENT NO. STEPS BY 1
 A204  27 07              BEQ END         ;END OF PULSES . FWD 7
 A206  5A        WAIT     DECB            ;WAIT LOOP TO GET TIMING
 A207  01                 NOP             ;RIGHT, 10 CLOCK CYCLES PER
 A208  01                 NOP             ;LOOP * 256 TIMES = 2.5 MICOSEC

 A209  26 FB              BNE WAIT        ;BACK 5
 A20B  20 EC              BRA LP          ;BRANCH BACK 20
 A20D  39        END      RTS             ;BACK TO BASIC
```

```
A20E            CHANO   02                  ;RESERVE SPACE FOR
                                            ;NUMBER OF CHANNELS TO BE
;                                           ;AVERAGED
;
A20F            CYCL    08                  ;RESERVWD FOR CYCLE COUNTER
                                            ;DATA TO BE AVERAGED OVER 8
;                                           ;READINGS
;
:START OF ANALOGUE DATA AVERAGING ROUTINE
;
A210  7F A3EF  AVELP   CLR $A3EF            ;CLEAR LOCATIONS USED FOR
;
A213  7F A3EE          CLR $A3EE            ;P MOD ANALOGUE SIG.
A216  7F A3ED          CLR $A3ED            ;A MOD ANALOGUE SIG.
A219  7F A3EC          CLR $A3EC            ;LO BYTE A MOD.
A21C  CE A3EE  CYCLE   LDX #$A3EE           :SET X TO TOP TOP ADDR.
                                           ;(LO BYTE OF P MOD)
;
A21F  C6 08            LDAB #08             ;FIRST FUNNEL ADDR.
A221  86 12            LDAA #$12            ;START TRANS. + LAMBDA STDY
A223  B7 7001          STAA $7001           ;OUTPUT IT
A226  B6 7005  HOLD    LDAA $7005           ;     WAIT FOR
A229  85 02            BITA 02              ;     HOLD=1
A22B  27 F9            REQ HOLD             ;BACK 6
A22D  86 02            LDAA#$02            ;CHANNEL COUNTER
A22F  B7 A20E          STAA A20E            ;STORE IN CHANO
A232  F7 7000  SCAN    STAB $7000           ;OUTPUT ADDR. TO LEDS
A235  F7 7002          STAB $7002           ;OUTPUT ADDR. TO FUNNEL
A238  BD A280          JSR ADDWRD           ;GET WORD AND ADD
A23C  09               DEX
A23D  09               DEX
A23E  5C               INCB                 ;NEXT FUNNEL ADDR.
A23F  7A A20E          DEC CHANO            ;DEC. CHANNEL COUNTER
A241  26 EF            BNE SCAN             ;ANOTHER READING PRINT
                                           ;YES THEN BACK 17
;
A243  86 11            LDAA #$11            ;END OF BLOCK +LAMBDA STDY.
A245  B7 7001          STAA $7001           ;OUTPUT IT
A243  7F 7001          CLR $7001            ;CLEAR THE OUTOUT PORT
A24B  7A A20F          DEC CYCL             ;DECREMENT CYCLE COUNTER
A24E  26 CC            BNE CYCLE            ;IF CYCL>0 THEN BACK 52
;   NOW D VIDE THE ACCUMULATED SIGNAL BY 8
;
A25C  CE A3EE          LDX #$A3EE           ;ADDR. OF P MOD DATA
A253  86 02            LDAA #$02
A255  B7 A20E          STAA CHANO           ;STORE NO. OF CHANNELS
A258  A6 01            LDAA 1,X             ;LOAD MSB OF DATA
A25A  0C               CLC                  ;CLEAR CARRY BIT
A25B  66 01            ROR 1,X              ;ROTATE DATA INTO CARRY
A25D  66 00            ROR 0,X              ;PICK UP CARRY AND LOSE
                                           ;LEAST SIGNIFICANT BIT
;
A25F  0C               CLC                  ;CLEAR CARRY
A260  66 01            ROR 1,X
A262  66 00            ROR 0,X
A264  0C               CLC
A265  66 01            ROR 1,X
A267  66 00            ROR 0,X
A269  A6 01            LDAA 1,X             ;CORRECT FORMAT FOR
A26B  85 08            BITA #$08            ;PROCESSING BY
A26D  27 C4            BEQ NXTCHN           ;ROUTINE AT $A1D1
A26F  8A F0            ORAA #$F0
A271  A7 01            STAA 1,X
A273  09               DEX
A274  09               DEX
A275  7A A20E          DEC CHANO
A278  26 DE            BNE CHANS            ;IF CHAN  0 THEN BACK 34
A27A  39               RTS                  ;RETUPN TO BASIC
;
;   SUBROUTINE ADDWD
;   GET AN A-D DATA WORD AND ACCUMULATE IT
;
A280  CA 10    ADDWD   ORAB #$10            ;RAISE DATA REQ.
A23A  F7 7002          STAB $7002           ;OUTPUT IT
A285  B6 7005  LOOP    LDAA $7005           ;  WAIT FOR
A288  85 01            BITA                 ;  DATA
A28A  27 F9            BEQ LOOP             ;  READY
A28C  B6 7007          LDAA $7005           ;INPUT MS BYTE
A28F  84 0F            ANDA #$0F            ;KILL MS 4 BITS
A291  AB 01            ANDA 1,X             ;ACCUMULATE
A293  A7 01            STAA 1,X             ;STORE IT
A295  B8 7006          LDAA $7006           ;INPUT LS BYTE
A298  0C               CLC                  ;CLEAR CARRY BIT
A299  AB 00            ADDA 0,X             ;ADD OLD VALUE
A29B  24 02            BCC NOIN             ;IF CARRY CLEAR FWD 2
A29D  6C 01            INC 1,X              ;ADD CARRY TO MSB
A29F  A7 00    NOIN    STAA 0,X             ;STORE LSB
A2A1  C4 0F            ANDB #$0F            ;DROP DATA REQ.
A2A3  F7 7002          STAB $7002           ;OUTPUT IT
                       RTS                  ;BACK TO $A23C
```

Appendix A1.4. Basic language program.

```
0001 REM   WAVELENGTH  SCAN.  FOUR  ZONES
0002 LINE= 100
0004 PRINT "RETYPE LINE 4 AS..... 4 D$='DATE' THEN RUN PROG AGAIN.":STOP
0005 DIM P(4,80),A(4,80).L0=80
0006 DIM O(4),O1(4),O9(4),R(4),I(4),D(4),P1(4)
0008 GOTO 420
0010 DIGITS= 5.L4=INT(M2*100).R4=M2-L4/100
0020 IF R4<0.00125 THEN M2=L4/100
0030 IF R4>=0.00125 IF R4<0.00375 THEN M2=L4/100+0.0025
0040 IF R4>=0.00375 IF R4<0.00625 THEN M2=L4/100+0.005
0050 IF R4>=0.00625 IF R4<0.00875 THEN M2=L4/100+0.0075
0060 IF R4>0.00875 THEN M2=L4/100+0.01
0070 DIGITS= 0.RETURN
0100 IF M1<9.35 T.  M2=965.60376/(L1-147.2)+2.5968983.G. 160
0150 LET M2=1328.3526/(L1-121.4)+1.4671389
0160 GOSUB 10
0170 IF M2=M1 THEN WAIT W . RETURN
0180 LET S=(M2-M1)*400.X9=0.IF S<0 THEN X9=6
0200 POKE( 41947,X9).J=ABS(S)
0210 LET B9=INT(J/256) B0=INT(J-B9*256)
0220 POKE( 41945,B9):POKE(41946,B0)
0230 POKE( 40,161).POKE(41,242) . A=USER(X)
0300 IF S<0 THEN M1=M1-J*0.0025 : WAIT W . RETURN
0350 IF S>0 THEN M1=M1+J*0.0025 . WAIT W : RETURN
0420 LET T9=1.I. "REF NO.  ",F$:I. "TITLE ",R$.R$=R$+F$
0430 PRINT "HOW MANY ZONES"; : I. Z1 : IF Z1>4 THEN 430
0440 IF Z1<1 THEN 430
0445 PRINT "WAIT PERIOD"; . I. W
0450 INPUT "LAMBDA FIXED, VARIED OR LASER (F, V OR L)",L$
0460 IF L$<>"F" IF L$<>"V" IF L$<>"L" THEN 450
0470 IF L$<>"L" THEN I. "POSN.  - MM ",M1
0480 IF L$="L" THEN M1=4.5654 : L=633 : L2=L . GOTO 600
0500 IF M1<9.35 THEN L=965.60376/(M1-2.5968983)+147.2:GOTO 600
0550 LET L=1328.3526/(M1-1.4671489)+121.4
0600 PRINT "LAMBDA=";L;"NM"
0610 IF L$="V" THEN 650
0620 IF L$="F" THEN I. "LAMBDA REQD. ",L2
0630 LET L1=L2 . L3=0 . I. "NO.  OF POINTS",L7 . IF L7<0 THEN 630
0640 IF L7>L0 THEN P. "MAX.=";L0 . GOTO 630
0645 GOTO 730
0650 INPUT "LAMBDA START,END,STEP ",J2,J9,J3.L2=J2:L9=J9:L3=J3
0700 IF L9<L2 IF L3>0 THEN P. "RETYPE INSTRUCTION":GOTO 650
0720 LET L7=(L9-L2)/L3+1. IF L7>L0 THEN P. "TOO MANY POINTS". GOTO 650
0725 INPUT "NUMBER OF TIMES AROUND AVERAGEING LOOP ",V7
0730 FOR Z=1 TO Z1 . T=1 : T9=1 . IF Z=2 THEN T=L7
0731 DIGITS= 0
0732 IF Z<>1 THEN P.CHR$(7)+"  TARGET ZONE":I. Z$:GOTO 734
0733 GOTO 752
```

```
0724 LET Z9=VAL(RIGHT$(Z$,1)).Z$=LEFT$(Z$,1)
 0735 LET P7=Z9-1
0737 LET Q7=Z9*3.Q8=INT(Q7/2).IF Q8>=4 THEN Q8=Q8-3
0739 IF Z$="A" THEN Q9=Q8.A7=90*(2-(INT((Z9+1)/2)))
0741 IF Z$="B" THEN Q9=4-Q8.A7=90*(INT((Z9+1)/2)-1)
 0743 IF Z$="C" THEN Q9=Q8.A7=90*(INT((Z9+1)/2)-1)
0745 IF Z$="D" THEN Q9=4-Q8.A7=90*(2-(INT((Z9+1)/2)))
0747 PRINT CHR$(7)+"SET CIRCLES  Q=";45*Q9;"   P=";45*P7;"-";45*(P7+1),
0749 PRINT "  A=";A7;"-";90+A7;"  RUN ";Z;"  RET.  TO CONT."
 0750 INPUT Z$
0751 GOTO 753
0752 PRINT CHR$(7)+"SET CIRCLES - RUN ";Z;"PRESS RETURN TO CONTINUE":I.Z$
0753 IF Z=4 THEN T=L7
0755 IF T9>L7 THEN 1930
0757 IF L$<>"V" THEN 770
0760 FOR L1=L2 TO L9 STEP L3
0770 LET L8=L2
0780 PRINT L1
0800 IF L$<>"L" THEN GOSUB 100
 1000 LET V9=0.V8=0.WAIT W.FOR Z9=1 TO V7
1010 POKE( 40,161).POKE(41,00):F=USER(X)
 1050 FOR C=5 TO 1 STEP -2
1100 POKE( 41,112).B=USER(C):B$=STR$(B)
1150 LET D=VAL(LEFT$(B$,3)).M=VAL(MID$(B$,4,2)):S=VAL(MID$(B$,6,2))
1160 LET A9=D+M/60+S/3600
 1200 IF C=5 THEN A=A9 . GOTO 1290
1250 IF C=3 THEN P=A9 : GOTO 1290
1260 LET Q1(Z)=A9
1290 NEXT C
1300 POKE( 41,209):F=USER(X).FOR R=41966 TO 41964 STEP -2
1350 LET X=PEEK(R).X1=PEEK(R+1)
1400 IF X1>64 THEN X1=-X1.X=-X:X1=X1+128
1450 IF R=41966 THEN P1=X+256*X1:NEXT R
1500 LET A1=X+256*X1
1600 IF M1>6.745 THEN 1750
1650 LET V=0.227645/(M1-28.45)+0.0090533
1655 LET V=-V
 1700 LET V1=V*0.97959 . GOTO 1850
1750 LET V=2.1903106/(M1-75.0) +0.03065835
1755 LET V=-V
1800 LET V1=V*0.97959
 1850 LET P(Z,T)=P+P1*V.A(Z,T)=A+A1*V1
1852 IF P(Z,T)>360 THEN P(Z,T)=P(Z,T)-360
1854 IF P(Z,T)>180 THEN P(Z,T)=P(Z,T)-180
1856 IF A(Z,T)>360 THEN A(Z,T)=A(Z,T)-360
1858 IF A(Z,T)>180 THEN A(Z,T)=A(Z,T)-180
1860 LET V9=V9+P(Z,T).V8=V8+A(Z,T)
 1862 DIGITS= 3.P."P = ",P(Z,T);"(";P1;")","A = ";A(Z,T);"(";A1;")";
1864 DIGITS= 0.GOS.3000.P."          "+Z$.NEXT Z9
 1670 LET P(Z,T)=V9/Z9:A(Z,T)=V8/Z9:DIG.3:P."AVE P = ",P(Z,T),"AVE A = ";A(Z,T)
1872 DIGITS= 0
```

```
1900 IF Z=2 THEN T=T-1.GOTO 1920
1910 IF Z=4 THEN T=T-1.GOTO 1920
1914 LET T=T+1
1920 IF L$<>"V" THEN T9=T9+1:GOTO 755
1925 NEXT L1
1930 LET L2=L9.L3=-L3:L9=L8:NEXT Z
1940 PRINT "O/P CH. NO. (VDU=1, PRINTER=4)".I.C
1950 IF C<>1 IF C<>4.THEN 1940
1990 PRINT £C,CHR$(27)+CHR$(15)+R$
1998 LET L7=INT(L7+0.1)
2000 FOR T=1 TO L7
2005 IF L$="L" T.P.£C,"632.8 nm":DIG.4:G.2150
2010 IF L$="F" THEN PRINT£C,L1;"nm" : GOTO 2150
2100 PRINT £C,J2+(T-1)*J3;" nm".DIG.4
2150 PRINT £C,"P ",P(1,T),TAB(15),P(2,T),TAB(28);P(3,T);TAB(39);P(4,T)
2156 PRINT £C,"A ";A(1,T);TAB(15);A(2,T);TAB(28);A(3,T);TAB(39);A(4,T);
2157 DIGITS= 0
2160 FOR Z=1 TO 4
2162 GOSUB 3000
2164 PRINT £C,"   ";Z$;
2166 NEXT Z
2168 PRINT £C," "
2200 NEXT T
2300 PRINT "   INPUT   C TO CONTINUE (CALC. DEL & PSI)"
2310 INPUT "                OR ANYTHING ELSE TO RE-PRINT P & A",W$
2320 IF W$<>"C" T. 1940
2400 INPUT "O/P CHANNEL NO.",C.IF C<>1 IF C<>4 T.2400
2500 GOTO 3900
3000 REM FIND ZONE
3010 LET P5=P(Z,T).IF P5>360 THEN P5=P5-360
3015 IF P5>180 THEN P5=P5-180
3020 LET A5=A(Z,T):IF A5>360 THEN A5=A5-360
3025 IF A5>180 THEN A5=A5-180
3030 LET Q5=INT(Q1(Z)+.5) . IF Q5>180 THEN Q5=Q5-180
3100 LET Z2=INT(P5/45+1) :Z5=4*INT(A5/90)+8*INT(Q5/130)
3400 LET Z$=MID$("CBADADCBBCDADABC",Z5+Z2,1) +STR$(Z2) : RETURN
3900 PRINT £C,R$,TAB(60);D$
4000 DIGITS= 4:P.£C,"Q =";:FOR Z=1 TO Z1:P.£C*TAB(5+(Z-1)*10);Q1(Z);:NEXT Z
4010 DIGITS= 0
4020 PRINT £C,TAB(50);"DELTA";TAB(60);"PSI"
4050 FOR T=1 TO L7 . D=0 . P=0
4100 FOR Z=1 TO Z1
4110 LET Q(Z)=TAN(Q1(Z)*PI/180)
4130 LET A(Z,T)=TAN(A(Z,T)*PI/180)
4140 LET P(Z,T)=TAN((P(Z,T)-Q1(Z))*PI/180)
4200 LET Q9(Z)=Q(Z)*Q(Z)*P(Z,T)*P(Z,T)+1
4300 LET R(Z)=A(Z,T)*Q(Z)*(P(Z,T)*P(Z,T)-1)/Q9(Z)
4350 LET I(Z)=A(Z,T)*P(Z,T)*(Q(Z)*Q(Z)+1)/Q9(Z)
4370 IF R(Z)=0 THEN D(Z)=0 : GOTO 4750
4400 LET D(Z)=ATAN(I(Z)/R(Z))
```

```
4450 IF R(Z)>0 THEN 4600 .
4500 LET D(Z)=(D(Z)+PI)*180/PI . GOTO 4750
4600 IF I(Z)>0 THEN 4700
4650 LET D(Z)=(D(Z)+2*PI)*180/PI : GOTO 4750
4700 LET D(Z)=D(Z)*180/PI
4750 LET P1(Z)=(ATAN(SQR(R(Z)*R(Z)+I(Z)*I(Z))))*180/PI
4850 LET D=D+D(Z)/Z1 . P=P+P1(Z)/Z1 . NEXT Z
5000 REM PRINT
5015 IF L$="L" T. P. £C,"632.8 nm".G.5130
5017 IF L$="F" T. P. £C,L1;"nm" . GOTO 5130
5120 PRINT £C,J2+(T-1)*J3;" nm"
5130 DIGITS= 4
5140 FOR Z=1 TO Z1:P. £C,TAB(5+(Z-1)*10);D(Z), .NEXT Z
5160 PRINT £C,TAB(50);D
5170 FOR Z=1 TO Z1:P. £C,TAB(5+(Z-1)*10);P1(Z); .NEXT Z
5180 PRINT £C,TAB(60);P
5190 LET P(1,T)=P.A(1,T)=D.DIG.0.NEXT T
5200 INPUT "TAPE IDENTIFIER ",T$
5220 INPUT "TAPE SIDE        ",S9
5230 INPUT "POSITION         ",P9
5238 PRINT £C,"FILE NAME ",F$,
5240 PRINT £C," TAPE ";T$;"  SIDE ";S9;"  POSITION ";P9
5300 INPUT "RETURN TO START DATA DUMP",Z$
5500 OPEN O F$
5600 FOR T=1 TO L7
5620 LET L=J2+(T-1)*J3
5700 LET D=A(1,T):P=P(1,T)
5800 TWRITE D,P,L
5900 NEXT T
6000 CLOSE
6100 WAIT 10
6200 INPUT "PAPER TAPE DUMP (Y OR N)",Z$
6220 IF Z$<>"Y" THEN 9999
6240 PRINT £5,R$+"  "+D$
6260 FOR T=1 TO L7
6280 PRINT £5,A(1,T);",";P(1,T);",";L
6300 NEXT T
9999 END
```

Appendix A1.5 Peripheral interface adapter.

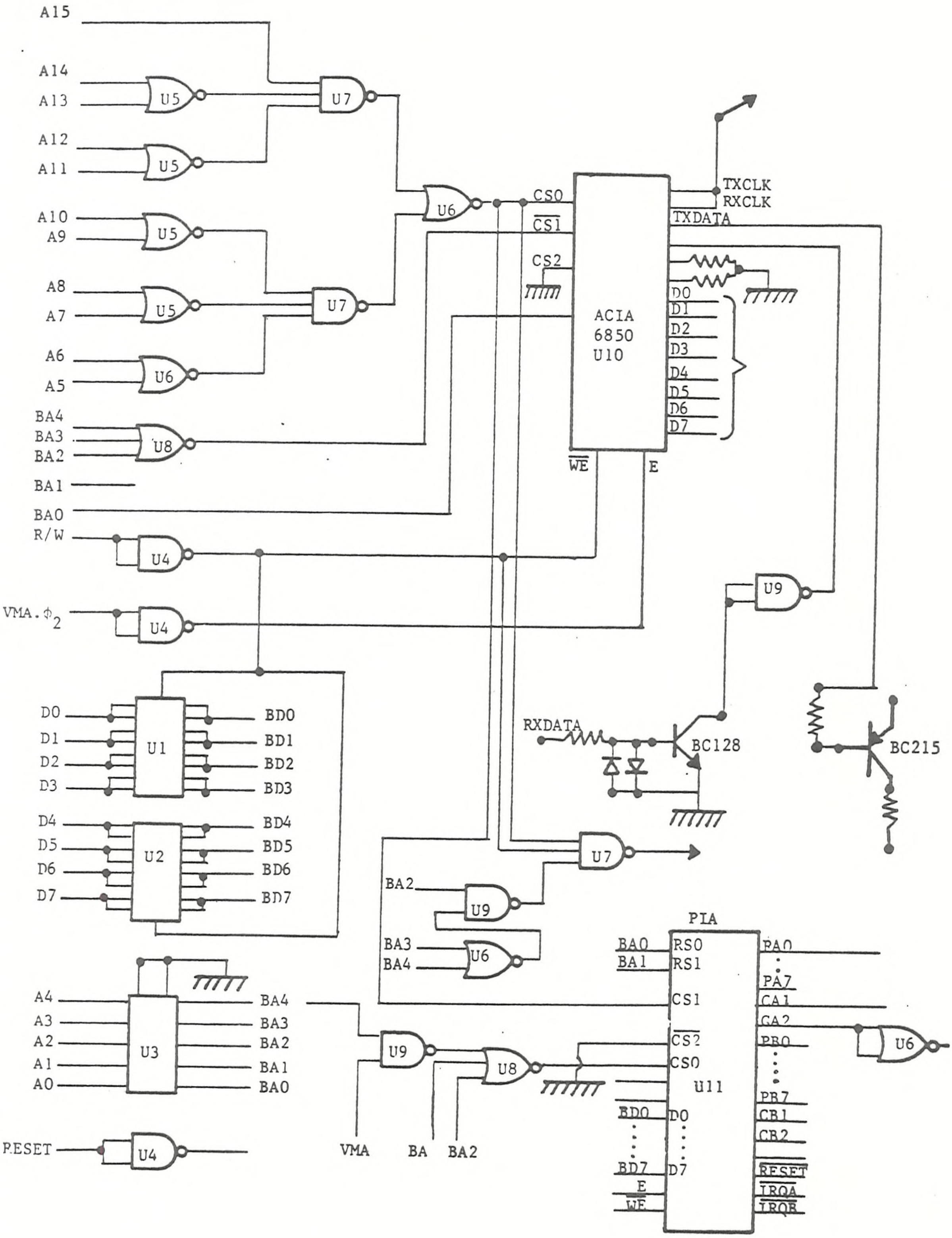

Appendix B

Complex dielectric function and optical constants of mercury

	Dielectric function		Optical constants		
E/eV	K'	K"	n	k	λ/nm
1.8	-25.94	25.50	2.284	5.582	688.8
2.0	-22.87	19.67	1.910	5.150	619.9
2.2	-19.94	15.40	1.621	4.751	563.6
2.4	-17.50	12.19	1.383	4.406	516.6
2.6	-15.32	9.071	1.186	4.090	476.9
2.8	-13.40	7.809	1.027	3.802	442.8
3.0	-11.71	6.354	0.898	3.538	413.3
3.2	-10.21	5.258	0.798	3.294	387.4
3.4	-8.938	4.383	0.713	3.074	364.7
3.6	-7.764	3.685	0.644	2.860	344.4
3.8	-6.754	3.141	0.589	2.665	326.3
4.0	-5.964	2.711	0.542	2.502	310.0
4.2	-5.225	2.372	0.506	2.341	295.2